

GEORGIA INSTITUTE OF TECHNOLOGY
OFFICE OF CONTRACT ADMINISTRATION
SPONSORED PROJECT INITIATION

Date: October 15, 1979

Project Title: The Structure and Reactivity of Heterogeneous Surfaces and Study of the Geometry of Surface Complexes

Project No: G-41-687 *Green card*

Project Director: Dr. Uzi Landman

Sponsor: Department of Energy; Oak Ridge Operations; Oak Ridge, TN 37830

Agreement Period: From 9/1/79 Until 10/31/80 (Mod. A002 Period)

Type Agreement: Contract No. DE-AS05-77ER05489 (Formerly EG-77-S-05-5489)

Amount: \$125,462 DOE (G-41-687) Incl. \$121,462 new funds
23,897 GIT (G-41-327)
\$149,359 Total

Reports Required: Publication Preprints; Publication Reprints; Progress Report;
Final Report

Sponsor Contact Person (s):

Technical Matters

Contractual Matters

(thru OCA)

Mr. A. H. Frost, Jr., Chief
Contract Management Branch
Procurement and Contracts Division
Department of Energy
Oak Ridge Operations
P. O. Box E
Oak Ridge, TN 37830

Walker Love, 615/576-0791

NOTE: Follow-on to G-41-674.

Defense Priority Rating: None

Assigned to: Physics (School/Laboratory)

COPIES TO:

Project Director
Division Chief (EES)
School/Laboratory Director
Dean/Director-EES
Accounting Office
Procurement Office
Security Coordinator (OCA)
Reports Coordinator (OCA)

Library, Technical Reports Section
EES Information Office
EES Reports & Procedures
Project File (OCA)
Project Code (GTRI)
Other _____

GEORGIA INSTITUTE OF TECHNOLOGY
OFFICE OF CONTRACT ADMINISTRATION
SPONSORED PROJECT TERMINATION

Date: 2/12/81

Project Title: The Structure and Reactivity of Heterogeneous Surfaces and
Study of the Geometry of Surface Complexes

Project No: G-41-687

Project Director: Dr. Uzi Landman

Sponsor: Department of Energy; Oak Ridge Operations; Oak Ridge, TN 37830

Effective Termination Date: 10/31/80

Clearance of Accounting Charges: 10/31/80

Grant/Contract Closeout Actions Remaining:

- Final Invoice and Closing Documents
- Final Fiscal Report
- ~~Final~~ Report of Inventions (Interim)
- Govt. Property Inventory & Related Certificate
- Classified Material Certificate
- Other Certified Statement of Costs (9/1/79 - 10/31/80)

Note: Continued by G-41-618

Assigned to: Physics (School/~~Library~~)

COPIES TO:

Project Director	Library, Technical Reports Section
Division Chief (EES)	EES Information Office
School/Laboratory Director	Project File (OCA)
Dean/Director—EES	Project Code (GTRI)
Accounting Office	Other <u>OCA Research Property Coordinator</u>
Procurement Office	
Security Coordinator (OCA)	
Reports Coordinator (OCA)	

PROGRESS REPORT

"THE STRUCTURE AND REACTIVITY OF HETEROGENEOUS SURFACES
AND STUDY OF THE GEOMETRY OF SURFACE COMPLEXES"

Period Covered: September 1, 1979 - October 31, 1980

U. S. Department of Energy

Contract Number DE-AS05-77ER05489

by

UZI LANDMAN

SCHOOL OF PHYSICS

GEORGIA INSTITUTE OF TECHNOLOGY

ATLANTA, GA. 30332

U.S. ENERGY RESEARCH & DEVELOPMENT ADMINISTRATION
UNIVERSITY-TYPE CONTRACTOR'S RECOMMENDATION FOR
DISPOSITION OF SCIENTIFIC AND TECHNICAL DOCUMENT

(See Instructions on Reverse Side)

1. ERDA REPORT NO. CONTRACT NO: EG-77-S-05-5489	2. TITLE The Structure and Reactivity of Heterogeneous Surfaces and Study of the Geometry of Surface Complexes
---	--

3. TYPE OF DOCUMENT (Check one):

a. Scientific and technical report

b. Conference paper:

Title of conference _____

Date of conference _____

Exact location of conference _____

Sponsoring organization _____

c. Other (Specify)

4. RECOMMENDED ANNOUNCEMENT AND DISTRIBUTION (Check one):

a. ERDA's normal announcement and distribution procedures may be followed.

b. Make available only within ERDA and to ERDA contractors and other U.S. Government agencies and their contractors.

5. REASON FOR RECOMMENDED RESTRICTIONS:

6. SUBMITTED BY: NAME AND POSITION (Please print or type)

Uzi Landman, Professor of Physics

Organization

School of Physics
Georgia Institute of Technology
Atlanta, Georgia 30332

Signature 	Date July 23, 1980
--	-----------------------

FOR ERDA USE ONLY

7. ERDA CONTRACT ADMINISTRATOR'S COMMENTS, IF ANY, ON ABOVE ANNOUNCEMENT AND DISTRIBUTION RECOMMENDATION:

8. PATENT CLEARANCE:

a. ERDA patent clearance has been granted by responsible ERDA patent group.

b. Report has been sent to responsible ERDA patent group for clearance

c. Patent clearance not required.

INSTRUCTIONS

Who uses this Form: ERDA contract administrators will designate the ERDA contractors who are to use this Form. Generally speaking, it will be used by educational institutions and other "not for profit" institutions. ERDA National Laboratories and other major contractors will generally use the longer Form ERDA-426.

When to use this Form: ERDA contractors are required under their contracts to transmit specified types of documents to the ERDA. Some, but not all, of these are transmitted by ERDA contract administrators to ERDA's Technical Information Center (TIC) and may be incorporated into ERDA's technical information documentation system. Types of documents which will be transmitted to TIC are identified in instructions which the contractor receives from his contract administrator. Each such document is to be accompanied by one copy of this transmittal Form recommending to TIC appropriate announcement and distribution of the document. Documents which the contractor may be required to submit to the ERDA under his contract but which are not of the type to be transmitted to TIC, e.g., contract proposals, should not be accompanied by a copy of this transmittal Form.

Where to send this Form: Send the document and the attached Form ERDA-427 to the ERDA contract administrator for transmittal to TIC unless the ERDA contract administrator specifies otherwise.

Item instructions:

Item 1. The first element in the number shall be an ERDA-approved code. This may be a code which is unique to the contractor, e.g., MIT, or it may be the code of the AEC operations office, i.e., COO, ORO, IDO, SRO, SAN, ALO, RLO, NVO. The contract administrator will specify the code which is to be used.

The code shall be followed by a sequential number, or by a contract number plus a sequential number, as follows: (a) Contractors with unique codes may complete the report number by adding a sequential number to the code, e.g., MIT-101, MIT-102, etc.; or they may add the identifying portion of the contract number and a sequential number, e.g., ABC-2105-1, ABC-2105-2, etc.; (b) Contractors using the

operations office code shall complete the report number by adding the identifying portion of the contract number and a sequential number, e.g., COO-2200-1, COO-2200-2, etc. Subcontractor reports shall be identified with the code used by the prime contractor.

- Item 2.** Give title exactly as on the document itself.
- Item 3.** If box c is checked, indicate type of item being sent, e.g., thesis, translation, etc.
- Item 4.** The "normal announcement and distribution procedures" for unclassified documents may include abstracting in "Nuclear Science Abstracts" (NSA); and distribution to appropriate TID-4500 ("Standard Distribution of Unclassified Scientific and Technical Reports") addressees, to libraries which through purchase of microfiche maintain collections of ERDA reports, and to the National Technical Information Service (NTIS) for sale to the public. Check 4b if there is need for limiting announcement and distribution procedures described above.
- Item 5.** If 4b is checked, give reason for recommending announcement or distribution restrictions, e.g., "preliminary information", "prepared primarily for internal use", etc.
- Item 6.** Enter name of person to whom inquiries concerning the recommendations on this Form may be addressed.
- Item 7.** ERDA contract administrator may use this space to show concurrence or nonconcurrence with the recommendation in item 4 and to make other recommendations.
- Item 8.** ERDA contract administrators may use this space to representative should check a, b, or c, and forward this Form and the document to:

USERDA-TIC
P.O. Box 62
Oak Ridge, TN 37830

U.S. DEPARTMENT OF ENERGY
NOTICE OF ENERGY RD&D PROJECT

FORM DOE 538
(7/78)

APPROVED FOR USE BY
SMITHSONIAN SCIENCE INFORMATION EXCHANGE

FORM APPROVED
OMB NO. 38 R-0190

1. DESCRIPTIVE TITLE OF WORK
The Structure and Reactivity of Heterogeneous Surfaces

2. PERFORMING ORGANIZATION CONTROL NUMBER
3. CONTRACT, GRANT OR PURCHASE ORDER NUMBER
EG-77-S-05-5489

4. CONTRACTOR'S PRINCIPAL INVESTIGATOR/PROJECT MANAGER AND ADDRESS WHERE WORK IS PERFORMED
a. NAME (Last, First, MI) Landman, Uzi PHONE (404) 894-3368
b. BUSINESS ADDRESS: STREET School of Physics, Georgia Institute of Technology
CITY Atlanta, STATE Georgia ZIP 30332

5. a. NAME OF PERFORMING ORGANIZATION
Georgia Institute of Technology School of Physics
(Organization) (Department)
b. MAILING ADDRESS (If Different From 4B)
c. TYPE OF ORGANIZATION PERFORMING THE WORK (Enter applicable code from instructions). C U

6. SUPPORTING ORGANIZATION
a. DOE PROGRAM DIVISION OR OFFICE (Full Name) Division of Materials Sciences, Office of Basic Energy Sciences
b. TECHNICAL MONITOR (Last, First, MI)
c. ADDRESS (If Different from DOE Hqs) DOE Hqs., Mail Stop J-309
d. ADMINISTRATIVE MONITOR (Last, First, MI) D. Stevens

7. PROJECT SCHEDULE (a) START DATE June 1977 (b) EXPECTED COMPLETION DATE N/A
(Month) (Year) (Month) (Year)

8. a. FUNDING OPERATING AND CAPITAL EQUIPMENT OBLIGATION (In Thousands of Dollars)

FUNDING ORGANIZATION(S)	APPROXIMATE CUMULATIVE PRIOR FISCAL YEARS	CURRENT FY		
1. DOE as in (6)	170	125		
2.				
3.				

b. DOE BUDGETING AND REPORTING CLASSIFICATION CODE _____

DIRECT SCIENTIFIC AND TECHNICAL MANPOWER

	PROFESSIONAL	GRAD. STUDENTS	OTHER	TOTAL
NUMBER	4	3		7
EQUIVALENT PERSONYEARS	3 1/3	1		4 1/3

DETACH HERE BEFORE SUBMITTING

10. SUMMARY OF WORK (Limit to 200 words or less - include a description, objective, approach and a final product expected.)

The objective of the project is to provide a coherent, fundamental understanding of the material parameters which control its' structure, electronic and vibronic characteristics and reactivity. The studies involve analytical and computer simulation methods. Various properties which influence transport, diffusion, reactivity, structure reconstruction, vibrational and electronic spectra, stability and phase transformations of systems relevant to energy technologies (such as solar, fusion and catalysis) are investigated.

11. PROGRESS SINCE LAST REPORT (Limit to 100 words.)

A surface molecular dynamics program which allows the investigation of equilibrium and non-equilibrium processes at surfaces and interfaces has been developed. A detailed study of epitaxial crystallization from a supercooled melt conducted. Vibrational spectra of catalytic heterogeneous surfaces. A microscopic theory of reaction processes catalyzed by surfaces. A theory of shallow donor impurities at semi-conductor interfaces. A theory of surface reconstruction in metals. Surface diffusion and diffusion controlled reactions.

12. List publications in the last year that are available to the public which have resulted from the product. (Please give a complete bibliographic citation. Use additional sheets if necessary.)

(On attached sheets)

13. GENERAL TECHNOLOGY CATEGORIES (Enter applicable code or codes from instructions.)

A 2 A 4 E 4 D 1 D 3 F 5 F 2

← Catalytic Reactions

PHASE OF RD&D (Enter Project Percentage: in Applicable Boxes)

a. 80% Basic Research

b. 20% Applied Research (Laser annealing)

c. Technology Development Liquid phase epitaxy.

d. Engineering Development

e. Demonstration

15. KEYWORDS: (Minimum of 5)

Surface Molecular Dynamics of Interfaces; Liquid-Phase Epitaxy; Semi-Conductor Interfaces; Surface Reactions; Surface Diffusion; Surface Reconstruction.

A. RESPONDENT'S NAME & ADDRESS

Uzi Landman, School of Physics
Georgia Institute of Technology

B. PHONE NO.

4 0 4 8 9 4 - 3 3 6 8

C. DATE

July 22, 1980

Atlanta, Georgia 30332

12. PUBLICATIONS (continued from previous page)

1. "Stochastic Theory of Multistate Diffusion in Perfect and Defective Systems. I. Formalism", Phys. Rev. B 19, 6207 (1979), Uzi Landman and M. F. Shlesinger.
2. "Stochastic Theory of Multistate Diffusion in Perfect and Defective Systems. II. Case Studies", Phys. Rev. B 19, 6220 (1979), Uzi Landman and M. F. Shlesinger.
3. "Electron Scavenging in Glasses", J. Chem. Phys. 70, 4813 (1979), M. F. Shlesinger.
4. "Conditions for a Rate-Maximizing Temperature in Heterogeneous Catalysis", J. Catalysis 61, 270 (1980), M. F. Shlesinger and Uzi Landman.
5. "Quadrupole Interaction in the Scattering of H₂ from the Surface of LiF: Rotational Transitions", Phys. Rev. B (June 15) 1979, N. R. Hill.
6. "High Energy Frequency Vibrational Modes at Stepped Pt(111) Surfaces", Phys. Rev. B 20, 1775 (1979), Mark Mostoller (ORNL) and Uzi Landman.
7. "Microscopic Theory of Thermal Desorption and Dissociation Processes Catalyzed by a Solid Surface", Phys. Rev. B 21, 3256 (1980), Gopa De and Uzi Landman (GIT); Mark Rasolt (ORNL).
8. "Lattice Relaxation at Metal Surfaces: An Electrostatic Model", Phys. Rev. B 21, 448 (1980), Uzi Landman and N. R. Hill (GIT); Mark Mostoller (ORNL).
9. "Substrate Effects on Long-Range Order and Scattering from Low-Dimensional Systems", Phys. Rev. B (August 15, 1980), C. L. Cleveland, C. S. Brown and Uzi Landman.
10. "Substrate Effects on Long-Range Order and Scattering from Low-Dimensional Systems" in "Ordering in Two-Dimensions", S. K. Sinha, Ed. (North-Holland, 1980), C. L. Cleveland, C. S. Brown and Uzi Landman.
11. "Epitaxial Crystallization from a Melt", in "Ordering in Two-Dimensions", S. K. Sinha, Ed. (North-Holland, 1980), Uzi Landman, C. L. Cleveland and C. S. Brown.
12. "Correlation Effects on Frequency Dependent Conductivity: Application to Superionic Conductors", Solid State Comm. 32, 1207 (1979), M. F. Shlesinger.
13. "Prospects for Studying Chemisorption Kinetics Using Current Fluctuations", Surface Science 95, 67 (1980), G. S. De and H. Suhl.

This progress report summarizes the main results of studies conducted by the Surface Science group under the sponsorship of the Department of Energy. The period covered by the report is September 1979 - October 31, 1980.

The program of studies of the group is designed as a broad, coordinated plan of investigations of certain surface phenomena. Our studies (both analytical and molecular dynamics simulation) probe structural (crystallography and phase transformations), electronic, vibronic, kinetical and dynamical aspects of surfaces in an attempt to provide a basic understanding of certain properties and interaction processes at surfaces which are of both fundamental and applied relevance.

The work done by members of the group combines the elements of basic research endeavors with training and education of young scientists as evidenced by the composition of the group which includes besides the principal investigator, post-doctoral fellows and three graduate students.

The report is organized as follows: statements of progress of the projects and manuscripts pertaining to the subjects of investigations are given in Chapter I. In Chapters II. and III. lists of publications and talks by members of the group are given. Members of the group are listed in Chapter IV.

CONTENTS

	page
I. STATEMENTS OF PROGRESS	
A. Surface Molecular Dynamics Studies of Surfaces and Interfaces. .	IA - 1
B. Surface Crystallography.	IB - 1
C. Surface Reactions.	IC - 1
D. Transport and Diffusion.	ID - 1
E. Structure and Scattering - Low Dimensional Systems	IE - 1
F. Cooper-Pairing in the Vicinity of a Localized Phonon Mode. . . .	IF - 1
G. Local Electronic Properties: Si.	IG - 1
H. Vacancy Formation and Migration at Metallic Surfaces	IH - 1
I. Shallow Donor Impurities at Semiconductor Interfaces	II - 1
II. LIST OF PUBLICATIONS FOR THE REPORT PERIOD	II. - 1
III. LIST OF CONFERENCE TALKS	III.- 1
IV. PERSONNEL.	IV. - 1

I. STATEMENTS OF PROGRESS

	page
A. Surface Molecular Dynamics Studies of Surfaces and Interfaces. . .	IA - 1
B. Surface Crystallography.	IB - 1
C. Surface Reactions.	IC - 1
D. Transport and Diffusion.	ID - 1
E. Structure and Scattering - Low Dimensional Systems	IE - 1
F. Cooper-Pairing in the Vicinity of a Localized Phonon Mode.	IF - 1
G. Local Electronic Properties: Si.	IG - 1
H. Vacancy Formation and Migration at Metallic Surfaces	IH - 1
I. Shallow Donor Impurities at Semiconductor Interfaces	II - 1

A. SURFACE MOLECULAR DYNAMICS STUDIES OF SURFACES AND INTERFACES

The main achievements of these studies are:

1. Development testing and implementation of a Surface Molecular Dynamics program which enables the investigation of equilibrium and non-equilibrium surface phenomena.
2. Development and implementation of an Interface Molecular Dynamics program which allows the study of equilibrium properties and non-equilibrium evolution at interfaces.
3. A detailed study of the epitaxial crystallization of a supercooled liquid film. Development of a novel picture of the process. The time evolution of a number of characteristic properties (such as particle number profiles vs. distance, positional and orientational order parameters, kinetic temperature, potential energies, pair distribution functions) has been monitored throughout the crystallization process. Stages of the phase transformation which involve cluster nucleation, layering of the fluid which precedes intralayer ordering, and interlayer order-disorder phenomena have been identified.
4. A study of the epitaxial crystallization of a hot liquid film.
5. A study of the annealing of surface defects via liquid-phase-epitaxy; identification of the kinetic steps of surface disordering and recrystallization.
6. Studies of the surface phase transformations of a bcc material (Rubidium) with pair-wise pseudo-potentials of interaction.
7. Development of graphic routines, and accumulation of frames for a computer movie of epitaxial crystallization and surface melting.

EPITAXIAL CRYSTALLIZATION FROM A MELT:

A SURFACE MOLECULAR DYNAMICS STUDY*

Uzi LANDMAN, Charles I. CLEVELAND and Charles S. BROWN

School of Physics, Georgia Institute of Technology, Atlanta, Georgia 30332

ABSTRACT

A newly developed Surface Molecular Dynamics method is described and employed to investigate the epitaxial crystallization of a supercooled melt. The procedure allows for thermal dissipation via a dynamic bulk reservoir, thus enabling the study of the approach to equilibrium. The early stages of the crystallization involve layering in the fluid, followed by intralayer ordering. The kinetics and dynamic coupling between fluid and solid regions is exhibited in particle number, temperature, potential energy, orientational and translational order-parameter profiles.

Epitaxial solidification of materials from a melt is an important scientific and technological process. The earliest theoretical models of crystallization at interfaces due to Wilson¹ and Frenkel² assume a continuous growth mode. Later models employ a two-dimensional nucleation and growth process³ and an attempt at a phenomenological unification of the above approaches has been advanced by Cahn⁴. In addition, kinetic models⁵ based on phenomenological mass transport and atomic incorporation into the crystal and studies of kinetic Ising models and the roughening transition have been reported.⁶

The objective of this study is to explore the kinetics, dynamics and microscopic elementary processes of epitaxial phase transformation. We employ the molecular dynamics (MD) technique, which proved to be a powerful tool for the study of liquids⁷, condensed matter and certain phase transformations⁸. In order to use the method for our study of the liquid-solid interface we must first provide an adequate description of the substrate surface.

Surface Molecular Dynamics (SMD): In MD the classical equations of motions of an interacting collection of particles are integrated and the recorded phase-space trajectories $(\vec{r}(t), \vec{v}(t))$ are then analyzed. In most MD studies periodic boundary conditions (pbc) are used. 3D pbc's are appropriate for the description of bulk properties. A different situation is presented for a system which contains a surface. While for a two-dimensional system the question of pbc's is simple, a semi-infinite system is a much harder problem. A schematic description of the system is shown in Fig. 1. The "bulk block" (B) and "surface block" (S), consist each of 500 particles, interacting via a 6-12 Lennard-Jones potential. The B-system possesses 3D pbc's and the S-system possesses only 2D pbc's and is free in the z direction. Consequently, while the dynamics of particles in the S-system is influenced by that of

particles in the B-system, the reverse statement does not hold, (in the spirit of a bulk being an infinite reservoir whose dynamics and properties should not be influenced by surface effects). To provide for Newton's third-law (or fluctuation-dissipation), the first 3 layers of the S-B interface are used as a "coupling region" on which we impose (time-step by time-step) a scaling of velocities such that the average kinetic energies (kinetic temperature) in these layers is equal to the corresponding bulk ones. The integration of the equations of motions is performed using a predictor-corrector method⁷ with a time step $\Delta t^* = 0.0075^9$ and the evolution of the S and B systems is synchronized at each time-step. The S-B system has been equilibrated as an fcc crystal (the density of the B system is adjusted to yield a vanishing average equilibrium pressure) exposing the (001) face, at a temperature $T^* = 0.4$ (Ar melts at $T^* = 0.7$). The above SMD technique has an advantage over slab configurations or calculations in which a static or a random matrix representation of the bulk are used. It allows the investigation of equilibrium and non-equilibrium surface and interface phenomena in which the dynamics of the bulk reservoir is included. Using our method we currently investigate: surface melting, defects, surface alloy dynamics, and transport phenomena.

Surface - Liquid System: Having equilibrated the surface described above we prepare an equilibrated liquid sample. In the following we describe the results for a supercooled L-J liquid film¹⁰ (2D pbc's and free in the third direction) consisting of 500 particles, at $T^* = 0.4$ (see block L in Fig. 1. other liquids such as: bulk 3D pbc's sample, and a liquid film at $T^* = 0.737$ have also been investigated by us). Once equilibrated the L system is positioned at a distance chosen such that the smallest distance between a surface and a liquid particle is equal to 1.12σ , (the location of minimum of the L-J

potential) and the evolution of the coupled system is followed. Sample particle-number versus z profiles at various time steps are shown in Fig. 2.

It is observed that while the layers in the solid are well defined, those in the liquid fluctuate, averaging to the density profile of a liquid film.

However, as time progresses a permanent layering of the liquid occurs. In fact stratification of the liquid in the z , (001), direction precedes the achievement of intralayer good crystalline order. Note also that the topmost layer distance of the surface (layer 10) first expands (in fact it is expanded already at $t = 0$) and upon solidification of the liquid it contracts to the bulk spacing. In the following, layers in the liquid region are defined as regions in space whose thickness in the (001) direction is that of the next to the top-most layer of the solid surface (layer 9). Samples of the layer kinetic temperatures $T^* = k_B T / \epsilon$, defined as the mean kinetic energy of particles in layer ℓ , and layer potential energies versus time are shown in Figs. 3-6. Also shown are the orientational order parameters O_4 and O_6 defined as

$$O_n^\ell(t) = |N_\ell^{-1} \sum_{I, J \in \ell} N_{I, nn}^{-1} \exp(in \theta_{IJ}) \textcircled{H}(R_{nn} - |\vec{r}_I - \vec{r}_J|)|^2, \quad n = 4, 6 \quad (1)$$

and the translational structure factors $S(\vec{k})/N_\ell = |N_\ell^{-1} \sum_{I \in \ell} \exp(i\vec{k} \cdot \vec{r}_I)|^2$.

N_ℓ is the number of particles in layer ℓ at time t , \textcircled{H} is the Heavyside step function, R_{nn} is the neighbor distance, $N_{I, nn}$ is the number of neighbors to particle I within a sphere of radius R_{nn} , θ_{IJ} is the "bond" angle between I and J with reference to an arbitrary direction. O_4 and O_6 take the values 1 and 0, respectively, for a perfect cubic crystal, while in the liquid state O_6 is generally larger than O_4 , \vec{k} is a bulk reciprocal vector.

Observation of the T^* plot reveals that they undergo a maximum around $t/\Delta t = 1000$ for layers 9-13. This is also the time at which the monotonic decrease in the layers potential energies achieve a plateau. In addition, the structure factors for $\vec{k} = (2\pi/a) (0, 0, 2)$, i.e., a reciprocal vector in the normal direction, exhibit a noted increase at this time. Notice that while at $t = 0$ layers 9 and 10 (solid surface) were less stable, less coordinated, than a deeper layer they, along with the crystallized layers of the liquid, achieve eventually a bulk value. The time variation of the orientational order parameters reveals the dynamically coupled nature of the process. While the maximum in T^* indicates the expulsion of latent heat of ordering and is associated mainly with the "layering" of the fluid (and occurs at approximately the same time for a wide region of the liquid), the variations in O_4 and O_6 reflect intralayer ordering. Following the peak in O_4 designated by an arrow from layer to layer it is seen that it shifts to longer times for higher layers and in consecutive layers the peaking of O_4 is associated with a minimum in a neighboring layer. From the time delay of ordering in consecutive regions in the liquid the velocity of crystallization is estimated to be ~ 100 m/sec. This systematic variation reflects the thermal coupling of the layers (there is no mass transport between layers at these times) and the transient order - disorder transformations which they undergo during the evolution of the system. Similar behaviour is observed in O_6 . Added confirmation that crystal-liquid layering precedes intralayer fcc crystalline ordering is provided via the $S(\vec{k})$'s for an in-plane reciprocal vector $\vec{k} = (2\pi/a) (2, 0, 0)$. Additionally, we observe that layer 10 (and even 9) initially partially disorder (roughened?) and eventually order (smoothed?). We have also observed that in case of a surface which contains a planar defect an annealing occurs.

Finally, it is of interest to comment upon the embryonic stage of the crystallization process. The formation of the first epitaxial layer involves a cluster of supercooled liquid atoms rather than random single particle adsorption described by lattice-gas models. This cautions against the direct extrapolation of theories of gas-solid epitaxial crystallization to liquid phase epitaxy.

We gratefully acknowledge most valuable help and advise by Aneesur Rahman. The assistance and services of the GIT computer center, Rand Childs and Jerry Segers in particular, proved invaluable to this work.

REFERENCES

*Work supported by U.S. DOE Contract No. EG-S-05-5489.

1. H. A. Wilson, *Phil. Mag.* 17, 283 (1900).
2. J. Frenkel, *Physik Z. Sovjet union* 1, 498 (1932).
3. D. P. Woodruff, *The Liquid State* (Cambridge University Press, 1973), chap. 8.
4. J. W. Cahn, *Acta Met.* 8, 554 (1960).
5. J. C. Brice in *Current Topics in Materials Science*, Vol. 2, Eds., E. Kaldis and H. J. Scheel (North-Holland, Amsterdam, 1977), pp. 572, and references therein.
6. H. Muller-Krumbhaar, in *ibid*, pp. 116; G. H. Gilmer and K. A. Jackson, in *ibid*, pp. 80.
7. A. Rahman, *Phys. Rev.* 136, A405 (1964).
8. In particular, see the recent studies of homogeneous nucleation by C. S. Hsu and A. Rahman, *J. Chem. Phys.* 70, 5234 (1979), and *ibid.* 71, 4974 (1979).
9. Reduced units are used throughout the paper. The reduced time is $t^* = \mu\sigma^2/\epsilon$ where μ is mass, σ and ϵ are the 6-12 Lennard-Jones parameters. For Argon $\sigma = 3.4 \text{ \AA}$, $\epsilon/k_B = 120^\circ\text{K}$, and $t^* = 1.65 \times 10^{-12}$ sec. Energy is in units of ϵ . The potential cutoff is 2.5σ . In the figures, length is given in units of 7.94σ . Layers are numbered increasingly from the surface bulk interface, with layer 10 being the top-most layer of the solid surface. $t = 0$ is the time the equilibrated B-S and L systems are put together.
10. This non-equilibrium system in which initially no thermal gradients exist is intrinsically interesting since we follow the approach to equilibrium of a meta-stable state.

FIGURE CAPTIONS

Figure 1. Schematic description of the bulk (B) - surface (S) - liquid (L) system. The bulk block possesses 3D pbc's, the S and L possesses 2D pbc's. The coupling region is hatched. Also included is the particle number versus z profile of the system at $t = 0$, consisting of an equilibrated surface and supercooled liquid film at $T^* = 0.4$. Distance in units of 7.94σ .

Figure 2. Particle number versus z at 4 different times during the evolution of the system. Note the layering in the liquid region. The small peak at $z \approx 1.1$, at the 250th time step corresponds to the embryonic cluster (see text).

Figures 3-6. Time evolution of the kinetic temperature $T^* = kT/\epsilon$, potential energy (PE), orientational order parameters, O_4 and O_6 , and structure factor $S(\vec{k})$, for layers 9-12, respectively. Note peaking of T^* , plateau in PE and increase in $S(0, 0, 2)$ at $t/\Delta t = 1000$, associated with layering in the solid. Order-disorder transformations in the layers are indicated by the behaviour of O_4 and O_6 . Compare positions of the arrowed peaks in O_4 and $S(2, 0, 0)$ which indicate intra-layer ordering and dynamic coupling between layers. Layers 11 and 12 are regions of crystallizing fluid.

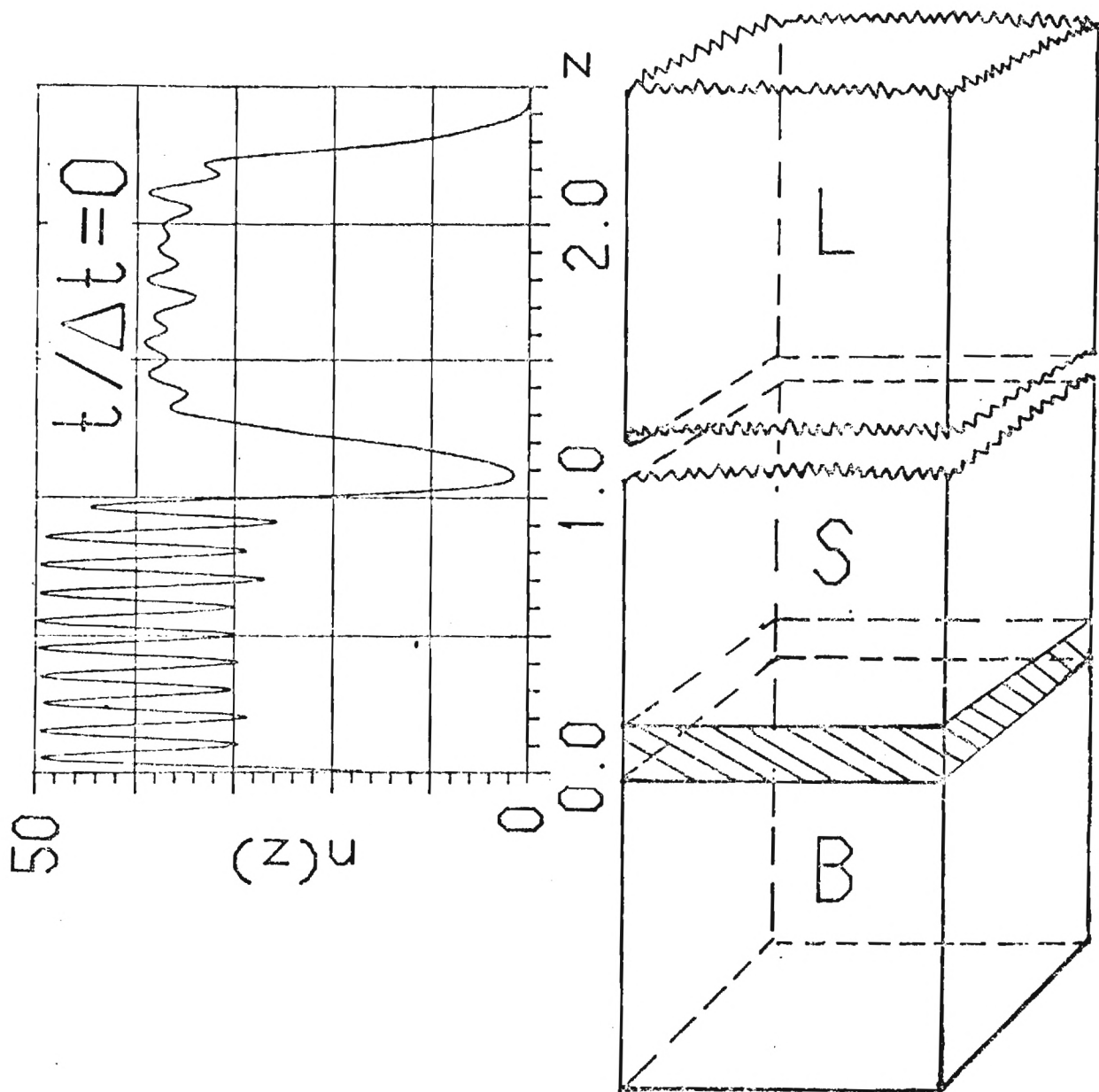


FIGURE 1

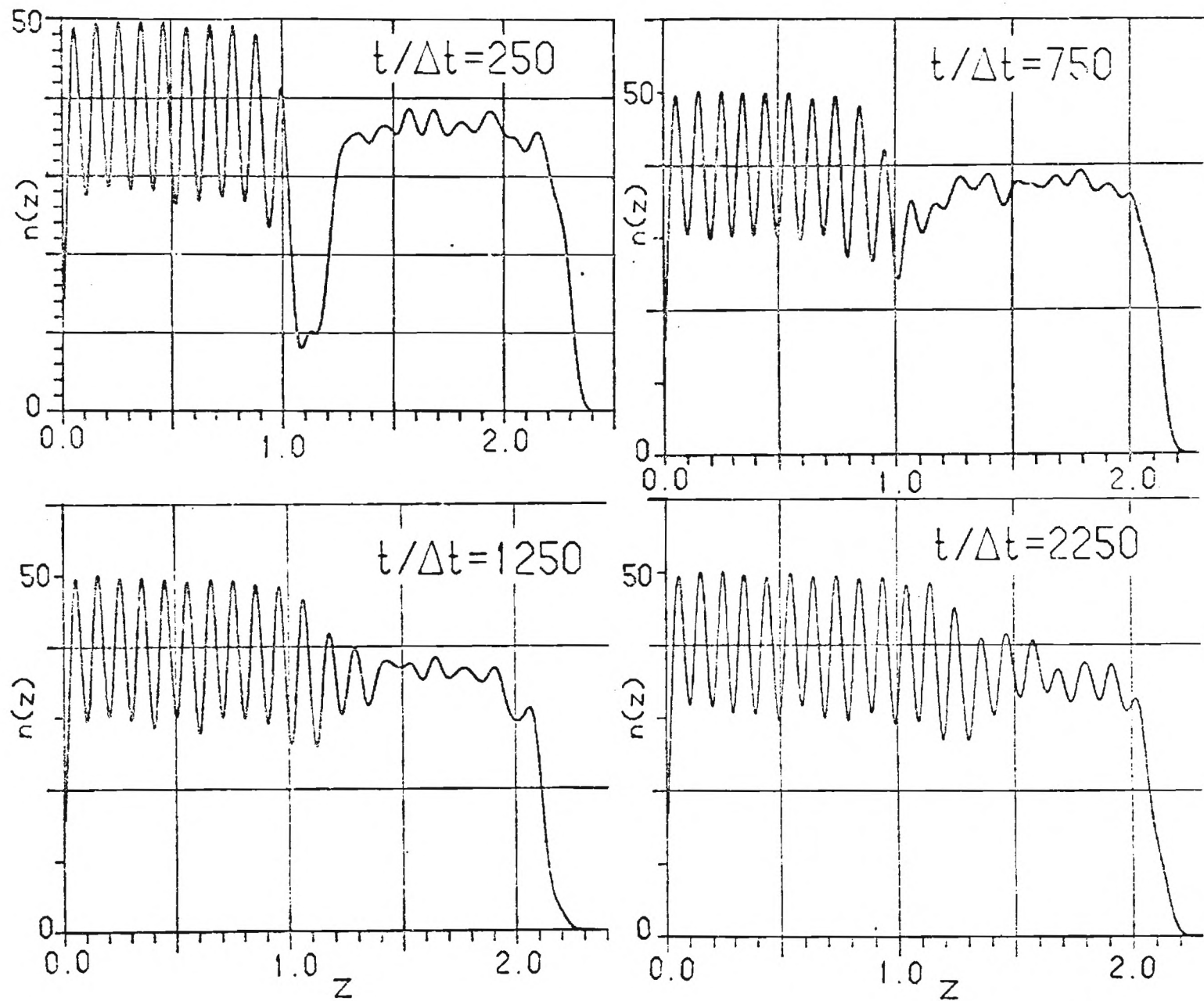


FIGURE 2

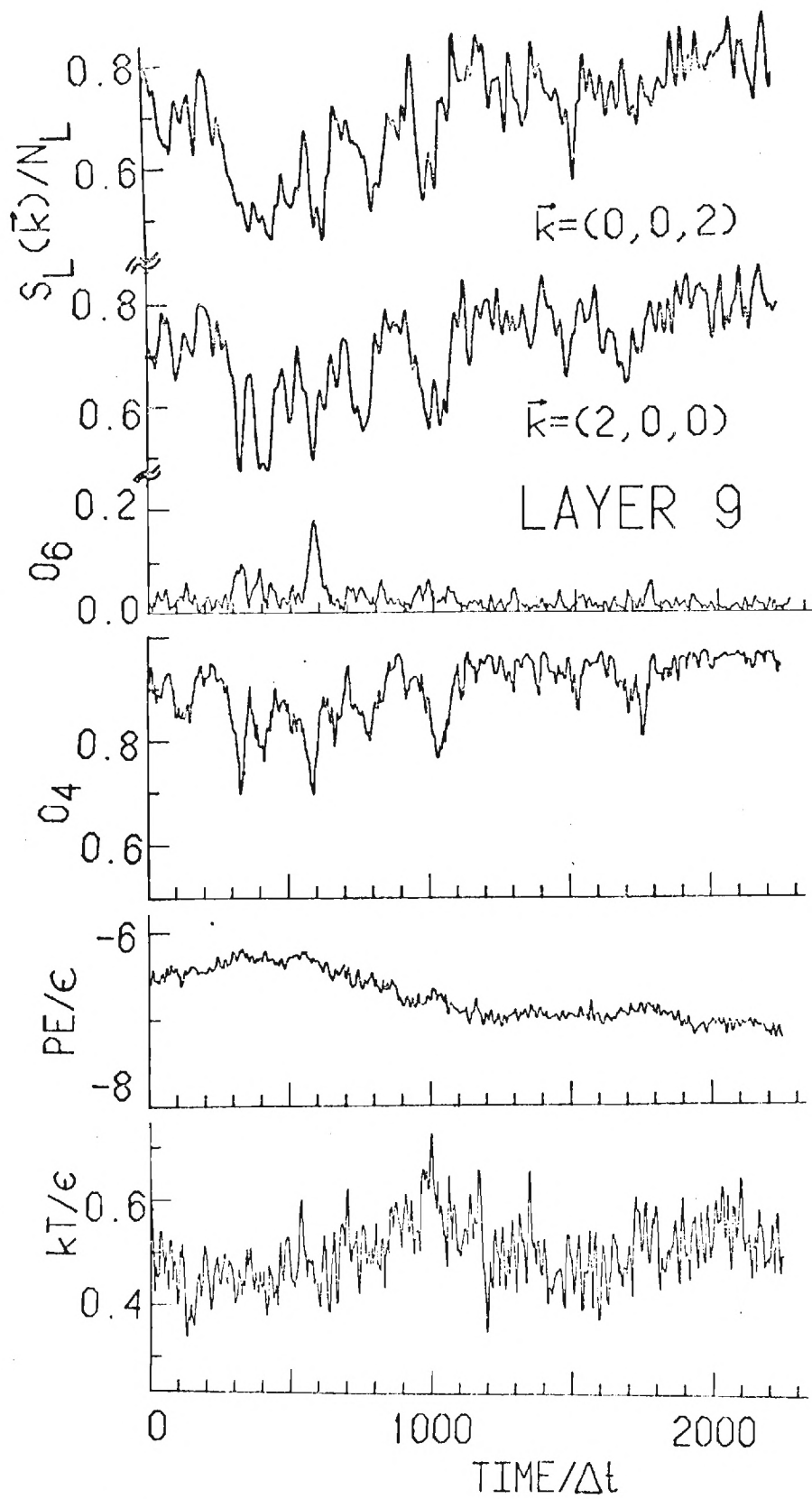


FIGURE 3

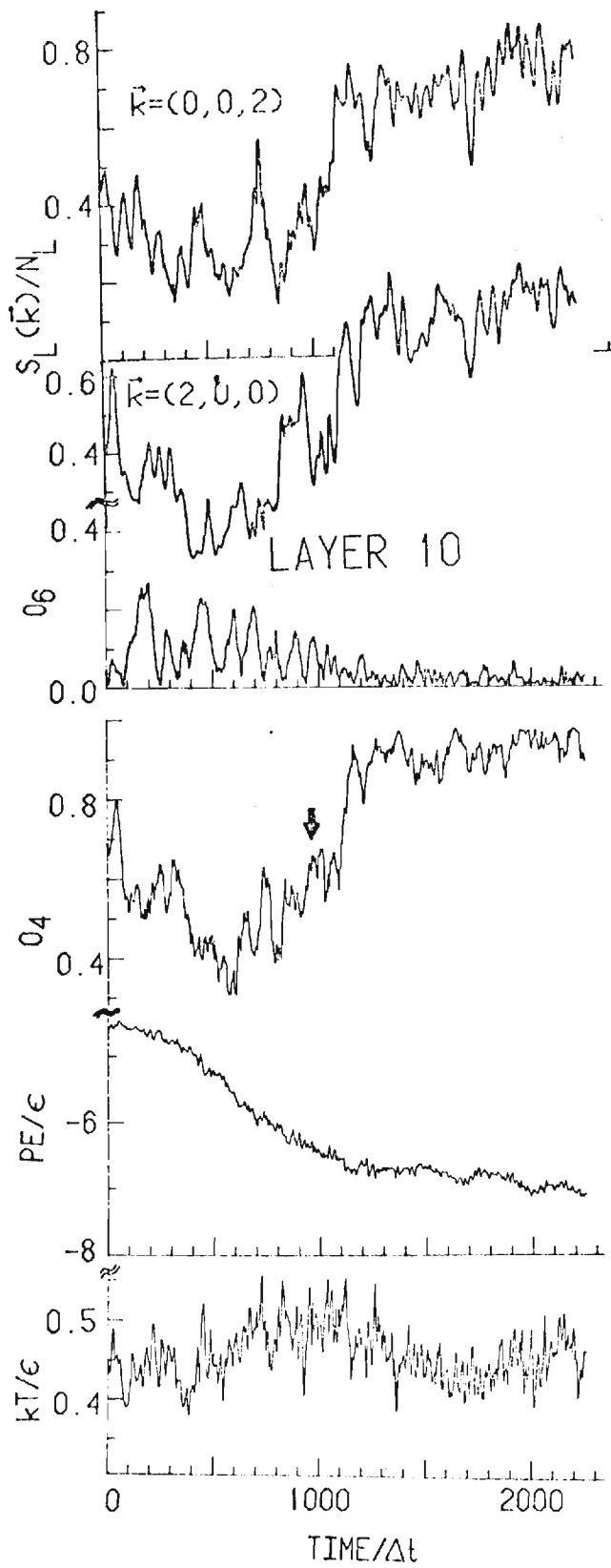


FIGURE 4

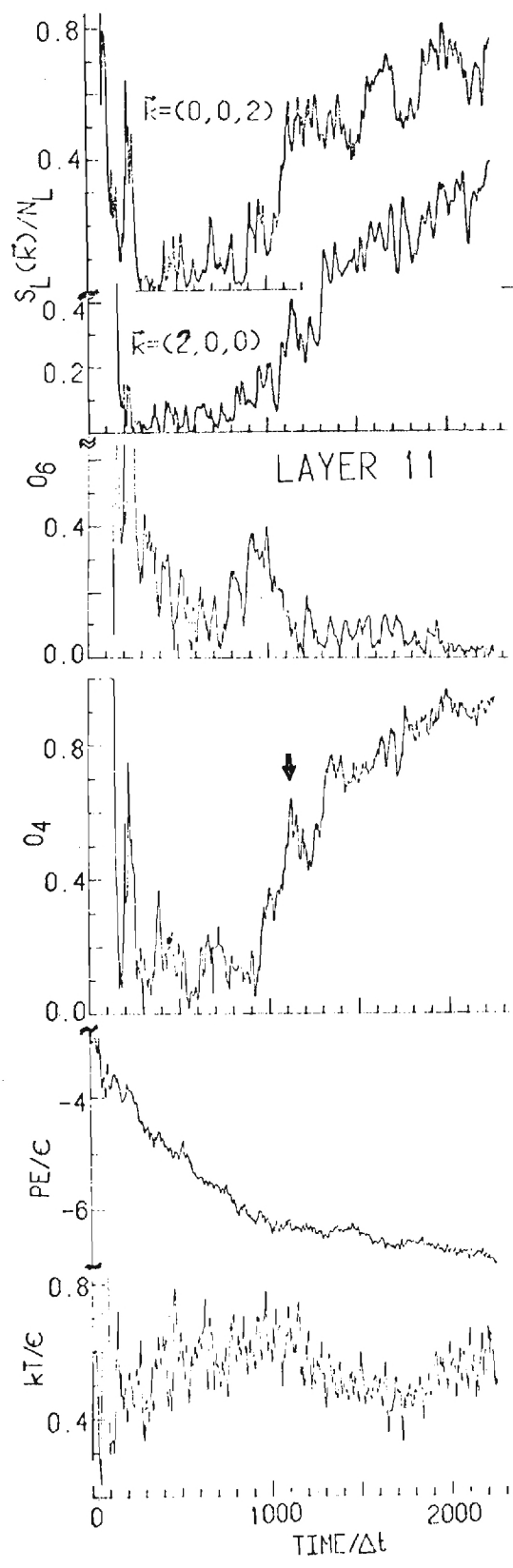


FIGURE 5

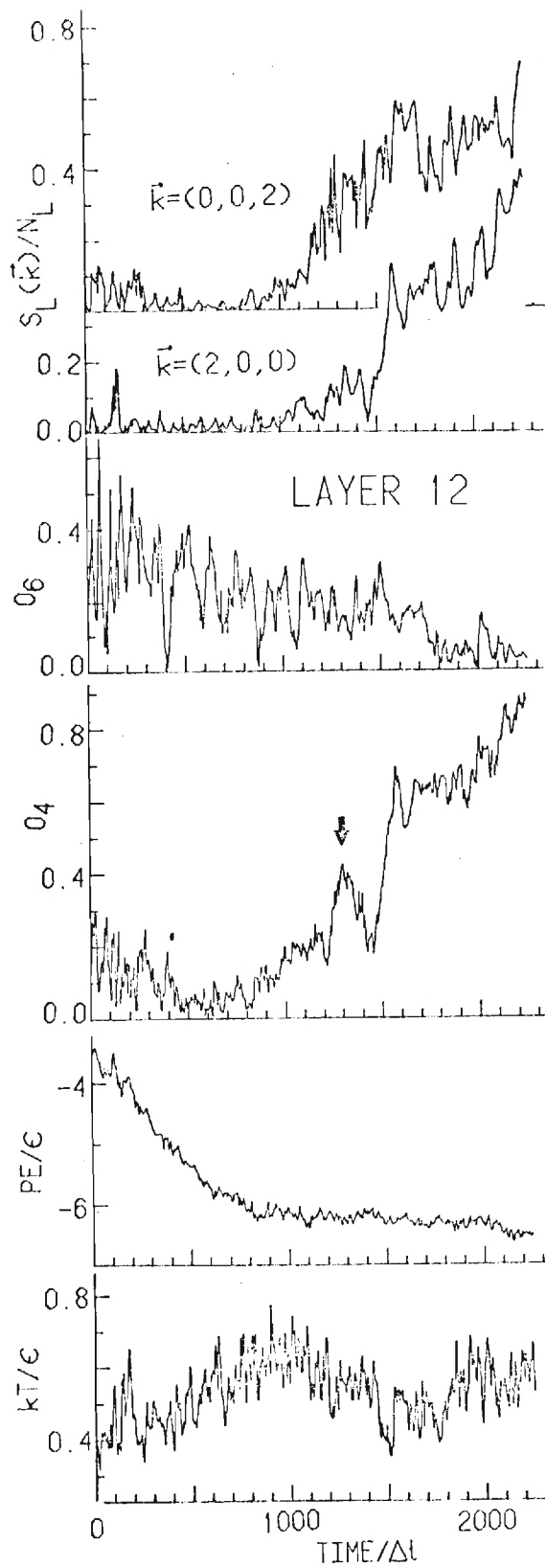


FIGURE 6

B. SURFACE CRYSTALLOGRAPHY

The main achievements of these studies are:

1. Development and evaluation of an electrostatic model for surface relaxation of metals. The model combines the contribution to the force on ions in surface layers due to the delocalized valence electron distribution with that due to the interaction with positive ionic charges.
2. Analysis of surface relaxation yielding adequate agreement with experimental observations for the low-index faces of Al, Li Na and Cu.
3. Comparative study of the effect of the surface electronic density on the relaxation.
4. Demonstration of the importance of multi-layer relaxation mechanisms, and their face-dependence.
5. Analysis of the effects of pseudo-potential descriptions of the ion-cores.
6. Computation of the density of vibrational states at stepped Pt(111) surfaces and demonstration of high-frequency modes for edge and ledge atoms.
7. Initiation of modifications to the real-space recursion method for the calculation of the vibrational spectra of reconstructed Silicon surfaces, and adsorption systems.

Lattice relaxation at metal surfaces: An electrostatic model

Uzi Landman and Ross N. Hill

School of Physics, Georgia Institute of Technology, Atlanta, Georgia 30332

Mark Mostoller

Solid State Division, Oak Ridge National Laboratory, Oak Ridge, Tennessee 37830

(Received 30 August 1979)

Surface relaxation in metals is investigated via an electrostatic model, using an iterative scheme allowing for the participation of many layers in the relaxation process. Comparative studies of surface relaxation are performed for the low-index faces of Al, Li, Na, and Cu, using three models for the electronic density: (a) step function, (b) exponential, (c) Lang-Kohn. The results demonstrate the importance of multilayer relaxation mechanisms, and the sensitivity of the results to the model of the surface electronic density. For the exponential density profile, simple pseudopotential corrections are also included and shown to have significant effects. The relaxation trends predicted are consistent with available results obtained by analyses of low-energy-electron-diffraction data.

I. INTRODUCTION

Knowledge of the atomic arrangement in the surface region of metals is basic for the understanding of a large number of surface phenomena and interaction processes. This recognition has led to major efforts in the development of experimental and theoretical methods for the determination of surface structures.^{1,2} The termination of a solid by a surface modifies both the atomic coordination and the conduction-electron distribution. In response, normal surface relaxation (deviations of distances between atomic planes from their bulk values) and surface reconstruction (lateral structural modifications) may occur. Surface relaxation has been observed¹ for a number of fcc, bcc, and hcp low-index clean metal surfaces and is the subject of the present investigation.

To elucidate the nature of the underlying forces which govern the surface crystallography, it is of interest to investigate surface structure theories of a predictive nature, which apart from their fundamental value could provide a source of model structures to employ in the analysis of experimental data. The first-principles determination of ionic positions at surfaces is hindered by difficulties in carrying out a self-consistent energy minimization for the coupled system of ions and conduction electrons. Semiempirical methods, on the other hand, which were developed originally mainly for the study of bulk defect configurations (pseudopotential pairwise interactions, empirically fitted pair potentials, and lattice statics methods) have usually predicted outward relaxations for low-index faces.³⁻⁷ These results are in contradiction with experimental evidence indicating that contraction of the top interlayer spacing occurs in many if not most cases.

The inadequacies of surface relaxation models

based on bulk-derived pair-potential interactions only have been emphasized by Finnis and Heine (FH).⁸ Following the conclusion of Smoluchowski⁹ (made in the context of a study of the work function) concerning the lateral smoothing of the electronic charge density at surfaces to lower the kinetic energy, FH presented a heuristic model of surface relaxation in *sp*-bonded materials. In this model the asymmetrical electron density at the cleaved surface is redistributed in surface Wigner-Seitz cells with a sharp cutoff at the solid-vacuum interface. As a result the ions at their first layer, truncated bulk positions experience a net electrostatic force to which they react via an inward relaxation. The original application of the model to the low-index faces of Al yielded results in qualitative agreement with experimental observations. Subsequent investigations have emphasized the importance of crystalline effects, as well as the influence of the inhomogeneous charge density distribution at the surface.¹⁰ Most recently, a model which combined *ad hoc* short-range empirical pair interactions with forces on the first few layers arising from a step-function *sp*-electron density at the surface was employed to study the (100) face of α -Fe and Cu.¹¹

To complement the above studies we describe here a simple electrostatic model for surface relaxation. The method combines the contribution to the force on ions in surface layers due to the delocalized valence electron distribution with that due to the interaction with the positive ionic charges in the planar nets. Three models for the electronic density in the surface region are studied and compared: (a) an abrupt terminated step density profile, (b) an exponential variational form (Smith),¹² and (c) a self-consistent distribution derived from the jellium model (Lang-Kohn).¹³ For the exponential density profile, pseudopotential

corrections are also incorporated in a simple way. Under the influence of the forces acting on them, ions in an arbitrary number of surface planes are allowed to relax from their bulk positions, and the coupled set of equations governing the planar displacements are solved by a fast-converging iterative technique. The method is material dependent, in contrast to the original FH method. It is easy to apply and yields correct trends when compared with experimentally determined relaxation values for several materials. Following the derivation of the basic relations given in Sec. II, results obtained by the method are discussed in Sec. III.

II. EVALUATION OF THE SURFACE ELECTROSTATIC FORCES

In this section we derive expressions for the electrostatic interactions between ions in surface planes. For the sake of brevity we discuss first the case of a step-terminating electron density which is then generalized to the other density profiles considered. The arrangement of ions in the bulk terminated lattice is shown in Fig. 1(a): For simplicity, we consider only surfaces characterized by a single interlayer spacing d before relaxation. Ionic layers located at $-nd$ are embedded in slabs of thickness d and of uniform negative charge density $-(Ze/Ad)$, where Z is the valency of the material and A is the area of the unit cell of the surface net. The system after relaxation occurs is shown in Fig. 1(b).

The force on an ion in layer m due to the charge in a different layer n is evaluated by using a layer summation method.^{11,14} The quantity of interest is the electrostatic potential at point r due to the charge in slab n :

$$\phi_n(\vec{r}) = \int \frac{\rho_n(\vec{r}')}{|\vec{r} - \vec{r}'|} d^3r'. \quad (1)$$

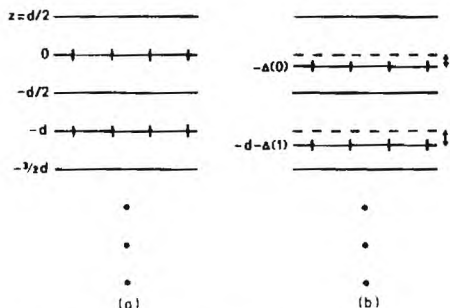


FIG. 1. Schematic picture of the layer arrangement in the terminated bulk crystal prior to (a) and after (b) relaxation. The bulk spacing is denoted by d and the displacement of ions in layer n from their bulk position by $\Delta(n)$.

Using the identity

$$\frac{1}{|\vec{r} - \vec{r}'|} = \frac{1}{2\pi} \int d^2K \frac{e^{-K|z - z'|}}{K} e^{i\vec{K} \cdot (\vec{R} - \vec{R}')} , \quad (2)$$

where \vec{K} and \vec{R} denote the projections of the vectors \vec{k} and \vec{r} onto the plane parallel to the surface plane, Eq. (1) can be written as

$$\phi_n(\vec{r}) = \frac{1}{2\pi} \int d^2K \frac{e^{*Kz}}{K} e^{i\vec{K} \cdot \vec{R}} \times \int d^3r' \rho_n(r') e^{*Kz'} e^{i\vec{K} \cdot \vec{R}'} ; \quad z \geq z' . \quad (3)$$

Owing to the translational periodicity in the $2D$ net, the second integral in Eq. (3) can be written as

$$I = \frac{4\pi^2}{A} \sum_{\vec{G}} \delta(\vec{K} - \vec{G}) \int_{uc} d^3r' \rho_n(\vec{r}') e^{*Gz'} e^{-i\vec{G} \cdot \vec{R}'} , \quad (4)$$

where \vec{G} is a reciprocal vector of the $2D$ net, and the integral remaining is over a neutral unit cell in slab n .

We now allow the ions in layer n to relax from their bulk position to a new location $z' = -[nd + \Delta(n)]$. Next we need to specify the layer-shift vectors defining the origins for the unit cells in the various layers. For the fcc (100) and (110) faces and the bcc (100) face, the layer shift vectors are

$$\vec{R}_n = \begin{cases} (0, 0), & n \text{ even} \\ (a_1/2, a_2/2), & n \text{ odd}, \end{cases} \quad (5)$$

where a_1, a_2 are the magnitudes of the sides of the $2D$ unit cell; other cases are treated in Appendices A and B. Expressing the reciprocal lattice vector as $\vec{G} = \mu \vec{b}_1 + \nu \vec{b}_2$ (μ, ν integers), and introducing the function $P_{\vec{G}}(n)$ defined as

$$P_{\vec{G}}(n) = \begin{cases} 1, & n \text{ even} \\ (-1)^{\mu+\nu}, & n \text{ odd}, \end{cases} \quad (6)$$

we obtain

$$I = \frac{4\pi^2}{A} (Ze) \sum'_{\vec{G}} \delta(\vec{K} - \vec{G}) P_{\vec{G}}(n) e^{*G[nd + \Delta(n)]} , \quad (7)$$

where the $-$ and $+$ signs correspond to the observation point \vec{r} located above or below slab n , respectively. The prime on the sum in Eq. (7) indicates that the $\vec{G} = 0$ term is excluded as a result of charge neutrality. Combining Eq. (7) with (3) yields for the z component of the electrostatic

field at $\vec{r}[E_z(\vec{r}) = -\partial\phi_n(\vec{r})/\partial z]$,

$$E_z(\vec{r}) = \pm \frac{2\pi}{A} (Ze) \sum_{\vec{r}}' e^{*Gz} e^{i\vec{G}\cdot\vec{r}} P_{\vec{G}}(n) e^{*G(md+\Delta(m))}. \quad (8)$$

Taking $z = -[md + \Delta(m)]$, and noting that $e^{i\vec{G}\cdot\vec{r}} = P_{\vec{G}}^*(m)$ for an ion in layer m , we find that the force on ions in layer m due to the charge in layer n is, in units of $2\pi(Ze)^2/A$,

$$F_{mn} = \text{sgn}(n-m) \sum_{\vec{G}}' P_{\vec{G}}^*(m) P_{\vec{G}}(n) \exp[-G|(n-m)d + \Delta(n) - \Delta(m)|], \quad m \neq n. \quad (9)$$

The interaction of the ions in slab m with the negative charge in the same slab is obtained by using the Poisson equation, which yields for the z component of the force in the same units as above,

$$F_{mm} = 2\Delta(m)/d. \quad (10)$$

Let us assume that relaxation from bulk positions occurs up to layer L , i.e., for $n > L$, $\Delta(n) = 0$, and sum the contributions to the force on ions in layer m from these deep layers. The result is

$$F_m = \sum_{n=L+1}^{\infty} F_{mn} = \sum_{\vec{G}}' P_{\vec{G}}^*(m) e^{G(md+\Delta(m))} \sum_{n=L+1}^{\infty} P_{\vec{G}}(n) e^{-Gdn}. \quad (11)$$

For two-layer repeat sequences in the 2D layer shift vectors as in Eq. (5), F_m is given by

$$F_m = \sum_{\vec{G}}' \frac{P_{\vec{G}}(L+1)e^{-Gd} + P_{\vec{G}}(L+2)e^{-2Gd}}{1 - e^{-2Gd}} P_{\vec{G}}^*(m) e^{-G(L-m)d - \Delta(m)}. \quad (12)$$

The simultaneous set of equations for static equilibrium is

$$0 = \sum_{n=0}^L F_{mn}(\Delta_m, \Delta_n) + F_m(\Delta_m) \quad \text{for } m = 0, 1, \dots, L. \quad (13)$$

The solution of the above set of equations is achieved by a simple iterative method in which we set $\Delta_{i+1}(n) = \Delta_i(n) + \delta_i(n)$, where i is the iteration number. The procedure is started with $\Delta_1(n) = 0$ for all n . Expansion of the forces in Eq. (13) to first order in $\delta_i(n)$ yields the following set of equations:

$$\sum_{l'=0}^L a_{ll'} \delta_i(l') = b_l; \quad l = 0, 1, \dots, L, \quad (14)$$

$$a_{ll'} = - \sum_{\vec{G}}' P_{\vec{G}}^*(l) P_{\vec{G}}(l') G \exp[-G|(l'-l)d + \Delta_i(l') - \Delta_i(l)|], \quad l \neq l', \quad (15a)$$

$$a_{ll} = \sum_{n \neq l} \sum_{\vec{G}}' P_{\vec{G}}^*(l) P_{\vec{G}}(n) G \exp[-G|(n-l)d + \Delta_i(n) - \Delta_i(l)|] + \sum_{\vec{G}}' \frac{P_{\vec{G}}(L+1)e^{-Gd} + P_{\vec{G}}(L+2)e^{-2Gd}}{1 - e^{-2Gd}} P_{\vec{G}}^*(l) G \exp[-G|(L-l)d - \Delta_i(l)|] + 2/d, \quad (15b)$$

$$b_l = - \sum_{n \neq L} \text{sgn}(n-l) \sum_{\vec{G}}' P_{\vec{G}}^*(l) P_{\vec{G}}(n) \exp[-G|(n-l)d + \Delta_i(n) - \Delta_i(l)|] - \sum_{\vec{G}}' \frac{P_{\vec{G}}(L+1)e^{-Gd} + P_{\vec{G}}(L+2)e^{-2Gd}}{1 - e^{-2Gd}} P_{\vec{G}}^*(l) \exp[-G|(L-l)d - \Delta_i(l)|] - 2\Delta_i(l)/d. \quad (15c)$$

The values of $\delta_i(l)$ in each iteration are obtained from Eq. (14) by simple matrix inversion. Typically the solution converges after 3-5 iterations.

Exponential density profile

Having derived the basic relations for the step-terminating electronic distribution, we turn now to a generalization of the theory to include more realistic descriptions of the surface electron density profile. First we employ an exponential form.

$$\rho_e(z) = n_0 \left(1 - \frac{e^{\beta(z-d/2)}}{2} \right), \quad z < \frac{1}{2}d \quad (16a)$$

$$\rho_e(z) = \frac{1}{2}n_0 e^{-\beta(z-d/2)}, \quad z > \frac{1}{2}d \quad (16b)$$

where $n_0 = -Ze/Ad$ and β is a variational parameter.¹² Let us consider first the electronic field at a point z in the first layer. Integration of the Poisson equation yields

$$E_z(z) = 4\pi \int_{-\infty}^z \rho_e(z') dz' + E_z(z \rightarrow \infty), \quad (17)$$

where $E_z(z \rightarrow \infty) \rightarrow 4\pi n_0 d/2$. Using Eqs. (16a) and (16b), we obtain

$$E_z(z) = 4\pi n_0 \left[z - \frac{e^{\beta(z-d/2)}}{2\beta} \right]. \quad (18)$$

Setting $z = -\Delta(0)$, we find that the force on the first layer of ions due to the negative charge in the outermost region is, in units of $2\pi(Ze)^2/A$,

$$F_{00} = \frac{2}{d} \left(\Delta(0) + \frac{e^{-\beta[\Delta(0)+d/2]}}{2\beta} \right). \quad (19)$$

In the language of our iterative algorithm ($\Delta_{i+1} = \Delta_i + \delta_i$),

$$F_{00} = \frac{2}{d} \left(\Delta_i(0) + \frac{e^{-\beta[\Delta_i(0)+d/2]}}{2\beta} \right) + \frac{2}{d} \left(1 - \frac{e^{-\beta[\Delta_i(0)+d/2]}}{2} \right) \delta_i(0). \quad (20)$$

Thus to b_0 in Eq. (15c) we need to add the factor $-(\beta d)^{-1} \exp\{-\beta[\Delta_i(0)+d/2]\}$ and to a_{00} in Eq. (15b) the factor $-d^{-1} \exp\{-\beta[\Delta_i(0)+d/2]\}$.

Next we consider the change in the force acting on ions in the second slab. Since we require a division of the material into neutral regions we need to adjust the location of the boundary between the outermost and the next region from its original position at $-d/2$ to $-d/2+s$. The shift in the boundary is determined by the condition $E(s-d/2) = -4\pi n_0 d/2$, or using Eq. (18),

$$2\beta s = e^{\beta(s-d)}. \quad (21)$$

The electric field in the second layer is given by

$$E_z(z) = 4\pi \int_{-d/2+s}^z \rho(z) dz + E_z(z \rightarrow \infty). \quad (22)$$

Substituting Eq. (16a) in Eq. (23) and using Eq. (22), then setting $z = -[d+\Delta(1)]$ for the second layer and employing our iterative scheme, we obtain

$$F_{11} = \frac{2}{d} \left[\Delta_i(1) + \delta_i(1) + \frac{e^{-\beta[\Delta_i(1)+3d/2]}}{2} \left(\frac{1}{\beta} - \delta_i(1) \right) \right]. \quad (23)$$

Thus to b_1 in Eq. (15c) we need to add $-(\beta d)^{-1} \exp\{-\beta[\Delta_i(1)+3d/2]\}$ and to a_{11} in Eq. (15b) that term multiplied by β .

Lang-Kohn density profile

The importance of self-consistency in the calculation of a number of surface properties such as surface energies, work functions, adsorption, and geometrical structure has been investigated and demonstrated. Since the exponential density does not include some features characteristic of the electronic density at surfaces, such as Friedel oscillations, we employ next the self-consistent surface electronic density calculated by Lang and Kohn¹³ (LK) for a uniform positive background model. These charge densities have been tabulated for various r_s values in Table I of Ref. 13 and will be denoted by n_{LK} . Using our previous notation, the z component

of the electric field on ions in the first layer of the solid can be written as

$$E_z[-\Delta_i(0) - \delta_i(0)] = E_z[-\Delta_i(0)] + 4\pi n_{LK}[-\Delta_i(0)] \delta_i(0) - 4\pi \frac{Ze}{Ad} \int_{-\Delta_i(0)}^{-\Delta_i(0)} n_{LK}(z) dz - 4\pi \frac{n_0 Ze}{Ad} \frac{d}{2} - 4\pi \frac{Ze}{Ad} n_{LK}[-\Delta_i(0)] \delta_i(0), \quad (24)$$

from which the force F_{00} follows. Accordingly the term $-2\Delta_i(0)/d$ in Eq. (15c) for b_0 is replaced by $(2/d) \int_{-\Delta_i(0)}^{-\Delta_i(0)} n_{LK}(z) dz + 1$, and in Eq. (15b) for a_{00} the term $2/d$ is replaced by $(2/d) n_{LK}[-\Delta_i(0)]$. To include effects on ions in the second layer the corresponding replacements in b_1 and a_{11} are made with the terms evaluated at $z = -[d+\Delta_i(1)]$. Notice also that due to a difference in the choice of origin for the location of the first layer of ions at the surface, the LK coordinates are shifted by $+d/2$ to agree with our convention.

Pseudopotential corrections

To incorporate pseudopotential corrections within the framework of our model, we use a simplified Heine-Abarenkov pseudopotential^{15,16} for the electron-ion interaction. The difference from the Coulomb interaction used in Eq. (1) and subsequently is given by the function

$$f(|\vec{r}' - \vec{r}|) = \theta(r_0 - |\vec{r}' - \vec{r}|) \left(\frac{1}{a_0} - \frac{1}{|\vec{r}' - \vec{r}|} \right), \quad (25)$$

where r_0 and a_0 are the pseudopotential radius and well-depth parameter, respectively, and θ is the Heaviside step function [$\theta(x) = 1, x > 0$ and $\theta(x) = 0, x < 0$]. For $a_0 \rightarrow \infty$, the simplified Heine-Abarenkov pseudopotential becomes an Ashcroft pseudopotential.¹⁷

If the pseudopotential cores do not overlap, then the only change in the potential acting on an ion is that due to the difference of its own pseudopotential core from the Coulomb interaction,

$$\begin{aligned} \Delta \phi_n \{ \vec{r} = -[nd + \Delta(n)] \hat{z} + \vec{R} \} &= - \int d^3 r' \rho_e(\vec{r}') f(|\vec{r}' - \vec{r}|) \\ &= -2\pi \int_{-r_0}^{r_0} dz \rho_e \{ z - [nd + \Delta(n)] \} \\ &\quad \times \left(\frac{1}{2a_0} (r_0^2 - z^2) - r_0 + |z| \right). \end{aligned} \quad (26)$$

For a constant charge density ρ_0 across the pseudopotential core, the integral in Eq. (26) yields a constant potential,

$$\Delta \phi_n \{ \vec{r} = -[nd + \Delta(n)] \hat{z} + \vec{R} \} = 2\pi \rho_0 r_0^2 \left[1 - \frac{2}{3} (r_0/a_0) \right], \quad (27)$$

and no change occurs in the forces exerted on the ion. However, when the planes of ions relax in regions of nonuniform electronic charge density, the pseudopotential corrections do modify the forces acting on the ions, as we illustrate for the

$$\Delta \phi_n \{ \vec{r} = -[nd + \Delta(n)]\hat{z} + \vec{R} \} = 2\pi n_0 \left\{ r_0^2 \left[1 - \frac{2}{3}(r_0/a_0) \right] - \frac{1}{\beta^2} e^{-\beta[nd + \Delta(n) + d/2]} \left([1 - (r_0/a_0)] \coth \beta r_0 + \frac{1}{\beta a_0} \sinh \beta r_0 - 1 \right) \right\}. \quad (28)$$

The change in the force on an ion in plane n is $\Delta F_{nn} = d\Delta \phi_n/d\Delta(n)$, which in units of $2\pi(Ze)^2/A$ is

$$\Delta F_{nn} = \frac{1}{\beta d} e^{-\beta[nd + \Delta(n) + d/2]} \left([1 - (r_0/a_0)] \coth \beta r_0 + \frac{1}{\beta a_0} \sinh \beta r_0 - 1 \right), \quad (29)$$

which for the Ashcroft pseudopotential ($a_0 \rightarrow \infty$) reduces to

$$\Delta F_{nn} \rightarrow \frac{1}{\beta d} e^{-\beta[nd + \Delta(n) + d/2]} (\coth \beta r_0 - 1). \quad (30)$$

Note that this is the change relative to the results obtained for the exponential density profile with a Coulomb electron-ion interaction. The changes with respect to the step-function density profile results given in Eqs. (15a)–(15c) are

$$\begin{aligned} \delta a_{ii} &= \beta \delta b_i \\ &= -\frac{1}{d} e^{-\beta[nd + \Delta(n) + d/2]} \left([1 - (r_0/a_0)] \coth \beta r_0 + \frac{1}{\beta a_0} \sinh \beta r_0 \right) \\ &\xrightarrow{a_0 \rightarrow \infty} -\frac{1}{d} e^{-\beta[nd + \Delta(n) + d/2]} \coth \beta r_0. \end{aligned} \quad (31)$$

If the pseudopotential core for an ion in the first layer intersects the plane at $d/2$, i.e., $\Delta(0) + d/2 < r_0$, the pseudopotential corrections are obtained by using both (16a) and (16b) for ρ_e in the appropriate ranges in the integral in Eq. (26). For this case, we will simply give expressions for the changes relative to the step function density results in Eqs. (15a)–(15c):

$$\delta a_{ii} = \frac{1}{d} \left[\left(1 - (r_0/a_0) - \frac{1}{\beta a_0} \right) e^{-\beta r_0} \sinh \{ \beta [\Delta(0) + d/2] \} - 1 + \frac{1}{a_0} [\Delta(0) + d/2] \right], \quad (32a)$$

$$\begin{aligned} \delta b_i &= -\frac{1}{\beta d} \left[\left(1 - (r_0/a_0) - \frac{1}{\beta a_0} \right) e^{-\beta r_0} \right. \\ &\quad \times \coth \{ \beta [\Delta(0) + d/2] \} \\ &\quad \left. + \frac{1}{\beta a_0} + \beta \{ r_0 - [\Delta(0) + d/2] \} \right] \\ &\quad \times \left(1 - \frac{1}{2a_0} [r_0 + \Delta(0) + d/2] \right). \end{aligned} \quad (32b)$$

exponential density profile.

We consider first the case, where $nd + \Delta(n) + d/2 > r_0$, and the exponential density to use in Eq. (26) is that given in Eq. (16a). Carrying through the integration in Eq. (26), we obtain

III. RESULTS

We have applied the methods described in the previous section to investigate relaxation at the low-index faces of several fcc and bcc materials. A summary of characteristic parameters for the (001), (110), and (111) faces of fcc and bcc crystals is given in Appendix B.

Several studies of electrostatic contributions to surface relaxation have been reported previously.^{8,10,11} In all of these, it was concluded that the contribution of electrostatic forces arising from the smoothed sp -electron charge density is important, and cannot be neglected with respect to short-range forces and broken bonds which generally, by themselves, predict outward relaxations. No systematic investigation has yet been made, however, of the effects of physically reasonable variations within an electrostatic model. We will show that three such variations produce quantitatively significant effects: (1) multilayer relaxation, (2) charge density profiles, and (3) pseudopotential corrections.

Table I illustrates the importance of multilayer relaxation mechanisms for exponential charge density profiles at Al and Na surfaces with no pseudopotential corrections. Similar results are obtained with the step function and Lang-Kohn densities. The effect of allowing more than one or two layers to relax is significant for those surfaces which undergo large relaxations, which in Table I are the fcc (110) and the bcc (100) faces (these are the least densely packed faces). Inspection of the layer-by-layer displacements for these surfaces reveals that allowing more layers to relax does not merely give nonzero values for the displacements of the deeper planes, but also modifies the displacements of previously considered layers. For these faces, 3–6 layers participate in the relaxation as compared to 1–3 layers for the other faces. A tendency of the displacements to alternate in sign is noted, although for Na(111), for example, all layers relax outward. In general, after the first one or two layers, the magnitude of the relaxation decreases exponentially as one goes into the solid from the surface. In Table I and elsewhere, we use values

TABLE I. Relaxation of the spacing between the first and second layers, $\Delta_{12} = [\Delta(1) - \Delta(2)]/d$, in % (- denotes a contraction and + an expansion), and layer by layer displacements for the low-index faces of Al and Na using the exponential electron density, with values for the variational parameters β of 1.24 and 1.27 (a.u.)⁻¹, respectively, from Ref. 12. The integer L denotes the number of planes allowed to relax. The numbers in the fourth column are the values obtained for $\Delta(n)/a$, where $n = 0, 1, \dots$ is the layer index.

Surface	L	Δ_{12} (%)	$\Delta(n)/a$
Al(100)	1	-1.1	-0.0054
	10	-1.2	-0.0054, 0.0008, -0.0001
Al(110)	1	-8.7	-0.0309
	2	-18.2	-0.0397, 0.0248
	5	-21.2	-0.0435, 0.0316, -0.0148, 0.0080, -0.0035
	10	-21.3	-0.0436, 0.0318, -0.0151, 0.0086, -0.0045
Al(111)	1	+0.6	+0.0036
	10	+0.6	+0.0036, 0.00001
Na(100)	1	-6.3	-0.0317
	2	-9.5	-0.0349, 0.0127
	5	-9.9	-0.0353, 0.0139, -0.0044, 0.0015, -0.0004
	10	-9.9	-0.0353, 0.0139, -0.0044, 0.0015, -0.0005
Na(110)	1	-0.6	-0.0043
	10	-0.7	-0.0043, 0.0003
Na(111)	1	+3.7	+0.0108
	2	+3.6	+0.0108, 0.0003
	10	+3.6	+0.0108, 0.0003, 0.0001

for β taken from Smith.¹² We have repeated all exponential density calculations using β values given in the more recent work of Ma and Sahni,¹⁸ and found qualitatively similar results.

The possibility that a number of layers may participate in the relaxation is potentially significant for LEED model calculations of scattered electron intensity versus incident energy (IV) profiles. In most LEED analyses of clean metal surfaces, only the top layer of ions has been allowed to relax in attempting to fit the experimental data. In a recent study of Cu(110) LEED intensity spectra, it was found that the structural model which fit the data best is an ~10% contraction of the first-second layer spacing, accompanied by perhaps a slight contraction or expansion between the second and third layers.¹⁹ Similarly, for the Re(10 $\bar{1}$ 0) surface, about a 17% contraction of the first-second layer distance and a modest expansion between the second and third layers appear to give the best agreement with experiment.²⁰ In light of these recent studies and our results it is suggested that multilayer relaxation models be considered more routinely in LEED analyses and in the interpretation of ion scattering and channeling experiments.

Table II illustrates the dependence of the relaxation upon the model used for the electron charge density. The step-function density yields contractions for all of the faces studied. The exponential density profile produces smaller contractions than the step-function density for the (001) and

(110) faces, and predicts expansion of the first-second layer distance for the (111) faces of all three materials. With the Lang-Kohn densities, the calculated relaxations are generally of the same sign as the exponential density results, but in some cases are significantly different in size. The charge density dependence of the relaxation appears to be stronger for the higher ν_s -value materials. This can be rationalized by considering the Lang-Kohn charge densities for Al, Li,

TABLE II. Relaxation of the first-second and second-third layer spacings Δ_{12} and Δ_{23} , $\Delta_{mn} = [\Delta(m) - \Delta(n)]/d$, for the low-index faces of Al, Li, and Na using three models for the charge density: (a) step-terminating, (b) exponential, and (c) Lang-Kohn. Values for Δ_{12} and Δ_{23} are given in percent. For the exponential density profile results, the parameter β was taken to be 1.24, 1.24, and 1.27 (a.u.)⁻¹ for Al, Li, and Na, respectively. Ten layers were allowed to relax for all results listed.

Surface	Step		Exponential		Lang-Kohn	
	Δ_{12}	Δ_{23}	Δ_{12}	Δ_{23}	Δ_{12}	Δ_{23}
Al(100)	-2.4	0.3	-1.2	0.2	-2.0	0.1
Al(100)	-26.3	15.8	-21.3	13.3	-23.9	14.4
Al(111)	0.0	0.0	+0.6	0.0	+0.3	0.0
Li(100)	-10.9	4.0	-8.7	3.3	-16.3	7.4
Li(110)	-0.9	0.1	-0.3	0.0	-2.0	-0.4
Li(111)	-0.9	0.0	+6.7	0.3	+9.0	-3.1
Na(100)	-10.9	4.0	-9.9	3.7	-20.3	9.4
Na(110)	-0.9	0.1	-0.7	0.0	-2.6	-0.6
Na(111)	-0.9	0.0	+3.6	0.1	+4.0	-4.1

and Na, which are shown in Fig. 2; the Li density was obtained via a six-point, two-dimensional interpolation of the charge densities given in Table I of Ref. 13. As seen in the figure, the Friedel oscillations at the surface of Al ($r_s = 2.0$) are much smaller than for the higher r_s materials. In an electrostatic force model, such differences in negative charge accumulations can have a significant effect on the results. As noted by Alldredge and Kleinman (AK),¹⁰ this may account for the apparent success of the calculation by FH⁹ for Al, where a step-function density was assumed.

The effect of pseudopotential corrections is shown in Table III. Both Ashcroft (empty core)^{17,21} and simplified Heine-Abarenkov pseudopotentials¹⁶ have been employed in conjunction with the exponential density profiles. The pseudopotential corrections lead to substantial changes in the relaxations calculated, and generally tend to favor expansion, or equivalently, to reduce contraction. Plausible variations in the pseudopotential parameters produce modest but in some cases non-negligible changes. Unrealistically large expansions are predicted for the bcc (111) faces; these are the only cases treated for which the Ashcroft pseudopotential cores for atoms in the first layer extend well beyond the plane at $\frac{1}{2}d$.

In Table IV, we compare our results for Al, Li, and Na with available previous studies,^{1, 8, 10, 22, 23} in-

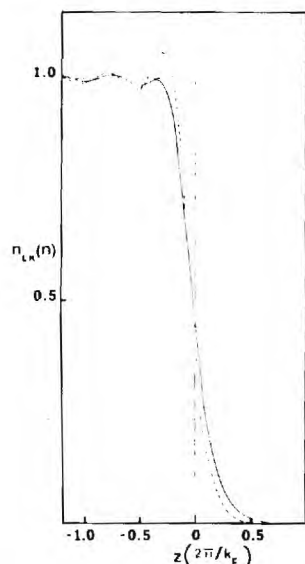


FIG. 2. Lang-Kohn charge densities derived for a uniform jellium model (after Ref. 15), for $r_s = 2.0, 3.25,$ and 4.0 , solid, dashed, and dotted curves, respectively. The coordinate z is in units of the Fermi wavelength, and the densities n_{LK} in units of the bulk density $n_0 = ze/Ad$. To agree with our convention that the first layer is located at $z = 0$, the coordinates in this figure are to be shifted by $(+d/2)$, where d is the layer spacing of the unrelaxed lattice.

cluding LEED analyses. For the step-function density there are substantial differences between the one-layer relaxation results and those obtained with the original FH model,⁹ which considered only the interaction of a surface ion with the smoothed electron density in its own surface Wigner-Seitz cell. Further changes are evident when more layers are allowed to relax. Using a one-layer relaxation model, AK¹⁰ have emphasized the importance of crystalline effects in their study of the Li(100) surface. They conclude that the Lang-Kohn density yields an electrostatic force on the first layer of about one fourth of the total crystalline result. Table IV shows again that multilayer relaxation mechanisms, electron density variations and pseudopotential corrections all can produce large changes comparable in magnitude to other crystalline effects. Our electrostatic model is sufficiently simple that we do not want to belabor

TABLE III. The effect of pseudopotential correction on relaxation of the first-second layer spacing Δ_{12} for the low-index faces of Al, Li, and Na. Values for Δ_{12} are given as a percentage of the bulk interlayer spacing d . The first column in the top half of the table, labeled None, gives the results obtained with the exponential charge density profile and no pseudopotential corrections. The next four columns, labeled A1, A2, HA1 and HA2, list values obtained using the exponential density and two Ashcroft and two simplified Heine-Abarenkov pseudopotentials. The pseudopotential radii and well-depth parameters for the four models are given (in atomic units) in the lower half of the table. Values used for β were $1.24, 1.24,$ and 1.27 (a.u.)⁻¹ for Al, Li and Na, respectively, and ten layers were allowed to relax in the calculations.

Surface	None	Al ^a		Li ^b		Na ^c	
		A1	A2	HA1	HA2	A1	A2
Al(100)	-1.2	+0.2	+0.2	+0.1	+0.5		
Al(110)	-21.3	-14.5	-14.7	-15.2	-13.1		
Al(111)	+0.6	+1.4	+1.4	+1.3	+1.5		
Li(100)	-8.7	+0.1	-6.2	-4.6	-3.8		
Li(110)	-0.3	+1.4	+0.2	+0.4	+0.6		
Li(111)	+6.7	+41.0	+18.7	+23.5	+24.8		
Na(100)	-9.9	-5.5	-6.2	-6.0	-3.7		
Na(110)	-0.7	+0.1	0.0	-0.1	+0.5		
Na(111)	+3.6	+29.8	+26.7	+21.7	+26.1		
		Al		Li		Na	
		r_0	a_0	r_0	a_0	r_0	a_0
A1		1.131	∞	1.678	∞	1.758	∞
A2		1.12	∞	1.06	∞	1.66	∞
HA1		2.0	1.82	2.8	2.32	3.4	2.87
HA2		2.0	1.99	2.8	2.38	3.4	3.11

^a Reference 21.

^b Table XV of Ref. 17.

^c Table 8-3 of Ref. 16; $Z/a_0 = (A_0 + A_1 + A_2)/3$.

^d Table 8-3 of Ref. 16; $Z/a_0 = (A_0 + A_1)/2$.

TABLE VI. Crystallographic relationships for the low-index faces of cubic structures. (See Appendix B for notation.)

Crystal face	\vec{a}_1	\vec{a}_2	\vec{b}_1	\vec{b}_2	A	B	d	n_0	$P_G(n)$
fcc (001)	$(a/2)(1\bar{1}0)$	$(a/2)(110)$	$(2\pi/a)(1\bar{1}0)$	$(2\pi/a)(110)$	$a^2/2$	$2(2\pi/a)^2$	$a/2$	2	$P_G(2l+1) = 1, P_G(2l-2) = (-1)^{l+1}$
fcc (110)	$a(001)$	$(a/2)(1\bar{1}0)$	$(2\pi/a)(001)$	$(2\pi/a)(1\bar{1}0)$	$a^2/\sqrt{2}$	$\sqrt{2}(2\pi/a)^2$	$a/2\sqrt{2}$	2	$P_G(2l+1) = 1, P_G(2l-2) = (-1)^{l+1}$
fcc (111)	$(a/2)(\bar{1}10)$	$(a/2)(0\bar{1}1)$	$(4\pi/3a)(\bar{2}11)$	$(4\pi/3a)(1\bar{1}2)$	$\sqrt{3}a^2/4$	$(4/\sqrt{3})(2\pi/a)^2$	$a/\sqrt{3}$	3	$P_G(2l+1) = 1, P_G(2l-2) = (-1)^{l+1}$
bcc (001)	$a(100)$	$a(010)$	$(2\pi/a)(100)$	$(2\pi/a)(010)$	a^2	$(2\pi/a)^2$			
bcc (110)	$a(001)$	$(a/2)(1\bar{1}\bar{1})$	$(\pi/a)(1\bar{1}2)$	$(2\pi/a)(1\bar{1}0)$	$a^2/\sqrt{2}$	$\sqrt{2}(2\pi/a)^2$			
bcc (111)	$(a/2)(\bar{1}10)$	$(a/2)(0\bar{1}1)$	$(4\pi/3a)(\bar{2}11)$	$(4\pi/3a)(1\bar{1}2)$	$\sqrt{3}a^2/4$	$(4/\sqrt{3})(2\pi/a)^2$			

ACKNOWLEDGMENTS

I am grateful to Mark Rasolt and his colleagues for their critical comments on the manuscript. This work was supported by the U. S. Department of Energy, Office of Materials Science, U. S. DOE under contract No. EG-77-S-05-5489 and by the Office of Basic Energy Sciences, U. S. DOE under contract No. 405-eng-26 with the Union Car-

APPENDIX A

The electrostatic forces present in the fcc (100) and (110) faces of cubic structures is extended in this Appendix to include the bcc and fcc (111) faces of these cubic structures. Following to Eq. (9), we obtain for the m th layer due to those faces the following identical expression, but with the same notation as in Appendix B)

$$P_G^*(n) = \exp[2\pi i(\mu + \nu) \text{mod}(n, 3)/3], \quad (\text{A1})$$

where the $\text{mod}(a, b)$ function is defined as

$$\text{mod}(a, b) = a - [a/b]b,$$

and $[x]$ is the largest integer which does not exceed x . For the expression for F_m corresponding to Eq. (12), we obtain

$$F_m = \sum_G \frac{e^{-Gd}}{1 - e^{-3Gd}} (1 + X + X^2) P_G^*(L + 1) \times P_G^*(m) e^{-G[(L-n)d - \Delta(m)]}, \quad (\text{A2})$$

where

$$X = \exp[-Gd + (2\pi i/3)(\mu + \nu)]. \quad (\text{A3})$$

APPENDIX B

In this Appendix we compile crystallographic relationships for the low-index faces of cubic structures. The following notations are used:

\vec{a}_1, \vec{a}_2 are the primitive real-mesh translation vectors.

\vec{b}_1, \vec{b}_2 are the primitive reciprocal-mesh vectors; $\vec{a}_i \cdot \vec{b}_j = 2\pi \delta_{ij}$.

$\vec{G} = \mu \vec{b}_1 + \nu \vec{b}_2$ is the reciprocal-mesh vector.

A, B are real and reciprocal unit mesh areas.

d is the interlayer spacing in the unrelaxed real lattice.

n_0 is the repeat sequence for planes, i.e., plane $n + n_0$ has the same origin as plane n (in $2D$).

$P_G^*(n) = \exp[-i\vec{G} \cdot \vec{R}_n]$ is the phase function for plane n . The indexing of planes is $n = 0, 1, \dots$, with $n = 0$ being the top-most surface plane.

Table VI lists the above for the various fcc and bcc faces.

- ¹F. Jona, *J. Phys. C: Solid State Phys.* **11**, 4271 (1978).
- ²E. G. McRae and H. D. Hagstrum, in *Treatise on Solid State Chemistry*, edited by N. B. Hannay (Plenum, New York, 1976), Vol. 6A(I), Chap. 2.
- ³D. P. Jackson, *Can. J. Phys.* **49**, 2093 (1971).
- ⁴S. Kato, *Jpn. J. Appl. Phys.* **13**, 218 (1974).
- ⁵J. W. Flocken, *Phys. Rev. B* **9**, 5133 (1974).
- ⁶R. A. Johnson and P. J. White, *Phys. Rev. B* **13**, 5293 (1976).
- ⁷R. Benedek, *J. Phys. F* **8**, 1119 (1978).
- ⁸M. W. Finnis and V. Heine, *J. Phys. F* **4**, L37 (1974).
- ⁹R. Smoluchowski, *Phys. Rev.* **60**, 661 (1941).
- ¹⁰G. P. Alldredge and L. Kleinman, *Phys. Lett.* **48A**, 37 (1974); *J. Phys. F* **4**, L207 (1974); G. P. Alldredge, in *Computer Simulation for Materials Applications*, Nuclear Metallurgy, edited by R. J. Arsenault, J. R. Beeler, Jr., and J. A. Simmons (NBS, Washington, D.C., 1976), Vol. 20, p. 582.
- ¹¹S. K. S. Ma, F. W. de Wette, and G. P. Alldredge, *Surface Sci.* **78**, 598 (1978); G. P. Alldredge and S. K. S. Ma, *Phys. Lett.* **51A**, 155 (1975).
- ¹²J. R. Smith, *Phys. Rev.* **181**, 522 (1969).
- ¹³N. D. Lang and W. Kohn, *Phys. Rev. B* **1**, 4555 (1970).
- ¹⁴C. A. Sholl, *Proc. Phys. Soc.* **91**, 434 (1967); F. W. de Wette and G. E. Schacher, *Phys. Rev.* **137**, A78, A92 (1965).
- ¹⁵I. V. Abarenkov and V. Heine, *Phil. Mag.* **12**, 529 (1965).
- ¹⁶W. A. Harrison, *Pseudopotentials in the Theory of Metals* (Benjamin, New York, 1966).
- ¹⁷M. L. Cohen and V. Heine, in *Solid State Physics*, edited by F. Seitz, D. Turnbull, and H. Ehrenreich (Academic, New York, 1970), p. 37.
- ¹⁸C. Q. Ma and V. Sahni, *Phys. Rev. B* **19**, 1290 (1979).
- ¹⁹H. L. Davis, J. R. Noonan, and L. H. Jenkins, *Surface Sci.* **83**, 559 (1979).
- ²⁰H. L. Davis and D. M. Zehner, *J. Vac. Sci. Technol.* (to be published).
- ²¹F. Perrot, *Phys. Status Solidi B* **81**, 205 (1977).
- ²²C. Tejedor and F. Flores, *J. Phys. F* **6**, 1647 (1976).
- ²³We note that in Ref. 13, Appendix E, a calculation in which the topmost layer of ions at the (111) face of an fcc structure was allowed to shift from its truncated bulk position yielded an expansion $\Delta_{12} = 0.5\%$ for aluminum.
- ²⁴J. R. Noonan and H. L. Davis, *J. Vac. Sci. Technol.* (to be published); D. L. Adams and U. Landman, *Phys. Rev. B* **15**, 3775 (1977).
- ²⁵R. Monnier, J. P. Perdew, D. C. Langreth, and J. W. Wilkins, *Phys. Rev. B* **18**, 656 (1978).
- ²⁶A. J. E. Foreman and W. M. Lomer, *Proc. Phys. Soc. London Sec. B* **70**, 1143 (1957).
- ²⁷B. N. Brockhouse, T. Arase, G. Caglioti, K. R. Rao, and A. D. B. Woods, *Phys. Rev.* **128**, 1099 (1962).

High-frequency vibrational modes at stepped Pt(111) surfaces

Mark Mostoller

*Solid State Division, Oak Ridge National Laboratory,
Oak Ridge, Tennessee 37830*

Uzi Landman

*School of Physics, Georgia Institute of Technology,
Atlanta, Georgia 30332*

(Received 16 November 1978)

We show that vibrational modes with frequencies above the maximum in the bulk can occur at the steps of the Pt(332) or $6(111) \times (11\bar{1})$ surface, as observed by Ibach and Bruchmann, if the largest force constants are increased by $\sim 30\text{--}40\%$ at the steps. The calculations are done by applying the recursion method within clusters of thousands of atoms, with a rotationally invariant first- and second-neighbor bond-angle model for the interatomic forces.

Ibach and Bruchmann¹ have recently reported inelastic-electron-loss measurements of localized phonons at the (332) or $6(111) \times (11\bar{1})$ surface of platinum. The most interesting feature of their results is that the observed phonon loss peak occurs at a frequency of 25.4 meV, slightly higher than the maximum frequency of 24.3 meV in bulk Pt, and roughly 15% above the highest frequency peak at ~ 22 meV in the bulk density of states.² This is somewhat unexpected, because the usual picture is that phonon frequencies will decrease at surfaces to reflect the missing bonds. To explain higher-frequency surface vibrational modes, it is necessary to invoke relaxation accompanied by increased force constants in the surface region. Arguing by analogy to a linear chain with nearest-neighbor interactions, Ibach and Bruchmann estimated that the force constants for atoms at the steps must be increased by a factor of approximately 1.7 to explain their data.

Drawing conclusions for three dimensions from one-dimensional models is generally somewhat risky. On the other hand, high Miller index surfaces with regularly stepped structures like the fcc (332) surface are difficult to treat by either exact methods^{3,4} or approximate, slab calculations⁵ that rely on use of the two-dimensional transform with respect to surface wave vectors. An approach that does not vary in complexity with surface normal, i.e., one that can be programmed to deal with (hkl) surfaces in the same way as (100), (110), or (111), is the recursion method.⁶ We have applied this method to large clusters of atoms to investigate vibrational modes at stepped fcc surfaces.

We use a rotationally invariant, first- and second-neighbor (1nn + 2nn) bond-angle force model like that described by Keating.⁷ Scalar products of vectors are invariant under rotations, so the potential energy

is expanded in powers of scalar product differences S ,

$$S(n_1, n_2; n_3, n_4) = \bar{R}(n_1, n_2) \cdot \bar{R}(n_3, n_4) - \bar{R}_0(n_1, n_2) \cdot \bar{R}_0(n_3, n_4) \quad (1)$$

where $\bar{R}_0(n, n')$ is the equilibrium spacing between atoms at sites n and n' , and

$$\bar{R}(n, n') = \bar{R}_0(n, n') + \bar{u}(n) - \bar{u}(n')$$

includes the displacements $\bar{u}(n)$ and $\bar{u}(n')$ away from equilibrium. The expansion is truncated at second order in the displacements to yield a harmonic phonon Hamiltonian. For the present calculations, we include squares of the following scalar product differences in the potential energy, giving an example for each: 1nn bonds— $S^2(110,0;110,0)$; 2nn bonds— $S^2(200,0;200,0)$; 1nn-1nn-1nn angles— $S^2(110,0;011,0)$; 1nn-1nn-2nn angles— $S^2(110,0;1\bar{1}0,0)$, $S^2(110,0;200,0)$. In the bulk, this five-parameter bond-angle model is equivalent to a general 1nn + 2nn Born-von Kármán model. At surfaces, however, the bond-angle model is automatically rotationally invariant, unlike a truncated Born-von Kármán model.

We generate our clusters in a way designed to eliminate boundary effects in the recursion procedure. Suppose that we want to calculate the density of states for displacements of a particular atom along a given direction, e.g., for [111] displacements of an atom at a step on an fcc (332) surface. Then level 1 of the cluster consists solely of this atom. Level 2 includes the first and second neighbors of the single atom in level 1. Level 3 comprises all first and second neighbors of the atoms in level 2 not already included in levels 1 and 2, etc. If an $N+1$ level cluster is generated, then recursion is performed at level N , before the 1nn + 2nn Hamiltonian reaches cluster

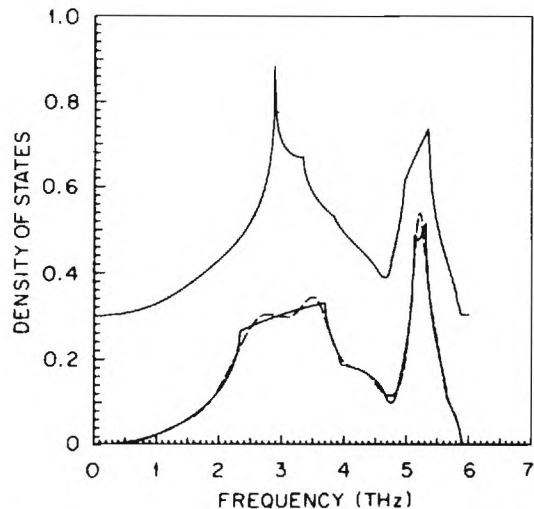


FIG. 1. Phonon densities of states for bulk Pt calculated by the Gilat-Raubenheimer (GR) and recursion methods: top—GR, six-neighbor force model of Ref. 2; bottom—GR (full line) and recursion (dashed line) results for the 1nn + 2nn force model fitted to the 90 K data in Ref. 2. All densities of states shown here and in Fig. 3 are normalized to integrate to unity.

boundary atoms in level $N + 1$ that are the only atoms in the cluster with missing neighbors.

The first step in the calculations was to fit the 1nn + 2nn force model to the neutron scattering data of Dutton *et al.*² Reasonably good agreement with the measured dispersion curves was obtained, although forces of longer range are needed to fit all details of the spectrum. Figure 1 compares the bulk Pt density of states calculated by the Gilat-Raubenheimer method⁸ for our 1nn + 2nn force model with the results of the six-neighbor model of Ref. 2. The details of the curves are somewhat different, but the major spectral features appear in the same places.

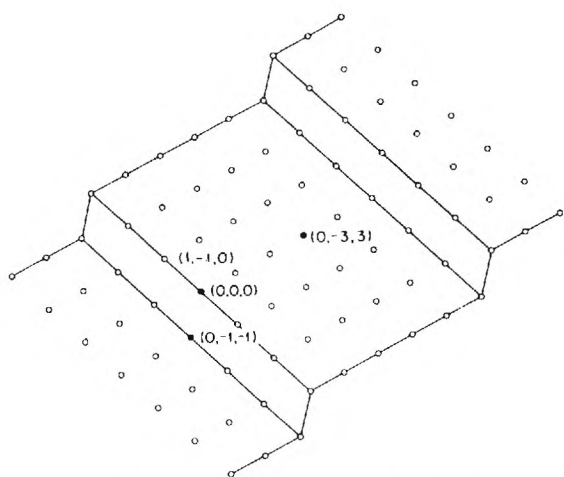


FIG. 2. Fcc (332) or $6(111) \times (11\bar{1})$ surface.

Figure 1 also shows level-9 recursion results, calculated within a level-10 cluster of 4579 atoms, for the 1nn + 2nn force model. These compare very well with the corresponding Gilat-Raubenheimer results.

For a surface as complex as the fcc (332) surface of a transition metal, it is difficult to argue what relaxation will occur and how the force constants will

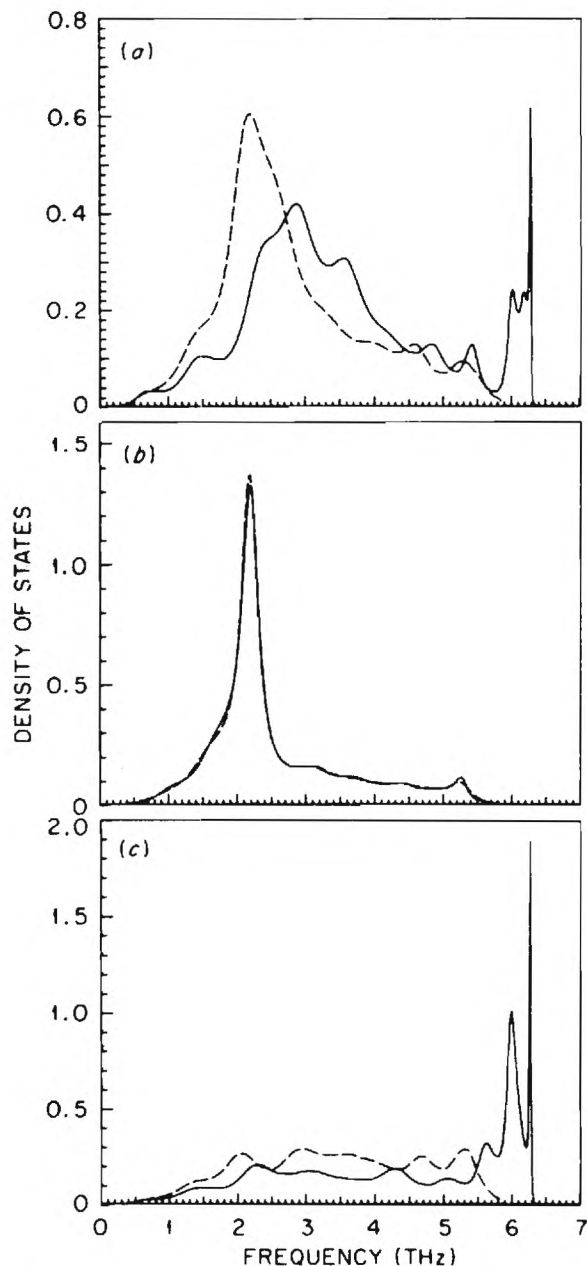


FIG. 3. Normalized densities of states for [111] vibrations at the Pt(332) surface. (a), (b), and (c) give results for edge, terrace, and corner atoms, respectively; full lines are for 1nn bond-stretching force constant increases of 15000 dynes/cm at the steps as described in the text, dashed lines for no force-constant changes.

change. We have therefore adopted a pragmatic viewpoint, focused our attention on the step edges, and set out to illustrate the magnitude of the changes needed to produce high-frequency step modes like those observed. Specifically, we allow changes only in the 1nn bond-stretching force constants for atoms at the top and bottom of the step edges, and no attempt is made to include relaxation to new equilibrium spacings $\bar{R}_0(n,n')$ near the surface.

Figure 2 shows the surface we are dealing with. The atoms at (0,0,0), (0,-1,-1), and (0,-3,3) will be referred to as edge, corner, and terrace atoms, respectively. Any atom that does not occupy a site on a surface step will be called a bulk atom.

Figure 3 compares densities of states for edge, terrace, and corner atoms for vibrations along the [111] direction, the normal to the steps. To obtain these results, recursion was performed at level 11 in level-12 clusters of 4099, 4313, and 4468 atoms, respectively. The dashed curves are those obtained with no changes in the forces at the surface except for the absence of interactions involving missing neighbors. The solid curves were calculated by assuming that all 1nn bond-stretching force constants for edge-corner, edge-bulk, and corner-bulk atom pairs were increased by about 35%, that is, by 15000 dynes/cm from the value of 41500 in the bulk.

Figure 3 shows that no high-frequency modes occur for edge, corner, or terrace atoms in the absence of force-constant changes, although the [111] densities of states for the three atoms are quite different from one another and from the bulk results. With 1nn forces at the steps increased by $\sim 35\%$ as specified, high-frequency peaks appear for both edge and corner atoms, while essentially no change is seen in the terrace atom density of states. In fact, the results shown for the terrace atom are virtually the same as those for Pt(111) vibrations along [111] with no force-constant changes. The pronounced high-frequency structure for edge and corner atoms extends from about the top of the bulk spectrum at 24.4 meV to about 26.1 meV (5.9–6.3 THz; 1 THz=4.135 meV). The electron-loss peak observed by Ibach and Bruchmann¹ fell at 25.4 meV (6.15 THz); this was considerably broader than the calcu-

lated results in Fig. 3, but most of the experimental width appears to have been instrumental.

In the results shown for edge and corner atoms with increased forces, the high-frequency modes are nearly split off above the bulk spectrum. The one-band recursion procedure we have used gives only semiquantitative accuracy for such cases. Thus, while the overall shape of the solid curves in Figs. 3(a) and (c) is reliable, the fine structure does vary with changes in such computational parameters as the recursion level. This does not affect our conclusions; the variations in the calculated results are small with respect to the experimental resolution.

Other sets of force-constant changes at the steps yield high-frequency modes for vibrations along the step-normal direction. These can be distinguished from one another by the structure they give for [111] vibrations and by their effects for other atoms and vibrational directions. All that we have tested require substantial (30–40%) increases in the force-model parameters at the steps, but not of the magnitude (70%) inferred by Ibach and Bruchmann from one-dimensional arguments. We have also performed calculations for another stepped surface similar to the (332) or 6(111)×(1 $\bar{1}$ 1), namely, the (755) or 6(111)×(100) and found similar results.

For these illustrative calculations, we have only considered changes in the 1nn bond-stretching force constants for atoms at the step edges and corners, because this provides a relatively simple model with few parameters that concentrates on the regions where the largest perturbations are expected. However, other force-constant changes no doubt occur at these surfaces, and we intend to explore more general phenomenological models to investigate the effects of such other changes.

ACKNOWLEDGMENTS

We would like to thank L. H. Jenkins, H. L. Davis, M. T. Robinson, and T. Kaplan for helpful discussions. This research was sponsored by the Division of Materials Sciences, U. S. DOE under Contract No. W-7405-eng-26 with the Union Carbide Corporation and Contract No. EG-77-S-05-5489.

¹H. Ibach and D. Bruchmann, *Phys. Rev. Lett.* **41**, 958 (1978).

²D. H. Dutton, B. N. Brockhouse, and A. P. Müller, *Can. J. Phys.* **50**, 2915 (1972).

³D. Kalkstein and P. Soven, *Surf. Sci.* **26**, 85 (1971).

⁴M. Mostoller and T. Kaplan, *Phys. Rev. B* **19**, 552 (1979).

⁵See, for example, D. Castiel, L. Dobrzynski, and D. Span-

jaard, *Surf. Sci.* **59**, 252 (1976).

⁶R. Haydock, V. Heine, and M. J. Kelly, *J. Phys. C* **5**, 2845 (1972).

⁷P. N. Keating, *Phys. Rev.* **145**, 637 (1966).

⁸G. Gilat and L. J. Raubenheimer, *Phys. Rev.* **144**, 390 (1966).

C. SURFACE REACTIONS

The main achievements of these studies are:

1. Development of a microscopic model of thermal desorption and dissociation from metallic surfaces.
2. Evaluation of rates for the above process.
 - (i) Derivation of the thermal adatom-solid coupling.
 - (ii) A stochastic incoherent multiphonon mechanism of bond rupture.
 - (iii) Coupling to final state reaction channels.
3. Comparative study of rates for a truncated harmonic and Morse potential descriptions of the chemisorptive bonds.
4. Analysis of rate data of thermal desorption for both a weak (Xe/W) and strong (K/W) chemisorption system, in agreement with experiments.
5. Development of a theoretical model for catalytic dissociation on surfaces. The model involves a doorway-state mechanism in which thermal excitations are fed into bond-rupture modes via low-frequency vibrational modes of the adsorbate which couple efficiently to the substrate.
6. Evaluation of temperature rate-maximizing conditions for Langmuier-Hinshelwood diffusion controlled catalytic reactions which involve surface heterogeneities and internal states. Interpretation of experimental observations for certain catalytic hydrocarbon disproportionation reactions.

Microscopic theory of thermal desorption and dissociation processes catalyzed by a solid surface

Gopa Sarkar De and Uzi Landman

School of Physics, Georgia Institute of Technology, Atlanta, Georgia 30332

Mark Rasolt

Solid State Division, Oak Ridge National Laboratory, Oak Ridge, Tennessee 37830

(Received 2 October 1979)

A microscopic model of thermal desorption and dissociation from metallic surfaces which exhibits explicit dependences on characteristic parameters of the adsorption system is developed. The evaluation of the rates of these processes involves: (i) a derivation of the thermal adatom-solid coupling, (ii) a stochastic incoherent multiphonon mechanism for the evolution of an excitation for bond rupture, and (iii) coupling to final-state reaction channels. Transition probabilities and rates obtained by using both truncated-harmonic and Morse-potential descriptions of the chemisorptive bond are presented and compared with experimental data for xenon and potassium desorption from a tungsten substrate. The results show agreement with experiment and exhibit a linear relationship of the logarithm of the rate versus inverse temperature.

I. INTRODUCTION

The fundamental understanding of the mechanisms of surface-catalyzed reactions is one of the major objectives of past and current surface-science studies. The three main methodologies which have been developed towards that goal can be classified as: (i) Phenomenological kinetic approach,^{1,2} which consists of a reaction scheme and a corresponding system of kinetic equations which incorporate rate constants and species concentrations. In this class of studies the rate constants are regarded as parameters to be determined by fitting the solutions of the kinetic equations to experiments performed at a number of system conditions (temperature, pressure, etc.). (ii) Thermodynamical and statistical-mechanical approaches,²⁻⁹ in which rate constants (at equilibrium) are evaluated using statistical quantities such as partition functions in juxtaposition with certain models of the reaction. Most notable among these methods are the transition-state theory² and "phase-space theories", Rice-Ramsperger-Kassel-Marcus (RRKM) and variants thereof,¹⁰ and theoretical trajectory analysis¹¹ (although the latter, RRKM in particular, while most popular in gas-phase kinetics, have not been thoroughly investigated in surface-reaction studies). (iii) Microscopic models of the reaction mechanism.¹²⁻²² In these theories the underlying physical processes governing the reacting system (such as, excitation, energy transfer, mode-mode couplings, transport) are investigated and an expression for the reaction rate is derived.

While all the above provide valuable information,

it is obvious that the microscopic models carry the largest potential of providing fundamental understanding of the reaction processes. Studies of this kind would allow the investigation of the dependence of reaction paths and rates on characteristics of the reaction system and could provide *criteria* for matching catalytic partners and ambient conditions such as to allow for optimal catalytic selectivity and specificity. It should be recognized, however, that studies of type (iii) present great theoretical difficulties and thus are scarce. Nevertheless, current advents of theoretical methods and novel surface experimental techniques, in particular electronic and vibrational spectroscopies (ultraviolet photoemission, Auger chemical shifts, electron-loss spectroscopies, surface infrared techniques—to name a few)^{23,24} and kinetic measurements (molecular beams²⁵ and mass- and state-selective spectroscopies), provide the impetus for an increased activity in the above direction.

In discussing the kinetics of a reaction it is convenient to formulate it in terms of elementary reaction steps.^{1,25} For a surface reaction, typical elementary reaction steps are: adsorption, transport (diffusion), excitation, dissociation, association, and desorption, not all of which necessarily occur for one given reaction. In the present study we focus on bond-rupture elementary reactions, i.e., dissociation and desorption.²⁶ Moreover, we investigate the thermal phenomena as distinct from the corresponding induced processes^{26(a)}: electron-stimulated desorption (ESD), electron-impact desorption (EID), photodesorption (PD), and field desorption (FD). In the present study we formulate a theory of thermal desorption processes,

which exhibits explicitly the dependence on the rates on parameters characteristic to the adsorption system.

To facilitate our discussion we specify the following ingredients of the theory (a) coupling of an atom or a molecule to the surface, (b) substrate-induced thermal-energy transfer and excitation, and (c) temporal evolution of the system, i.e., time evolution and calculation of reactional probabilities and rates. Accordingly, the organization of the paper is as follows: The Hamiltonian and couplings are derived in Sec. II. Models of the excitation mechanism and temporal evolution yielding expressions for reaction rates are discussed in Sec. III. A systematic analysis and discussion of results of the models and further remarks are given in Sec. IV.

II. HAMILTONIAN AND COUPLINGS

A. Hamiltonian

The first step in our formulation is a statement of the Hamiltonian of the system. The total Hamiltonian of the adsorption system may be written as

$$H = T_e + T_N + V(\vec{r}, \vec{R}), \quad (2.1)$$

where T_e and T_N represent kinetic energies of electrons and nuclei of the system (molecule and substrate) and $V(\vec{r}, \vec{R})$, various contributions to the potential energy ($\vec{r} \equiv \{\vec{r}_M, \vec{r}_s\}$, $\vec{R} \equiv \{\vec{R}_M, \vec{R}_s\}$, where \vec{r}_M and \vec{r}_s are the electronic coordinates of the adsorbed molecule and solid respectively, and \vec{R}_M, \vec{R}_s the corresponding nuclear coordinates). In the adiabatic approximation the total wave function is taken as²⁷

$$\psi(\vec{r}, \vec{R}) = \phi(\vec{r}, \vec{R}) \chi_N(\vec{R}). \quad (2.2)$$

The electronic wave function satisfies the equation

$$[T_e + V(\vec{r}, \vec{R})] \phi(\vec{r}, \vec{R}) = \epsilon_e(\vec{R}) \phi(\vec{r}, \vec{R}) \quad (2.3)$$

solved for fixed \vec{R} , where the direct interaction between nuclei is included in $V(\vec{r}, \vec{R})$. The equation for the nuclear motion can be found variationally²⁸

$$\left(- \sum_{\mu=1}^N \frac{1}{2M_{\mu}} \nabla_{\mu}^2 + [\epsilon_e(\vec{R}) + V'(\vec{r})] \right) \chi_N(\vec{R}) = \epsilon_N \chi_N(\vec{R}), \quad (2.4)$$

where

$$V'(\vec{R}) = \sum_{\mu=1}^N \int d\vec{r} \phi^* \left(- \frac{1}{2M_{\mu}} \nabla_{\mu}^2 \right) \phi, \quad (2.5)$$

and the summations are over all the nuclei. The effective potential [expression in square brackets in Eq. (2.4)] for the nuclear motion is dominated by the electronic energy $\epsilon_e(\vec{R})$ and the term $V'(\vec{R})$

is small. It is interesting to note here that the *exact* eigenvalue ϵ_{exact} is bounded between ϵ_N [the solution to Eq. (2.4)] and ϵ'_N [the solution to Eq. (2.4) with $V'(R)$ neglected]; i.e., $\epsilon_N \geq \epsilon_{\text{exact}} \geq \epsilon'_N$.²⁹

At this stage the electronic energy $\epsilon_e(\vec{R})$ may be modeled in the following manner. First one identifies in $\epsilon_e(\vec{R})$ those components which correspond to intramolecular bonds and to binding between atoms of the molecule and a localized region in the solid. The electronic interactions for a fixed configuration of nuclear molecular coordinates $\{\vec{R}_M\}$ and solid nuclear coordinates $\{\vec{R}_s\}$ determine the adsorption potential between the solid and the adsorbate. We separate the interaction into two parts: one in which the solid is kept stationary and the other where the solid is allowed to vibrate. It is via the latter contribution that an energy exchange between the molecule and solid (which may eventually yield desorption or dissociation) becomes possible. The first contribution to these "bond potential energies" may then be modeled by some analytical potential formulas such as a harmonic well, a Morse potential, or other suggested potential formulas. The rest of $\epsilon_e(\vec{R})$, i.e., that part which can be identified with the solid coordinates, may then be replaced by a certain model of the solid [remember that internuclear interactions were included in $\epsilon_e(\vec{R})$].

The corresponding nuclear-motion equations (2.4) may then be solved with the above-mentioned model replacement for $\epsilon_e(\vec{R})$, and their solutions provide the vibrational spectrum for the modeled system.

B. Coupling

In this section we derive, under certain approximations, an expression for the coupling between a point charge (of charge $+Z_A^*e$, where Z_A^* is the effective charge of the ion) adsorbed at a distance z_1 from a metal surface and the *fluctuating* part of the metal substrate. As discussed previously, in the model in which we develop the role of the electronic (including direct nuclear interactions) energy is to establish a bounded molecule-solid system characterized by, for example, a Morse potential with an equilibrium distance d_1 of the atomic constituents from the surface, with an associated manifold of vibrational levels.

To make the calculation tractable and yet preserving the essential physical features, we model the surface in the following manner. We consider an electron gas bounded by an infinite potential barrier (Fig. 1). The *static* ions are then placed within this potential and the first plane is positioned at a distance $L - z_0$ with $z_0 \rightarrow 0$ from the

potential barrier, where L is the linear dimension of the slab.

We now relax the static ions and allow them to fluctuate by emitting phonons. Denoting such a density fluctuation of the ions as $\delta n_b(\vec{r})$ and the electronic response to such a fluctuation as $\delta n_e(\vec{r})$, the coupling may be written as

$$v(\vec{r}) = \delta u_b(\vec{r}) + \delta u_e(\vec{r}),$$

where $\delta u_b(\vec{r})$ and $\delta u_e(\vec{r})$ are the fluctuating ionic and electronic interaction potentials with the adsorbed charge ($+Z_A^*e$) positioned at \vec{r} ; i.e.,

$$\delta u_b(\vec{r}) = Z_A^* Z_s e^2 \int \frac{d\vec{r}' \delta n_b(\vec{r}')}{|\vec{r} - \vec{r}'|}, \quad (2.6)$$

$$\delta u_e(\vec{r}) = -Z_A^* Z_s e^2 \int \frac{d\vec{r}' \delta n_e(\vec{r}')}{|\vec{r} - \vec{r}'|}, \quad (2.7)$$

with Z_A^* and Z_s atomic charges (possibly screened) of the adatom and metal ions, re-

spectively. The position vector \vec{r} of the point charge is set equal to $z_1 + L$ in Eqs. (2.6) and (2.7), where L is the thickness of the sample (Fig. 1). We choose next a wave vector \vec{q} of the fluctuating ionic background and express the single Fourier component of the density fluctuation as

$$\delta n_b(z, \vec{r}_\parallel) = \delta n_b(q_\perp, \vec{q}_\parallel) \times \exp[i(q_\perp z + \vec{q}_\parallel \cdot \vec{r}_\parallel)] + \text{c.c.} \quad (2.8)$$

In the following we omit writing explicitly the parallel components $\vec{r}_\parallel, \vec{q}_\parallel$ from δn_b due to translational invariance in planes parallel to the surface, and denote $\delta n_b(z) \equiv \delta n_b(z, \vec{r}_\parallel)$ and $\delta n_b(q) \equiv \delta n_b(q_\perp, \vec{q}_\parallel)$. It is convenient to define an extension of $\delta n_b(z)$ (see below) by an even function $\delta n_b'(z)$ such that for z in the range $(-L, 0)$, $\delta n_b'(z) = \delta n_b(-z)$.

The potential $v(\vec{r})$ (for $\vec{r} = z_1 + L$) can be evaluated yielding

$$\begin{aligned} v(z_1 + L) &= Z_A^* Z_s e^2 \int d\vec{r}' \int_0^L dz' \left(\frac{\delta n_b'(\vec{r}')}{|z_1 + L - \vec{r}'|} - \frac{\delta n_e'(\vec{r}')}{|z_1 + L - \vec{r}'|} \right) \\ &= 2\pi Z_A^* Z_s e^2 e^{-\alpha_0 z_1} \left(\frac{\delta n_b'(q_\perp)}{q_\perp^2 + q_\parallel^2} - \sum_{k_\perp} \frac{1}{k_\perp^2 + q_\parallel^2} \delta n_e'(k_\perp) \right). \end{aligned} \quad (2.9)$$

[In Eq. (2.9) we have neglected exponential terms like e^{-L} and also recall that, e.g., $\delta n_e'(k_\perp) \equiv \delta n_e'(k_\perp, \vec{q}_\parallel)$.] Note that the sum over k_\perp in Eq. (2.9) reflects the fact that the electronic charge density responds with all k_\perp values to the single Fourier component of the background fluctuation in Eq. (2.8).

Our final task is to evaluate the sum over k_\perp in Eq. (2.9). To do that we treat the electrons semiclassically, which amounts to solving the linearized static collisionless Boltzmann equation^{30,31}

$$\frac{\vec{p}}{m} \cdot \frac{\partial}{\partial \vec{r}} \delta f(\vec{p}, \vec{r}) = \frac{\partial}{\partial \vec{p}} f_0(\epsilon_p) \cdot \frac{\partial}{\partial \vec{r}} \delta u(\vec{r}), \quad (2.10)$$

where $\epsilon_p = p^2/2m$, $f_0(\epsilon_p)$ is the Fermi-Dirac dis-

tribution function and $\delta u(\vec{r})$ the self-consistent field given by Eqs. (2.6) and (2.7) (with Z_A^* omitted).

The electron density $\delta n_e(\vec{r})$ is given by

$$\delta n_e(\vec{r}) = \int \frac{d^3 p}{(2\pi)^3} f(\vec{p}, \vec{r}). \quad (2.11)$$

The boundary conditions dictated by the infinite barrier at the surface are those of specular reflection.

$$\delta f(p_\perp, z=0, L) = \delta f(-p_\perp, z=0, L). \quad (2.12)$$

The solution of Eqs. (2.10)–(2.12) is not difficult³¹ and we present in the following only the key relationships. It is convenient to extend the definition of Eq. (2.10) to the range $(-L, L)$ by defining the primed quantities $\delta u'(z)$, $\delta f'(p_\perp, z)$, ... as even function extensions of $\delta u(z)$, $\delta f(p_\perp, z)$, ... A Fourier transformation of Eq. (2.10) yields

$$\delta f'(p_\perp, k_\perp) = \frac{\partial f_0(\epsilon_p)}{\partial \epsilon_p} \delta u'(k_\perp), \quad (2.13)$$

where

$$\delta f'(p_\perp, k_\perp) \equiv \frac{1}{2L} \int_{-L}^L dz e^{ik_\perp z} \delta f'(p_\perp, z) \quad (2.14)$$

and

$$k_\perp = n\pi/L, \quad n = 0, \pm 1, \pm 2, \dots$$

$\delta u'(k_\perp)$ can be easily derived from the even extension of Eqs. (2.6) and (2.7) and is given as

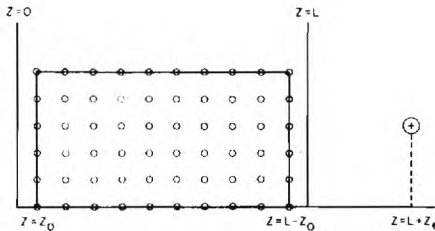


FIG. 1. Model adsorption system. The electron gas is bounded in a slab of linear dimension L . The first plane of substrate ions is located at $z=L-z_0$ with $z_0 \rightarrow 0$. The adsorbed ion is located at $z=L+z_1$.

$$\delta u'(k_{\perp}) = \delta u'_b(k_{\perp}) + \bar{v}(k_{\perp}) \delta n'_s(k_{\perp}) - \frac{q_{\parallel} \bar{v}(k_{\perp})}{L} \sum_{k'_1} \frac{\delta n'_s(k'_1)}{k'^2_1 + q^2_{\parallel}}, \quad (2.15)$$

where $\bar{v}(k_{\perp}) \equiv 4\pi e^2 / (k^2_{\perp} + q^2_{\parallel})$ and the sum over k'_1 is over even integers if k_{\perp} is even and odd integers if k_{\perp} is odd. We note from Eqs. (2.13)-

(2.15) that the solution of Eq. (2.13) satisfies the specular reflection boundary condition automatically which was the motivation underlying the extension of the functions from $-L$ to 0. Integrating both sides of Eq. (2.13) over \bar{p} and using Eq. (2.15) for $\delta u'(k_{\perp})$ gives the following self-consistent equation for $\delta n'_s(k_{\perp})$:

$$[1 + \bar{v}(k_{\perp})N(0)] \delta n'_s(k_{\perp}) = -N(0)\delta u'_b(k_{\perp}) + \bar{v}(k_{\perp})N(0) \frac{q_{\parallel}}{L} \sum_{k'_1} \frac{\delta n'_s(k'_1)}{k'^2_1 + q^2_{\parallel}}, \quad (2.16)$$

where the density of states at the Fermi level $N(0)$ is

$$N(0) = - \int \frac{\partial f_0(\epsilon_p)}{\partial \epsilon_p} \frac{d^3p}{(2\pi)^3}.$$

Dividing both sides of Eq. (2.16) by $1 + \bar{v}(k_{\perp})N(0)$, multiplying by $(k^2_{\perp} + q^2_{\parallel})^{-1}$, and summing over k_{\perp} , we can finally solve for the restricted sum over k'_1 to give the final form

$$\delta n'_s(k_{\perp}) = - \frac{N(0)}{1 + N(0)\bar{v}(k_{\perp})} \left(\delta u'_b(k_{\perp}) + \frac{q_{\parallel} N(0)\bar{v}(k_{\perp})}{DL} \sum_{k'_1} \frac{1}{1 + N(0)\bar{v}(k'_1)} \frac{\delta u'_b(k'_1)}{k'^2_1 + q^2_{\parallel}} \right), \quad (2.17)$$

where

$$D = 1 - \frac{q_{\parallel}}{L} \sum_{k'_1} \frac{N(0)\bar{v}(k'_1)}{(k'^2_1 + q^2_{\parallel})[1 + N(0)\bar{v}(k'_1)]} = 1 - \frac{\lambda^2_{TF}}{2(q^2_{\parallel} + \lambda^2_{TF})^{1/2}} \frac{\lambda^2_{TF}}{[q_{\parallel} + (q^2_{\parallel} + \lambda^2_{TF})^{1/2}]} \quad (2.18)$$

where

$$\lambda^2_{TF} = 4\pi e^2 N(0),$$

$$\delta u'_b(k_{\perp}) = \frac{4\pi e^2}{q_{\parallel}} \delta n_b(q_{\perp}) \times \left(\frac{q_{\parallel}}{q^2_1 + q^2_{\parallel}} \delta_{q_1, k_1} - \frac{q^2_{\parallel}}{L(q^2_1 + q^2_{\parallel})(q^2_{\parallel} + k^2_1)} \right) \quad (2.19)$$

and TF represents Thomas-Fermi. Substituting Eq. (2.19) in Eq. (2.17), the sum over k_{\perp} in Eq. (2.9) may now be evaluated yielding our final expression for $v(z_1 + L)$:

$$v(z_1 + L) \equiv v(z_1) = \frac{Z_A^* Z_s e^{2\pi} \delta n_b(q_{\perp}) \exp(-q_{\parallel} z_1)}{(q^2_1 + q^2_{\parallel}) D} \times \left(1 - \frac{\lambda^2_{TF}}{q^2_1 + q^2_{\parallel} + \lambda^2_{TF}} \right). \quad (2.20)$$

Within the context of the infinite surface barrier as a model for the static semi-infinite crystal the generalization of Eq. (2.20) to include crystallinity of the substrate would involve simply treating $\delta n_b(q_{\perp}, \bar{q}_{\parallel})$ in terms of the phonon crystal propagator. In the present calculation we, however, would use a continuum Debye model of the solid.

In a continuum model of the solid the Fourier components of the positive background number-density fluctuations, $\delta n_b(\bar{q})$ see Eq. (2.8), are defined by the relation

$$\delta n_b(\bar{r}) = \sum_{\bar{q}} \delta n_b(\bar{q}) e^{i\bar{q} \cdot \bar{r}} \quad (2.21)$$

and $\delta n_b(\bar{r})$ is given as³¹

$$\delta n_b(\bar{r}) = -Z_s n_0 \bar{\nabla} \cdot \bar{D}, \quad (2.22)$$

where n_0 is the ionic number density of the solid and \bar{D} is the displacement of the background from its equilibrium position. From Eqs. (2.21) and (2.22) it follows that

$$\delta n_b(q_{\perp}, \bar{q}_{\parallel}) \equiv \delta n_b(q_{\perp}) = Z_s n_0 \left(\frac{\hbar}{2M_s n_0 \Omega \omega_{\bar{q}}} \right)^{1/2} q(b_{\bar{q}} + b_{-\bar{q}}^{\dagger}), \quad (2.23)$$

where M_s is the atomic mass of a solid atom, Ω is the volume of the solid, and $b_{\bar{q}}(b_{\bar{q}}^{\dagger})$ are the annihilation (creation) operators of a phonon of wave vector \bar{q} and frequency $\omega_{\bar{q}}$. We now express the instantaneous position of the adsorbed atom z_1 as $z_1 = d_1 + u_1$, where d_1 is the equilibrium distance of the atom from the surface, and expand the exponent in Eq. (2.20) as

$$e^{-q_{\parallel} z_1} = e^{-q_{\parallel} d_1} (1 - q_{\parallel} u_1 + \frac{1}{2} q^2_{\parallel} u^2_1 + \dots). \quad (2.24)$$

Substitution of Eqs. (2.23) and (2.24) into Eq. (2.20) yields an expression for $v(z_1)$, which may be written as

$$v(z_1) = v_0(\bar{q}; d_1) + \delta v_1(\bar{q}; u_1) + \delta v_2(\bar{q}; u_1) + \dots, \quad (2.25)$$

$$\delta v_1(\bar{q}; u_1) = g_{\bar{q}}^{(1)} u_1 (b_{\bar{q}} + b_{-\bar{q}}^{\dagger}), \quad (2.26a)$$

$$\delta v_2(\bar{q}; u) = g_{\bar{q}}^{(2)} u^2_1 (b_{\bar{q}} + b_{-\bar{q}}^{\dagger}), \quad (2.26b)$$

where $\delta v_1(\bar{q}; u_1)$ is the potential corresponding to bilinear coupling between the vibrations of the atom and the phonons of the solid. Assuming for simplicity an acoustic continuum model for the solid, i.e., $\omega_{\bar{q}} = s q$, where s is the sound velocity, $g_{\bar{q}}^{(1)}$ in Eq. (2.26) is given by

$$g_{\vec{q}}^{(1)} = -F \frac{q^{1/2} q_{\parallel}}{q^2 + \lambda_{\text{TF}}^2} \left(1 + \frac{\lambda_{\text{TF}}^2}{2(q_{\parallel}^2 + \lambda_{\text{TF}}^2)^{1/2} [q_{\parallel} + (q_{\parallel}^2 + \lambda_{\text{TF}}^2)^{1/2}] - \lambda_{\text{TF}}^2} \right) e^{-a_{\parallel} a_{\parallel}}, \quad (2.27a)$$

where

$$F = 2\pi Z_A Z_A^* e^2 \left(\frac{\hbar n_c}{2M_s \Omega_s} \right)^{1/2}. \quad (2.27b)$$

The above derivation of the vibrational coupling can be applied to any of the atoms of the molecule which interacts with the surface by simply using the appropriate effective atomic charge Z_A^* and equilibrium distance d_1 . For the sake of simplicity, we will limit ourselves in the following to a single adsorbed atom (the extension to a polyatomic molecule is easy and will be presented elsewhere). Our results can be summarized by writing the Hamiltonian for our model system as

$$H = \epsilon_e^0 + H_v^0 + H', \quad (2.28a)$$

$$H' = \sum_i v(z_i), \quad (2.28b)$$

[the index i in Eq. (2.28b) simply generalizes our coupling to several adsorbates] where ϵ_e^0 is the electronic energy (including direct nuclear-nuclear interactions) for equilibrium nuclear positions and H_v^0 is the zeroth-order Hamiltonian for the adsorption system

$$H_v^0 = \sum_{\vec{q}} \hbar \omega_{\vec{q}} (b_{\vec{q}}^{\dagger} b_{\vec{q}} + \frac{1}{2}) + \sum_m H_{v,m}, \quad (2.29)$$

where the first term on the right corresponds to the harmonic solid (and in our model a Debye model is employed), and the second term corresponds to the vibrational energies of intramolecular and chemisorptive bonds (the m summation extends over all bonds). The last term [Eq. (2.28b)] in Eq. (2.28a) contains couplings between the vibrations of intramolecular and chemisorptive bonds and fluctuations in the solid, see Eqs. (2.25)–(2.27). We note that in a more refined description local modes due to the adsorbate could be included.

C. Transition rate

The final quantity which we require before turning to the stochastic evolution of the system (see Sec. III) is the transition rate between vibrational levels of the adsorbed system. These transitions occur due to the coupling Hamiltonian H' in Eq. (2.28a). To lowest order in perturbation theory the transition rates can be calculated by the golden-rule formula³²

$$W_{v-v'} = \frac{2\pi}{\hbar} \sum_{n_q, n_q'} p(n_q) |\langle v', n_q' | H' | v, n_q \rangle|^2 \times \delta(\epsilon_{v'} - \epsilon_v + \epsilon_{n_q'} - \epsilon_{n_q}), \quad (2.30)$$

where we sum over phonon final states n_q' and average over phonon initial states n_q using the probability distribution $p(n_q)$.

In order to evaluate $W_{v-v'}$, we need to specify the manner in which we model the vibrational spectrum of the adsorbed molecule.

(i) In the crudest approximation the vibrations are modeled by harmonic oscillators, truncated at the appropriate predissociation levels (see Sec. III). Keeping only terms up to bilinear coupling [δv_1 , see Eq. (2.25)] allows only for single quantum transition ($v \rightarrow v \pm 1$), accompanied by the absorption (emission) of a phonon. Denoting the harmonic frequency by ω_0 , δv_1 in Eq. (2.26a) can be written as

$$\delta v_1(\vec{q}) = g_{\vec{q}}^{(1)} \left(\frac{\hbar}{2\omega_0 M_A} \right)^{1/2} (a + a^{\dagger})(b_{\vec{q}} + b_{-\vec{q}}^{\dagger}), \quad (2.31)$$

where M_A is the mass of the adsorbed atom and $a(a^{\dagger})$ are creation (annihilation) operators of the harmonic-oscillator states. Substitution of Eq. (2.31) in Eq. (2.30) yields for the transition rate between levels

$$W_{v-v+1} = \frac{2\pi}{\hbar} \left(\frac{\hbar}{2\omega_0 M_A} \right) (v+1) \times \sum_{\vec{q}} |g_{\vec{q}}^{(1)}|^2 \bar{n}_{\omega_{\vec{q}}} \delta(\hbar\omega_{\vec{q}} - \hbar\omega_0), \quad (2.32)$$

where the phonon occupation number is given by $\bar{n}_{\omega_{\vec{q}}} = [\exp(\beta\hbar\omega_{\vec{q}}) - 1]^{-1}$, $\beta = (k_B T)^{-1}$. For an isotropic Debye model of the solid, i.e., $\omega_{\vec{q}} = sq$, and a cutoff frequency ω_D given by $\hbar\omega_D = \hbar sq_D = k\Theta_D$ where Θ_D is the Debye temperature, we replace the summation over \vec{q} by an integral. Using the energy-conservation Dirac delta function and cylindrical coordinates the integration is straightforward, yielding

$$\frac{W_{v-v+1}}{v+1} \equiv A(\omega_0) = \frac{3\pi^3 e^4 (Z_A^* Z_A)^2 n_c^2 \lambda_{\text{TF}}^4}{M_A M_s \omega_D^3 (q_0^2 + \lambda_{\text{TF}}^2)^2} \bar{n}_{\omega_0} (J_1 + J_2 + J_3), \quad (2.33a)$$

$$J_1 = \int_0^{\omega_0} x^3 \exp(-2\lambda_{\text{TF}} d_1 x) dx, \quad (2.33b)$$

$$J_2 = 2 \int_0^{\omega_0} x^3 \exp(-2\lambda_{\text{TF}} d_1 x) / [1 + 2x^2 + 2x(x^2 + 1)^{1/2}] dx, \quad (2.33c)$$

$$J_3 = \int_0^{\delta} x^3 \exp(-2\lambda_{\text{TF}} d_1 x) / \{1 - 4[1 + x^2 + x(x^2 + 1)^{1/2}] + 4(1 + x^2)[1 + 2x^2 + 2x(x^2 + 1)^{1/2}]\} dx, \quad (2.33d)$$

where equal sound velocities for transverse and longitudinal modes have been used, $\delta = q_{D_0} / \lambda_{\text{TF}}$, ($q_{D_0}^2 = \frac{2}{3} q_D^2$), and $s q_0 = \omega_0$. The integrals J_2 and J_3 are easily computed by numerical quadrature.

The superscript (h) in $W_{v \rightarrow v+1}^{(h)}$ is introduced in reference to the harmonic-oscillator model. An analysis of the dependence of the transition rate $W_{v \rightarrow v+1}^{(h)}$ [Eq. (2.33a)] on characteristics of the adsorption system is presented below.

(ii) As an improved model of the bond potential energy between an adsorbed atom and the surface, we consider the Morse potential³³

$$\epsilon_{\bullet}(z - d_1) = D_{\bullet} \{1 - \exp[-\beta(z - d_1)]\}^2 - D_{\bullet}, \quad (2.34)$$

where D_{\bullet} is the dissociation energy referred to the minimum, d_1 the equilibrium distance of the adsorbed atom from the surface, and the parameter β determines the width of the potential. One often defines the anharmonicity parameter $x_{\bullet} = \hbar \omega_0 / 4D_{\bullet}$ where ω_0 is the vibrational frequency for infinitesimal amplitudes (x_{\bullet} is often determined empirically). The eigenvalues of the one-dimensional Schrödinger equation with the Morse potential are given by^{34,35}

$$\epsilon_v = \hbar \omega_0 (v - x_{\bullet} v^2) - D_{\bullet}, \quad (2.35)$$

and therefore the vibrational level spacing is

$$\Delta \epsilon_{v \rightarrow v+1} = \hbar \omega_0 [1 - x_{\bullet} (2v + 1)]. \quad (2.36)$$

Using Eq. (2.30) for $W_{v \rightarrow v'}$ with H' given by Eqs. (2.28b), (2.25), and (2.26a), i.e., to linear order in u_1 (the derivation of the bond length from equilibrium), we observe that we need to compute the matrix elements $|\langle v' | u_1 | v \rangle|^2$, where $|v\rangle$ is the Morse eigenfunction corresponding to ϵ_v in Eq. (2.35). These matrix elements have been calculated by several authors.^{35,36} While the results given in Eqs. (21)–(24) of Ref. 35 are valid for all v, v' we will be interested only in nearest and next-nearest level transitions, i.e., $v \rightarrow v \pm 1$ and $v \rightarrow v \pm 2$. In addition the expressions simplify significantly in the approximation $(v' + v'')x_{\bullet} \ll 1$, yielding³⁶

$$|\langle v + 1 | u_1 | v \rangle|^2 = (d_1 B_{\bullet} / \omega_0) (v + 1) [1 + x_{\bullet} (1 + v)] \quad (2.37)$$

$$|\langle v + 2 | u_1 | v \rangle|^2 = (d_1^2 B_{\bullet} x_{\bullet} / 4\omega_0) (v + 1)(v + 2). \quad (2.38)$$

The expression for the transition rate between Morse levels v and v' can now be written as

$$W_{v \rightarrow v'}^{(h)} = \frac{2\pi}{\hbar} \sum_{\mathbf{q}} |g_{\mathbf{q}}^{(h)}|^2 \bar{n}_{\mathbf{q}} |\langle v' | u_1 | v \rangle|^2 \times \delta(\epsilon_{v'} - \epsilon_v - \hbar \omega_{\mathbf{q}}). \quad (2.39)$$

Using the matrix elements given by Eqs. (2.37) and (2.38) and the Debye model for the solid we obtain to first order in the anharmonicity x_{\bullet} the following expressions for $v' = v + 1$ and $v + 2$,

$$\frac{W_{v \rightarrow v+1}^{(h)}}{v+1} = A(\omega_0) \{1 + x_{\bullet} [(v+1) - (2v+1)B(\omega_0)]\}, \quad (2.40)$$

where

$$B(\omega_0) = \frac{\omega_0}{A(\omega_0)} \frac{\partial A(\omega_0)}{\partial \omega_0} \quad (2.41)$$

and

$$\frac{W_{v \rightarrow v+2}^{(h)}}{(v+1)} = \frac{1}{4} x_{\bullet} (v+1)(v+2) A(2\omega_0), \quad (2.42)$$

where $A(\omega_0)$ is given in Eq. (2.33).

To demonstrate the dependence of the transition rates between vibrational levels on the model of the potential well, the temperature and characteristics of the adsorption system such as the equilibrium distance and fractional charge on the atom, we present the numerical evaluation of Eqs. (2.33) and (2.34) in Figs. 2–4. In Fig. 2, the variation of $W_{v \rightarrow v'}$ for potassium adsorption on tungsten,³⁷ with temperature and model potential is displayed. The differences between the results using harmonic and Morse potentials are evident. Note that for the Morse potential $W_{1 \rightarrow 2} \gg W_{1 \rightarrow 3}$. In addition the transition rates between high-lying vibrational levels in the Morse potential are much larger than between the bottom-lying levels. This indicates that transitions between the low-lying levels may be the bottle neck in the incoherent multiphonon evolution of the system (see Sec. III). The marked dependence of the transition rates on temperature should also be noted, and is associated with the temperature-dependent phonon occupation number $\bar{n}_{\omega_{\mathbf{q}}}$.

Similar dependences are seen for xenon adsorbed on tungsten^{38–40,9} (Fig. 3) where in addition the sensitivity to the equilibrium distance d_1 and fractional charge on the atom are demonstrated. Finally, in Fig. 4, $W_{v \rightarrow v+1}^{(h)}$ as a function of the level number v for Xe/W system at $T = 100$ K is shown to increase markedly. The influence of these results on the rates of desorption will be investigated in Sec. III.

III. EVALUATION OF FIRST PASSAGE TIMES FOR THE TRUNCATED-HARMONIC-OSCILLATOR AND MORSE-POTENTIAL MODELS

Having obtained explicit expressions for the couplings between the adsorbate and the substrate

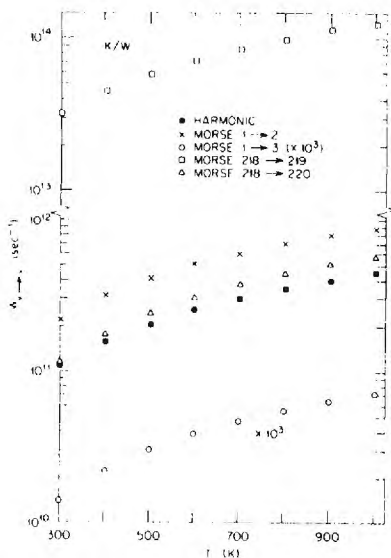


FIG. 2. Transition rate ($W_{v \rightarrow v'}$) vs temperature for potassium adsorbed on tungsten. The parameter used in the calculation: fractional charge on the potassium $z_A^* = 0.27e$ and equilibrium distance of the adsorbate from the substrate, $d_1 = 2.38 \text{ \AA}$, were chosen after Ref. 37. The transition rate, $W_{v \rightarrow v+1}$, for a harmonic-well description of the chemisorption bond, is marked by solid dots, using a vibrational quanta $\hbar\omega_0 = 13.7 \text{ meV}$ [after L. M. Kahn and S. C. Ying, Solid State Commun. 16, 799 (1975)]. The rest are results of calculations employing a Morse-potential description, for $W_{1 \rightarrow 2}^{(M)}$, $W_{1 \rightarrow 3}^{(M)}$, $W_{218 \rightarrow 219}^{(M)}$, and $W_{218 \rightarrow 220}^{(M)}$, where $v = 220$ is the predissociation level. Note the change of scale in $W_{1 \rightarrow 3}^{(M)}$. The Debye temperature of the substrate was taken as $\Theta_D = 220 \text{ }^\circ\text{K}$, the electron number density of the substrate was $n_e = 38 \times 10^{22} \text{ cm}^{-3}$ and $x_e = 6.5 \times 10^{-4}$.

and for the rates of transitions between vibrational levels of the binding potential, induced by the couplings, we turn next to the temporal evolution of the excitations. Since for most systems of interest the allowed quanta of excitation, dictated by the characteristics of the phonon spectrum of the substrate are much smaller than the barrier for bond rupture, an incoherent multiphonon mechanism is formulated. This, however, is applicable to systems in which the spacings between vibrational levels of the potential associated with the reaction coordinate do not exceed the maximum phonon frequencies. When the above is not satisfied coupling may occur through a mode other than the bond-rupture reaction coordinate which serves as a "doorway" state (see Sec. IV).

Consider an oscillator system with $x_n(t)$ the distribution describing the population of vibronic levels n at time t . The time evolution of this distribution is governed under certain approximations by a master equation⁴¹

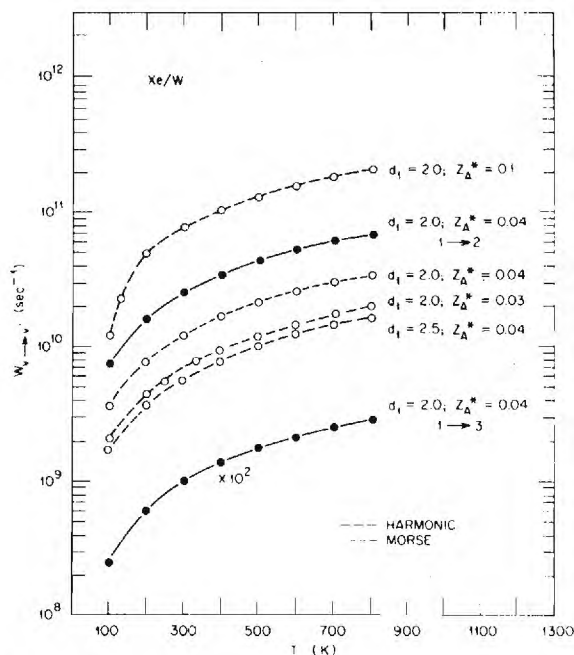


FIG. 3. Transition rates, $W_{v \rightarrow v'}$, using both harmonic (dashed) and Morse (solid line) potentials for Xe adsorbed on tungsten, vs temperature. The harmonic vibrational quanta $\hbar\omega_0$ was chosen as 3.0 meV . The sensitivity of the transition rates to variations in the equilibrium distance d_1 (in Å) and fractional charge on the adsorbed xenon are shown. The substrate parameters were taken as $\Theta_D = 220 \text{ }^\circ\text{K}$, $n_e = 38 \times 10^{22} \text{ cm}^{-3}$, and $x_e = 1.25 \times 10^{-3}$.

$$-\frac{dx_n}{dt} = \sum_{\nu=0}^{N+1} W_{\nu n} x_n - \sum_{m=0}^N W_{nm} x_m, \quad n = 0, 1, \dots, N \quad (3.1)$$

where N is the predissociation level, W_{nm} is the transition probability per unit time from m to n . In the above equation second-order terms due to recombination are neglected. The initial distribution ($t = 0$) is normalized according to

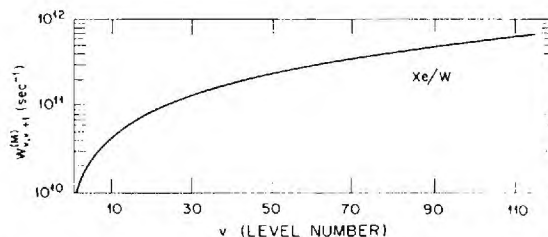


FIG. 4. Morse transition rate, $W_{v \rightarrow v+1}^{(M)}$ vs level number v , for Xe adsorption on tungsten, at $T = 100 \text{ }^\circ\text{K}$. The equilibrium distance was taken at $d_1 = 2.0 \text{ \AA}$ and fractional charge $z_A^* = 0.04e$. Note the monotonous increase in $W_{v \rightarrow v+1}^{(M)}$ as v increases. The substrate parameters are as given in the caption to Fig. 3.

$$\sum_{n=0}^N x_n(0) = 1, \quad (3.2)$$

and the $x_n(0)$'s are given by a Boltzmann distribution at temperature T ; i.e.,

$$x_n(0) = e^{-\beta\epsilon_n} \sum_{n=0}^N e^{-\beta\epsilon_n}. \quad (3.3)$$

For the calculation of the reaction rate we will be interested in the mean time for the system specified above, to pass the N th level for the first time—i.e., the mean first passage time, \bar{t} . The distribution of first passage times $P(t)$ is given by⁴¹

$$P(t) = -\frac{d}{dt} \sum_{n=0}^N x_n(t) \quad (3.4)$$

and \bar{t} is the first moment of $P(t)$; i.e.,

$$\bar{t} = \int_0^\infty tP(t)dt, \quad (3.5)$$

An expression for the mean first passage time for an initial population distribution $x_n(0) = \delta_{n,0}$ for a truncated-harmonic-oscillator system and transitions between neighboring levels only, was first given by Montroll and Shuler.⁴¹ This has been generalized by Kim⁴² for the Boltzmann initial distribution [Eq. (3.3)] for both a truncated harmonic and Morse oscillators with nearest- and next-nearest-neighbor transitions.

(i) For the truncated harmonic oscillator the result is⁴²

$$\bar{t}^{(h)} = \frac{(v+1)}{W_{v-v+1}^{(h)}(1-e^{-\theta})} \sum_{j=1}^{N+1} j^{-1}(e^{j\theta}-1)(1-e^{-j\theta}), \quad (3.6)$$

with $\theta = \hbar\omega_0/kT$, where ω_0 is the harmonic-oscillator frequency.

(ii) To obtain an expression for the mean first passage time out of a Morse-potential well $\bar{t}^{(M)}$ with transitions between nearest and next-nearest levels, we adopt the methods developed by Kim. The generalization of Kim's result [Eqs. (6.15) and (6.16) of Ref. 42] amount to taking into account

that in our case the exchange of excitation is with a solid characterized by thermal occupation numbers

$$\bar{n}_{\omega_0} = [\exp(\hbar\omega_0/kT) - 1]^{-1}.$$

Consequently contributions corresponding to transitions between the Morse-potential levels must be weighted appropriately. Starting from Eq. (6.6) of Ref. 42,

$$\bar{t}^{(M)} = \sum_{p=0}^N \frac{Q_p u_p}{D_p} - \sum_{p=0}^N Q_p \left(\frac{h_{p+1,p-1}}{D_p D_{p-1}} u_{p-1} + \frac{h_{p+2,p}}{D_p} \frac{u_{p+1}}{D_{p+1}} \right), \quad (3.7)$$

with Q_p , u_p , and D_p given by

$$Q_p = \sum_{n=0}^p e^{-\beta\epsilon_n}, \quad (3.8a)$$

$$u_p = \sum_{n=0}^p x_n(0) \quad (3.8b)$$

$$D_p = h_{p+1,p} + h_{p+2,p} + h_{p+1,p-1}, \quad (3.8c)$$

see Eqs. (4.13), (4.4), and (6.1) in Ref. 42, and the h_{mn} given explicitly by

$$h_{p+1,p} = A(\omega_0)(p+1) \times \{1 + x_e[(p+1) - B(\omega_0)(2p+1)]\} e^{-\beta\epsilon_{p+1}}, \quad (3.9a)$$

$$h_{p+2,p} = A(2\omega_0)(x_e/4)(p+1)(p+2)e^{-\beta\epsilon_{p+2}}, \quad (3.9b)$$

$$h_{p+1,p-1} = A(2\omega_0)(x_e/4)p(p+1)e^{-\beta\epsilon_{p+1}}, \quad (3.9c)$$

we obtain

$$\bar{t}^{(M)} = \bar{t}_0 + [x_e/A(\omega_0)] \bar{t}_1. \quad (3.10)$$

In Eq. (3.10)

$$\bar{t}_0 = \frac{1+a}{A(\omega_0)} \sum_{p=1}^{N+1} \frac{e^{\beta\epsilon_p}}{p} (1 - e^{-\theta})^2, \quad (3.11)$$

where $\theta = (\hbar\omega_0/kT)$, $A(\omega_0)$ is given by Eq. (2.33a), and $a = 1/(e^\theta - 1)$. \bar{t}_1 in the above equation is given by

$$\begin{aligned} \bar{t}_1 = & A(\omega_0) \bar{t}_0 [a\theta(1+2a) + Z(\omega_0)/[4(1+a)] - B(\omega_0)] + e^{\beta\epsilon_{N+1}} \frac{1}{4} Z(\omega_0) [2+a/(1+N) + 3a] \\ & - \sum_{p=1}^{N+1} e^{\beta\epsilon_p} [1+a + \frac{1}{4} Z(\omega_0)(3+4a) - 2(1+a)B(\omega_0)] - N\theta(N+1)(1+a) \\ & + (2N-a)[1+a + \frac{1}{2} Z(\omega_0)(1+2a) - 2(1+a)B(\omega_0)] + 2\theta a(1+a)(1+3a-2N) - \frac{1}{4} Z(\omega_0)(1+a), \end{aligned} \quad (3.12)$$

where

$$Z(\omega_0) \equiv \frac{A(2\omega_0)}{A(\omega_0)} = \frac{\bar{n}_{2\omega_0}}{\bar{n}_{\omega_0}} \left(\frac{q_0^2 + \lambda_{TF}^2}{4q_0^2 + \lambda_{TF}^2} \right)^2 \quad (3.13)$$

and $sq_0 = \omega_0$.

In the stochastic formulation of nonequilibrium kinetics which we have employed, the reaction rate R is given by the inverse of the mean-first-passage time \bar{t} (see also discussion in Sec. IV). Results for the rates of desorption of potassium

and xenon from a tungsten substrate are shown in Figs. 5-7. In Fig. 5 results for the two models of the binding potential (harmonic—solid line, and Morse—dashed line) using experimentally³⁷ suggested values for the desorption energy $D_e = 2640$ meV, equilibrium distance $d_1 = 2.38 \text{ \AA}$ and fractional charge $Z_A^* = 0.27e$ are compared, along with the experimentally obtained³⁴ rate, given by $R = 10^{12.8} \times \exp(-D_e/kT)$ (open circles). It is evident that the results for the Morse-potential and truncated-harmonic-oscillator models yield both an Arrhenius-like straight line in the semilogarithmic plot of R vs $1/T$. The pre-exponential factors, however, differ markedly with the Morse potential in agreement with experiment. It should

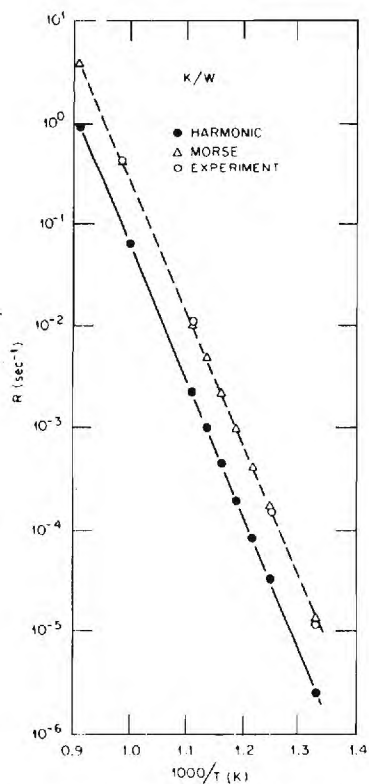


FIG. 5. Semilogarithmic plots of desorption rates vs inverse temperature for the system potassium adsorbed on tungsten. The desorption energy D_e was taken as 2.64 eV after Ref. 37, and the rest of the characteristic parameters are as given in the caption to Fig. 2. The experimental points (open circles) were taken after Ref. 37, $R(T) = 10^{12.8} \times \exp(-D_e/kT)$. Both the Morse potential (dashed) and truncated harmonic (solid) yield linear relationships in the plot of $\ln R(T)$ vs inverse temperature, parallel to one another (same activation energy for desorption) but with different intercepts (frequency factors). The results based on the Morse-potential description of the chemisorptive bond are in better agreement with the experimentally deduced results than those derived from a truncated-harmonic potential.

be noted that the differences between the two models are less pronounced than those which were exhibited in the transition rates (see Figs. 2 and 3). Similar results, with a somewhat less pronounced difference between the two models and in agreement with experiment³⁸ are shown for xenon desorption from tungsten (with the parameters given in the figure captions) in Figs. 6 and 7. In Fig. 7 the rather weak dependence of the results for the rate of desorption on the equilibrium distance parameter is exhibited.

IV. DISCUSSION AND PERSPECTIVES

We have formulated a theoretical model for the calculation of desorption rates of an adatom from a metal surface. The formulation relied on several key stages: (a) the evaluation of the coupling between the solid and the adatom induced by the

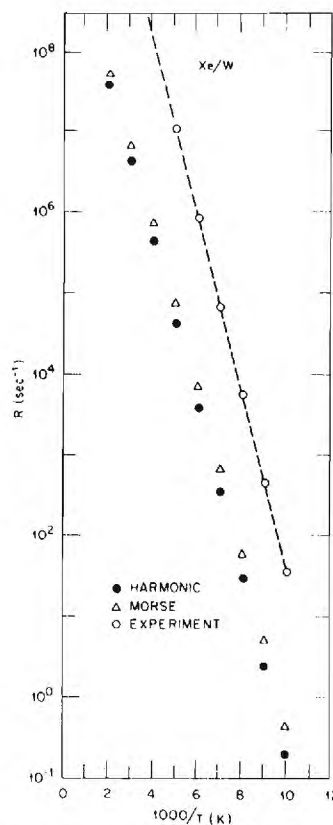


FIG. 6. Semilogarithmic plots of desorption rates $R(T)$ vs inverse temperature for the system xenon adsorbed on tungsten. The characteristic parameters are those given in the caption to Fig. 2 and the desorption energy D_e was taken as 217 meV after Ref. 38. The experimental points (open circles) were calculated from the rate expression given in the above reference $R(T) = 10^{12} \times \exp(-D_e/kT)$. Results obtained by using Morse (triangles) and truncated-harmonic potentials (dots) are shown.

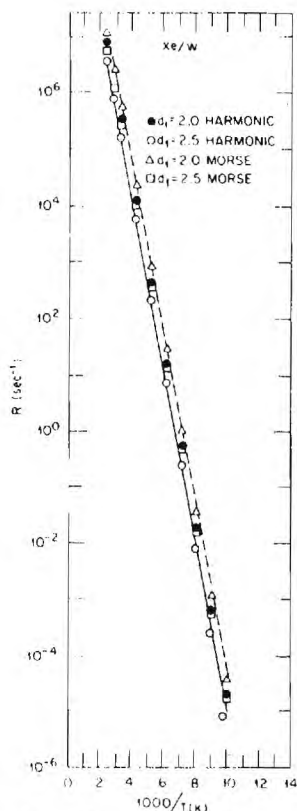


FIG. 7. Semilogarithmic plots of desorption rates $R(T)$ vs inverse temperature for Xe adsorbed on tungsten, characteristic parameters are as in Fig. 4 with $D_e = 300$ meV. Results are shown for both truncated-harmonic (solid and open dots) and Morse (triangles and squares) potentials. The apparent slight sensitivity of the rates to the equilibrium distance of the adsorbed atom from the surface is shown.

nonstationary substrate, (b) the stochastic incoherent multiphonon mechanism of excitation, and (c) the coupling to the final-state channels. From the results presented in Figs. 5–7, it is apparent that the model provides a rather adequate description of desorption for both weak (Xe/W) and strong (K/W) chemisorption systems. The principal merit of this model is that it exhibits explicitly the dependencies on various microscopic quantities characteristic to the substrate and adatom. Due to the complexity of the problem, our model relies on a number of simplifying assumptions certain of which we enumerate below: (a) the substrate was modeled as a continuum structureless solid, (b) surface phonons have been ignored, (c) the electron response to fluctuations of the ionic charge was calculated semiclassically (quantum interference effects neglected) and with specular boundary conditions imposed, (d) electronic band-structure effects were ignored which implies weak electron-ion coupling in the substrate,

(e) bilinear coupling between the nonstationary adatom and substrate was used in the numerical examples and transition rates due to these couplings were calculated using the Fermi golden rule, and (f) an immobile adsorbate was assumed. The inclusion of adsorbate migration on the surface will add an entropy correction to the rate expression. While further improvements within this model are possible, the present study allows for a first evaluation of the sensitivity of desorption kinetics to the various microscopic parameters.

The standard approaches to reaction kinetics, such as absolute rate theory² (ART) and the various statistical methods¹⁰ (e.g., RRKM) rely upon certain criteria of applicability. The main requirement of the above is that the initial and final (or transition complex) states are uncorrelated.² As discussed originally by Kramers¹² and further investigated recently,^{13,14,43} the applicability of ART is related to the strength of the fluctuating part of the coupling (friction in the nomenclature of the above studies) between the adsorbate and the adparticle. The analytical results obtained¹² in the limits of small and large coupling support the assertion that the applicability of ART is limited to an intermediate regime of the coupling strength. In this regime the coupling is strong enough as to replenish instantaneously the equilibrium Maxwellian tail of particle momenta, necessary for surmounting the reaction barrier, and thus the rate becomes independent of the coupling. Outside this regime the Arrhenius behavior of the rate constant gets modified by multiplicative factors which vary with temperature. Our calculation of \bar{t} [e.g., in Eq. (3.6)] in principle assumes the weak-coupling regime since our transition rates W_{v-v+1} are treated to lowest order in perturbation [e.g., Eq. (2.30)]. This assumption of weak coupling has internal consistency in that our low-order treatment does yield good agreement with experiment (Figs. 6 and 7). While clearly the interplay between the temperature dependence of W_{v-v+1} and the usual statistical occupations [the sum over j in Eq. (3.6)] is a complicated one and cannot rigorously reduce to an Arrhenius-like form our numerical results (displayed in Figs. 6 and 7) give a measure for the *weak* deviation from such a behavior. This conclusion cannot be inferred directly from the evaluated transition rates alone (Figs. 2–4) but requires an analysis of the rates. In this context it is important, however, to notice the dependence of the results on the model potential used (truncated-harmonic vs Morse potentials), and that the difference in rates of desorption corresponding to the two model potentials is smaller than that exhibited in the associated level transition probabilities.

The stochastic treatment of the time evolution of the vibrational excitations leading to desorption which we have used, is a convenient formulation of nonequilibrium kinetic processes. In the equilibrium theory the rate constant depends only upon transitions which couple bound vibrational levels directly to the dissociated state,⁴² $N + 1$, and similar to the basic assumption of ART there is no dependence on the details of the excitation mechanism. The first passage time \bar{t} calculated via the stochastic nonequilibrium formulation does not in general equal the reciprocal of the equilibrium rate constant.⁴² One limit in which the above equality holds is when the energy required for a transition is large compared to the available thermal energy. This condition was not obeyed in our cases. Thus, it was necessary to investigate the full stochastic behavior.

The order of coupling in our model should also be commented on. While we have used bilinear coupling [Eq. (2.26)], a generalization would in principle allow treatment of higher-order coupling terms. In this context we could argue that by a proper transformation of the coordinates $\{R_S\}$ and $\{R_M\}$ the bilinear coupling term could be removed and the frequencies of the substrate-atom system renormalized accordingly. The coupling enters now through the new frequencies in these transformed canonical coordinates. It is now, *in principle* possible to calculate desorption rates with the simple assumption of a Boltzmann occupation of these new levels, and with proper retransformation of our coordinates to define the stage of dissociation. Such a calculation is expected to yield similar results to ours (particularly in the weak coupling limit) but it is rather complex and has not as yet been carried out for the model systems discussed in this study.

A detailed investigation of reaction mechanisms requires an analysis of the reaction products. Indeed a well-established practice in gas-phase kinetic studies⁴⁴ is to perform state-selective measurements, i.e., identification of products, their center-of-mass translational energies, and excitation of internal degrees of freedom. This mode of investigation is not common practice in current studies of surface reactions. In most, if not all, studies to date the experimental information consists only of mass, and in certain cases angular, distribution of the products. In the following we remark briefly on the possibility of *final-state branching* and suggest methods for its evaluation.

Having achieved the $(N + 1)$ th level, ϕ_{N+1} , whose energy E_{N+1} lies above the dissociation energy, the system may evolve via several channels. For example the ϕ_{N+1} state may decay into the trans-

lational continuum which corresponds to desorption, it may couple to a manifold of bound vibrational states associated with an excited electronic term or to a bound vibrational manifold or translation continuum corresponding to binding or diffusion along the surface. The problem is formally similar to that encountered in the study of autoionization⁴⁵ and predissociation^{46-48,18} phenomena, and applied also to the study of radiationless transitions in molecules⁴⁹⁻⁵¹ and photodissociation⁵²⁻⁵⁶ for which a number of methods of solution have been suggested. In the following we outline results obtained through the use of one of these methods.^{45,49} Consider the case in which the excited vibrational state ϕ_{N+1} is embedded and coupled to two manifolds of states: (i) a manifold of bound vibrational states, $\{\psi_n\}$ associated with an excited electronic state of the adsorption system, (ii) a translational continuum, $\{\xi_E\}$. These two manifolds are assumed uncoupled to one another. Coupling of ϕ_{N+1} to $\{\psi_n\}$ is achieved via the nonadiabatic nuclear-kinetic-energy terms in the total Hamiltonian, and the corresponding matrix element will be taken as a constant v_1 . The matrix element coupling ϕ_{N+1} to the translational continuum $\{\xi_E\}$ is denoted by v_2 . The manifolds are normalized with $\langle \psi_n | H | \psi_j \rangle = \delta_{n,j} E_n$ and $\langle \xi_E | H | \xi_{E'} \rangle = E \delta(E - E')$. The configurational mixing of ϕ_{N+1} with the above final-state manifolds results in a stationary state Ψ_E , given by

$$\Psi_E = a(E)\phi_{N+1} + \sum_{n=-\infty}^{\infty} b_n(E)\psi_n + \int C_{E'}(E)\xi_{E'} dE', \quad (4.1)$$

where the vibrational energies of the $\{\psi_n\}$ manifold are taken⁴⁹ as $E_n = E_{N+1} - \alpha + n\epsilon$, $n = 0, \pm 1, \pm 2, \dots$ etc. and $\alpha = E_{N+1} - E_0$.

The probabilities for finding the system in the vibrational manifold $\{\psi_n\}$, $P_v(t)$, for remaining in ϕ_{N+1} , $P_d(t)$ and for being in the translational continuum, $P_f(t)$, are given by⁵²

$$P_v(t) = \sum_{n=-\infty}^{\infty} \left| \int_{-\infty}^{\infty} dE e^{-(iE/\hbar)(t-\bar{t})} a^*(E) b_n(E) \right|^2, \quad (4.2a)$$

$$P_d(t) = \left| \int_{-\infty}^{\infty} dE e^{-(iE/\hbar)(t-\bar{t})} |a(E)|^2 \right|^2, \quad (4.2b)$$

$$P_f(t) = \int_{-\infty}^{\infty} dE' \left| \int_{-\infty}^{\infty} dE e^{-(iE/\hbar)(t-\bar{t})} a^*(E) C_{E'}(E) \right|^2, \quad (4.2c)$$

where \bar{t} is the mean first passage time calculated in Sec. III, i.e., the mean time for "preparation" of the system in state ϕ_{N+1} . In addition $P_d + P_v + P_f = 1$. Using the by now standard methods^{45,51} with the appropriate scattering boundary conditions

closed form approximate solutions can be obtained in the "statistical limit,"⁵⁰ i.e., for time t , such that $\tau \equiv t - \bar{t} \ll \hbar/\epsilon$,

$$P_r(\tau) = \frac{|v_1|^2}{|v_1|^2 + \epsilon |v_2|^2} (1 - e^{-\tau/\Gamma}), \quad (4.3a)$$

$$P_d(\tau) = \exp(-\tau/\Gamma), \quad (4.3b)$$

$$P_f(\tau) = 1 - P_d(\tau) - P_r(\tau), \quad (4.3c)$$

$$\Gamma = (\hbar\epsilon/2\pi)(|v_1|^2 + \epsilon |v_2|^2)^{-1}. \quad (4.3d)$$

If the decay into the final states is fast the above expressions allow us to follow the reaction through its evolution. It is seen from Eqs. (4.3c), (4.3a), and (4.3b) that the average lifetime of the ϕ_{N+1} state is given by Γ where Γ is given by Eq. (4.3d). Thus, if a two-step process is postulated, i.e., preparation of the excited ϕ_{N+1} state followed by coupling to final states, the total rate of desorption is $R = (\bar{t} + \Gamma)^{-1}$. The probabilities given by Eqs. (4.3) could be used for the elucidation of the reaction products. The task of evaluating the matrix elements v_1 and v_2 which determine the magnitudes of the above quantities is the subject of further investigation. In particular we should note that in our results transverse motions of the adsorbates have not been considered. In a classical sense such motions would correspond to activated diffusion of the adsorbate near saddle point of the Born-Oppenheimer potential surface. Associated with these motions is an activation entropy which would modify the value of the rate constant. Indeed recent data for the desorption of CO from metals shows pre-exponential factors much larger than previously measured.⁵⁷

Finally we comment on the application of our model to adsorbed molecular species. These systems possess additional degrees of freedom certain of which are of bond-stretching character and others which describe bond-bending, wagging, etc. While the energies typical to molecular bond-stretching modes might (and often do) exceed in magnitude those of single-phonon excitation by the solid, the energies associated with the non-stretching modes are smaller. Consequently it is suggested that the latter modes through their coupling to the vibrations of the solid may be excited up to high levels via an incoherent multi-

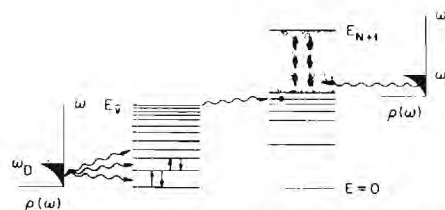


FIG. 8. Schematic picture of the doorway-state model for thermal surface desorption or dissociation reaction mechanism. A characteristic Debye phonon density of states $\rho(\omega)$ is shown on the left and right. Excitation of a low-frequency, doorway, mode of vibration (typically a nonstretching mode) occurs via an incoherent multiphonon mechanism. Upon achieving the level E_D the excitation is transferred to the high-lying levels of a stretching mode (or combination of such modes) via anharmonic coupling. Further excitation in the dense vibrational manifold corresponding to the bond-rupture coordinate can occur via direct incoherent multiphonon excitations induced by thermal coupling to the substrate. The predissociation level is denoted by E_{N+1} . Having achieved this level the reaction proceeds through coupling to possible final-state channels such as dissociation, desorption, or migration.

phonon mechanism similar to that used in the present investigation and subsequently couple via anharmonicity to the high-lying, densely spaced levels of the bond-stretching modes. Once these high-lying levels have been populated, the excitation may propagate further via direct coupling to the substrate, eventually leading to fragmentation (see Fig. 8). In other words the nonstretching modes may serve as doorway states⁵⁸ towards bond rupture via intramolecular energy redistribution.^{57,56} Quantitative studies of this model of admolecule desorption and dissociation are in progress.

ACKNOWLEDGMENTS

Useful conversations at the early stages of this study by W. Plummer, T. Madey, and R. Fox and comments on the manuscript by T. Kaplan are gratefully acknowledged. This work was supported by USDOE under Contract No. EG-77-S-05-5489 and by the Division of Materials Science under Contract No. W-7405-eng-26 with the Union Carbide Corporation.

¹M. Boudart, in *Physical Chemistry: An Advanced Treatise*, Vol. VII, edited by H. Eyring (Academic, New York, 1975) Chap. 7; K. J. Laidler, *Reaction Kinetics* (Pergamon, New York, 1963), Vols. 1 and 2.

²S. Gladsstone, K. J. Laidler, and H. Eyring, *The Theory*

of Rate Processes (McGraw-Hill, New York, 1941).

³L. S. Kassel, *The Kinetics of Homogeneous Gas Reactions* (The Chemical Catalog Co., New York, 1932).

⁴H. S. Johnston, *Gas Phase Reaction Rate Theory* (Ronald, New York, 1966).

- ⁵D. O. Hayward and B. M. Trapnell, *Chemisorption* (Butterworths, London, 1964).
- ⁶R. Gomer, *Adv. Sol. Stat. Phys.* **30**, 94 (1975).
- ⁷C. G. Goymour and D. A. King, *J. Chem. Soc. Faraday Trans. 1*, **68**, 280 (1972).
- ⁸A. K. Mazumdar and H. W. Wassmuth, *Surf. Sci.* **30**, 617 (1972).
- ⁹M. J. Dresser, T. E. Madey, and J. T. Yates, Jr., *Surf. Sci.* **42**, 533 (1974).
- ¹⁰P. J. Robinson and K. A. Holbrook, *Unimolecular Reactions* (Wiley-Interscience, London, 1972); W. Frost, *Theory of Unimolecular Reactions* (Academic, New York, 1973).
- ¹¹D. L. Bunker, *Theory of Elementary Gas Reaction Rates* (Pergamon, New York, 1966); W. L. Hase, in *Dynamics of Molecular Collisions*, Part B, edited by W. H. Miller (Plenum, New York, 1976).
- ¹²I. A. Kramers, *Phys. Fenn.* **7**, 284 (1940).
- ¹³(a) H. Suhl, J. H. Smith, and P. Kumar, *Phys. Rev. Lett.* **25**, 1442 (1970); (b) E. G. d'Agliano, W. L. Schaich, P. Kumar, and H. Suhl, in *Collective Properties of Physical Systems*, 24th Nobel Symposium 1973 (Academic, New York, 1974), p. 200; (c) E. G. d'Agliano, P. Kumar, W. Schaich, and H. Suhl, *Phys. Rev. B* **11**, 2122 (1973).
- ¹⁴P. B. Visscher, *Phys. Rev. B* **13**, 3272 (1976); **14**, 347 (1976).
- ¹⁵G. Iche and P. Nozières, *J. Phys.* **37**, 1313 (1976).
- ¹⁶N. B. Slater, *Theory of Unimolecular Reactions* (Methuen, London, 1959).
- ¹⁷N. Rosen, *J. Chem. Phys.* **1**, 319 (1933).
- ¹⁸O. K. Rice, *J. Chem. Phys.* **55**, 439 (1971); **1**, 625 (1933).
- ¹⁹P. J. Pagni and J. C. Keck, *J. Chem. Phys.* **58**, 1162 (1973); R. M. Logan and J. C. Keck, *ibid.* **49**, 860 (1968); P. J. Pagni, *ibid.* **58**, 2940 (1973).
- ²⁰J. E. Lennard-Jones and C. Strachan, *Proc. R. Soc. (London) Ser. A* **150**, 442 (1935); J. E. Lennard-Jones and A. Devonshire, *Proc. R. Soc. (London) Ser. A* **156**, 6, 29 (1936).
- ²¹B. Bendow and S. C. Ying, *Phys. Rev. B* **7**, 622 (1973); **7**, 637 (1973).
- ²²B. J. Garrison, D. J. Diestler, and S. A. Adelman, *J. Chem. Phys.* **67**, 4317 (1977); B. J. Garrison and S. A. Adelman, *ibid.* **67**, 2379 (1977).
- ²³T. N. Rhodin and D. L. Adams, in *Treatise on Solid State Chemistry*, edited by N. B. Hannay (Plenum, New York, 1976), Vol. 6A1.
- ²⁴H. D. Hagstrum and E. G. McRae, Ref. 23.
- ²⁵R. J. Madix, in *Physical Chemistry of Fast Reactions*, edited by D. O. Hayward (Plenum, New York, 1977).
- ²⁶For recent reviews see (a) D. Menzel, in *Topics in Applied Physics*, edited by R. Gomer (Springer, Berlin, 1975), Vol. 4, p. 101; (b) T. E. Madey and J. T. Yates, *Surf. Sci.* **63**, 203 (1977); (c) L. A. Peterman, in *Progress in Surface Science*, edited by S. G. Davison (Pergamon, New York, 1972), Vol. 3; (d) D. A. King, *Surf. Sci.* **47**, 384 (1975); (e) D. Menzel, in *The Physical Basis for Heterogeneous Catalysis*, edited by E. Dragulis and R. I. Jaffee (Plenum, New York, 1975), p. 437.
- ²⁷M. Born and K. Huang, *Dynamical Theory of Crystal Lattices* (Oxford University, London, 1954).
- ²⁸H. C. Longuet-Higgins, *Proc. Phys. Soc. (London)* **60**, 270 (1948).
- ²⁹S. Epstein, *J. Chem. Phys.* **44**, 836 (1966).
- ³⁰S. Ichimaru, *Basic Principles of Plasma Physics* (Benjamin, Reading, Mass., 1973).
- ³¹A. L. Fetter and J. D. Walecka, *Quantum Theory of Many-Particle Systems* (McGraw-Hill, New York, 1971), pp. 390-399; V. Peuckert, *Z. Phys.* **241**, 191 (1971); J. Harris and A. Griffin, *Phys. Rev. B* **11**, 3669 (1975).
- ³²L. I. Schiff, *Quantum Mechanics* (McGraw-Hill, New York, 1955).
- ³³P. M. Morse, *Phys. Rev.* **34**, 57 (1929).
- ³⁴G. Herzberg, *Spectra of Diatomic Molecules* (Van Nostrand, New York, 1950).
- ³⁵H. S. Heaps and G. Herzberg, *Z. Phys.* **133**, 48 (1952).
- ³⁶R. Herman and K. E. Shuler, *J. Chem. Phys.* **21**, 373 (1953); **22**, 954 (1954).
- ³⁷L. Schmidt and R. Gomer, *J. Chem. Phys.* **42**, 3573 (1965).
- ³⁸G. Erlich, in *Advances in Catalysis* (Academic, New York, 1963), Vol. 14, p. 255.
- ³⁹W. J. M. Rootsart, L. L. van Reigen, and W. M. H. Sachtler, *J. Catal.* **1**, 416 (1962).
- ⁴⁰T. Engel and R. Gomer, *J. Chem. Phys.* **52**, 5572 (1970).
- ⁴¹E. W. Montroll and K. E. Shuler, *Adv. Chem. Phys.* **1**, 361 (1958).
- ⁴²S. K. Kim, *J. Chem. Phys.* **28**, 1057 (1958).
- ⁴³J. L. Skinner and P. G. Wolyness, *J. Chem. Phys.* **69**, 2143 (1978).
- ⁴⁴D. R. Herschbach, in *Advances in Chemical Physics*, edited by J. Ross (Wiley, New York, 1966), Vol. 10.
- ⁴⁵U. Fano, *Phys. Rev.* **124**, 1866 (1961).
- ⁴⁶O. K. Rice, *Phys. Rev.* **35**, 1551 (1930).
- ⁴⁷F. Mies and M. A. Krauss, *J. Chem. Phys.* **45**, 4455 (1966); F. Mies, *ibid.* **51**, 798 (1969).
- ⁴⁸R. W. Numrich and K. G. Kay, *J. Chem. Phys.* **70**, 4343 (1979), and references cited therein.
- ⁴⁹M. Bixon and J. Jortner, *J. Chem. Phys.* **48**, 715 (1968).
- ⁵⁰M. Bixon and J. Jortner, *J. Chem. Phys.* **50**, 4061 (1969); **48**, 715 (1968).
- ⁵¹J. Jortner and S. Mukamel, in *The World of Quantum Chemistry*, edited by R. Daudel and B. Pullman (Reidel, Amsterdam, 1973).
- ⁵²S. A. Rice, I. McLaughlin, and J. Jortner, *J. Chem. Phys.* **49**, 5756 (1968).
- ⁵³K. G. Kay and S. A. Rice, *J. Chem. Phys.* **57**, 3041 (1972).
- ⁵⁴E. J. Heller and S. A. Rice, *J. Chem. Phys.* **61**, 936 (1974).
- ⁵⁵D. F. Heller, M. L. Elert, and W. M. Gelbart, *J. Chem. Phys.* **69**, 4061 (1978).
- ⁵⁶S. Mukamel and J. Jortner, *J. Chem. Phys.* **65**, 5204 (1976).
- ⁵⁷R. J. Madix, *Surface Reaction-1979*, edited by U. Landman (AIP, New York, to be published).
- ⁵⁸A doorway-state mechanism has been suggested in studies of multiphoton molecular fragmentation; for a recent review, see N. Blombergen and E. Yablono-vitch, *Phys. Today* **31**, 23 (1978).

Conditions for a Rate-Maximizing Temperature in Heterogeneous Catalysis¹

Conditions are derived for Langmuir-Hinshelwood and Eley-Rideal heterogeneous catalytic reactions to have a reaction rate maximum as a function of temperature. Experimental results contradict previously derived conditions which assumed that the surface diffusion was governed by a single transition rate. More than one transition rate will enter the analysis of surface diffusion if the surface is heterogeneous or, as observed in field ion microscope experiments, the reactant passes through several nonequivalent configurations while migrating. An analysis of the rate of reaction when more than one transition rate is involved leads to a condition which could facilitate the interpretation of rate maximum reaction mechanisms.

A number of heterogeneous catalytic reactions exhibit a reversible maximum rate of reaction as a function of temperature (1-4). For example, Moffat and Clark (4) found a rate-temperature maximum in their study of the disproportionation of olefins (propylene) on cobalt-molybdate-alumina (Co-Mo-Al₂O₃) catalyst. At temperatures below T_{max} they found the reaction rate, r , to obey a Langmuir-Hinshelwood equation for bimolecular reactions

$$r = k[Kp/(1 + Kp)]^2, \quad (1)$$

where k is the transition rate of diffusion and reaction of the reactants on the surface, K is the ratio of adsorption to desorption rates, and p is the pressure of the gaseous species. The factor in square brackets in the above equation is the equilibrium fractional surface coverage.

Usually, Arrhenius activated forms are assumed for both k and K (4-6), i.e.,

$$k = A \exp(-E/RT)$$

and

$$K = \exp(\Delta S/R) \exp(-\Delta H/RT), \quad (2)$$

where E is the activation energy for diffusion, ΔS is the differential entropy of adsorption, ΔH is the heat of adsorption, and

¹ Work supported by U.S. DOE Contract EG-77-S-005-5489.

A is a preexponential (frequency) factor. Substituting Eq. (2) into the equation for r and setting the derivative of the resulting expression with respect to temperature equal to zero yields the condition for a rate-temperature maximum. When the adsorption step of the reaction is exothermic ΔH is always negative, and the rate maximum condition is (4-6)

$$|\Delta H| > \frac{E(\beta + 1)}{2}, \quad (3)$$

where $\beta = p \exp(\Delta S/R)$ which is usually much smaller than unity. Note, that from Eq. (1), a plot of $1/r^{1/2}$ versus $1/p$ would yield values for k and K from which the activation energy E is obtained as

$$E = - \frac{\partial \ln k}{\partial (1/RT)}, \quad (4)$$

The heat of adsorption, ΔH , is obtained from the adsorption equilibrium constant K via

$$-\Delta H = \frac{\partial \ln K}{\partial (1/RT)}, \quad (5)$$

Moffat and Clark (4) found the values $E = 8.2$ kcal/mole and $|\Delta H| = 2.8$ kcal/mole in a system which exhibited a rate-temperature maximum. However, these values violate the condition for a rate maximum as given in Eq. (3). To reconcile this problem Aldag and Clark (5) invoked het-

erogeneity of the surface toward adsorption and desorption. A critique of their interpretation is presented in Appendix A.

We proceed to propose mechanisms where the Langmuir-Hinshelwood form of Eq. (1) is preserved, but the rate-temperature maximum condition (Eq. (3)) is modified, leading to conclusions consistent with the experimental data. Common to the mechanism which we propose is the property that the reactant transport (diffusion) on the surface is characterized by more than one rate constant. Two possible mechanisms are considered: (i) multistate diffusion, and (ii) diffusion on a heterogeneous substrate.

(i) *Multistate diffusion.* When the propagation of the diffusing species involves transitions between more than one state the mechanism is termed multistate diffusion. Such a mechanism occurs when the reactants perform transitions between several spatial configurations in the course of propagation. A number of systems exhibiting such a behavior have been observed using field ion microscopy (FIM) (7). For example, the motion of tungsten dimers on a W(211) surface (8, 9) involves transitions between alternating staggered and straight configurations which are characterized by different rate constants. It is plausible that the motion on a surface of a species as complex as an olefin would involve a number of transitions between distinct configurations of the molecule. Out of these transitions those with the highest activation energies would be the rate-limiting steps of the migration. Another multistate mechanism occurs when the adsorbed reactants may exist in two (or more) states which are distinguished as mobile and immobile states (Lennard-Jones mechanism (10)). When in the immobile state the particle merely vibrates in the potential well which binds it to the site and also performs transitions to a higher energy state through which it may propagate. (At normal temperatures propagation through the mobile state is the dominant mode of activated intersite transitions.

At low temperatures one may include in addition spatial transitions through the lower-energy states which correspond to nonactivated, tunneling transport).

For systems in which the motion of the diffusing particles involves more than a single transition rate, the diffusion constant and hence the rate k (see Eq. (1)) is modified from the customary single-exponential, Arrhenius activated form (see Eq. (2)). For example, for the motion of a species which is characterized by two distinct states (configurational or energetic in origin) participating in the migration mechanism (with corresponding transition rates A and B), a random-walk model allowing for the presence of internal states yields (8, 9, 11-13) (see also Appendix B) for k the expression

$$k = \frac{AB}{A + B} \quad (6)$$

where the rates A and B may both be written in activated Arrhenius forms. We choose

$$\begin{aligned} A &= \nu_A \exp(-E_A/RT) \\ B &= \nu_B \exp(-E_B/RT) \end{aligned} \quad (7)$$

where ν_A, ν_B are frequency factors and E_A, E_B are the activation energies for the two states, respectively. If a straight line results from an experimental plot of $\log k$ versus $(RT)^{-1}$, this does not necessarily imply that $k = \nu \exp(-E/RT)$ and that k cannot be of the form given in Eqs. (6) and (7). In practice, a plot of $\log k$ given by Eqs. (6) and (7) versus $(RT)^{-1}$ for typical experimental temperature ranges will yield a straight line of slope $-E_A$ if

(i) $E_A \approx E_B$;

$$\text{or (ii) } E_A \gg E_B + RT \ln \frac{\nu_A}{\nu_B}. \quad (8)$$

Such cases have been encountered in the analysis of multistate cluster motion on surfaces observed via FIM (9), where more than one rate-limiting step is involved in the transport, but still the semilogarithmic plot

of mean squared diffusion distance versus inverse temperature yields an apparent straight line. It is only recently (11, 12) that an analysis has been given to find all the individual activation energies and frequency factors which comprise the diffusion constant, from field ion microscope data.

Using the transition rate as given in Eqs. (6) and (7) the following condition is found for a rate maximum of r to occur,

$$\frac{1 + p \exp[\Delta S/R - |\Delta H|/RT_m]}{2|\Delta H|} = \frac{A + B}{E_B A + E_A B}, \quad (9)$$

where T_m is the maximizing temperature. Let us denote the RHS by Γ . A linear analysis shows that if p is decreased by an amount δp then T_m will be decreased by an amount δT_m , where

$$\delta T_m = \delta p \exp[\Delta S/R + |\Delta H|/RT_m] RT_m^2 / \Delta H \times \{2|\Delta H|\Gamma - 1 + 2AB [\Gamma(E_A - E_B)/(A + B)]^2\}^{-1}. \quad (10)$$

This is in accord with the experimental result that a decrease in pressure lowers the maximizing temperature (4). Neglecting $p \exp(\Delta S/R)$ compared to unity (4) we find for the existence of a rate maximum the inequality

$$\nu_A(2|\Delta H| - E_B) > \nu_B(E_A - 2|\Delta H|), \quad (11)$$

where we have assumed, without loss of generality, that $E_A > E_B$. In contrast to Eq. (3) this inequality could be satisfied by the measurements of Moffat and Clark (4) who found $E_A = 8.2$ kcal/mole, $|\Delta H| = 2.8$ kcal/mole, if $0 < E_B < 5.6 - 2.6(\nu_B/\nu_A)$ kcal/mole. In order for the diffusion to apparently be well described by a single transition rate, the second inequality in Eq. (8) must also be obeyed.

(ii) *Diffusion on a heterogeneous substrate.* Another possible mechanism for introducing more than one transition rate in the description of reactant diffusion is if the surface is heterogeneous. Consider a sur-

face consisting of N_A and N_B sites, characterized by release rates A and B , respectively, of the diffusing species (with A and B given as in Eq. (7)). For a random placement of the two types of sites, in an approximation which neglects correlations between sites, the diffusion rate for the system is given by (14)

$$k = k_0 \left\{ 1 - c \left[\frac{\nu_B}{\nu_A} e^{(E_A - E_B)/RT} - 1 \right] \right\}, \quad (12)$$

where $k_0 = \nu_B \exp\left(-\frac{E_B}{RT}\right)$ and $c = \frac{N_A}{N_A + N_B}$. Using the above expression the condition for a rate-temperature maximum is

$$(1 - c)\nu_A(2|\Delta H| - E_B) > c\nu_B(E_A - 2|\Delta H|) \quad (13)$$

for $E_A > E_B$. For the system studied by Moffat and Clark (4) the above inequality will be consistent with the data if $0 < E_B <$

$$\left[5.6 - 2.6 \frac{c\nu_B}{(1 - c)\nu_A} \right] \text{ kcal/mole.}$$

A similar analysis of an Eley-Rideal mechanism, with rate r given by

$$r = \frac{kKp^2}{1 + Kp}, \quad (14)$$

when the diffusion rate k is governed by two transition rates (Eq. (6)), yields the following expression for the maximizing temperature, T_m ,

$$T_m = \frac{E_A - E_B}{R} \times \left\{ \ln \frac{\nu_A}{\nu_B} \left(\frac{|\Delta H| - E_B}{E_A - |\Delta H|} \right) \right\}^{-1}. \quad (15)$$

In the above $p \exp(\Delta S/R) \ll 1$, and $\Delta H < 0$ have been used. Assuming $E_A > E_B$ yields the following inequality

$$\nu_A(|\Delta H| - E_B) > \nu_B(E_A - |\Delta H|) \quad (16)$$

for the existence of a rate-maximizing temperature. When k is governed by only one rate-limiting step, i.e., $k = \nu \exp(-E/RT)$ then the analogous inequality is (4)

$$E(\beta + 1) < |\Delta H|. \quad (17)$$

As is the case with a Langmuir-Hinshelwood reaction mechanism when Eq. (17) is not satisfied by the experimental data but a rate maximum occurs nevertheless, this may suggest that the surface diffusion of the reactants involves more than one transition rate, perhaps due to multistates (spatial or energetic) of the reactants, or surface heterogeneities. If more than two transition rates are involved inequalities more complicated than Eq. (11) can be derived.

Our objective in this note has been to incorporate possible diffusion mechanisms in the analysis of reactions obeying Langmuir-Hinshelwood or Eley-Rideal mechanisms which exhibit rate-temperature maxima. We have derived inequalities which constitute conditions for the existence of such rate maxima for heterogeneous systems and for multistate diffusion mechanisms. Subject to certain constraints the above derived inequalities could be satisfied by the experimental data. It is suggested that additional controlled experiments such as measurements of the rate-maximizing temperature as a function of pressure or field ion microscope multistate diffusion data would allow the estimation of the additional parameters [ν_B and E_B , see Eqs. (11) and (16)] introduced by our model.

APPENDIX A

In a recent study, Aldag and Clark (5) reconsidered the analysis of the experiments (4) of olefin disproportionation which exhibited a rate-temperature maximum for a Langmuir-Hinshelwood reaction. Their investigation was motivated by the fact that the values for ΔH and E determined from the pressure and temperature dependence of the data were inconsistent with the inequality given in Eq. (3). They consider that the Langmuir-Hinshelwood rate for a nonuniform surface can be represented by

$$r = kp^2 \sum_{i=1}^N \frac{K_i^2}{(1 + K_i p)^2} \quad (A1)$$

or an appropriate continuum limit. In the above the summation incorporates heterogeneity of the surface toward adsorption-desorption while the diffusion represented by k is regarded as taking place on a uniform surface. However, since the data (4) fit Eq. (1), i.e., the $N = 1$ case, they attempted to rewrite Eq. (A1) in a form with $N = 1$. They denote the sum in Eq. (A1) by $F(p)$, and write what is equivalent to the following identities:

$$\begin{aligned} r &= kp^2 F \equiv kp^2 F^3 / F^2 \\ &\equiv \frac{kp^2 F^3}{(F - H)^2} \frac{(F - H)^2}{F^2} \\ &\equiv \left[\frac{kp^2 F^3}{(F - H)^2} \right] \\ &\quad \times \left[\frac{F/H - 1}{1 + (F/H - 1)} \right]^2. \quad (A2) \end{aligned}$$

The first bracket in Eq. (A2) is identified with k in Eq. (1) and pK in Eq. (1) is identified with $[F(p)/H(p)] - 1$. $H(p)$ is chosen to be equal to $\sum_{i=1}^N K_i^2 / (1 + K_i p)^3$. After these identifications, the resemblance of Eq. (A2) to Eq. (1) is only symbolic. The essential point is that Eq. (A1) is not equivalent to Eq. (1) and $H(p)$ which enters Eq. (A2) is completely arbitrary, thus making the choice of K arbitrary, as well as the apparent heat of adsorption, ΔH , which is calculated from K .

APPENDIX B

In this appendix we outline the derivation of the expression for the diffusion constant for a system which exhibits a multistate diffusion mechanism. The derivation proceeds via the continuous-time-random-walk with internal states model which we have developed recently. Since detailed discussions of the technique can be found elsewhere (11-14) we limit ourselves to a presentation of the main underlying ideas.

Consider a crystalline system where the propagation of the diffusing entity (single particle, multiparticle cluster) is characterized by transitions between internal states (energetic, e.g., mobile and immobile states, configurational). The spatial motion of the centroid of the diffusant can be mapped onto a lattice with a number of states in each unit cell. Such a mapping is shown in Fig. 1 where the case of a diffusant with two configurational internal states is considered. Transitions in the system are governed by a waiting-time probability density function $\Psi_{ij}(\mathbf{l}, \mathbf{l}'; \tau)$, for transitions $(\mathbf{l}', j) \rightarrow (\mathbf{l}, i)$, where the couple (\mathbf{l}, i) represents position \mathbf{l} in internal state i . For the above function we choose the form

$$\Psi_{ij}(\mathbf{l}, \mathbf{l}'; \tau) \equiv p_{ij}(\mathbf{l}' - \mathbf{l})\psi_j(\tau). \quad (\text{B1})$$

The factor $p_{ij}(\mathbf{l}' - \mathbf{l})$, structural in origin, is the probability that the transition is from (\mathbf{l}', j) to (\mathbf{l}, i) and $\psi_j(\tau)d\tau$ is the probability that a transition out of state j occurs in the time interval $(\tau, \tau + d\tau)$. The function $\psi_j(\tau)$ reflects the underlying potential surface, and in the following we would take it to be of the form

$$\psi_j(\tau) = \lambda_j e^{-\lambda_j \tau}, \quad (\text{B2a})$$

$$\lambda_j = \nu_j e^{-E_j/RT}, \quad (\text{B2b})$$

where λ_j is the total rate of leaving state j and ν_j, E_j are the frequency factor and activation energy in the Arrhenius activated form for that rate.

The diffusion coefficient, D , is related to the variance, $\sigma^2(t)$ [$\sigma^2(t) = \langle l^2(t) \rangle$, for an unbiased motion], in the position of the centroid, in the long-time (diffusion) limit via

$$D = \lim_{t \rightarrow \infty} \frac{\sigma^2(t)}{2 \epsilon t}, \quad (\text{B3})$$

where ϵ is the dimensionality of the random-walk lattice. Thus to calculate $\sigma^2(t)$ we need to derive an expression for the second moment of the probability distribution, $P_{ij}(\mathbf{l}, \tau)$. The probability P of being at (\mathbf{l}, i) at time t (starting from the origin in internal state j at $t = 0$) is related to the probability propagator R of reaching (\mathbf{l}, i) exactly at time t by

$$P_{ij}(\mathbf{l}, t) = \int_0^t R_{ij}(\mathbf{l}, t - \tau) \times \left[1 - \int_0^\tau \psi_j(\tau') d\tau' \right] d\tau, \quad (\text{B4})$$

where the factor in square brackets takes into account events in which the centroid arrived at (\mathbf{l}, i) at an earlier time $t - \tau$ and no further transition has occurred by time t . The variance, $\sigma^2(t)$, is related to P as follows (12):

$$\langle l^2(t) \rangle = - \lim_{k \rightarrow 0} \left[\frac{\partial^2}{\partial k^2} \sum_{ij} \sum_{\mathbf{l}} e^{i\mathbf{k} \cdot \mathbf{l}} P_{ij}(\mathbf{l}, t) g_j \right], \quad (\text{B5})$$

where g_j is the initial occupation probability of state j .

For a semi-Markovian (continuous time)

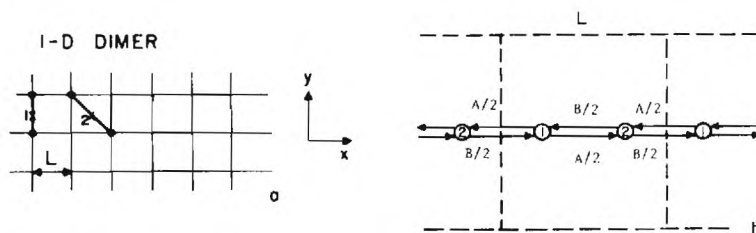


FIG. 1. One-dimensional two-state migration of a dimer. (a) The two nonequivalent states of the dimer which participate in the migration mechanism on the lattice are denoted by 1 (straight) and 2 (staggered). The lattice spacing is denoted by L and the dimer centroid is marked by x . (b) A mapping of the two-state mechanism shown in (a) onto a random-walk lattice with two states in the unit cell. The total transition rates out of states 1 and 2 are denoted by A and B , respectively. The arrows show the direction of the transitions between the states.

random walk the probability propagator R is related to $\underline{\Psi}_j(\mathbf{l}, \mathbf{l}'; \tau)$, the fundamental function characterizing the motion, via (12, 14)

$$R_{ij}(\mathbf{l}, t) = \sum_s \sum_{\mathbf{l}'} p_{is}(\mathbf{l} - \mathbf{l}') \int_0^t \psi_s(\tau) R_{sj}(\mathbf{l}', t - \tau) d\tau = \delta_{i,0} \delta_j \delta(t). \quad (\text{B6})$$

Since the above is in convolution form in both the spatial and temporal variables, Fourier ($\mathbf{l} \rightarrow \mathbf{k}$) and Laplace ($t \rightarrow u$) transformations, respectively, allow us to solve Eq. (B6) for R . Expressing all quantities as matrices of dimensions $N \times N$, where N is the number of internal states we obtain (12, 14)

$$\underline{\mathbf{R}}(\mathbf{k}, u) = [\underline{\mathbf{1}} - \underline{\mathbf{p}}(\mathbf{k}) \underline{\Psi}(u)]^{-1}. \quad (\text{B7})$$

Substitution of Eq. (B7) in Eq. (B4) for P and subsequent use of Eq. (B5) allow the calculation of the diffusion constant by taking the long-time limit of the resulting expression. We emphasize that the quantities specifying the transition rates between the internal states (frequency factors ν_j and activation energies E_j) determine $\underline{\Psi}$ and thus the diffusion constant D (denoted by k in the main text, see Eqs. (1), (2), and (6)).

For the special case of propagation via a two-internal-state mechanism in one dimension specific to the motion of a dimer (see Fig. 1) (other cases of higher dimensionality and increased complexity have been discussed by us elsewhere (11-14)) the matrix $\underline{\Psi}$ is given by (for nearest-neighbor transitions)

$$\underline{\Psi}(\mathbf{l}, t) = \begin{pmatrix} 0 & \frac{1}{2} B e^{-\mu(\delta_{l,0} + \delta_{l,L})} \\ \frac{1}{2} A e^{-\mu(\delta_{l,0} + \delta_{l,-L})} & 0 \end{pmatrix}, \quad (\text{B8})$$

where L is the lattice spacing. Substituting Eq. (B8) in (B7) and following the subsequent steps yield

$$\sigma^2(t) \equiv \langle l^2(t) \rangle = \frac{AB}{A+B} (L^2 t/2). \quad (\text{B9})$$

A similar analysis has been performed for other two-state diffusion mechanisms, such

as mobile and immobile states (12-14). In all these cases the expressions for $\sigma^2(t)$ are in terms of the transition rates between states of the diffusant, and the transition rate of diffusion, k , in the kinetic equation (Eq. 1) cannot be expressed as a simple single-exponential Arrhenius form.

Turning to the case of diffusion on a heterogeneous surface, i.e., a surface which contains two types of sites, with different rates of release out of these sites, two alternative methods of calculation have been developed (14). The first is a defect-renormalization technique, in which the probability propagators are renormalized to include the effect of the nonhomogeneity of the surface. For lack of space we will not describe it further, and refer the reader to a recent publication (14). A second method is a generalization of the internal-state technique described above and consists of constructing superlattices with equivalent unit cells each containing an identical distribution of sites A and B. Thus, for example, the mapping in Fig. 1 can be considered as representing diffusion on a lattice with alternating sites A and B. For sites B a distance n lattice spacings apart, a unit cell with $n-1$ sites of type A, and one of type B is used. The resulting expression for the diffusion constant is that given in Eq. (12). It is of interest to note that this expression is equivalent to that which is derived for a random distribution of the defects (sites B) in the average- t -matrix approximation, in which correlations between sites are neglected.

REFERENCES

1. Holm, V. C. F., and Blue, R. W., *Ind. Eng. Chem.* **44**, 107 (1952).
2. Ashmead, D. R., Eley, D. D., and Rudham, R., *J. Catal.* **3**, 280 (1964).
3. Harris, J. R., and Rossington, D. R., *J. Amer. Ceram. Soc.* **51**, 511 (1968).
4. Moffat, A. J., and Clark, A., *J. Catal.* **17**, 264 (1970).
5. Aldag, A. W., and Clark, A., *J. Catal.* **54**, 98 (1978).
6. Maatman, R. W., Leenstra, D. L., Leenstra, A.,

- Blankespoor, R. L., and Rubingh, D. N., *J. Catal.* **7**, 1 (1967).
7. Ehrlich, G., *Crit. Rev. Solid State Sci.* **4**, 205 (1974); Bassett, D. W., in "Surface and Defect Properties of Solids" (R. W. Roberts and J. M. Thomas, Eds.), Vol. 2, p. 34. Chem. Soc., London, 1971; Graham, W. R., and Ehrlich, G., *Thin Solid Films* **25**, 85 (1975); Rhead, G. E., *Surface Sci.* **47**, 207 (1975).
8. Reed, D. A., and Ehrlich, G., *J. Chem. Phys.* **64**, 4616 (1976).
9. Stolt, K., Graham, W. R., and Ehrlich, G., *J. Chem. Phys.* **65**, 3206 (1976).
10. Lennard-Jones, J. E., *Proc. Phys. Soc. (London)* **49**, 140 (1937).
11. Landman, U., Montroll, E. W., and Shlesinger, M. F., *Phys. Rev. Lett.* **38**, 285 (1977).
12. Landman, U., and Shlesinger, M. F., *Phys. Rev. B* **16**, 3389 (1977).
13. Landman, U., and Shlesinger, M. F., *Solid State Commun.* **27**, 939 (1978).
14. Landman, U., and Shlesinger, M. F., *Phys. Rev. B* **15**, 6207, 6220 (1979).

MICHAEL F. SHLESINGER
UZI LANDMAN

*School of Physics
Georgia Institute of Technology
Atlanta, Georgia 30332*

Received March 5, 1979; revised September 4, 1979

Surface Science 95 (1980) 67-88
© North-Holland Publishing Company

PROSPECTS FOR STUDYING CHEMISORPTION KINETICS USING CURRENT FLUCTUATIONS †

Gopa Sarkar DE * and Harry SUHL

Physics Department, University of California, San Diego, La Jolla, California 92093, USA

Received 14 September 1979; accepted for publication 29 January 1980

The rates of surface catalytic reactions are, in principle, reflected in the frequency spectrum of adsorbate density fluctuations. These fluctuations change the incremental current (i.e., increment over the average current corresponding to the average surface coverage) noise due to electron transfer between the adsorbate and the substrate and to the scattering of the substrate electrons from the adsorbates. In an adiabatic limit, the incremental current noise is proportional to the conductivity modulation induced by the adsorbate density fluctuations and to the square of the applied voltage. Thus, the noise in the substrate current provides information about the surface reaction kinetics. This reaction may proceed either in equilibrium or in non-equilibrium. The adsorbate density spectrum has been calculated both in and out of equilibrium for two specific reactions. No major difference is found between the in and out of equilibrium cases. When these involve two-step processes, the adsorbate density correlation function is the sum of two decaying exponentials and the spectrum is the sum of two Lorentzians.

1. Introduction

Fluctuation spectroscopy provides a unique method for measuring the kinetic parameters of a chemical reaction. This method has been used by Feher and Weissman [1] to investigate the dissociation reaction of beryllium sulphate in an electrolytic solution. In this study we explore prospects for similar measurements in heterogeneous surface catalytic reactions using conductivity modulations of the substrate.

The adsorption-desorption process modulates the substrate current in two different ways; first, the adsorbates act as additional scattering centers for substrate electrons thereby decreasing the conductivity; second, there is some charge shared between the adsorbate and the substrate in forming the chemisorptive bond, thereby increasing or decreasing the current depending on whether the charge flows to or

† Work supported by NSF DMR-77-24957.

* The writing of this work was supported by US DOE contract No. EG-77-S-05-5989.

* Present address: School of Physics, Georgia Institute of Technology, Atlanta, Georgia 30332, USA.

from the substrate. Thus, either in equilibrium or in the steady state of a substrate driven externally by an electric field, its conductivity is changed by the surface adsorbed layer. References of experimental evidence and theoretical investigations of this effect can be found in the review paper by Wissman [2]. In fact, modulations in the conductivity of a thin film about its average value as the density of the adsorbed layer fluctuates about the mean coverage has been used by Shanabarger [3] to measure reaction rates of hydrogen chemisorption on nickel.

In equilibrium, the fluctuations in the current constitute the well known Johnson noise. However, when an electric field is applied, there is an additional field dependent term in the fluctuations which varies quadratically with the electric field in the lowest order; the magnitude of this term is shown to be large enough to be detectable above the Johnson noise with current technology. We calculate this lowest order field dependent term in the adiabatic limit viz, in the limit when the characteristic reaction times are long compared to the interval between successive electron-impurity collisions in the substrate. In this regime, the incremental current (i.e., increment over the average current corresponding to the average surface coverage) fluctuations are entirely due to conductivity modulations for times of the order of the surface reaction time and the conductivity modulation itself arises from the fluctuations in the adsorbate density. We calculate the adsorbate density fluctuations both under equilibrium and non-equilibrium conditions for specific reactions.

Care needs to be exercised in evaluating the terms in the current noise varying quadratically with the electric field. In order to maximize the fluctuations it may be necessary to use fine point contacts around which the electric field is also intense. In such strong fields non-linear effects in the current-field response lead to a term in the current noise varying quadratically with the field. This needs to be compared with noise terms of the same order resulting from the surface reaction. In assessing this non-linear effect inherent in the pure sample we found it has spurious divergences at low frequencies if only elastic electron-impurity collisions are taken into account. Inclusion of inelastic scattering effects lead to a realistic and finite result for the non-linear effect and its magnitude is further shown, in the Appendix, to be small.

2. Theory

2.1. The adiabatic approximation

In considering the effects of adsorbates on the substrate conductivity we have essentially two time scales. One is the collision time characterizing the electron-impurity and electron-phonon scatterings in the bare substrate which is typically of the order of 10^{-13} s; the other is the time associated with the surface kinetics, characteristically 10^{-2} to 10^{-6} s depending on the temperature. With such disparate

time scales, if adsorbate desorption reaction dynamics limit, the current fluctuation

$$\langle j_x(t) j_x(t_0) \rangle$$

where the overbar denotes time average and the subscript t_0 is the time of the conductivity modulation dictated by the adsorbate density fluctuation of a thickness d of the adatom layer.

2.2. Conductivity

We approximate the electrons as a free electron gas scattered from randomly arranged scatterers on a clean surface. The conductivity is the average of the conductivity of the surface layer is treated as a thin layer is treated as a thin layer is given by

$$V(z) = V_0 \exp(-\alpha z)$$

where

$$V_0 = -2\pi e^2 \alpha n_s$$

where n_s , n_0 are the surface and bulk chemical potentials

$$n(z) = n_0 + \frac{1}{2} \alpha z$$

The steady state current is obtained by an appropriate average

$$\frac{p_z}{m} \frac{\partial f}{\partial z} - \frac{\partial V}{\partial z} \frac{\partial f}{\partial p_z}$$

time scales, it is reasonable to assume the electrons equilibrate to the instantaneous adsorbate density by rapid collisions so that the noise in the current reflects the reaction dynamics only at low frequencies, – this is the adiabatic limit. In this limit, the current density correlation function has a field-squared dependent contribution

$$\overline{\langle j_x(t) j_x(t_0) \rangle} \xrightarrow{(t-t_0) \gg \text{collision time}} \overline{\langle j_x(t) \rangle \langle j_x(t_0) \rangle} = E^2 \overline{\sigma_x(t) \sigma_x(t_0)}, \quad (1)$$

where the overhead bar represents an averaging over the adatom density distribution and the triangular brackets an averaging over the electron distribution. The conductivity $\sigma(t)$ is now time dependent and corresponds to its instantaneous value dictated by the adsorbate density at that instant. We will first calculate the conductivity of a thick film with a constant adsorbate density and then allow it to follow the adatom density fluctuations exactly and instantaneously.

2.2. Conductivity of a thick film

We approximate the thick film (thick compared to the bulk mean free path of the electrons) by an infinite system containing free electrons suffering elastic collisions from randomly distributed bulk impurities. In addition, there is a layer of scatterers confined to a small thickness d around $z = 0$ but otherwise quite randomly arranged in the x - y plane – these represent the adatoms. In this model, the clean surface reflects the electrons specularly resulting in no change in the conductivity – the adsorbed layer, however, scatters the electrons elastically but not specularly. Each adatom shares some charge with the substrate and thus is itself charged. Let αe be the charge on each adparticle. The screening of this charged layer is treated in the Thomas–Fermi approximation – the screened potential $V(z)$ is given by

$$V(z) = V_0 \exp(-\lambda|z|),$$

where

$$V_0 = -2\pi e^2 \alpha n_s d / \lambda \quad \text{and} \quad \lambda^2 = 6\pi n_0 e^2 / \epsilon_F,$$

where n_s, n_0 are the densities of adparticles and electrons respectively and ϵ_F , the bulk chemical potential. The electronic density $n(z)$ adjusts itself to

$$n(z) = n_0 + \frac{1}{2} \alpha \lambda \, dn_s \exp(-\lambda|z|). \quad (2)$$

The steady state Boltzmann transport equation for the substrate electrons accelerated by an applied electric field, E , in the x -direction is

$$\frac{p_z}{m} \frac{\partial f}{\partial z} - \frac{\partial V}{\partial z} \frac{\partial f}{\partial p_z} + eE \frac{\partial f}{\partial p_x} = -[k_0 + dk_1 \delta(z)](f - f^0); \quad (3)$$

where the local electronic density is

$$n(z) = 2 \int \frac{dp}{(2\pi)^3} f(p, z),$$

the bulk electronic density is

$$n_0 = 2 \int \frac{dp}{(2\pi)^3} f^0(p);$$

and k_0 and k_1 are the scattering probabilities from bulk and surface impurities respectively.

The scattering probability can be clearly separated into the bulk and surface parts for low surface impurity concentrations. Assuming the form

$$f = f^0 + \frac{p_x}{m} g(p, z)$$

and making a contact transformation from (z, p_z) to energy (ϵ) and epoch (τ) we have

$$\frac{\partial p_z}{\partial \tau} = -\frac{\partial V}{\partial z} \quad \text{and} \quad \frac{p_z}{m} = \frac{\partial z}{\partial \tau} = \left(\frac{2}{m} (\epsilon - V(z)) \right)^{1/2}. \quad (4)$$

For $V_0 > 0$, $g(\epsilon, \tau)$ is found to be

$$g(\epsilon, \tau) = -\frac{eE}{k_0} \frac{\partial f^0}{\partial \epsilon} \left[1 - \frac{k_1 d (m/2(\epsilon - V_0))^{1/2} \theta(\epsilon - V_0) \theta(\tau) \exp(-k_0 \tau)}{1 + k_1 d (m/2(\epsilon - V_0))^{1/2} \theta(\epsilon - V_0)} \right], \quad (5)$$

where $\theta(x) = 0$ for $x < 0$ and $\theta(x) = 1$ for $x > 0$. The factor $\theta(\epsilon - V_0)$ is absent for $V_0 < 0$. The total current

$$\langle J_x^{\text{total}} \rangle = 2 \int_0^{\infty} \langle j_x(z) \rangle dz$$

is given in terms of the average current density

$$\langle j_x \rangle = \frac{2e}{m^2} \int p_x^2 g(p, z) \frac{dp}{(2\pi)^3}. \quad (5a)$$

For a sample of thickness L , the conductivity in the two limiting cases $d \ll v_f/k_1$ and $d \gg v_f/k_1$ is

$$\sigma_x = \frac{J_x^{\text{total}}}{LE} = \begin{cases} \frac{\bar{n}e^2}{mk_0} \left[1 - \frac{n(0) k_1 d}{\bar{n} k_0 L} \right], & \text{for } d \ll v_f/k_1, \\ \frac{\bar{n}e^2}{mk_0} \left[1 - \frac{3 n(0) v_f}{8 \bar{n} k_0 L} \left(1 - \frac{V_0}{\epsilon_F} \right) \right], & \text{for } d \gg v_f/k_1, \end{cases} \quad (6)$$

where

$$\bar{n} = \frac{1}{L} \int_{-L/2}^{+L/2} n(z) dz$$

The first term is \bar{n} .

The two small or large d an electron result remind scatterers are rule to be v_f that result is the bulk and collisions in the bulk con

The effect model, in the that of the p

$$(\sigma_x - \sigma_b)/\sigma_b$$

for all values for low ads $n_0 = 10^{23}/\text{cm}^3$ absence of c is entirely du

$$(\sigma_x - \sigma_b)/\sigma_b$$

For $k_1 d \ll v_f/k_1$ n_s/n_b ; then cm; then $(\sigma_x$

Fuchs [4

is

$$\sigma = \sigma_b \left[1 - \frac{3}{8} \frac{n(0) v_f}{\bar{n} k_0 L} \left(1 - \frac{V_0}{\epsilon_F} \right) \right]$$

where σ_b is probability of $\sigma \rightarrow \sigma_0(1 - 3/8)$ scattering (t

where

$$\bar{n} = \frac{1}{L} \int_{-L/2}^{+L/2} n(z) dz \quad \text{and} \quad n(0) = n_0 + \frac{1}{2} \alpha \lambda n_s d.$$

The first term in eq. (6) is the conductivity of a bulk sample with electronic density \bar{n} .

The two limiting cases correspond to the thickness of the surface layer being small or large compared to the surface mean free path of the electrons. For $v_f/k_1 \gg d$ an electron samples both types of scatterers between collisions and we expect a result reminiscent of Matthiessen's rule, but not exactly, since the two types of scatterers are not uniformly distributed throughout the sample for Matthiessen's rule to be valid strictly. This is indeed seen to be true in the first case of eq. (6); that result is the first term in the expansion of the total resistance being the sum of the bulk and the surface resistances. In the opposite limit an electron suffers many collisions in the surface layer before being scattered out of it — the correction to the bulk conductivity is seen to be independent of the surface mean free path.

The effect of charge sharing is evident in the factors \bar{n} , $n(0)$ and V_0 ; in this model, in the absence of scattering from impurities the change in conductivity from that of the pure sample is entirely due to charge sharing and is given by

$$(\sigma_x - \sigma_b)/\sigma_b = (\bar{n} - n_0)/n_0,$$

for all values of the surface mean free path (although eq. (3) is strictly valid only for low adsorbate densities). For $\alpha = 0.1$, $L = 10^{-6}$ cm, surface area = 10^{-3} cm², $n_0 = 10^{23}$ /cm³ and $dn_s = 10^{14}$ cm², $(\bar{n} - n_0)/n_0 \sim 10^{-3}$. On the other hand, in the absence of charge sharing ($\alpha = 0$, i.e., $\bar{n} = n_0$, $n(0) = n_0$) the change in conductivity is entirely due to scattering and is given by

$$(\sigma_x - \sigma_b)/\sigma_b = \begin{cases} -k_1 d/k_0 L, & \text{for } k_1 d \ll v_f, \\ -3v_f/8k_0 L, & \text{for } k_1 d \gg v_f. \end{cases}$$

For $k_1 d \ll v_f$ we take $dn_s = 10^{14}$ /cm², $n_b = 10^{22}$ /cm³, $v_f/k_0 = 10^{-7}$ cm and $k_1/k_0 = n_s/n_b$; then $(\sigma_x - \sigma_b)/\sigma_b \sim 10^{-2}$. For $k_1 d \gg v_f$ we take $n_b = 10^{23}$ /cm³, $v_f/k_0 = 10^{-8}$ cm; then $(\sigma_x - \sigma_b)/\sigma_b \sim 10^{-3}$.

Fuchs [4] has shown that the conductivity of a film of thickness L for $L \gg v_f/k_0$ is

$$\sigma = \sigma_b \left[1 - \frac{3}{8} \frac{v_f/k_0}{L} (1 - S) \right],$$

where σ_b is the bulk conductivity of the material i.e., $\sigma_b = n_0 e^2 / m k_0$ and S is the probability of specular reflection. In our equation (6) it is evident that for $k_1 \rightarrow \infty$, $\sigma \rightarrow \sigma_0 (1 - 3v_f/8k_0 L)$, where $\sigma_0 = \bar{n} e^2 / m k_0$; this corresponds to totally diffuse scattering (the amplitude of the forward wave being zero). Also, for $k_1 \rightarrow 0$, $\sigma \rightarrow \sigma_b$;

this corresponds to specular reflection. These two limits agree with Fuchs' results for $S \rightarrow 0$ and $S \rightarrow 1$ respectively.

2.3. The current autocorrelation function

The current autocorrelation function is given by

$$\langle j_x(t) j_x(t_0) \rangle = \frac{e^2}{m^2} \int p_x p_{0x} f(\mathbf{p}, z, t/p_0, z_0, t_0) f(p_0, z_0) d\mathbf{p} dp_0 dz dz_0, \quad (7)$$

where the conditional probability $f(\mathbf{p}, z, t/p_0, z_0, t_0)$ is a solution of the time dependent Boltzmann equation

$$\frac{\partial f}{\partial t} + \frac{p_z}{m} \frac{\partial f}{\partial z} - \frac{\partial V}{\partial z} \frac{\partial f}{\partial p_z} + eE \frac{\partial f}{\partial p_x} = -[k_0 + k_1 d \delta(z)] (f - f^0), \quad (8)$$

with the initial condition

$$f(\mathbf{p}, z, t_0/p_0, z_0, t_0) = \delta^3(\mathbf{p} - \mathbf{p}_0) \delta(z - z_0). \quad (9)$$

Transforming to (ϵ, τ) coordinates defined in (4) and noting that $\partial\tau/\partial t = \{\tau, H\} = 1$, the solution of (6) becomes

$$\begin{aligned} f(p_x, \tau, \epsilon, \tau_c) &= f(p_x - eE(t - t_0), t_0, \epsilon, \tau_c) \exp[-k_0(t - t_0)] \\ &+ k_0 \int_0^{t-t_0} d\tau' \exp[-k_0(t - t_0 - \tau')] f^0(p_x - eE(t - \tau' - t_0), \epsilon) \\ &- \frac{k_1 d \theta(\tau_c) \theta(t - t_0 - \tau_c) \left(\frac{m}{2(\epsilon - V_0)} \right)^{1/2} \theta(\epsilon - V_0)}{1 + k_1 d \left(\frac{m}{2(\epsilon - V_0)} \right)^{1/2} \theta(\epsilon - V_0) \theta(\tau_c)} \\ &\left[-\exp(-k_0 \tau_c) f^0(p_x - eE(t - t_0 - \tau_c), \epsilon) + f(p_x - eE(t - t_0), t_0, \epsilon, \tau_c) \right. \\ &\left. + k_0 \int_0^{\tau_c} \exp(k_0 \tau') f^0(p_x - eE(t - t_0 - \tau'), \epsilon) d\tau' \right] \exp[-k_0(t - t_0)], \quad (10) \end{aligned}$$

where τ_c is defined by the equation

$$\exp(\lambda z/2) \left(\frac{\epsilon}{V_0} \right)^{1/2} = \cosh \left[\pm \frac{\lambda}{2} \left(\frac{2\epsilon}{m} \right)^{1/2} (\tau - \tau_c) + \cosh^{-1} \left(\frac{\epsilon}{V_0} \right)^{1/2} \right],$$

and $\tau = t - t_0$. For $t - t_0 \gg k_0^{-1}$ (i.e., times much longer than that between consecutive electronic collisions) the right hand side of (10) goes over to the steady state solution as it indeed should. We now use the distribution function in (10) with the initial condition (9) to calculate the current autocorrelation function (7) up to E^2

terms. The

$$\langle j_x(t) j_x(t_0) \rangle$$

$$-\frac{1}{n} \exp$$

$$+\frac{ne^2}{m^2} \exp$$

$$-eE(t -$$

$$+\frac{ne^2}{m^2} \left(\frac{e}{k} \right)$$

$$\times [2 + k$$

$$\times \phi(\epsilon^0, J$$

where

$$\phi(\epsilon^0, y^0) =$$

$\langle j_x^0 \rangle$ is the current through quantities v (11) are

$$(a) \langle j_x(t) \rangle$$

$$(b) \langle j_x(t) \rangle$$

\times

which can

So far, over the el the adatom tion, avera further ave adiabatic li for two lim

terms. The result is

$$\begin{aligned}
 \langle j_x(t) j_x(t_0) \rangle = & -\frac{k_0}{n} \left[(t - t_0) + \frac{1}{k_0} \right] \exp[-k_0(t - t_0)] \langle j_x^b \rangle \langle j_x^{s+b} \rangle \\
 & - \frac{1}{n} \exp[-k_0(t - t_0)] \left[1 + k_0^2(t - t_0) \left\{ t - t_0 + \frac{1}{k_0} \right\} \right] [\langle j_x^{s+b} \rangle - \langle j_x^b \rangle] \langle j_x^{s+b} \rangle \\
 & + \frac{ne^2}{m^2} \exp[-k_0(t - t_0)] \int p_{0x}^2 f^0(p_0, z_0) [1 - \phi(\epsilon^0, y^0) \theta(t - t_0 - y^0)] dp_{0x} d\epsilon^0 dy^0 \\
 & - eE(t - t_0) \exp[-k_0(t - t_0)] \langle j_x^{s+b} \rangle \\
 & + \frac{ne^2}{m^2} \left(\frac{eE}{k_0} \right)^2 \exp[-k_0(t - t_0)] \int p_{0x} \frac{\partial f^0}{\partial p_x} [1 - \phi(\epsilon^0, y^0) \exp(-k_0 y^0)] \\
 & \times [2 + k_0(t - t_0)] \\
 & \times \phi(\epsilon^0, y^0) \theta(t - t_0 - y^0) dp_{0x} d\epsilon^0 dy^0 + \frac{2}{n} \exp[-k_0(t - t_0)] \langle j_x^{s+b} \rangle \langle j_x^b \rangle, \quad (11)
 \end{aligned}$$

where

$$\phi(\epsilon^0, y^0) = \frac{k_1 d \theta(\epsilon^0 - V_0) \theta(y^0)}{k_1 d + (2(\epsilon^0 - V_0)/m)^{1/2}};$$

$\langle j_x^b \rangle$ is the average total current through a bulk sample; $\langle j_x^{s+b} \rangle$ is the average total current through a thick film as calculated from (5a) above; $y = \tau - \tau_c$; and the quantities with superscript zero refer to their values at t_0 . The limiting values of (11) are

$$\begin{aligned}
 \text{(a)} \quad \langle j_x(t) j_x(t_0) \rangle & \xrightarrow{(t-t_0)k_0 \gg 1} \langle j_x^{s+b} \rangle^2 \quad \text{as it should;} \\
 \text{(b)} \quad \langle j_x(t) j_x(t_0) \rangle & \xrightarrow{E=0} \frac{ne^2}{m^2} \exp[-k_0(t - t_0)] \int p_{0x}^2 f^0(p_0, z_0) \\
 & \times [1 - \phi(\epsilon^0, y^0) \theta(t - t_0 - y^0)] dp_{0x} dp_{0y} d\epsilon^0 dy^0,
 \end{aligned}$$

which can easily be shown to be the Johnson noise term.

So far, the current and the current autocorrelation function have been averaged over the electronic distribution function only. This has to be further averaged over the adatom distribution function. Eq. (11) gives the current autocorrelation function, averaged over the electronic distribution, for all values of t and t_0 . When further averaged over the adatom distribution function it reduces to (1) in the adiabatic limit ($t - t_0 \gg 1/k_0$). For a thick film, σ has already been calculated in (6) for two limiting cases, (a) $k_1 d \ll v_f$ and (b) $k_1 d \gg v_f$.

For case (a), $k_1 d \ll v_f$

$$\sigma(t) = \frac{\bar{n}(t) e^2}{mk_0} - \frac{n(z=0, t) e^2}{mk_0^2} \frac{d}{L} k_1(t),$$

where

$$\bar{n}(t) = n_0 + \alpha(d/L) n_s(t),$$

$$n(z=0, t) = n_0 + \frac{1}{2} \lambda \alpha d n_s(t),$$

$$k_1(t) = \frac{m n_s(t) p_f}{(2\pi)^2} \int |u(\theta)|^2 d\Omega;$$

$k_1(t) = (n_s(t)/n_b) k_0$, assuming the same scattering potential for both bulk and surface impurities. Now, $n_s(t)$ is the adsorbate density varying about its mean coverage value and n_b , the density of the bulk scatterers. The fluctuation $\delta\sigma(t)$ of $\sigma(t)$ about its average value up to first order in $\delta n_s(t)$ is

$$\frac{\delta\sigma(t)}{\sigma_b} = \frac{d}{L} \frac{\delta n_s(t)}{n_0} \left[\alpha - \frac{n_0}{n_b} \left(1 + \frac{\alpha \lambda d n_s}{n_b} \right) \right] \approx - \frac{d}{L} \frac{\delta n_s(t)}{n_b}$$

for $\alpha = 0.1$, $n_0 = 10^{23}/\text{cm}^3$, $n_b = 10^{22}/\text{cm}^3$, $\lambda = 10^8 \text{ cm}^{-1}$, $d n_s = 10^{14}/\text{cm}^2$. To make an order of magnitude estimate of the reaction noise, we take a Ni film 10^{-6} cm thick, 1 cm long and 10^{-3} cm wide. The resistance of such a film is 10 k Ω and the current flowing through it is 1 mA for 10 V applied across the film. The incremental current autocorrelation function is given by

$$\overline{\langle \delta j(t) \delta j(0) \rangle} \sim E^2 \sigma_b^2 (d/L)^2 \overline{\delta n_s(t) \delta n_s(0)} / n_b^2.$$

We assume the coverage correlation function to be of the form

$$\overline{\delta\theta(t) \delta\theta(0)} = (\delta\theta)^2 e^{-t/\tau}$$

and $\tau = 10^{-3} \text{ s}$. The reaction noise has to be compared with the inherent Johnson noise due to the resistance of the film. Nyquist's theorem for Johnson noise states that

$$\overline{(\delta V)_{\text{Johnson}}^2} = \int_{-\infty}^{+\infty} c(\omega) d\omega = 4RK_B T \Delta\omega,$$

where $\overline{(\delta V)_{\text{Johnson}}^2}$ is the mean squared voltage fluctuation across the sample; $c(\omega)$, the spectral density of $V(t)$ — this is also the Fourier transform of $\overline{\delta V(t) \delta V(0)}$ according to the Wiener-Khinchine theorem; R , the resistance of the sample; K_B , Boltzmann's constant; T , the temperature and $\Delta\omega$, the bandwidth. Johnson noise is white up to a frequency ω_0 , where ω_0^{-1} is the electron-impurity collision time. For our sample,

$$c(\omega) = 4RK_B T \sim 10^{-16} \text{ V}^2 \cdot \text{s at } 300 \text{ K}.$$

Defining the reaction noise in

$$c_{\text{reaction}}(\omega)$$

where S is the

$$c_{\text{reaction}}(\omega =$$

For case (b),

$$\sigma(t) = \frac{\bar{n}(t) e^2}{mk_0}$$

so that

$$\delta\sigma(t)/\sigma_b \sim \alpha$$

where we take the same as above

$$c_{\text{reaction}}(\omega =$$

2.4. Adsorbate

2.4.1. Equilib

We have seen that the function becomes assumed to be reaction time kinetics with model a partial unit sticking called the resist surface is vacant. The probability

$$p(t+dt) = [1 -$$

where ν and λ in this equation is

$$p(t) = \frac{\nu}{\lambda + \nu} + e$$

The average of $c(t)$ is defined as

$$c(t) = \overline{\delta n(t) \delta n($$

Defining the mean squared voltage fluctuation and the spectral density for the reaction noise in a similar manner, we obtain

$$c_{\text{reaction}}(\omega) = \frac{V^2 dn_s}{n_b^2 LS} \frac{2\tau}{1 + (\omega\tau)^2},$$

where S is the surface area of the film. Thus,

$$c_{\text{reaction}}(\omega = 0)/c_{\text{Johnson}} \sim 10.$$

For case (b), when $k_1 d \gg v_f$,

$$\sigma(t) = \frac{\bar{n}(t) e^2}{mk_0} - \frac{3 n(0) e^2 v_f}{8 mk_0^2 L} \left(1 - \frac{V_0}{\epsilon_F}\right),$$

so that

$$\delta\sigma(t)/\sigma_b \sim \alpha dn_s(t)/Ln_b,$$

where we take $n_b = 10^{23}/\text{cm}^3$, $\alpha = 0.1 v_f/k_0 = 10^{-8}$ cm and all other quantities the same as above. In this case

$$c_{\text{reaction}}(\omega = 0)/c_{\text{Johnson}} \sim 10^{-3}.$$

2.4. Adsorbate correlation function

2.4.1. Equilibrium reaction

We have seen that in the adiabatic approximation the current auto-correlation function becomes proportional to the adsorbate density correlation; the latter was assumed to bear an exponential character decaying with a life time equal to the reaction time. We can calculate this quantity using a simple model for reaction kinetics with two constant rates, viz. the rates of adsorption and desorption. In this model a particle arriving at a site is always adsorbed (low gas phase pressure and unit sticking coefficient); it stays on the surface on the average for a length of time called the residence time until thermal fluctuations force it out of the surface. The surface is vacant for an average length of time until another particle gets adsorbed. The probability $p(t)$ that a site is occupied at time t obeys the equation

$$p(t + dt) = [1 - p(t)] \nu dt + (1 - \lambda dt) p(t),$$

where ν and λ are the adsorption and desorption rates respectively. The solution of this equation is

$$p(t) = \frac{\nu}{\lambda + \nu} + \exp[-(\lambda + \nu)t] \left[p(0) - \frac{\nu}{\lambda + \nu} \right].$$

The average occupation at a site is $\nu/(\lambda + \nu)$. The occupation correlation function $c(t)$ is defined as

$$c(t) = \overline{\delta n(t) \delta n(0)} = [p(t)]_{p(0)=1} \frac{\nu}{\lambda + \nu} - \left(\frac{\nu}{\lambda + \nu} \right)^2,$$

or

$$c(t) = \frac{\nu\lambda}{(\nu + \lambda)^2} \exp[-(\lambda + \nu)t] \quad \text{and} \quad c(\omega) = \frac{2\nu\lambda}{(\nu + \lambda)} \frac{1}{\omega^2 + (\lambda + \nu)^2},$$

where $c(\omega)$ is the Fourier transform of $c(t)$ and equals the power spectrum by the Wiener-Khintchine theorem. We thus obtain the exponential form of the adsorbate correlation function. For low gas pressures, $\lambda \gg \nu$ and $c(t) \approx n_{\text{equil}} e^{-\lambda t}$. The single Lorentzian form for $c(\omega)$ is a consequence of assuming constant reaction rates ν and λ - this is the case for a single step activated reaction process. However, for more complicated processes, viz. those involving two or more adsorption wells, the reaction rates vary with time and the correlation function becomes a sum of decaying exponentials, the correlation times being functions of all the rates involved. The corresponding spectrum is a sum of Lorentzians.

As an illustrative example of such a reaction we consider the adsorption of hydrogen on nickel in equilibrium:



The chemisorption of atomic hydrogen proceeds via a precursor physisorbed state for molecular hydrogen [3,5] as shown in fig. 1. We assume that the two adsorption

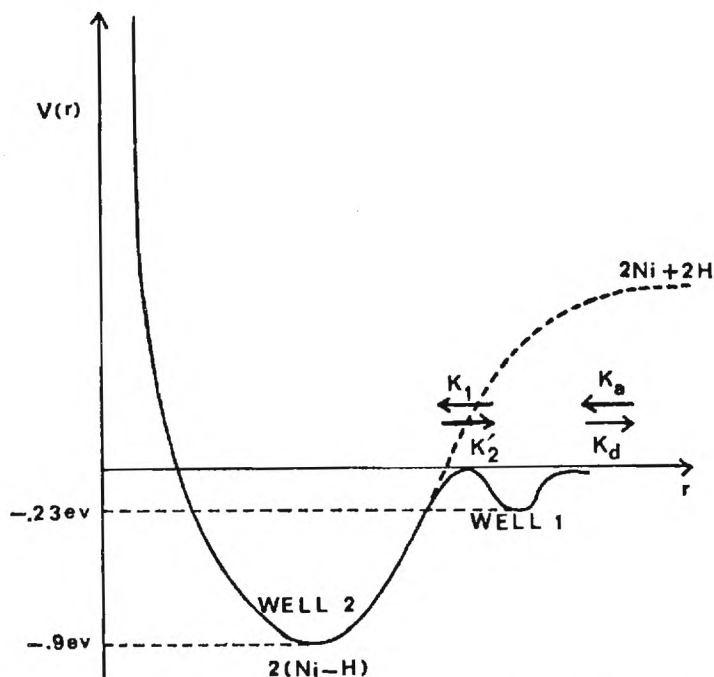


Fig. 1. Potential energy curve for two-step adsorption of hydrogen on nickel.

wells are either probability

$$\frac{d}{dt} n_g = K_d n_1$$

$$\frac{dN_1}{dt} = -K_d n_1$$

$$\frac{1}{2} \frac{dN_2}{dt} = K_2 n_1$$

where $n_g =$ probability of adsorbates in the vicinity of adsorption area of the surface, and $\phi =$ surface area.

The rate of change of n_1 from the equation

$$\frac{d}{dt} \delta n = M' \delta n$$

where M' is a matrix of the eigenvalues of the matrix involving δn_1

$$\frac{d}{dt} \delta n = M \delta n$$

and

$$M = \begin{bmatrix} -K_d + \frac{K_1}{2} & \frac{K_2}{2} \\ 2K_2 \frac{\bar{n}_2}{\bar{n}_1} & -K_d \end{bmatrix}$$

where $K_a = \phi \nu$

$$\lambda^2 - \lambda \left[K_d + \frac{K_1}{2} \right] + \frac{K_2}{2} \frac{\bar{n}_2}{\bar{n}_1} = 0$$

$$+ \frac{4\bar{n}_1 K_1 (1 - \bar{n}_1)}{\bar{n}_2}$$

and the corresponding

$$\tilde{n}_\lambda = \begin{pmatrix} 1 \\ \lambda \end{pmatrix},$$

wells are either at two different sites or, if they are at the same site, the occupation probability of one is independent of that in the other. The rate equations are

$$\frac{d}{dt} n_g = K_d N_1 \frac{S}{V} - \mathcal{C} \frac{S}{V} n_g v_{th} \left(1 - \frac{N_1}{N_s}\right),$$

$$\frac{dN_1}{dt} = -K_d N_1 + \mathcal{C} n_g v_{th} \left(1 - \frac{N_1}{N_s}\right) + K_2' \left(1 - \frac{N_1}{N_s}\right) S N_2^2 - K_1 \left(1 - \frac{N_2}{N_s}\right)^2 N_1,$$

$$\frac{1}{2} \frac{dN_2}{dt} = K_2' \left(1 - \frac{N_1}{N_s}\right) S N_2^2 - K_1 \left(1 - \frac{N_2}{N_s}\right)^2 N_1,$$

where n_g = density of gas phase hydrogen molecules, N_1 = surface density of adsorbates in well 1, N_2 = surface density of adsorbates in well 2, N_s = surface density of adsorption sites, v_{th} = thermal velocity of hydrogen in gas phase, S = surface area of the sample, V = volume of the gas, V/S = mean free path of the hydrogen gas, and \mathcal{C} = sticking coefficient.

The rate equations can be linearized in the excursions δn (where $n_1 = N_1/N_s$) from the equilibrium value \bar{n} . In matrix form, the linearized equation is

$$\frac{d}{dt} \delta n = M' \delta n,$$

where M' is a 3×3 matrix. However, since $V n_g + S(N_1 + \frac{1}{2}N_2)$ is a constant, one of the eigenvalues of M' is zero. The three component equation can be reduced to two involving δn_1 and δn_2 only. Thus

$$\frac{d}{dt} \delta n = M \delta n, \quad \text{where} \quad \delta n_{1,2} = \frac{\delta N_{1,2}}{n_s},$$

and

$$M = \begin{bmatrix} -K_d + \frac{K_a}{N_s} \bar{n}_g + K_a \frac{S}{V} (1 - \bar{n}_1) + K_2 \frac{\bar{n}_2^2}{n_1} & \frac{2\bar{n}_1 K_1 (1 - \bar{n}_2)}{\bar{n}_2} - \frac{K_a (1 - \bar{n}_1) S/V}{2} \\ 2K_2 \frac{\bar{n}_2^2}{\bar{n}_1} & -4 \frac{K_1 \bar{n}_1 (1 - \bar{n}_2)}{\bar{n}_2} \end{bmatrix},$$

where $K_a = \mathcal{C} v_{th}$ and $K_2 = K_2' S N_s$. The eigenvalues $\lambda_{1,2}$ of M are the roots of

$$\lambda^2 - \lambda \left[K_d + \frac{K_a}{N_s} \bar{n}_g + K_a \frac{S}{V} (1 - \bar{n}_1) + \frac{K_2 \bar{n}_2^2}{\bar{n}_1} + \frac{4\bar{n}_1 K_1 (1 - \bar{n}_2)}{\bar{n}_2} \right] + \frac{4\bar{n}_1 K_1 (1 - \bar{n}_2)}{\bar{n}_2} \left[K_d + \frac{K_a}{N_s} \bar{n}_g + K_a \frac{S}{V} (1 - \bar{n}_1) \right] + \frac{K_2 \bar{n}_2^2}{\bar{n}_1} K_a (1 - \bar{n}_1) \frac{S}{V} = 0, \quad (12)$$

and the corresponding eigenvector \tilde{n}_λ is

$$\tilde{n}_\lambda = \begin{pmatrix} 1 \\ A \end{pmatrix}, \quad \text{where} \quad A = \frac{\lambda_1 + \lambda_2 - \lambda - 4\bar{n}_1 K_1 (1 - \bar{n}_2)/\bar{n}_2}{4\bar{n}_1 K_1 (1 - \bar{n}_2)/\bar{n}_2 - K_a (1 - \bar{n}_1) S/V}.$$

The deviation of the adsorbate density from equilibrium is then

$$\delta n_{1,2} = \sum_{i=1}^2 C_{\lambda_i} \exp(-\lambda_i t) \tilde{n}_{\lambda_i}$$

In particular,

$$\delta n_1(t) = \delta n_1(0) [(1 - D) \exp(-\lambda_1 t) + D \exp(-\lambda_2 t)],$$

$$\delta n_2(t) = \delta n_2(0) [(1 - C) \exp(-\lambda_1 t) + C \exp(-\lambda_2 t)],$$

where

$$D = \frac{1}{\lambda_1 - \lambda_2} \left[\frac{4\bar{n}_1 K_1 (1 - \bar{n}_2)}{\bar{n}_2} - \lambda_2 + \frac{\delta n_2(0)}{2 \delta n_1(0)} \left(\frac{4\bar{n}_1 K_1 (1 - \bar{n}_2)}{\bar{n}_2} - K_a \frac{S}{V} (1 - \bar{n}_1) \right) \right]$$

and

$$C = 2D \frac{\delta n_1(0)}{\delta n_2(0)} \left[\frac{\lambda_1 - 4\bar{n}_1 K_1 (1 - \bar{n}_2) / \bar{n}_2}{4\bar{n}_1 K_1 (1 - \bar{n}_2) / \bar{n}_2 - K_a (S/V) (1 - \bar{n}_1)} \right].$$

When a two step chemical reaction, as in our example, occurs on the surface, adsorbates in both wells act as scattering centres for the substrate electrons, so the relevant correlation function is ($n = n_1 + n_2$)

$$\begin{aligned} \langle \delta n(t) \delta n(0) \rangle &= \exp(-\lambda_1 t) \langle (\delta n(0))^2 \rangle - \left(\frac{\exp(-\lambda_1 t) - \exp(-\lambda_2 t)}{\lambda_1 - \lambda_2} \right) \\ &\times \left(1 + 2 \frac{\lambda_1 - 4\bar{n}_1 K_1 (1 - \bar{n}_2) / \bar{n}_2}{4\bar{n}_1 K_1 (1 - \bar{n}_2) / \bar{n}_2 - K_a (S/V) (1 - \bar{n}_1)} \right) \left[\left(\frac{4\bar{n}_1 K_1 (1 - \bar{n}_2)}{\bar{n}_2} - \lambda_2 \right) \right. \\ &\times \langle \delta n_1(0) \delta n(0) \rangle + \frac{1}{2} \langle \delta n(0) \delta n_2(0) \rangle \left. \left(\frac{4\bar{n}_1 K_1 (1 - \bar{n}_2)}{\bar{n}_2} - K_a \frac{S}{V} (1 - \bar{n}_1) \right) \right]. \end{aligned}$$

However, only the chemisorbed atoms are engaged in forming a chemisorptive bond involving charge sharing – for this effect the relevant correlation function is

$$\begin{aligned} \langle \delta n_2(t) \delta n_2(0) \rangle &= \langle (\delta n_2(0))^2 \rangle \exp(-\lambda_1 t) - 2 \left[\frac{\exp(-\lambda_1 t) - \exp(-\lambda_2 t)}{\lambda_1 - \lambda_2} \right] \\ &\times \left[\frac{\lambda_1 - 4\bar{n}_1 K_1 (1 - \bar{n}_2) / \bar{n}_2}{4\bar{n}_1 K_1 (1 - \bar{n}_2) / \bar{n}_2 - K_a (S/V) (1 - \bar{n}_1)} \right] \left[\left(\frac{4\bar{n}_1 K_1 (1 - \bar{n}_2)}{\bar{n}_2} - \lambda_2 \right) \right. \\ &\times \langle \delta n_1(0) \delta n_2(0) \rangle \\ &\left. + \frac{1}{2} \langle (\delta n_2(0))^2 \rangle \left(\frac{4\bar{n}_1 K_1 (1 - \bar{n}_2)}{\bar{n}_2} - K_a \frac{S}{V} (1 - \bar{n}_1) \right) \right]. \end{aligned}$$

The equal time correlation functions can be calculated from thermodynamic considerations. For this chemical reaction, given by $\sum_j A_j \nu_j = 0$, where A_j denotes

the chemical potential expanded ab

$$S = S_0 + \sum_i$$

Furthermore reaction take ith species. T

$$S = S_0 - \frac{1}{2T}$$

for non-inte entropy S is

$$\langle (\delta N_i)^2 \rangle = K$$

$$\langle \delta N_i \delta N_j \rangle =$$

In the react limiting step state, i.e., K_2

$$\lambda_1 = \frac{K_2 \bar{n}_2}{\bar{n}_1} +$$

The slower sorptive well as indicated pared to K_d 2 to the bat high gas pre K_2 is small root λ_1 now in the react

Since the steps in the ranges. For heated from Lichtman, S (a) Between

the chemical symbol of the j th species and ν_j are integers; the corresponding chemical potential μ_j satisfy the equation $\sum_j \nu_j \mu_j = 0$. The entropy S of the system can be expanded about its equilibrium value S_0 in the deviations δN_i as

$$S = S_0 + \sum_i \frac{\partial S}{\partial N_i} \delta N_i + \frac{1}{2} \left[\sum_i \frac{\partial^2 S}{\partial N_i^2} (\delta N_i)^2 + \sum_{i,j} \frac{\partial^2 S}{\partial N_i \partial N_j} \delta N_i \delta N_j \right] + \dots$$

Furthermore, $\delta N_i = \nu_i \delta N$, where δN is the increment of the number of times the reaction takes place, and $\mu_i = -T \partial S / \partial N_i$, where μ_i is the chemical potential of the i th species. Then

$$S = S_0 - \frac{1}{2T} \sum_i \nu_i^2 \frac{\partial \mu_i}{\partial N_i} (\delta N)^2$$

for non-interacting species of reactants. The probability P that the system has entropy S is $\exp(-S/K_B)$ and therefore,

$$\langle (\delta N_i)^2 \rangle = K_B T \nu_i^2 \left(\sum_i \nu_i^2 \frac{\partial \mu_i}{\partial N_i} \right)^{-1},$$

$$\langle \delta N_i \delta N_j \rangle = K_B T \nu_i \nu_j \left(\sum_i \nu_i^2 \frac{\partial \mu_i}{\partial N_i} \right)^{-1}$$

In the reaction considered here, $A_1 = H_2^a, A_2 = H^a, \nu_1 = 1$ and $\nu_2 = -2$. If the rate limiting step in this two step reaction is between the gas phase and the precursor state, i.e., $K_a, K_d \ll K_1, K_2$ [3], then from (12)

$$\lambda_1 = \frac{K_2 \bar{n}_2}{\bar{n}_1} + 4K_1 \frac{\bar{n}_1(1 - \bar{n}_2)}{\bar{n}_2} \gg \lambda_2 = K_d + \frac{K_a}{n_s} \bar{n}_g + K_a \frac{S}{V} (1 - \bar{n}_1).$$

The slower rate λ_2 dominates the approach to equilibrium. Although the chemisorptive well is deeper than the precursor well, the reaction may still be rate limited as indicated above if the prefactor in K_d is so small as to make K_2 seem large compared to K_d . One possible reason for this may be due to a stronger coupling of well 2 to the bath compared to well 1. On the other hand, if we assume that for fairly high gas pressures well 1 fills up rapidly and then slowly empties into well 2, and K_2 is small at room temperatures, then $K_1, K_2 \ll K_a, K_d$ and $\lambda_1 \ll \lambda_2$. The smaller root λ_1 now governs the approach to equilibrium. Thus, if a true bottleneck exists in the reaction, it is reflected in the rate at which the correlation function decays.

Since the individual rates K_a, K_d, K_1 and K_2 are functions of temperature, some steps in the reaction are more important than others at different temperature ranges. For instance, when a (100) nickel film with adsorbed hydrogen is slowly heated from 300 K to 1300 K, electron-impact desorption technique applied by Lichtman, Simon and Kirst [5] indicate that the following picture is reasonable:

(a) Between 300 K and 500 K, adatoms empty from well 1 into well 2, K_2 and K_d

are negligible and

$$\lambda_1 = \frac{K_a}{N_s} \left[\bar{n}_g + \frac{N_s S}{V} (1 - \bar{n}_1) \right], \quad \lambda_2 = \frac{4K_1 \bar{n}_1 (1 - \bar{n}_2)}{\bar{n}_2}.$$

Then,

$$\langle \delta n_2(t) \delta n_2(0) \rangle = \exp(-\lambda_2 t) \langle \delta n_2^2 \rangle,$$

so that the effect of charge sharing contains only one decaying exponential. The other correlation function $\langle \delta n(t) \delta n(0) \rangle$ contains both the exponential factors.

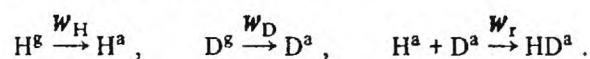
(b) Between 500 K and 730 K the adsorbates in well 2 have enough activation energy to desorb thermally, so that K_2 and K_d are large whereas K_1 and K_a are small. Then, $\lambda_1 = 0$, $\lambda_2 = K_d + K_2 \bar{n}_2^2 / \bar{n}_1$.

It should be mentioned that a large discrepancy exists among the results of various experimentalists for the case of hydrogen adsorbed on nickel. In particular, in the electron probe surface spectroscopy experiments by Lichtman, Simon and Kirst [6] there is a possibility that the state of the adsorbate might be modified during the electron-induced desorption [7]. Furthermore, their experiment shows desorption to be essentially complete by about 730 K whereas flash desorption experiments by Lapujoulade and Neil [7] exhibit complete desorption by 500 K.

Again, the correlation functions have only one decaying exponential factor; assuming a reasonable value for K_d , K_2 can now be determined from λ . Thus, working at suitable temperature ranges furnishes the possibility of obtaining the individual reaction rates which are otherwise buried in the general rate constants λ_1 and λ_2 .

2.3.2. Steady state reaction

So far we have considered the surface reaction proceeding in equilibrium. Often experiments are easier to be carried out in non-equilibrium (steady state) such as maintaining a constant gas pressure while removing the products as they are formed. The fluctuations in the adsorbate density in non-equilibrium are therefore the relevant quantity for these experiments. We select a particular reaction in the steady state under non-equilibrium conditions and calculate the adsorbate density noise. We choose the reaction



The superscript g stands for the gas phase and a for the adsorbed state. The absence of all reverse reactions ensures non-equilibrium. This is realistic if H^a and D^a combine rapidly so that there is only a small probability for desorption and if HD^a is removed from the system rapidly. The probability $p(n_H^g, n_D^g, n_H, n_D, n_{HD})$ that there are the corresponding number of particles in the system obeys the rate equation

$$\frac{d}{dt} p(n_H^g, n_D^g, n_H, n_D, n_{HD}) = W_H p(n_H^g + 1, n_D^g, n_H - 1, n_D, n_{HD}) (n_H^g + 1)$$

$$\times \left[1 - \right.$$

$$\left. + W_D p(n_H^g, n_D^g + 1, n_H, n_D - 1, n_{HD}) \right]$$

$$- (W_H n_H^g + W_D n_D^g + W_r p(n_H^g, n_D^g, n_H, n_D, n_{HD})) p(n_H^g, n_D^g, n_H, n_D, n_{HD})$$

$$+ W_r p(n_H^g, n_D^g, n_H - 1, n_D + 1, n_{HD})$$

$$- W_r p(n_H^g, n_D^g, n_H + 1, n_D - 1, n_{HD})$$

where S is

Defining

$$\bar{n}_H = \sum_{\text{all } n} n_H p(n_H^g, n_D^g, n_H, n_D, n_{HD})$$

the first n_H

$$\frac{d\bar{n}_H}{dt} = W_H$$

and the first

$$\frac{d\bar{n}_D}{dt} = W_D$$

We ignore

eqs. (14) and

$$W_H n_H^g = W_D n_D^g$$

This means

same rate

we take to

ations in n_H

manner will

In this a

$$\bar{n} = \frac{2}{W_r} \left[- \right.$$

The second

$$W \left(1 + 2\bar{n} - \right.$$

where we ha

$$\frac{n_H^g n_D^g}{n_H^g n_D^g} = \frac{n_H^g n_D^g}{n_H^g n_D^g}$$

$$\begin{aligned}
& \times \left[1 - \frac{(n_H - 1)}{S} - \frac{n_D}{S} \right] \\
& + W_D p(n_H^g, n_D^g + 1, n_H, n_D - 1, n_{HD})(n_D^g + 1) \left[1 - \frac{n_H}{S} - \frac{(n_D - 1)}{S} \right] \\
& - (W_H n_H^g + W_D n_D^g) p(n_H^g, n_D^g, n_H, n_D, n_{HD}) \left[1 - \frac{n_H}{S} - \frac{n_D}{S} \right] \\
& + W_r p(n_H^g, n_D^g, n_H + 1, n_D + 1, n_{HD} - 1)(n_H + 1)(n_D + 1) \\
& - W_r p(n_H^g, n_D^g, n_H, n_D, n_{HD}) n_H n_D, \tag{13}
\end{aligned}$$

where S is the total number of surface sites.

Defining

$$\bar{n}_H = \sum_{\text{all } n} n_H p(n_H^g, n_D^g, n_H, n_D, n_{HD}),$$

the first n_H moment of p obeys the equation

$$\frac{d\bar{n}_H}{dt} = W_H \left[\bar{n}_H^g - \frac{n_H^g \bar{n}_H}{S} - \frac{n_H^g n_D}{S} \right] - W_r \bar{n}_H n_D, \tag{14}$$

and the first n_D moment of p obeys the equation

$$\frac{d\bar{n}_D}{dt} = W_D \left[\bar{n}_D^g - \frac{n_D^g \bar{n}_D}{S} - \frac{n_D^g n_H}{S} \right] - W_r \bar{n}_H n_D. \tag{15}$$

We ignore the fluctuations in the partial gas pressures. Then, in the steady state, eqs. (14) and (15) imply

$$W_H \bar{n}_H^g = W_D \bar{n}_D^g = W.$$

This means \bar{n}_H and \bar{n}_D are adsorbed at the same rate. They are also removed at the same rate to form HD – so, \bar{n}_H and \bar{n}_D may differ at most by a constant which we take to be zero i.e., $\bar{n}_H = \bar{n}_D = \bar{n}$. Furthermore, in calculating \bar{n} we ignore fluctuations in n_H and n_D so that $\bar{n}_H n_D = \bar{n}^2$. Breaking up the higher moments in a similar manner will be justified at the end of this section.

In this approximation,

$$\bar{n} = \frac{2}{W_r} \left[-\frac{W}{S} + \left(\frac{W^2}{S^2} + W W_r \right)^{1/2} \right].$$

The second n_H moment of p is given in the steady state by the equation

$$W \left(1 + 2\bar{n} - \frac{2\bar{n}}{S} - \frac{2\bar{n}^2}{S} - 2 \frac{\bar{n}_H^2}{S} \right) + W_r \bar{n} (\bar{n} - 2\bar{n}_H^2) = 0,$$

where we have again assumed

$$\bar{n}_H^2 n_D = \bar{n}_H^2 \bar{n}.$$

So,

$$\bar{n}_H^2 = \frac{W(1 + 2\bar{n} - 2\bar{n}/S - 2\bar{n}^2/S) + W_r\bar{n}^2}{2W/S + 2W_r\bar{n}},$$

from whence

$$\overline{\Delta n_H^2} = \frac{W(1 - 2\bar{n}/S)}{W/S + W_r\bar{n}} = \frac{\bar{n}(1 - 2\bar{n}/S)}{(1 - \bar{n}/S)}.$$

In a similar manner it can be shown that

$$\overline{\Delta n_H^2} = \overline{\Delta n_D^2}.$$

Identical results for \bar{n} and $\overline{\Delta n_H^2}$ are obtained if we start from the master equation (13) for p and take the thermodynamic limit. This limit is a "largeness" limit in volume — the procedure is thus often referred to as a "system size expansion" as shown by Kurtz [8] and Fox [9]. In this method one writes down the master equation for \bar{n} in the limit $V \rightarrow \infty$. This essentially amounts to ignoring all fluctuations in n and calculating \bar{n} . To calculate the fluctuations, one chooses the variable $\mu = \sqrt{V(n - \bar{n})}$ and then lets $V \rightarrow \infty$ in the master equation for μ . This limiting procedure again removes all higher moments from the equation. We assumed this limit implicitly in decoupling our moment equations above.

For the particular reaction considered here, the density fluctuation approximately equals \bar{n} in the non-equilibrium state for low coverages, whereas under equilibrium conditions, it would equal \bar{n}_{equil} .

3. Conclusions

We have presented an analysis relating the fluctuations of the conductivity of a metal film to the fluctuations in adsorbate density accompanying the adsorption-desorption process. We find that it should be possible to determine at least the time constant of the rate limiting step in the reaction from the spectral characteristics of the conductivity. A crude estimate indicates that the resulting noise power can be up to one order of magnitude larger than Johnson noise. We propose that this method provides a viable alternative to various types of real-time measurements of the rates (e.g. observing the decay of film resistance to equilibrium upon change in gas pressure).

In the course of this work it was necessary to estimate the non-equilibrium part of Johnson noise in the bare sample up to terms quadratic in the applied voltage. The usual relaxation time approximation to the Boltzmann equation turns out to be adequate for our purpose.

Appendix

We invest
sample. At f
in the relaxa
Then,

$$eE \partial f / \partial p_z =$$

so that,

$$f = f^0 - eE\tau$$

Then the ave

$$\langle j_z \rangle = (ne^2\tau/n$$

where n is t
However, if
equation is

$$f = f^0 - eE\tau$$

in which case

$$\langle j_z \rangle = \frac{ne^2\tau}{m} E$$

up to cubic te

$$\langle (\Delta j_z)^2 \rangle = \langle j_z^2 \rangle e$$

up to quadrat
effects in the
electron. How
ous expressio
although the s

$$\frac{\partial f}{\partial t} + eE \frac{\partial f}{\partial p_z} =$$

with

$$f = f^0(p) + \sum_{l=0}^{\infty}$$

and the scatte

nomials is

$$W_{pp'} = \frac{\hbar^2 p}{m} \sum_{l=0}^{\infty} (2l+1) \omega_l(p) P_l(\hat{p} \cdot \hat{p}') \delta(\epsilon_p - \epsilon_{p'}) .$$

This expansion for $W_{pp'}$ is valid for elastic scattering from a spherically symmetric potential. Eqs. (A.3) and (A.4) show that it is inconsistent to take f up to $l=2$ but still leave the collision term in the relaxation time approximation, as was done in deriving eqs. (A.1) and (A.2).

The quantities of interest are

$$\langle j_z \rangle = \frac{em}{\pi^3} \left(\frac{\pi}{3} \right)^{1/2} \int_0^{\infty} \epsilon g_1(\epsilon) d\epsilon , \quad (\text{A.5})$$

$$\langle j_z^2 \rangle = \langle j_z^2 \rangle_{\text{equil}} + \frac{e^2 (2m)^{3/2}}{3m\pi^{5/2}} \int_0^{\infty} \epsilon^{3/2} \left(\frac{1}{2} g_0 + \frac{1}{\sqrt{5}} g_2 \right) d\epsilon , \quad (\text{A.6})$$

$$\langle \epsilon \rangle = \frac{m(2m)^{1/2}}{\pi^2} \int_0^{\infty} \epsilon^{3/2} (f^0 + g_0 Y_0) d\epsilon , \quad (\text{A.7})$$

where $\epsilon = p^2/2m$. Combining (A.3) and (A.4) we get the equation of motion of each component g_l ;

$$\begin{aligned} \frac{\partial g_l}{\partial t} + eE \left[v \frac{l}{[(2l-1)(2l+1)]^{1/2}} g'_{l-1} + \frac{v(l+1)}{[(2l+1)(2l+3)]^{1/2}} g'_{l+1} \right. \\ \left. - \frac{l(l-1)}{p[(2l-1)(2l+1)]^{1/2}} g_{l-1} + \frac{(l+1)(l+2)}{p[(2l+1)(2l+3)]^{1/2}} g_{l+1} \right. \\ \left. + \left(\frac{4\pi}{3} \right)^{1/2} v \frac{\partial f^0}{\partial \epsilon} \delta_{l,1} \right] = -\frac{g_l}{\tau_l} . \end{aligned} \quad (\text{A.8})$$

Eq. (A.8) shows g_0 has no steady state solution. To lowest order in E , $g_0 \sim E^2$, $g_1 \sim E$, $g_2 \sim E^2$, $g_3 \sim E^3$, $g_4 \sim E^4$, etc. Up to second order terms in E , the solutions for g_0 and g_2 are

$$g_0 = \frac{4\pi^{1/2}(eE)^2}{3m\epsilon^{1/2}} \frac{\partial}{\partial \epsilon} \left[\tau_1 \epsilon^{3/2} \frac{\partial f^0}{\partial \epsilon} \{t + \tau_1 [\exp(-t/\tau_1) - 1]\} \right] , \quad (\text{A.9})$$

$$\begin{aligned} g_2 = \left(\frac{\pi}{5} \right)^{1/2} \frac{8(eE)^2}{3m} \epsilon \left[\left\{ \frac{\partial}{\partial \epsilon} \left(\tau_1 \frac{\partial f^0}{\partial \epsilon} \right) \right\} \{ \tau_2 [1 - \exp(-t/\tau_2)] - \tilde{\tau} [\exp(-t/\tau_1) \right. \right. \\ \left. \left. - \exp(-t/\tau_2)] \right\} - \frac{\partial f^0}{\partial \epsilon} \frac{\tau_1'}{\tau_1} \{ \tilde{\tau}^2 [\exp(-t/\tau_2) - \exp(-t/\tau_1)] + t \tilde{\tau} \exp(-t/\tau_1) \} \right] , \end{aligned} \quad (\text{A.10})$$

where $\tilde{\tau}^{-1} =$
(A.5), (A.8)

$$\langle j_z \rangle = -\frac{Ee^2}{\pi^3}$$

$$+ \left(\frac{2}{3m} \right)^{1/2}$$

$$+ \frac{4}{(30m)^{1/2}}$$

The first term

$$\frac{ne^2 \tau_1(\epsilon_F)}{m} E$$

where n is the
and the third
can be easily
terms turn out

$$\frac{4e^4 E^3}{9\pi^2} \left(\frac{2}{m} \right)^{1/2}$$

Thus the average
To see clearly
up to quadratic

$$\langle \epsilon \rangle = \langle \epsilon \rangle_{\text{equil}}$$

Eq. (A.14) shows
the electric field
Evidently, the
the failure to
heat bath for
phonon collision
Debye temperature
already finite
latter only to

The electric field
as [10]

$$\frac{\partial f_k}{\partial t} \Big|_{\text{collision}}$$

where $\bar{\tau}^{-1} = \tau_2^{-1} - \tau_1^{-1}$. So, g_2 has a steady state solution whereas g_0 does not. From (A.5), (A.8), (A.9) and (A.10),

$$\begin{aligned} \langle j_z \rangle = & -\frac{Ee^2m}{\pi^3} \left(\frac{\pi}{3}\right)^{1/2} \int_0^\infty d\epsilon \int_0^t dt' \left[2\left(\frac{2\pi}{3m}\right)^{1/2} \epsilon^{3/2} \frac{\partial f^0}{\partial \epsilon} \exp(-t'/\tau_1) \right. \\ & + \left(\frac{2}{3m}\right)^{1/2} \epsilon^{3/2} \frac{\partial g^0}{\partial \epsilon}(\epsilon, t') \exp[-(t-t')/\tau_1] \\ & \left. + \frac{4}{(30m)^{1/2}} \frac{\partial}{\partial \epsilon} (\epsilon^{3/2} g_2(\epsilon, t')) \exp[-(t-t')/\tau_1] \right]. \end{aligned} \quad (\text{A.11})$$

The first term in the squared brackets of (A.11) gives the linear response and equals

$$\frac{ne^2\tau_1(\epsilon_F)}{m} E [1 - \exp(-t/\tau_1)], \quad (\text{A.12})$$

where n is the electronic density. If τ_1 is independent of ϵ , then both the second and the third terms individually give zero contribution to the average current, as can be easily seen from (A.11), (A.9) and (A.10). For $t \gg \tau_1, \tau_2$, these non-linear terms turn out to equal

$$\frac{4e^4E^3}{9\pi^2} \left(\frac{2}{m}\right)^{1/2} \tau_1(\epsilon_F) \left[t \frac{\partial}{\partial \epsilon} (\epsilon^{5/2}\tau_1)_{\epsilon=\epsilon_F} + \frac{4}{5} \frac{\partial}{\partial \epsilon} (\epsilon^{5/2}\tau_1\tau_2)_{\epsilon=\epsilon_F} \right]. \quad (\text{A.13})$$

Thus the average current grows linearly with time for times longer than τ_1 and τ_2 . To see clearly why this happens, we calculate the average energy of the electrons — up to quadratic terms in E this is

$$\langle \epsilon \rangle = \langle \epsilon \rangle_{\text{equil}} + \frac{ne^2\tau_1(\epsilon_F)}{m} E^2 t. \quad (\text{A.14})$$

Eq. (A.14) shows that the average kinetic energy of the electrons increases due to the electric field exactly by the amount $\langle j \rangle Et$ that the field feeds into the system. Evidently, the absence of a steady state solution for both $\langle j \rangle$ and $\langle \epsilon \rangle$ results from the failure to include the coupling of the electrons to the lattice which provides a heat bath for the former. To exhibit this quantitatively, we include a electron-phonon collision term in the Boltzmann equation for temperatures higher than the Debye temperature for the solid and in the limit of weak coupling. Since g_2 is already finite at long times even in the absence of lattice effects, we include the latter only to obtain a steady state value for g_0 .

The electron-phonon collision term in the Boltzmann equation can be written as [10]

$$\left. \frac{\partial f_k}{\partial t} \right|_{\text{collision}} = \int \frac{dk'}{(2\pi)^3} [W_{k'k} f_{k'} (1 - f_k) - W_{kk'} f_k (1 - f_{k'})], \quad (\text{A.15})$$

where the scattering probability $W_{kk'}$ is given by

$$W_{kk'} = \frac{C^2 \Delta |k - k'|^2}{2M \nu_{|k - k'|}} \{ (n_{|k - k'|} + 1) \delta(\epsilon_k - \epsilon_{k'} + h\nu_{|k - k'|}) + n_{|k - k'|} \delta(\epsilon_k - \epsilon_{k'} - h\nu_{|k - k'|}) \}, \quad (\text{A.16})$$

with Δ , the unit cell volume; M , mass of a lattice point; $\nu_{|k - k'|}$ the phonon frequency; C is a constant, being of the same order as the average energy of an electron and lies between 1 and 10 eV [10]; $n_{|k - k'|}$, the phonon occupation function — it is assumed to have its equilibrium value. Detailed balance requires

$$W_{k'k}/W_{kk'} = \exp[(\epsilon_{k'} - \epsilon_k)/K_B T].$$

For temperatures much higher than the Debye temperature, f_k and its derivatives being smooth functions of energy, the δ -function occurring in $W_{kk'}$ may be approximated by

$$\delta(\epsilon_k - \epsilon_{k'} + h\nu_{|k - k'|}) \approx \delta(\epsilon_k - \epsilon_{k'}) + h\nu_{|k - k'|} \frac{\partial}{\partial \epsilon_k} \delta(\epsilon_k - \epsilon_{k'}).$$

This approximation allows us to break up $W_{kk'}$ into $W_{kk'}^S$, which is symmetric and $W_{kk'}^A$, which is antisymmetric in k and k' ; i.e.,

$$W_{kk'}^S = A \frac{|k - k'|}{\nu_{|k - k'|}} (1 + 2n_{|k - k'|}) \delta(\epsilon_k - \epsilon_{k'}), \quad (\text{A.17a})$$

$$W_{kk'}^A = A |k - k'|^2 h \frac{\partial}{\partial \epsilon_k} \delta(\epsilon_k - \epsilon_{k'}), \quad (\text{A.17b})$$

with $A = C^2 \Delta / 2M$.

Since both $W_{kk'}^A$ and $W_{kk'}^S$ depend on the angle between k and k' only, we expand these functions in a complete set of Legendre polynomials:

$$W_{kk'}^S = \frac{2\pi^2 \hbar^2}{mk} \sum_{l=0}^{\infty} (2l+1) U_l(kk') P_l(\hat{k} \cdot \hat{k}') \delta(\epsilon_k - \epsilon_{k'}), \quad (\text{A.18a})$$

$$W_{kk'}^A = \frac{2\pi^2 \hbar^3}{m(2m)^{1/2}} \sum_{l=0}^{\infty} (2l+1) V_l(kk') P_l(\hat{k} \cdot \hat{k}') \frac{\partial}{\partial \epsilon_k} \delta(\epsilon_k - \epsilon_{k'}). \quad (\text{A.18b})$$

It is also seen that both U_l and V_l are symmetric in $|k|$ and $|k'|$; also, V_l is non-zero for $l=0$ and 1 only.

The collision term can then be rewritten as

$$\left. \frac{\partial f_k}{\partial t} \right|_{\text{collision}} = - \sum_{l=0}^{\infty} \frac{g_l(k) Y_l(\hat{k})}{\tau_l^P(k)} + (1 - 2f_k) \sum_{l=0}^{\infty} Y_l(\hat{k}) \frac{\partial}{\partial \epsilon_k} \{ \phi_l(kk') g_l(k') \}_{\epsilon_k = \epsilon_{k'}}$$

$$+ f_k \frac{\partial}{\partial \epsilon_k}$$

where

$$\tau_l^P(k) = (U_l(kk') + f_k)$$

When (A.15) is integrated over the solid angle Ω_k

$$g_1 \left[eE \left(\frac{2}{3m} \right) \right]$$

where $\alpha = A$

From the order terms

$$g_1 \approx -2eE$$

and thus, from

$$\frac{g_0}{(4\pi)^{1/2}} \approx -$$

in the limit for g_0 and t

$$\frac{4e^4 E^3}{9\pi^2} \left(\frac{2}{m} \right)$$

which is the phonon collision mean square

$$\langle (\Delta j_z)^2 \rangle = \langle$$

$$+ n \left(\frac{e^2 E}{\tau} \right)$$

The first two terms are obtained by taking

order of magnitude

$\tau_2 \sim \tau_{\text{eff}}$, and

order of magnitude

three terms are

adequate to

time approximation

$$+ f_k \frac{\partial}{\partial \epsilon_k} \phi_0(kk')|_{\epsilon_k = \epsilon_k'}, \quad (\text{A.19})$$

where

$$\tau_i^p(k) = (U_0 - U_i)^{-1} \quad \text{and} \quad \phi_i(kk') = (\epsilon_k')^{1/2} V_i(kk').$$

When (A.19) is added to the Boltzmann transport equation and the latter integrated over the solid angle of k , then up to second order in E , the result is

$$g_1 \left[eE \left(\frac{2}{3m} \right)^{1/2} - \frac{\alpha}{(12\pi)^{1/2}} g_1 \epsilon_k \right] = \alpha g_0 \epsilon_k, \quad (\text{A.20})$$

where $\alpha = A(2m)^{5/2}/\pi\hbar^4$.

From the $Y_1(k)$ moment of the transport equation, the value of g_1 up to first order terms in E is found to be

$$g_1 \simeq -2eE \tau_{\text{eff}} (2\pi\epsilon_k/3m)^{1/2} f_0',$$

and thus, from (A.20)

$$\frac{g_0}{(4\pi)^{1/2}} \simeq - \frac{(eE)^2 \tau_{\text{eff}}}{3\alpha m \epsilon_k^{1/2}} f_0', \quad (\text{A.21})$$

in the limit of small α ; $1/\tau_{\text{eff}} = 1/\tau_1 + 1/\tau_1^p$. Eq. (A.21) is the steady state solution for g_0 and the non-linear terms in $\langle j \rangle$ are now (from (A.11))

$$\frac{4e^4 E^3}{9\pi^2} \left(\frac{2}{m} \right)^{1/2} \tau_{\text{eff}} \left[\frac{1}{2\alpha \epsilon_F^{1/2}} \frac{\partial}{\partial \epsilon} (\tau_{\text{eff}} \epsilon^{3/2})_{\epsilon = \epsilon_F} + \frac{4}{5} \frac{\partial}{\partial \epsilon} (\epsilon_F^{5/2} \tau_{\text{eff}} \tau_2)_{\epsilon = \epsilon_F} \right], \quad (\text{A.22})$$

which is to be compared with eq. (A.13) obtained in the absence of electron-phonon collisions. From (A.21), (A.6) and (A.10), up to quadratic terms in E , the mean squared current fluctuation is now

$$\begin{aligned} \langle (\Delta j_z)^2 \rangle &= \langle j_z^2 \rangle_{\text{equil}} + n \left(\frac{e^2 E \tau_{\text{eff}}}{m} \right)^2 \\ &+ n \left(\frac{e^2 E \tau_{\text{eff}}}{m} \right)^2 \left[-2 + \frac{1}{3\tau_{\text{eff}}} \left(\frac{1}{2\alpha \epsilon_F^{1/2}} + \frac{8}{5} \epsilon_F \tau_2' + 4\tau_2 \right) \right]. \end{aligned} \quad (\text{A.22})$$

The first two terms on the r.h.s. of (A.22) equal the r.h.s. of (A.1) which was derived by taking the collision term in the relaxation time approximation. To make an order of magnitude estimate of the last term in squared brackets, we assume $\tau_2' = 0$, $\tau_2 \sim \tau_{\text{eff}}$, and for $C = 10$ eV, $\Delta = 10^{-21}$ cm³, $(\alpha \epsilon_F^{1/2})^{-1}$ also turns out to be of the order of τ_{eff} for a mean free path l_0 of 10 Å given by $l_0 = \tau_{\text{eff}} v_f$. So, the sum of the three terms in the squared brackets is approximately zero. It is, therefore, quite adequate to restrict the collision term in the transport equation to the relaxation time approximation in calculating the mean squared current fluctuation.

References

- [1] G. Feher and M. Weissman, Proc. Natl. Acad. Sci. 70 (1973) 870.
- [2] P. Wissmann, Springer Tracts in Modern Physics, Vol. 77, Surface Physics (Springer, Berlin, 1975) p. 1.
- [3] M.R. Shanabarger, Solid State Commun. 14 (1974) 1015.
- [4] H. Fuchs, Proc. Cambridge Phil. Soc. 34 (1938) 100.
- [5] M.R. Shanabarger, Surface Sci. 44 (1974) 297.
- [6] D. Lichtman, F.N. Simon and T.R. Kirst, Surface Sci. 9 (1968) 325; 12 (1968) 299.
- [7] J. Lapujoulade and K.S. Neil, J. Chem. Phys. 57 (1972) 3535; Surface Sci. 35 (1973) 288.
- [8] T.G. Kurtz, J. Appl. Prob. 7 (1970) 49; 8 (1971) 344.
- [9] R.F. Fox, Phys. Rept. 48 (1978) 179.
- [10] A.H. Wilson, The Theory of Metals, 2nd ed. (Cambridge Univ. Press, 1953) p. 258.

AN ANGLE-RESOLVED PHOTOEMISSION SPECTROSCOPY STUDY OF CHALCOGEN MONOLAYERS ON Cu(100) +

D.T. LING *,
I. LINDAU and
Stanford Elect

Received 11 Sep

Starting with a clean surface, the (2×2) O overlayers were examined in the photoemission spectra. Changes were found in the momentum of the scattered electrons and the relaxation of the d-bands was observed. The attenuation of the photoemission spectra along the $\bar{\Gamma}$ direction was clearly detected. The d-bands were observed in the bulk [011] direction.

1. Introduction

In the previous paper [1], the photoemission spectra of a clean surface of Cu(100) were described. The results were compared to accurately measured photoemission spectra. The data were found to well with the bulk self-consistent

* Present address:
10598, USA.

D. TRANSPORT AND DIFFUSION

The main achievements of these studies are:

1. Further development of the theory of rates of diffusion controlled catalytic reactions on surfaces. The structure dependence of unimolecular and bimolecular reactions has been analytically evaluated.
2. A review article on "Transport and Reaction on Surfaces: A Stochastic Approach" to be published in "Surface Reactions", Edited by U. Landman (AIP, N.Y., 1980) has been written.
3. Using our method of continuous-time random walks with internal states the effect of temporal and spatial correlations on transport and conductivity in superionic conductors has been analyzed. Saturation of the conductivity, at large frequencies, below the D.C. level (observed in AgI) due to a caterpillar mechanism is obtained.
4. A study of surface transport which may involve participation of subsurface channels of migration has been initiated. A formalism which combines the principles of the stochastic treatment of diffusion developed by us with the continued fraction method for the calculation of a Green's function is being developed.
5. Using the method mentioned in (4) a calculation of $S(\vec{k}, \omega)$ for incoherent quasi-elastic neutron scattering from hydrogen diffusing in thin film is being performed, and modifications in line-shapes due to differences between surface and subsurface diffusion are analyzed.

TRANSPORT AND REACTION ON SURFACES:
A STOCHASTIC APPROACH*

Michael F. Shlesinger and Uzi Landman
School of Physics, Georgia Institute of Technology
Atlanta, Georgia 30332

I. INTRODUCTION

In recent years surface physics has received a resurgent interest because of its importance in fields such as heterogeneous catalysis, thin film and crystal growth, interfacing electronic devices, and photovoltaic cells. Essential to this renewed interest in surface physics has been the advent of new and improved experimental techniques which enable detailed investigation of structure (geometrical, electronic and vibronic) and reaction processes under well controlled conditions.

It is convenient to describe surface reactions in terms of "elementary processes" such as adsorption, desorption, migration, dissociation and association. The fundamental understanding of each of the above steps comprises rather broad fields of study. In this paper we will concentrate on the migration or diffusion step and on some aspects of certain diffusion controlled reactions on surfaces. Basic knowledge of these processes which would enable the optimization of the parameters of catalytic materials, requires an understanding on a microscopic level. Recent developments and refinements of measurement techniques, such as Field Ion Microscopy (FIM) and Field Emission Microscopy (FEM) serve as the impetus for the development of theoretical microscopic models and refined methods of data analysis. In Section II we will review recent developments in the analysis of FIM diffusion experiments. These new methods when applied to the analysis of experimental data provide a spectroscopy of the migration mechanism, i.e. allow the detailed determination of kinetic parameters (frequency factors and activation energies) corresponding to elementary steps of the diffusion process. The recent direct observations using FIM of the diffusion of adatom clusters where the migration of the cluster proceeds via alternating spatial configurations (internal states of the cluster), provide data which when properly analyzed yields the above mentioned spectroscopy.

Our basic approach employs stochastic techniques. While single particle diffusion is described commonly in terms of a random walk process, a generalization of the formalism is needed in order to describe complex diffusion mechanisms, and diffusion in defective systems. Propagating systems may be endowed with internal states which may represent spatial configurations, mobile and immobile states, spin states, different band components in a Wannier site localized representation or even a temporal correlation memory.

*Supported by DOE Grant No. EG-77-S-05-5489

Mapping the internal states onto a random walk lattice and using matrix Green's function techniques enables us to analyze such complex systems. These methods and their generalization to periodically defective lattices by introducing supercell Green's function are described in Section II.

In Section III we present a different approach to studying diffusion on defective lattices which has computational advantages (particularly for small defect concentrations) over the method described in Section II. The method is based on a defect renormalized Green's function.

Kinetics of unimolecular and bimolecular diffusion controlled reactions on surfaces, catalyzed by active sites is the subject of Section IV. The reaction rate which appears in the master equation description of the reaction is expressed as the conditional probability first passage time density which is related to the more well known first passage time density. The reaction rate is related to the probability distributions governing migration on the surface which reflects the geometrical structure and potential surface. It is found that the reaction rate is in general time dependent, approaching a constant value at long times, and that it depends on the atomic arrangement at the surface. The structural dependence of the rates can become quite pronounced for a low concentration of active sites.

Finally in Section V we propose an explanation to a puzzle in heterogeneous catalysis. The bimolecular reaction of the disproportionation of propylene on the surface of a catalyst is seen to have a reaction rate maxima as a function of temperature. However, thermodynamic inequalities which must be satisfied for a rate maxima to occur are violated by the experimental data. We show how the thermodynamic inequalities may be satisfied if multistate diffusion mechanisms, such as described in Section II and III, are assumed.

The unifying feature to our treatment of the above studies of diffusion and reaction on surfaces is a stochastic description via random walk lattice Green's function propagators.

II. PARTICLE AND CLUSTER MOTION ON IDEAL AND DEFECTIVE SURFACES: GREEN'S FUNCTION WITH INTERNAL STATES METHOD

In order to analyze diffusion controlled reactions, as we do in Sections IV and V, we must first discuss the process of diffusion on a surface. The diffusive motion of adatoms and clusters of adatoms on surfaces has been dramatically revealed by Field Ion Microscope (FIM)¹⁻⁵ studies. Field Ion Microscopy which was conceived and developed by E. W. Müller in the early 1950's was used first for the investigation of adatom migration on surfaces by Ehrlich and Hudda⁶ in 1966. Later studies revealed that adatoms on metal surfaces can become correlated to move as a single cluster.⁷⁻¹⁶ One example we will analyze in detail is the motion of rhenium dimers on a W(211) surface⁷.

The FIM is, under certain conditions, able to give images from which one can determine the distance traveled by an adatom in a time t at a temperature T . For example, the motion of a single tungsten adatom on a W(211) surface is seen to occur⁶ (away from boundaries) as a one dimensional random walk with symmetric nearest neighbor hopping. Standard random walk theory gives for the mean squared displacement, $\sigma^2(t)$, after a time t ,

$$\sigma^2(t) = \lambda L^2 t \quad (2.1)$$

where λ is the hopping transition rate, L is the lattice spacing, and $\sigma^2(t)$ can be obtained from FIM pictures. The transition rate λ is seen to be in the Arrhenius form

$$\lambda = \nu \exp(-E/kT) \quad (2.2)$$

since a semilog semilogarithmic plot of $\sigma^2(t)L^2t$ vs. $1/kT$ yields a straight line of slope $-E$ and ordinate intercept $\log \nu$. Thus, an analysis of the FIM pictures can yield the activation energy, E , for diffusion, as well as, the frequency factor ν . We will now discuss how the maximum amount of information can be extracted from FIM data when the motion of a cluster occurs and several transition rates are involved. This will lead us to the study of random walks with several internal states.

The nature of the motion of a cluster on a surface depends on the substrate composition and morphology as well as on the type and number of atoms in the cluster. For example rhenium dimers⁷ are seen to undergo one dimensional motion on W(211) by alternating between straight and staggered configurations as shown in Fig. 1. If only one staggered position is allowed the center of mass motion of the dimer can be mapped onto a perfect lattice with two states per unit cell (Fig. 1b), and the motion is characterized by the transition rates, a, α, b , and β . If there is no bias caused by say, an external electric field then $\alpha = a$ and $b = \beta$. We express the rates in activated form,

$$\begin{aligned} a &= \nu_a \exp[(-E_a + V)/kT] , \\ \alpha &= \nu_a \exp[(-E_a - V)/kT] , \end{aligned} \quad (2.3)$$

As seen, a and α are not independent quantities even in the presence of a biasing electric potential V . Thus the dimer motion in Fig. 1b is characterized by only two transition rates. If a third more extended (non-dissociated) state is allowed then the center of mass motion can be mapped onto a lattice with three states per unit cell (two of which overlap) as shown in Fig. 1c. The motion is then characterized by the four transition rates a, b, c , and d . If the dimer can move in two dimensions then the center of mass motion can be mapped onto a two-dimensional lattice, as shown in Fig. 2., characterized by four transition rates, i.e, four activation energies

and four frequency factors.

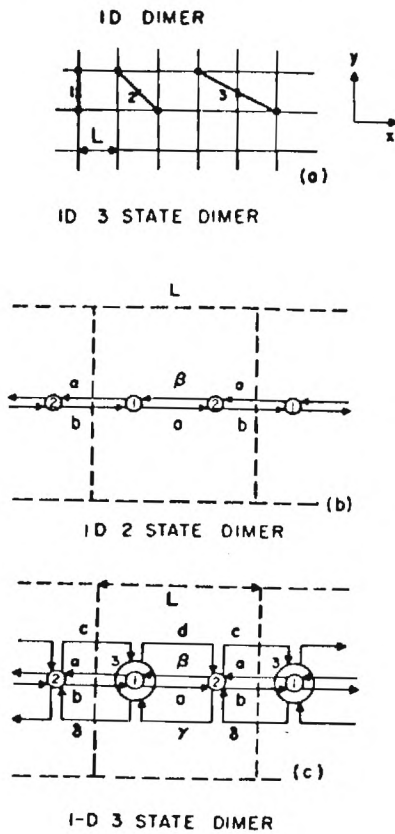
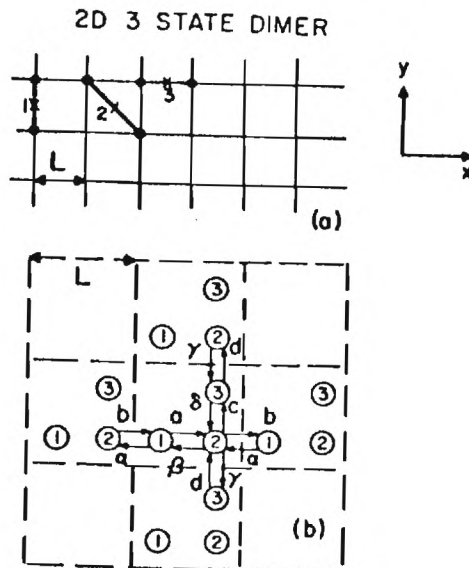


FIG. 1. One-dimensional dimer migration. (a) Three possible spatial configurations of a dimer (filled circles connected by heavy line) moving along the x direction (the allowed equivalent mirror-image configurations are not included): if only states 1 and 2 are allowed, a 2-state dimer; if all states are allowed, a 3-state dimer. The location of the dimer centroid is marked X. (b) Random-walk lattice describing the motion of the centroid of a 2-state dimer in (a). The unit cell is denoted by numbered circles. Lettered arrows indicate transitions to and from states. Note that transition rates connecting states can be different for transitions to the left or right (i.e., $a = \alpha$, $b = \beta$). (c) Random-walk lattice for the 3-state dimer shown in (a). Note that the centroid location is the same for states 1 and 3; however, they are distinguished by different transition rates.

FIG. 2. Two-dimensional dimer migration: (a) spatial configurations; (b) random-walk lattice.



Mathematical Formalism of Random Walks with Internal States

We will now develop the mathematical formulation of random walks on these lattices with internal states and show how to relate the unknown transition rates in terms of the known FIM observables such as diffusion distances and equilibrium occupation probabilities of the different internal states. Our generating (Green's) function analysis will be based on the semi-Markov continuous time random walk of Montroll and Weiss¹⁷ and its generalizations.¹⁸⁻²³ In addition this approach has been shown to be equivalent to a generalized master approach.²⁴

In the course of our study many probabilistic quantities will be introduced in order to calculate the values of FIM observables. Let us first introduce $R_{ij}(\vec{\ell}, t | \vec{\ell}_0)$ which is the probability density for reaching site $\vec{\ell}$ in internal state i , $(\vec{\ell}, i)$, exactly at time t given that $(\vec{\ell}_0, j)$ was attained at $t=0$. This quantity satisfies the following recursion relation²⁰, and identifies R as a Green's function propagator

$$R_{ij}(\vec{\ell}, t | \vec{\ell}_0) = \sum_{\vec{\ell}'} \sum_m \int_0^t \psi_{im}(\vec{\ell}-\vec{\ell}', \tau) R_{mj}(\vec{\ell}, t-\tau | \vec{\ell}_0) dt + \delta_{\vec{\ell}, \vec{\ell}_0} \delta_{ij} \delta(t) \quad (2.4)$$

where $\psi_{im}(\vec{\ell}, t)$ is the probability density that at time t a single jump occurs from $(0, m)$ to $(\vec{\ell}, i)$ given that the state $(0, m)$ was attained at $t=0$. If there are s internal states then \underline{R} and $\underline{\Psi}$ are $s \times s$ matrices and in matrix notation Eq. (2.4) becomes

$$\underline{R}(\vec{\ell}, u | \vec{\ell}_0) - \sum_{\vec{\ell}'} \underline{\Psi}(\vec{\ell}-\vec{\ell}', u) \underline{R}(\vec{\ell}', u | \vec{\ell}_0) = \delta_{\vec{\ell}, \vec{\ell}_0} \underline{1} \quad (2.5)$$

where we have Laplace transformed over time ($t \rightarrow u$). To proceed further one must examine the waiting time density matrix $\underline{\Psi}$. We write

$$\psi_{ij}(\vec{\ell}, t) = p_{ij}(\vec{\ell}) \psi_j(t) \quad (2.6)$$

where $\psi_j(t)$ is the probability density that a transition occurs at time t from an internal state j which was attained at time $t=0$. To keep a matrix notation we treat ψ_j as the jj element of a diagonal matrix. The probability that this jump goes into an internal state i is given by $p_{ij}(\vec{\ell})$. Using Eq. (2.5) in Eq. (2.6) and Fourier transforming ($\vec{\ell} \rightarrow \vec{k}$) over all lattices sites $\vec{\ell}$ we arrive at in matrix notation

$$\underline{R}(\vec{k}, u | \vec{\ell}_0) = [\underline{1} - \underline{p}(\vec{k}) \underline{\Psi}(u)]^{-1} \exp(+i\vec{k} \cdot \vec{\ell}_0) \quad (2.7)$$

where the Fourier transform and its inverse are defined in Appendix A. In our notation, functions of u have always been Laplace transformed over time, and functions of \vec{k} have been Fourier transformed over the lattice space.

The probability for being at (\vec{l}, i) at time t , $P_{ij}(\vec{l}, t | \vec{l}_0)$ when the stochastic process began at (\vec{l}_0, j) is related to $R_{ij}(\vec{l}, t | \vec{l}_0)$ by

$$P_{ij}(\vec{l}, t | \vec{l}_0) = \int_0^t R_{ij}(\vec{l}, t-\tau | \vec{l}_0) \left[\int_{\tau}^{\infty} \psi_i(\tau') d\tau' \right] d\tau \quad (2.8)$$

$$\equiv \int_0^t R_{ij}(\vec{l}, t-\tau | \vec{l}_0) \phi_i(\tau) d\tau$$

where the factor ϕ takes into account that the system may have reached (\vec{l}, i) at an earlier time $t-\tau$, and no transition out of (\vec{l}, i) occurs in the remaining time τ .

All the quantities one wishes to calculate are derivable from $P_{ij}(\vec{l}, t | \vec{l}_0)$ which in turn only depends on $\psi_{ij}(\vec{l}, t)$ as can be seen from Eqs (2.7) and (2.8). We choose $\underline{\psi}$ to be normalizable, i.e.,

$$\sum_{\vec{l}} \sum_{i,j} P_{ij}(\vec{l}) = 1, \quad \int_0^{\infty} \psi_i(\tau) d\tau = 1 \quad (2.9)$$

We now show how to calculate positional moments and equilibrium occupation probabilities from a knowledge of $\underline{\psi}$.

The positional moments of the probability distribution are given by

$$\langle l_r^n(t) \rangle = \sum_{\vec{l}} \sum_{i,j} (\vec{l}_r)^n P_{ij}(\vec{l}, t | 0) f_i \quad (2.10)$$

where f_i is the probability that an internal state j is occupied initially. Since from Eq. (2.8)

$$\underline{P}(\vec{k}, t) = \mathcal{L}^{-1} \left\{ u^{-1} [1 - \underline{\psi}(u)] \sum_{\vec{l}} e^{i\vec{k} \cdot \vec{l}} \underline{R}(\vec{l}, u) \right\} \quad (2.11)$$

where \mathcal{L}^{-1} is the inverse transform and $r=x, y$, or z , we see that Eq. (2.10) can be rewritten as

$$\langle l_r^n(t) \rangle = \lim_{k \rightarrow 0} \mathcal{L}^{-1} \left\{ (-i)^n \sum_{i,j} \partial^n R_{ij}(\vec{k}, u | 0) / \partial k_r^n \right. \\ \left. u^{-1} [1 - \psi_i(u)] f_i \right\} \quad (2.12)$$

where $\underline{R}(\vec{k}, u|0)$ is given in terms of $\underline{\Psi}$ in Eq. (2.7).

Note that the matrix \underline{R} is the inverse of the matrix $[1 - \underline{p}(\vec{k})\underline{\Psi}(u)]$ (see Eq. 2.7). Performing the matrix inversion we write \underline{R} as

$$\underline{R}(\vec{k}, u) = \underline{M}(\vec{k}, u) \Delta^{-1}(\vec{k}, u) \quad (2.13)$$

where Δ is the determinant of the cofactors in \underline{M} . All the physical quantities we will be interested are in the $t \rightarrow \infty$ limit and will only involve \underline{R} and its derivatives in the limit of both \vec{k} and u going to zero. In this limit²⁶ the elements of \underline{M} will approach constants, while Δ will diverge as u^{-1} . Thus $\partial^2 \underline{R} / \partial k^2$ in Eq. (2.12) (which enters the calculation of the variance $\sigma^2(t)$) will diverge as u^{-2} causing the mean squared displacement of the random walker to grow linearly with time as was given in Eq. (2.1). This is the standard diffusion limit ($t \rightarrow \infty$) result. It can be shown²⁶ that in the diffusion limit Eq. (2.12) for $\sigma^2(t)$ reduces to

$$\begin{aligned} \sigma^2(t) &= \langle \ell^2(t) \rangle - \langle \ell(t) \rangle^2 \\ &= \lim_{u \rightarrow 0} \lim_{k \rightarrow 0} \frac{u^2}{\Delta^2} \frac{\partial^2 \Delta}{\partial k^2} t \end{aligned} \quad (2.14)$$

Thus one only needs to calculate Δ and one does not have to perform the tedious matrix inversion to calculate \underline{M} .

Another quantity of interest which can be obtained from FIM data on cluster motion by simply counting the number of micrographs in which the cluster is found in the various spatial configurations is the equilibrium probability of occupying an internal state j , P_j , eq. This quantity is defined as

$$P_{j, \text{eq.}} = \lim_{t \rightarrow \infty} \sum_i \sum_{\vec{\ell}} P_{ji}(\vec{\ell}, t|0) f_i. \quad (2.15)$$

The RHS can be written in Laplace space as

$$P_{j, \text{eq.}} = \lim_{t \rightarrow \infty} \sum_i \sum_{\vec{\ell}} u P_{ji}(\vec{\ell}, u|0) f_i.$$

Since $\lim_{k \rightarrow 0} P_{ji}(\vec{k}, u|0) = \sum_{\vec{\ell}} P_{ji}(\vec{\ell}, u|0)$, we can express P_j , eq. as

$$P_{j, \text{eq.}} = \lim_{u \rightarrow 0} \lim_{k \rightarrow 0} \sum_i R_{ji}(\vec{k}, u|0) [1 - \psi_j(u)] f_i$$

Except in extreme cases where the mean time to make a transition between states is infinite, R_{ji} will not depend on the initial state i so

$$P_{j,eq} = \lim_{u \rightarrow 0} \lim_{k \rightarrow 0} R_{ji}(\vec{k}, u | 0) [1 - \psi_j(u)] \quad (2.16)$$

Dimer Diffusion in 1D

The set of transition rates $\{a\}$ connecting the different internal states of a cluster are assumed to be in an activated form, $a = v_a \exp(-E_a/kT)$.

To find all the individual activation energies and frequency factors characterizing the diffusion we need to consider a random walk with internal states.

Consider first the two state dimer in Fig. 1. The effect of a bias can be incorporated by choosing $a \neq \alpha$, $b \neq \beta$. The total rate of leaving state 1 is $A = a + \alpha$, and the probability that the transition is to the right is a/A , and the probability that the transition is to the left is α/A . We choose $a = \alpha$, $b = \beta$. The waiting time density matrix is then given by

$$\underline{\Psi}(\ell, t) = \begin{pmatrix} 0 & \frac{1}{2}B \exp(-Bt) (\delta_{\ell,0} + \delta_{\ell,1}) \\ \frac{1}{2}A \exp(-At) (\delta_{\ell,0} + \delta_{\ell,-1}) & 0 \end{pmatrix} \quad (2.17)$$

where if the transition is within the unit cell ℓ does not change value, and it changes by $\pm L$ depending on whether the transition moves the dimer centroid to the unit cell on the right or the left. We will measure lengths in units of the unit cell size L . The matrix \underline{R} is given by, from Eq. (2.7),

$$\underline{R}(k, u) = \underline{M}/\Delta = \left[1 - \frac{1}{2} \frac{AB}{(A+u)(B+u)} (1 + \cos kL) \right]^{-1} \times \begin{pmatrix} 1 & \frac{1}{2} \frac{B}{B+u} (1 + e^{ikL}) \\ \frac{1}{2} \frac{A}{A+u} (1 + e^{-ikL}) & 1 \end{pmatrix} \quad (2.18)$$

In the diffusion limit ($t \rightarrow \infty$) using Eq. (2.14) we find

$$\sigma^2(t) = \frac{1}{2} L^2 \frac{AB}{A+B} t = L^2 \frac{ab}{a+b} t \quad (2.19)$$

From the knowledge of $\underline{\Psi}$, detailed balance relations, Eq. (2.16) can be calculated to give

$$\frac{P_{1, \text{eq}}}{P_{2, \text{eq}}} = \frac{b}{a} \equiv R_{12}(T) \quad (2.20)$$

Eqs. (2.19) and (2.20) allow us to solve for the individual rates, i.e.,

$$v_a \exp(-E_a/kT) = a = L^{-2} t^{-1} \sigma^2(t) [1+R_{12}(T)] \quad (2.21a)$$

$$v_b \exp(-E_b/kT) = b = L^{-2} t^{-1} \sigma^2(t) [1+R_{12}(T)]^{-1} \quad (2.21b)$$

Experimentally $\sigma^2(t)$ and $P_{1, \text{eq.}}(T) = 1 - P_{2, \text{eq.}}(T)$ are measurable and $L^2 t$ is known. Thus, a semilogarithmic plot^{eq} of the RHS of Eq. (2.21a) vs. $1/kT$ would yield a straight line of slope $-E_a$, and ordinate intercept $\log v_a$. Similarly, the same plot for Eq. (2.21b) would yield E_b and v_b . Note, that for this case merely plotting $\log \sigma^2(t)$ vs. $1/kT$ (where $\sigma^2(t)$ is the variance of the dimer centroid position), does not allow the determination of E_a, v_a, E_b and v_b . Such a plot would in fact yield a "curved" Arrhenius line as can be seen by substituting activated forms for a and b in Eq. (2.19) for $\sigma^2(t)$. However, in a limited temperature range a plot of $\log \sigma^2(t)$ vs. $1/kT$ may appear to be a straight line, but its slope and intercept will not characterize the individual transition rates of the dimer motion. We emphasize that full use of all the FIM data such as both $\sigma^2(t)$ and detailed balance relations $R_{12}(T)$ must be employed to calculate the individual dimer transition rates. Reed and Ehrlich¹⁰ have also obtained Eq. (2.19) for the positional variance using Kolmogorov birth and death equations for the study of dimer motion. In a later paper⁷ pertaining to the motion of rhenium dimers on W(211) Graham, Stolt, and Ehrlich find $a = 17.5 \pm 4$ kcal/mole, while $b = 18.2 \pm 3$ kcal/mole, where as by just plotting $\log \sigma^2(t)$ for the dimer centroid vs. $1/kT$ yields a "straight line" with slope 18.0 ± 3 kcal/mole. This demonstrates the spectroscopic kinetic information available from such studies. We note that our matrix continuous-time random walk approach can be applied to a system with any number of states per unit cell, even if different states of the cluster have the same center of mass. This point was an obstacle to extending the approach of Reed and Ehrlich.¹⁰

Three State Dimer in 1D

We now consider the last case in Fig. 1 where the dimer is allowed to extend into a third (non-dissociative) state which we term the extended state. Note that the center of mass of the dimer is the same for states 1 and 3 and thus states 1 and 3 coincide spatially but are distinguished by the different transition rates connecting

them to state 2. Two new transition rates, c and d , are introduced to give us a total of four independent transition rates. We now inquire, "Is there sufficient FIM data to determine all four rates?" We can derive one equation for $\sigma^2(t)$, and two other independent detailed balance equations for $R_{12}(T)$ and $R_{23}(T)$. To obtain a fourth equation the diffusion experiment must be done under the influence of an electrical bias so the first spatial moment $\langle \ell(t) \rangle$ is non-vanishing. Such experiments have been performed by Tsong and Walko.²⁵ Thus the amount of information one wishes to extract from the data will determine what type of experiment should be undertaken. The solution for each of the four individual transition rates in terms of the FIM observables ($\sigma^2(t)$, $\langle \ell(t) \rangle$, $R_{12}(T)$, $R_{23}(T)$) has been given in reference 21, along with other examples, including diffusion on periodically defective lattices. The defects can be partially reflecting or absorbing or may just be described by different transition rates. The method used²¹ to include periodic defects was to construct identical super unit cells so that each of them contained the same defect structure. For example, in 1D consider the motion of a single adatom on a lattice with every n -th site being defective (e.g. described by a different transition rate from a normal site). We would construct identical unit cells (see Fig. 3) and a corresponding $n \times n$ matrix $\underline{\Psi}$ and use the internal state method of analysis described above. However, this can become difficult for large n and thus we present in the next section an alternative renormalization method.

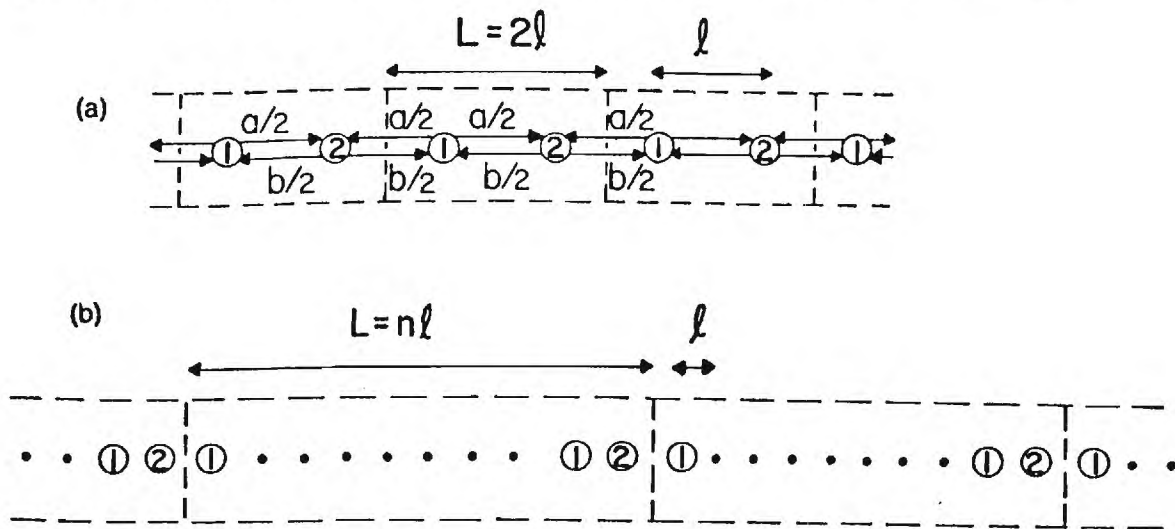


FIG. 3 (a) A 1D random-walk lattice with two alternating states is shown. The distance between sites 1 and 2 is l , and the unit cell (dashed lines) has length $2l$. The total rates of leaving states 1 and 2 are a and b , respectively. The probabilities of going to the left or right from states 1 or 2 are $1/2$. The lattice may represent the centroid positions of a dimer performing a 1D "channeled" motion on a

crystalline surface [e.g., W. dimer on a W(211) surface, or a 1D ordered, alternating two-component system. The random motion is solved by two methods. First, the lattice is treated as having two states per unit cell and 2×2 Green's-function propagator is derived. An alternative approach treats state 2 as a periodically occurring defect, and a defect-renormalized scalar Green's-function propagator is derived. (b) The defects (state 2) are now spaced a distance $n\ell$ apart. In the text, it is shown that the defect-renormalized-propagator solution is much simpler than the $n \times n$ matrix internal-state approach.

III. MOTION ON DEFECTIVE SURFACES: RENORMALIZED GREEN'S FUNCTION METHOD

In this section we develop an alternative to the internal state supercell approach to random walks on defective lattices.^{22,26,27} The fact that we only treat periodically placed defect does not render the model inapplicable to physical situations. It pertains to a.c. conductivity in ordered overlayer assemblies²⁸, transport in alloy or multicomponent systems, and ordered overlayer adsorption systems.²⁹ The results are shown to be similar to the average T-matrix approximation for diffusion in the presence of a low concentration of randomly placed defects.^{30,31} The coherent potential approximation may also be used for randomly placed low defect concentrations.³²

We return to the original Green's function equation (2.4) and treat the effects of defects as inhomogeneities rather than as extra internal states. Consider the case in 1D periodically placed defects spaced n lattice sites apart (see Fig. 3). The normal sites are characterized by

$$\psi(\ell, t) = \psi_0(t) p(\ell) = A \exp(-At)^{1/2} (\delta_{\ell,1} + \delta_{\ell,-1}) \quad (3.1)$$

and defect sites differ only by changing the transition rate from A to D , i.e.,

$$\psi_d(\ell, t) = \psi_d(t) p(\ell) = D \exp(-Dt)^{1/2} (\delta_{\ell,1} + \delta_{\ell,-1}) \quad (3.2)$$

Only nearest neighbor jumping is allowed. Eq. (2.4) becomes (when Laplace transformed over time) for a walker beginning at $\ell=0$,

$$\begin{aligned} R(\ell, u) &= \sum_{\ell'} p(\ell-\ell') \psi_0(u) R(\ell', u) - \delta_{\ell,0} \\ &= \sum_{j=-\infty}^{\infty} p(\ell-nj) \left\{ \psi_d(u) - \psi_0(u) \right\} R(nj, u) \end{aligned} \quad (3.3)$$

where the LHS represents propagation on an ideal lattice and the RHS is non-zero only for terms which involve transitions from a defect.

We wish to solve for $R(k,u)$. The solution to the ideal lattice problem in Fourier space (k) and Laplace space (u) is given by

$$\begin{aligned} R_0(k,u) &= [1-p(k)\psi_0(u)]^{-1} \\ &= [1-\cos(k)\psi_0(u)]^{-1} \end{aligned} \quad (3.4)$$

Fourier transforming Eq. (3.3) we obtain

$$[R_0(k,u)]^{-1} R(k,u) = 1 + p(k) [\psi_d(u) - \psi_0(u)] \sum_{j=-\infty}^{\infty} e^{iknj} R(nj,u) \quad (3.5)$$

Using the calculation of partial discrete Fourier transforms from Appendix A (Eqs. (A-3) and A-6)) we find the sum on the RHS of Eq. (4.5) can be written as

$$\frac{1}{n} \sum_{m=0}^{n-1} R(k + m \frac{2\pi}{n}, u) \quad (3.6)$$

where the first argument of R is calculated modulo 2π and $0 \leq k \leq 2\pi$. next write the defect term $D(k,u)$ as

$$D(k,u) = p(k) [\psi_d(u) - \psi_0(u)] . \quad (3.7)$$

For small u (long times) note that

$$D(k,u) \sim u \cos k [A^{-1} - D^{-1}] + O(u^2) \quad (3.8)$$

Using the notation

$$L(k,u) = [R_0(k,u)]^{-1} R(k,u) - 1 \quad (3.9)$$

Eq (4.5) becomes

$$L(k,u) = n^{-1} D(k,u) \sum_{m=1}^{n-1} R(k + m \frac{2\pi}{n}, u) . \quad (3.10)$$

Let us first consider k values in the first "Brillouin zone" denoted by K , such that $0 \leq K \leq \frac{2\pi}{n}$. Since

$$L(K + m \frac{2\pi}{n}, u) = n^{-1} D(K + m \frac{2\pi}{n}, u) \sum_{j=0}^{n-1} R(K + \frac{2\pi}{n}, u) \quad (3.11)$$

the $L(k,u)$ function for all values of k , ($0 \leq k \leq 2\pi$) and thus $R(k,u)$ can be related to $L(K,u)$ evaluated just in the first Brillouin zone by

$$L(K + m \frac{2\pi}{n}, u) = D(K + m \frac{2\pi}{n}, u) D^{-1}(K, u) L(K, u) \quad (3.12)$$

for $m = 0, 1, \dots, n-1$

and where $D(k, u)$ is easily evaluated for any k .

We now write $R(k = K + m \frac{2\pi}{n}, u)$ from Eq. (3.9) in terms of known quantities $D(k, m)$ and $R_0(k, u)$ evaluated just in the first Brillouin zone using Eq. (3.12)

$$\begin{aligned} R(K + m \frac{2\pi}{n}, u) &= R_0(K + m \frac{2\pi}{n}, u) [L(K + m \frac{2\pi}{n}, u) + 1] \\ &= R_0(K + m \frac{2\pi}{n}, u) [D(K + m \frac{2\pi}{n}, u) D^{-1}(K, u) L(K, u) + 1] \end{aligned} \quad (3.13)$$

Summing both sides of Eq. (3.13) from $m = 0, \dots, n-1$ we find

$$\begin{aligned} \sum_{m=0}^{n-1} R(K + m \frac{2\pi}{n}, u) &= R(K, u) \\ &+ \sum_{m=1}^{n-1} R_0(K + m \frac{2\pi}{n}, u) [D(K + m \frac{2\pi}{n}, u) D^{-1}(K, u) \\ &\times \{ [R_0(K, u)]^{-1} R(K, u) - 1 \} + 1] \end{aligned} \quad (3.14)$$

where the $m=0$ term has been separated from the sum on the RHS. Using Eq. (3.11) with $m=0$ the LHS of Eq. (3.14) can also be expressed in terms of $R(K, u)$. Thus one can solve for $R(K, u)$ in the first Brillouin zone and relate $R(K + m \frac{2\pi}{n}, u)$ to $R(K, u)$ using Eq. (3.12). The result is

$$R(K, u) = W^{-1}(K, u) V(K, u) \quad (3.15a)$$

where

$$\begin{aligned} W(K, u) &= [(R_0(K, u))^{-1} - n^{-1} D(K, u)] \\ &- n^{-1} (R_0(K, u))^{-1} \sum_{m=1}^{n-1} R_0(K + m \frac{2\pi}{n}, u) D(K + m \frac{2\pi}{n}, u) \end{aligned} \quad (3.15b)$$

and

$$V(K, u) = 1 + n^{-1} \sum_{m=1}^{n-1} \left(R_0(K + m \frac{2\pi}{n}, u) \left[D(K, u) - D(K + m \frac{2\pi}{n}, u) \right] \right) \quad (3.15c)$$

Note that $R_0(k,u) = [1 - \psi(u) \cos k]^{-1}$ diverges in the $u \rightarrow 0$ and $k \rightarrow 0$ limits only as u^{-1} , and that $D(k,u) \rightarrow u$ for small u (see Eq. (3.8)). The propagator $R_0(K + m \frac{2\pi}{n}, u)$ for $m \neq 0$ does not diverge. Thus all the terms in Eq. (3.15) do not contribute in the diffusion limit. As $u \rightarrow 0$, $k \rightarrow 0$ the reduced expression becomes in the diffusion limit.

$$R(K,u) = \{ [R_0(K,u)]^{-1} - \frac{1}{n} D(K,u) \}^{-1} \quad (3.16)$$

We see that the effect of the defects is to renormalize the Green's function propagator $R_0(k,u)$ to $R(K,u)$ as in Eq. (3.15). In the long time limit ($u \rightarrow 0$) the renormalization is a simple "self-energy" term

$$n^{-1} D(K,u) = n^{-1} \cos k [u(D-A)] / [(A+u)(D+u)] ,$$

In a previous publication we omitted the sum in Eq. (A.5) and kept only the $m=0$ term, which led us directly to Eq. (3.16) rather than Eq. (3.15). We thank Dr. Harvey Scher and Dr. C. H. Wu for pointing this out to us. In a preprint they have considered random walks on lattices with periodic defects along with a temperature dependent defect to defect hops instead of just nearest neighbor hops. This is shown to lead to different channels of transport as a function of temperature.

Using the renormalized $R(K,u)$ we can calculate the variance as

$$\begin{aligned} \sigma^2(t) &= \int_0^t \sum_{\ell} \ell^2 R(\ell, t-\tau) \phi(\ell, \tau) d\tau \\ &= \sum_{\ell} \ell^2 \int_0^t R(\ell, t-\tau) \{ \phi_A(\tau) + [\phi_B(\tau) - \phi_A(\tau)] \delta_{\ell, nj} \} d\tau \\ &= -\ell^2 \mathcal{L}^{-1} \{ \partial^2 R(K,u) / \partial K^2 \Big|_{K=0} [\phi_A(u) + n^{-1}(\phi_B(u) - \phi_A(u))] \} \\ &= \frac{n AB}{A + (n-1)B} \ell^2 t \quad (3.17) \end{aligned}$$

where $\phi_{A,B}(u) = u^{-1} [1 - \psi_{A,B}(u)]$ has been used (see Eq. (2.8)). For $n \rightarrow \infty$ or $A=B$, (no defects), we obtain the perfect lattice result, Eq. (2.1), $\sigma_0^2(t) = A \ell^2 t$. If the transition rate A is known then one can solve for the defective transition rate B to find

$$\frac{A \sigma^2(t)}{A n \ell^2 t - (n-1) \sigma^2(t)} = v_B \exp(-E_B/kT) = B \quad (3.18)$$

Thus a semilogarithmic plot of the experimentally known quantities on the LHS vs. $1/kT$ will yield the activation energy and frequency factor characterizing the rate B . Note again that $\sigma^2(t)$ itself is not of the Arrhenius forms, and a plot of $\log \sigma^2$ vs. $1/kT$ will not allow a determination of A and B .

By treating the defects as inhomogeneities in our Green's function Eq. (3.3) we were able to calculate $R(K,u)$ as a scalar quantity.

In contrast, with the supercell method of Section II, we would need to use $n \times n$ matrices and their inverses. Unless special symmetries exist the calculations with $n \times n$ matrices can become prohibitive, thus showing the advantage in those cases of renormalized propagator method.

It is interesting to observe that to first order in the concentration of defects $C=n^{-1}$ the expansion of Eq. (4.17) yields

$$\sigma^2(t) = \sigma_0^2(t) \{1 - C[(v_B/v_A)e^{-(E_A-E_B)/kT} - 1]\} + O(C^2) \quad (3.19)$$

Which is similar to the effective diffusion constant in a system containing randomly placed defects as given by the average $-T$ -matrix approximation.^{30,31}

The renormalization procedure used for calculating the variance for the example in Eq. (3.17) is actually more general and applies to cases in higher dimensions where the structure factor $p(\vec{k})$ is different at defective sites and when the diffusant contains internal states (configuration, energetic, etc.) and a set of defects can be periodically repeated. When internal states are present the renormalization equations become matrix equations. The solution in Eq. (3.15) is already in the correct order for the proper matrix multiplication. Only the definition of the "self-energy" needs to be generalized to

$$\underline{D}(\vec{k}, u) = \sum_{\underline{d}} \left[p_{\underline{d}}(\vec{k}) \underline{\psi}_{\underline{d}}(u) - p_{\underline{o}}(\vec{k}) \underline{\psi}_{\underline{o}}(u) \right] \quad (3.20)$$

where the sum is over the set of periodically repeating defects. When $p_{\underline{d}}(\vec{k}) \neq p_{\underline{o}}(\vec{k})$ care must be exercised arriving at asymptotic results since now $D(\vec{k}=\underline{o}, u \rightarrow \underline{o}) \sim \text{constant}$ while if $p_{\underline{d}}(\vec{k})=p_{\underline{o}}(\vec{k})$ then $D(\vec{k}=\underline{o}, u \rightarrow \underline{o}) \sim u$.

Before we proceed to discuss certain aspects of diffusion controlled reactions we comment on an interesting result concerning the effect of defects (inhomogeneities) on the lattice structure dependence of the diffusion constant. In reference (26) we have studied particle and cluster motion on defective surfaces. In one example, we considered square (sq.) hexagonal (hex), and triangular (tri) lattices with equal bond lengths and equal defect concentrations. In addition we let the effect of the defects to extend to nearest-neighbor sites. Normal, defect, and defect nearest neighbor sites were ascribed transition rates A, D, and B respectively. It was found for single particle motion that the variances in position (and thus the diffusion constants) order as $\sigma_{\text{tri}}^2(t) \leq \sigma_{\text{sq}}^2(t) \leq \sigma_{\text{hex}}^2(t)$ when $B \leq A$, i.e., when the migration of the particle is slowed in the vicinity of the defect. It should be noted that this structural (lattice connectivity) dependence occurs only for diffusion on defective lattices in which the range of influence of the defects extends to at least nearest neighbors.

Studies of particle diffusion on surfaces containing defects are not abundant. Recently an FIM investigation of diffusion on a 3% R_e substituted W(100) surface was performed¹⁰, since defects are of importance in catalytic reactions on surfaces, either as promoters or inhibitors of migration, and in eight of the above results it is suggested that detailed studies of diffusion on such systems be carried out.

IV. DIFFUSION CONTROLLED REACTIONS ON SURFACES

In this section we examine closely the meaning of "reaction rate" as it appears in probabilistic master equation descriptions of chemical kinetics. We show that the reaction rate is a conditional probability density, and describe its evaluation for certain model systems using the formalisms outlined in the previous sections. An explicit example of a diffusion controlled bimolecular reaction is discussed in Section V.

Unimolecular Reactions: What is a Reaction Rate?

The evolution of many physical systems can be viewed as unimolecular, bimolecular, or pseudo-unimolecular (if from two reactive species one species is vastly more abundant than the other) reactions. Unimolecular decay reactions involve the irreversible loss of independent reactants. McQuarrie³⁴ has reviewed the master equation approach to unimolecular and bimolecular reactions. This stochastic approach allows the calculation of fluctuations, which deterministic equations do not. McQuarrie's solutions are in terms of rate constants, but he does not discuss how to calculate these rate constants from first principles. In this section, we show that the rate constants are conditional first passage (coincidence) probability densities and we relate them to the probability that the lifetime of a reactant is greater than a time t .

The master equation governing unimolecular decay is

$$dP(N,t)/dt = K(t)[P(N+1,t) - NP(N,t)] , \quad (4.1)$$

where N is a random variable representing the number of reactants which have not yet reacted (decayed). The solution of Eq. (4.1) for the mean is

$$\langle N(t) \rangle = N_0 \exp\left[-\int_0^t K(\tau) d\tau\right] \quad (4.2a)$$

where N_0 is the initial number of reactants, and $N(t)$ satisfies the equation

$$d\langle N(t) \rangle / dt = -K(t) \langle N(t) \rangle . \quad (4.2b)$$

The major task involved with Eq. (4.1) is to calculate the reaction rate $K(t)$ which contains all the physics of the reaction under study.

The quantity $K(t)$ is the conditional probability of a reaction occurring, of a particular reactant, in the interval $(t, t + dt)$, given that no reaction occurred in the interval $(0, t)$. We assume the stochastic process began at $t=0$. The quantity $K(t) dt$ says that the stochastic process began at $t=0$ and that at time t one has the information that the particular reactant of interest has not yet decayed, and then asks with what probability will the decay occur at time $t+dt$. Thus, $K(t)$ is a prediction at time t of what will happen at time $t+dt$, given the information that the reactant did not decay in $(0, t)$. The conditional first passage density $K(t)$ can be related to the unconditional first passage density $F(t)$. The quantity $F(t)dt$ says that the stochastic process began at time $t=0$ and then asks for the probability that the decay takes place in the interval $(t, t + dt)$. So $F(t)$ is a prediction at time $t=0$ of what will happen at time $t+dt$.

To calculate $K(t)$, we first define $P(L>t)$ to be the probability that the lifetime of a particle is greater than t , i.e., that the decay takes place in the interval (t, ∞) :

$$P(L>t) = \int_t^{\infty} F(\tau) d\tau \quad (4.3)$$

Now, $P(L>t + dt)$ can be written terms of a conditional probability

$$P(L>t + dt) = P[L>t + dt | \text{no decay in } (0, t)] P(L>t), \quad (4.4)$$

where the last factor on the RHS is the probability that no decay has occurred in the interval $(0, t)$. Dividing both sides of Eq. (4.4) by $P(L>t)$ and expanding $P(L>t + dt)$ in a Taylor series about t , we find

$$\begin{aligned} P[L>t + dt | \text{no decay in } (0, t)] \\ = 1 + dt(d/dt) \log P(L>t) + O(dt)^2 \end{aligned} \quad (4.5)$$

Now,

$$\begin{aligned} K(t)dt &\equiv P[L \leq t + dt | \text{no decay in } (0, t)] \\ &= 1 - P[L>t + dt | \text{no decay in } (0, t)] \end{aligned} \quad (4.6a)$$

or

$$\begin{aligned} K(t) &= -(d/dt) \log P(L>t) \\ &= F(t) / \int_t^{\infty} F(\tau) d\tau. \end{aligned} \quad (4.6b)$$

Using Eq. (4.6b) in (4.2a) yield the intuitive result

$$\langle N(t) \rangle / N_0 = \exp\left[- \int_0^t K(\tau) d\tau\right] = \int_t^{\infty} F(\tau) d\tau \quad (4.7)$$

and shows the connection between the unconditional and conditional first passage distributions.

We see that if $P(L > t) \sim \exp(-\lambda t)$ as $t \rightarrow \infty$, then $K(t) \rightarrow \lambda$, a constant. This is the reason why constant reaction rates can often be used in Eq. (4.1). Note that

$$K(t) = - (d/dt) \log(\langle N(t) \rangle / N_0), \quad (4.8)$$

which is similar in structure to Eq. (4.6b). In Eq. (4.8), one uses experimental results to find $K(t)$, while in Eq. (4.6), one uses assigned microscopic parameters to predict $K(t)$. Together, Eqs. (4.6) and 4.8) help allow for a determination of the microscopic parameters governing $K(t)$.

Calculation of a Diffusion Controlled Unimolecular Reaction Rate

Consider now the situation where Eq. (4.1) represents N_0 reactants per active site at $t=0$, and where there is one active site per V lattice sites. A reaction occurs at the instant when a reactant reaches an active site on our periodic lattice. We divide our system into identical unit cells each initially with N_0 reactants and a active site at the origin of a unit cell with V sites. Periodic boundary conditions are used in each unit cell, so the study of one cell will yield the kinetics of the concentration of the reactants $C(t) = N(t)/V$. We could endow our reactants with internal states (energetic, configurational, spin, etc.) and the lattice with various types of defects (promoters or inhibitors of diffusion) using our matrix renormalized propagator as discussed in Section III. However we will choose for simplicity a single particle on a perfect 2D square lattice governed by nearest neighbor jumps and $\psi(t) = A \exp(-At)$. This model is then similar to Montroll's³⁷ and Lindenberg's³², Heminger, and Pearlstein's studies of exciton trapping. The equations which are now presented to calculate $K(t)$ (Eq. 4.6) should not be confused with the unimolecular reaction Eq. (4.1).

Given $\Psi(\vec{l}, t) = \psi(t)p(\vec{l})$ we now calculate the unconditional first passage time $F(t)$ for a reactant initial at a non-active site. The probability density $f(o, t | \vec{l}_0)$ for reaching the active site $\vec{l}=o$ at time t for the reactant starting at \vec{l}_0 , enters the following equation

$$\sum_{\vec{l}_0 \neq o} R(o, t | \vec{l}_0) g(\vec{l}_0) = \sum_{\vec{l}_0 \neq o} \int_0^t f(o, t - \tau | \vec{l}_0) g(\vec{l}_0) R(o, \tau | o) d\tau \quad (4.9)$$

where we have averaged over the initial probability of occupying \vec{l}_0 , and the RHS takes into account that for the reactant to reach the origin at time t it could have reached there at an earlier time $t - \tau$ and returned to the origin (any number of times) in the remaining time

τ . Here we are treating the origin as a normal site and calculating the first passage into $\vec{\ell}=0$. The propagator R was first discussed in Eq. (2.4). Eq (4.9) can be solved by Fourier and Laplace transforms to yield

$$F(t) = \frac{1}{V-1} \sum_{\vec{\ell}_0 \neq 0} f(o, t | \vec{\ell}_0) = \frac{1}{V-1} \mathcal{L}^{-1} \left[\frac{R(\vec{k}=0, u | o)}{R(\vec{\ell}=0, u | o)} - 1 \right] \quad (4.10)$$

The denominator on the RHS is the random walk Green's function for return to the origin and is given by, in 2D,

$$R(\vec{\ell}=0, u | o) = \frac{1}{V} \sum_{k_1=1}^{V_1} \sum_{k_2=1}^{V_2} [1 - p(\vec{k})\psi(u)]^{-1} \quad (4.11)$$

where $V=V_1V_2$ and $k_i=2\pi h_i/V_i$, $i=1,2$. While the Green's function has a simple form in Fourier and Laplace space (see Eq. (2.9)) it is not known, in general, in closed form in real space other than as in Eq. (4.11). Note however, that $R(\vec{\ell}=0, u | o)$ diverges for small u .¹⁷ This is because $\lim_{u \rightarrow 0} R^{-1}(\vec{\ell}=0, u | o)$ represents the probability that a random walker never returns to the origin after any number of steps, and this is zero for a finite lattice. Montroll³⁷ has analyzed the behavior of Eq. (4.11) in the small u limit. Using Montroll's results we obtain in 2D.

$$F(u) \sim 1 - S V [1 - \psi(u)] + O[1 - \psi(u)]^{3/2} \quad (4.12)$$

where $S=S_1 \log V + S_2 + S_3/V + S_4/V^2 + \dots$ and the values of S_1, \dots, S_4 are of the order of 0.1 to 1.0 and differ for hexagon, square, and triangular lattices. In our example $1-\psi(u) \sim u \langle t \rangle$ where $\langle t \rangle = \int_0^\infty t \psi(t) dt$ is the mean time between jumps. In the long time limit $F(t)$ and $\psi(t)$ will have the same form, but different parameters such that

$$\int_0^\infty t F(t) dt = S V \int_0^\infty t \psi(t) dt \quad (4.13)$$

so approximately SV steps are taken before the reaction occurs. Thus we arrive at the equation for the concentration of reactants $C(t)$ in the long time limit

$$\frac{C(t)}{C(o)} = \exp \left(- \frac{A}{SV} t \right) \quad (4.14)$$

For shorter times the reaction rate ($K(t) = A/SV$) will be time dependent. The structure of the substrate enters the rate through the quantity S . Using Montroll's values for S_1, S_2, \dots , it can be shown that the rates order as $K_{tri} > K_{sq} > K_{hex}$, which is the same ordering as the coordination numbers. The structural effect is more pronounced

for large V (low active site concentrations). For V=10, K_{sq} and K_{tri} are 23% and 29% larger, respectively, than K_{hex} .

Diffusion Controlled Bimolecular Reactions

Bimolecular reactions on a surface can be treated in a similar fashion as unimolecular reactions, but they are inherently more difficult.³⁶ First, the bimolecular master equations (Eqs. 4.15) and (4.16) are more complicated than the simple unimolecular one. Secondly, the calculation of $K(t)$ involves conditional first pair coincidences rather than first passage times. Thirdly, a single reactant upon reaching a reactive site will leave if the second reactant (which is necessary for the reaction) does not arrive in sufficient time. It is likely that the transition rate for a single particle to leave the reactive site is different than for it to leave a non-reactive site. In this case single particles will migrate on a defective lattice in the bimolecular reaction due to the nature of the reactive site, but not in the unimolecular reaction where they immediately react at the reactive (defective) site.

The bimolecular reaction master equation for identical particles $A+A \rightarrow 2A$ is³⁴

$$\frac{dP(N,t)}{dt} = K(t) \left[\binom{N+2}{2} P(N+2, t) - \binom{N}{2} P(N,t) \right] \quad (4.15)$$

where N is the number of reactants which have not decayed at time t. We assume N is initially even, and changed by two after a reaction.

For two different species $A+B \rightarrow C$ the bimolecular master equation is given by³⁴

$$\frac{dP(N,t)}{dt} = K(t) \left[(N+1)P(Z_0 + N + 1) - N(Z_0 + N) P(N,t) \right] \quad (4.16)$$

where N is the number of type A reactants, and $M = Z_0 + N$ is the number of B reactants. Recombination reactions such as annealing are of this type.

Eqs. (4.15) and (4.16) can be solved by generating function techniques³⁴ to yield respectively,

$$\langle N(t) \rangle = \sum_{N=2}^{N_0} A_N \exp \left[-2^{-1} N(N-1) \int_0^t K(\tau) d\tau \right] \quad (4.17)$$

where

$$A_N = \frac{1 - 2^N}{2^N} \left(\frac{\Gamma(N_0 + 1) \Gamma\left(\frac{N_0 - N - 1}{2}\right)}{\Gamma(N_0 - N + 1) \Gamma\left(\frac{N_0 + N + 1}{2}\right)} \right)$$

and N is even, and

$$\langle N(t) \rangle = \sum_{N=0}^{N_0} \frac{(2N+Z_0)\Gamma(N_0+1)\Gamma(N_0+Z_0+1)}{\Gamma(N_0-N+1)\Gamma(N_0+Z_0+N+1)} \exp\left(-N(N+Z_0) \int_0^t K(\tau) d\tau\right) \quad (4.18)$$

Here $K(t)dt$ is the conditional probability distribution that a reaction takes place between two particular reactants in the interval $(t, t+dt)$ given that the reaction did not occur before in $(0, t)$. As before we will be interested in diffusion controlled reactions at reactive sites which we take to be the origins of the defect superlattice cells of volume V with periodic boundary conditions. In analogy to Eq. (4.9) to find the probability density for a first coincidence at the reactive site $\vec{l}=0$, at time t , $f(0, t | \vec{l}_1, \vec{l}_2)$ of two reactants which were at \vec{l}_1 and \vec{l}_2 at $t=0$, we first need to calculate the probability density of any coincidence $C(0, t | \vec{l}_1, \vec{l}_2)$, of two particles which initially were situated at sites \vec{l}_1 , and \vec{l}_2 and coincide at the origin of their unit cell at time t .

$$\begin{aligned} C(t) &= \sum_{\vec{l}_2} \sum_{\vec{l}_1} C(0, t | \vec{l}_1, \vec{l}_2) g(\vec{l}_1) g(\vec{l}_2) \\ &= \sum_{\vec{l}_2} \sum_{\vec{l}_1} \int_0^t f(0, t-\tau | \vec{l}_1, \vec{l}_2) g(\vec{l}_1) g(\vec{l}_2) C(0, \tau | 0, 0) d\tau \end{aligned} \quad (4.19)$$

where we have averaged over all initial positions of the two particular reactants, except for both being at the origin initially. The above equation can be solved for the first coincidence density f to give

$$\begin{aligned} F(t) &\equiv \sum_{\vec{l}_1} \sum_{\vec{l}_2} f(0, t | \vec{l}_1, \vec{l}_2) g(\vec{l}_1) g(\vec{l}_2) \\ &= \mathcal{L}^{-1} [C(u)/C(0, u | 0, 0)] \end{aligned} \quad (4.20)$$

To proceed further we need to specify the allowable states of the reactants and the probability distributions governing transitions. We will treat the simplest case where all reactants are of the same type and have the waiting time density $\psi(t) = A \exp(-At)$ for hopping, and only nearest neighbor jumps occur. We also consider that the release rate from the reactive site is unchanged from that of the normal site when only one reactant is there at the origin. A reaction will occur at time t if one reactant already resides on the reactive site (having arrived there earlier) and a second reactant arrives there exactly at time t , or vice versa. Remembering that R is the probability density for just arriving at a site, and P is the probability for being at a site, we have

$$C(t) = \frac{2}{V(V-1)} \sum_{\vec{l}_1} \sum_{\vec{l}_2} P(0, t | \vec{l}_1) R(0, t | \vec{l}_2) \quad (4.21)$$

Thus for large V we have

$$F(t) = \mathcal{L}^{-1} \left(\frac{P(\vec{k}=0, u|0)R(\vec{k}=0, u|0)}{P(\vec{\ell}=0, u|0)R(\vec{\ell}=0, u|0)} \right) \quad (4.22)$$

Again using Montroll's³⁷ asymptotic ($u \rightarrow 0$) results for the terms in the denominator we find for the rate constant in Eq. (4.17)

$$\lim_{t \rightarrow \infty} K(t) = A/2S \quad (4.23)$$

where S is given in Eq. (4.12). Note that this rate is one half of the unimolecular reaction rate, but both rates enter completely different equations (Eq. (4.17) and Eq. (4.18)) for the mean number of reactants). For reaction between two species whose transition rates are characterized by rates A and B we find for large t the K to be used in Eq. (5.22) is

$$K(t) = (A+B)/(S[2 + A/B + B/A]) \quad (4.24)$$

V. CONDITIONS FOR A RATE MAXIMIZING TEMPERATURE IN LANGMUIR-HINSHELWOOD REACTIONS

In this section we illustrate the manner in which multistate diffusion mechanisms might provide an interpretation of certain experiments in which the rate of a catalytic reaction can be maximized as a function of temperature.

A number of heterogeneous catalytic reactions exhibit a maximum rate of reaction as a function of temperature. This may be due to the reaction mechanism or to changes in the catalytic structure as a function of temperature or a combination of both. We will consider the experiment of Moffat and Clark³⁸ who in 1969 found a rate temperature maximum for the olefin disproportionation reaction of propylene into ethylene on the cobaltmolybdate-alumina catalyst $\text{Co-Mo-Al}_2\text{O}_3$. They also found that the reaction obeys the bimolecular Langmuir-Hinshelwood law. This means that two adsorbed propylenes react, perhaps at an active site. Other reaction mechanisms are possible. For example, Begley and Wilson³⁹ found an Eley-Rideal mechanism (an adsorbed species reacting with a gas phase species) for olefin disproportionation on a tungsten-silica catalyst.

The Langmuir-Hinshelwood law is derived as follows. Let θ be the fractional surface coverage by the reactants. Then

$$\frac{d\theta}{dt} = Pk_1(1-\theta) - k_2\theta, \quad (5.1)$$

where k_1 is the adsorption rate and k_2 is the desorption rate and P is the pressure. At equilibrium

$$\theta = KP / (1 + KP), \quad (5.2)$$

where $K = k_1/k_2$. The bimolecular rate of reaction is proportional to θ^2 and to the diffusion controlled rate of reaction on the surface denoted by k . Thus the Langmuir-Hinshelwood rate of reaction r is

$$r = k \left[\frac{KP}{1+KP} \right]^2. \quad (5.3)$$

Note that Eq. (5.3) can be rewritten as

$$\frac{1}{\sqrt{r}} = \frac{1}{\sqrt{k}} \left(1 + \frac{1}{KP} \right) \quad (5.4)$$

Thus a plot of $r^{-1/2}$ vs. P^{-1} should yield a straight line, as is seen in the propylene disproportionation reaction studied by Moffat and Clark³⁸.

Usually, Arrhenius forms are assumed for both k and K ³⁸⁻⁴⁰, i.e.

$$k = A \exp(-E/RT)$$

$$K = \exp(\Delta S/R) \exp(-\Delta H/RT) \quad (5.5)$$

where E is the activation energy for diffusion, ΔS is the differential entropy of adsorption, ΔH is the heat of adsorption, and A is the frequency factor. Since k and K can be determined from the $r^{-1/2}$ vs. P^{-1} plot, one can further calculate the activation energy E by

$$E = - \frac{\partial \ln k}{\partial (1/RT)} \quad (5.6)$$

and the heat of adsorption by

$$-\Delta H = \frac{\partial \ln K}{\partial (1/RT)}$$

Moffat and Clark³⁸ found the values $E = 8.2$ K cal/mole and $|\Delta H| = 2.8$ K cal/mole as well as a rate maximizing temperature $T_m \sim 420^\circ\text{F}$. If Eq. (5.5) is substituted into the rate equation (5.3) and the derivative with respect to temperature of the resulting expression is set equal to zero, a condition for the appearance of a rate maximum as a function of temperature is obtained. When the adsorption step of the reaction is exothermic, $\Delta H < 0$, and the rate maximum condition is³⁸

$$|\Delta H| > E(\beta + 1) / 2 \quad (5.8)$$

where $\beta = P \exp(\Delta S/R)$ and is usually much smaller than unity. This condition Eq. (5.8) is not satisfied by the measurements of Moffat and

Clark and yet a rate maximum still occurs.

To explain this apparent paradox we⁴¹ propose mechanisms where the Langmuir-Hinshelwood form of Eq. (5.3) is preserved, but the rate maximum condition Eq. (5.8) is modified to a form which can be consistent with the experimental results. Common to the mechanisms which we propose is the property that k , which is related to the diffusive motion on the surface, is characterized by more than one rate constant. For example the motion of the nine atoms comprising the propylene $\text{CH}_3\text{CH}=\text{CH}_2$ may involve transitions between different configurations of this cluster each with its own transition rate. Out of all the possible transitions those with the highest activation energies will be the rate limiting steps. Considering the two most important rate limiting transitions with rate A and B , the diffusion constant in Eq. (5.3) will take the form, as in Eq. (2.19)

$$k = \frac{AB}{A+B} \quad (5.9)$$

We write both A and B in the Arrhenius form

$$\begin{aligned} A &= v_A \exp(-E_A/RT) \\ B &= v_B \exp(-E_B/RT) \end{aligned} \quad (5.10)$$

so k will not be of the Arrhenius form. If however a straight line results from an experimental plot of $\log k$ vs. $(RT)^{-1}$ this does not necessarily imply that $k=v \exp(-E/RT)$ and that k cannot be written as in Eqs. (5.9) and (5.10). In practice, a plot of $\log k$ from Eqs. (5.9) and (5.10) vs. $(RT)^{-1}$ will yield a straight line of slope $-E_A$, in an appropriate temperature range, if

$$(1) \quad E_A \approx E_B \quad (5.11a)$$

or

$$(2) \quad E_A \gg E_B + RT \ln(v_A/v_B) \quad (5.11b)$$

Using the k in Eqs. (5.9) and (5.10) the following condition is found for the occurrence of a rate maximizing temperature T_m in Eq. (5.3)

$$\frac{1 + P \exp[\Delta S/R - |\Delta H|/RT_m]}{2|\Delta H|} = \frac{A + B}{E_B A + E_A B} \quad (5.12)$$

Let us denote the RHS by Γ . A linear analysis shows that a small decrease in pressure δP will decrease T_m by the amount δT_m , where

$$\begin{aligned} \delta T_m &= \delta P \exp[\Delta S/R + |\Delta H|/RT_m] RT_m^2 / |\Delta H| \times \\ &\quad \left[2|\Delta H|\Gamma - 1 + 2AB[\Gamma(E_A - E_B)/(A + B)]^2 \right]^{-1} \end{aligned} \quad (5.13)$$

This is in accord with the experimental result that a decrease in pressure lowers the maximizing temperature.³⁸ Neglecting $P \exp(\Delta S/R)$ compared to unity we arrive at the following inequality for the existence of a rate maximum

$$v_A(2|\Delta H| - E_B) > v_B(E_A - 2|\Delta H|) \quad (5.14)$$

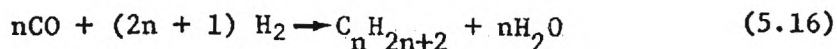
where we have assumed, without loss of generality, that $E_A > E_B$. In contrast to Eq. (5.8) this inequality can be satisfied by the measurements of Moffat and Clark³⁸, $E_A = 8.2$ Kcal/mole and $|\Delta H| = 2.8$ k cal/mole, if

$$0 < E_B < 5.6 - 2.6 \frac{v_B}{v_A} \text{ K cal/mole} \quad (5.15)$$

For k to be adequately described by an Arrhenius plot, Eq. (5.11b) must also be satisfied. A similar inequality can be derived by assuming the surface contains two types of sites with two different release rates⁴¹.

Not all reactions have reversible rate maxima. For example, Maatman et. al.⁴⁰ studied the cracking of isopropylbenzene $[C_6H_5CH(CH_3)_2]$ into benzene $[C_6H_6]$ and propylene $[C_3H_6]$ on a silica-alumina catalyst. They derived the condition that the heat of desorption from active sites must be greater than the activation energy for diffusion for a rate maxima to exist. This condition is not met and no rate maxima is seen.

It would be interesting to find the conditions for the existence of a rate maximizing temperature for the production of various hydrocarbons in a Fischer-Tropsch reaction where progressively heavier hydrocarbons are produced from a catalyzed gaseous CO and H_2 mixture.



APPENDIX A

PARTIAL DISCRETE FOURIER TRANSFORMS

We define the discrete Fourier transform (Eq. A.1) and its inverse (Eq. A.2) on an infinite lattice of dimension d , as

$$f(\vec{k}) = \sum_{\ell_1=-\infty}^{\infty} \cdots \sum_{\ell_d=-\infty}^{\infty} f(\vec{\ell}) e^{i\vec{k}\cdot\vec{\ell}}, \quad (\text{A.1})$$

$$f(\vec{\ell}) = (2\pi)^{-d} \int_0^{2\pi} \cdots \int_0^{2\pi} f(\vec{k}) e^{-i\vec{k}\cdot\vec{\ell}} d\vec{k}. \quad (\text{A.2})$$

Consider first a 1D lattice and define the partial Fourier transform

$$f_{\gamma,n}(k) = \sum_{\ell=-\infty}^{\infty} f(\gamma\ell + n) e^{ik(\gamma\ell + n)}. \quad (\text{A.3})$$

Using Eq. (A.2) we obtain

$$\begin{aligned} f_{\gamma,n}(\vec{k}) &= \sum_{\ell=-\infty}^{\infty} (2\pi)^{-1} \int_0^{2\pi} f(k') e^{i(k-k')(\gamma\ell + n)} dk' \\ &= \frac{1}{\gamma} \int_0^{2\pi} f(k') \delta(k-k' + \frac{2\pi m}{\gamma}) dk' \end{aligned} \quad (\text{A.4})$$

$$= \frac{1}{\gamma} \sum_m f(k + \frac{2\pi m}{\gamma}) \quad (\text{A.5})$$

where the summation is over all integer values of m (positive and negative) such that $k + \frac{2\pi m}{\gamma} \in (0, 2\pi)$. Eqs. (A.3) and (A.5) can be easily generalized to higher dimensions, say d , to yield

$$(\gamma_1 \cdots \gamma_d)^{-1} \sum_{m_1} \cdots \sum_{m_d} f(k_1 + \frac{2\pi m_1}{\gamma_1}, \dots, k_d + \frac{2\pi m_d}{\gamma_d}) \quad (\text{A.6})$$

For a finite lattice of d dimensions (the number of lattice points being $N_1 \times \cdots \times N_d$) the discrete Fourier transforms are defined as

$$f(\vec{k}) = \sum_{\ell_1=1}^{N_1} \cdots \sum_{\ell_d=1}^{N_d} f(\vec{\ell}) e^{i\vec{k}\cdot\vec{\ell}} \quad (\text{A.7})$$

and

$$f(\vec{\ell}) = (N_1 \cdots N_d)^{-1} \sum_{S_1=1}^{N_1} \cdots \sum_{S_d=1}^{N_d} f(\vec{k}) e^{-i\vec{k}\cdot\vec{\ell}} \quad (\text{A.8})$$

where $k_i = 2\pi s_i / N_i$, $i = 1, \dots, d$; and $s_i = 1, \dots, N_i$.

For the partial discrete transform

$$f_{\gamma}(\vec{k}) = \sum_{\ell_1=1}^{N_1} \dots \sum_{\ell_d=1}^{N_d} f(\gamma_1 \ell_1, \dots, \gamma_d \ell_d) e^{i\vec{k} \cdot (\gamma_1 \ell_1, \dots, \gamma_d \ell_d)} \quad (\text{A.9})$$

we obtain the same result as in Eq. (A.6), except k can only take on the $N_1 \times \dots \times N_d$ values in Eq. (A.8)

REFERENCES

1. E. W. Müller and T. T. Tsong, Field Ion Microscopy (Elsevier, N.Y., 1969).
2. D. W. Bassett, in Surface and Defect Properties of solids (The Chemical Society, London, 1973) Vol. 2, P. 34.
3. G. Ehrlich, Crit. Rev. Solid. State Sci. 4, 205 (1974).
4. W. R. Graham and G. Ehrlich, Thin Solid Films, 25, 85 (1975).
5. G. E. Rhead, Surf. Sci. 47, 207 (1975).
6. G. Ehrlich and F. G. Hudda, J. Chem. Phys. 44, 1039 (1966).
7. K. Stolt, W. R. Graham, and G. Ehrlich, J. Chem. Phys. 65, 3206 (1976).
8. T. T. Tsong, Phys. Rev. 136, 417 (1972).
9. W. R. Graham and G. Ehrlich, Phys. Rev. Lett. 31, 1407 (1973); 32, 1309 (1974); J. Phys. F 4, L212 (1974).
10. D. A. Reed and G. Ehrlich, J. Chem. Phys. 64, 4616 (1976).
11. S. Nishigaki and S. Nakamura, Jap. J. Appl. Phys. 14, 769 (1975).
12. T. T. Tsong, P. Cowan, and G. Kellogg, Thin Solid Films. 25, 97 (1975).
13. D. W. Bassett, J. Phys. C., 9, 2491 (1976).
14. D. W. Bassett and M. J. Parsley, Nature 221, 1046 (1969).
15. D. W. Bassett, Surf. Sci. 21, 181 (1970).
16. M. Audiffren, P. Traimond, J. Bardon, and M. Drechsler, Surf. Sci. 75, 751 (1978).
17. E. W. Montroll and G. H. Weiss, J. Math. Phys. 6, 67 (1965).
18. H. Scher and M. Lax, Phys. Rev. B7, 4491, 4502 (1973).
19. E. W. Montroll and H. Scher, J. Stat. Phys. 9, 101 (1973).
M. F. Shlesinger, J. Stat. Phys. 10, 421 (1974).
20. U. Landman, E. W. Montroll, and M. F. Shlesinger, Phys. Rev. Lett. 38, 285 (1977), Proc. Nat. Acad. Sci (USA) 74, 430 (1977).
21. U. Landman and M. F. Shlesinger, Phys. Rev. B16, 3389 (1977).
22. U. Landman and M. F. Shlesinger, Annals Israel Phys. Soc. 2, 682 (1978).
23. M. F. Shlesinger and U. Landman, in Applied Stochastic Processes, ed. G. Adomian, Academic Press (to be published).
24. V. M. Kenkre, E. W. Montroll, and M. F. Shlesinger, J. Stat. Phys. 9, 101 (1973).
25. T. T. Tsong and R. T. Walko, Phys. Stat. Sol. (a), 12, 111 (1972).

26. U. Landman and M. F. Shlesinger, Phys. Rev. B19, 6207, 6220 (1979).
27. U. Landman and M. F. Shlesinger, Solid State Comm. 27, 939, (1978).
28. M. Sugi and S. Iizima, Phys. Rev. B15, 574 (1977).
29. H. P. Bonzel in Surface Physics of Materials, J. M. Blakely, ed. (Academic Press, N.Y. 1975).
30. K. Schrader, Z. Phys. B25, 91 (1976).
31. K. W. Kehr and D. Richter, Solid State Comm. 20, 477 (1976).
32. K. Lakatos-Lindenberg, R. P. Hemenger, R. M. Pearlstein, J. Chem. Phys. 56, 4852 (1972).
33. P. L. Cowan and T. T. Tsong, Surf. Sci. 67, 158 (1977)
34. D. A. McQuarrie, in Meuthen's Monographs on Applied Probability and Statistics, J. Gani, ed. (Meuthen, London 1967).
35. M. F. Shlesinger, J. Chem. Phys. 70, 4813 (1979); and J. Non-Cryst. Solids (to appear).
36. U. Landman and M. F. Shlesinger, Phys. Rev. Lett. 41, 1174 (1978).
37. E. W. Montroll, J. Math. Phys. 10, 753 (1969).
38. A. T. Moffat and A. Clarke, J. Catal 17, 264 (1970).
39. J. W. Begley and R. T. Wilson, J. Catal. 9, 375 (1967).
40. R. W. Maatman, D. L. Leenstra, A. Leenstra, R. L. Blankespoor, and D. N. Rubingh, J. Catal. 7, 1 (1967).
41. M. F. Shlesinger and U. Landman, J. Catal, (to be published).



CORRELATION EFFECTS ON FREQUENCY DEPENDENT CONDUCTIVITY: APPLICATION TO SUPERIONIC CONDUCTORS*

Michael F. Shlesinger

School of Physics, Georgia Institute of Technology, Atlanta, Georgia 30332

(Received 1 August 1979 by A. A. Maradudin)

The Scher-Lax model for the calculation of a.c. conductivity is modified to allow for temporal and spatial correlations. If, due to, say, lattice relaxation effects, a charge is most likely to continue to move in the same direction (caterpillar mechanism), then the real part of the conductivity will saturate, at large frequencies, below the d.c. level. The reverse will be true if a bounce-back mechanism dominates. These two cases of correlation can be related to the behavior of the superionic conductors AgI and Na β -alumina, respectively. The degree of disorder in the hopping sites determines the distribution of ionic transition rates which in turn governs the details of the conductivity curve. The frequency dependent conductivity due to the motion of an ionic cluster (dimer) is also analyzed.

I. Introduction

In recent years attention has been focused on the frequency dependent conductivity $\sigma(\omega)$ of superionic conductors, as probed by optical, infrared, and microwave radiation, in order to gain information about the fast ion transport mechanism.¹ Several studies have suggested that ion-ion correlations play an important role in ionic transport in superionic conductors. For example, van Gool and Bottelberghs,² and Wang, Gaffari, and Choi³ have shown for Na β -alumina that the thermal activation energy, for transporting from a Beavers-Ross to an anti-Beavers-Ross site, decreases significantly when several Na⁺ ions are involved as opposed to a single ion. This is consistent with the x-ray data of Peters et al.,⁴ which suggests that the Na⁺ ions form clusters, as well as the measurements of Strom et al.,⁵ showing a broad distribution of collective ion modes. It has been suggested by Roth⁶ and by van Gool and Bottelberghs² that the excess cation concentrations in β -aluminas form domains. The recent EXAFS measurements, on AgI, of Boyce et al.,⁷ imply an ionic hopping model. In addition, Flynn⁸ has suggested that mobile ions can form small polarons, and Emin⁹ has shown how this can lead to correlated motion involving a time dependent activation energy. Kimball and Adams¹⁰ have studied the effects of correlation on $\text{Re } \sigma(\omega)$ by using a Green-Kubo formalism and keeping single and double hop terms. A kinetic Ising model is used to determine the transition rates between the states of the system. They find that $\text{Re } \sigma(\omega)$ always increases with ω , regardless of the type of correlation.

In the present paper, the Scher-Lax model¹¹ for calculating $\sigma(\omega)$ is modified to include the effects of correlation. Two types of correlation are studied,

- 1) bounce-back and caterpillar mechanism (lattice relaxation correlation)
- 2) cluster (dimer) motion (ion-ion correlation)

The first type of correlation treats the effect of lattice relaxation on altering the relative probabilities for an ion hopping in the same and opposite directions as the previous hop. In section III we will show for the bounce-back mechanism that $\text{Re } \sigma(\omega)$ will saturate above the d.c. level, and that the reverse will be true for the caterpillar mechanism. In Section IV the spatial correlations involved in the motion of a dimer are analyzed to show that $\text{Re } \sigma(\omega)$ increases with ω . Thus the Scher-Lax model¹¹ provides a unified approach equally well describing an increasing $\text{Re } \sigma(\omega)$, as observed in Na β -alumina,¹² or decreasing $\text{Re } \sigma(\omega)$, as observed in AgI.¹³

II. The Scher-Lax Model

Scher and Lax¹¹ have used the Nyquist-like Green-Kubo formalism, which relates mobility to noise, to calculate the conductivity $\sigma(\omega) = n(Ze)^2 D(\omega)/kT$ for impurity conduction in semiconductors in 3D where n is the density of carriers, Ze is the charge on a carrier, and $D(\omega)$ is the diffusion coefficient. They convert the usual expression containing the velocity correlation into an expression with a spatial displacement correlation, i.e.

$$D(\omega) = -\frac{1}{6} \omega^2 C(\omega, T) \int_0^{\infty} \exp(i\omega t) \langle [\vec{\ell}(t) - \vec{\ell}(0)]^2 \rangle dt, \quad (1)$$

where $C(\omega, T) = (\hbar\omega/2kT) \coth(\hbar\omega/2kT)$ and is close to unity for $\hbar\omega < 2kT$. This is the case for the temperatures at which superionic

*Supported by DOE Grant No. EG-77-S-05-5489

there, then Feller has shown the first transition in an ongoing random process must be treated differently than the succeeding transitions, as pointed out by Tunaley.¹⁷ This consideration will lead to

$$D(\omega) = \frac{\ell^2}{2} \left(\frac{1 + (p-q) \frac{\tilde{\psi}(i\omega)}{\tilde{\psi}(i\omega)}}{1 - (p-q) \frac{\tilde{\psi}(i\omega)}{\tilde{\psi}(i\omega)}} \right) \lim_{\omega \rightarrow 0} \left(\frac{i\omega \tilde{\psi}(\omega)}{1 - \tilde{\psi}(\omega)} \right) \quad (6)$$

Lax and Scher¹⁸ have argued that the procedure, for $p = q$, leading to Eq. (5) is correct for the case of impurity conduction. In any event, both results are equivalent and yield frequency independent conductivities if $\psi(t) = \lambda \exp(-\lambda t)$ and $p = q$. The transition rate is usually written in an activated form $\lambda = \nu \exp(-E/kT)$. However, if $p \neq q$, this $\psi(t)$ yields, using Eq. (4) with $\alpha = 0$,

$$D(\omega) = \frac{\lambda \ell^2}{2} \left(\frac{\omega^4 + (1+4pq)\omega^2 \lambda^2 + 4pq\lambda^4 - 2i(p-q)\omega\lambda(\omega^2 + \lambda^2)}{(\omega^2 + 2q\lambda^2)^2 + (p-q)^2 \omega^2 \lambda^2} \right) \quad (7)$$

where the real part of the term in brackets varies from p/q at $\omega=0$ to 1 at $\omega=\infty$. Thus for $p > q$ (caterpillar mechanism) $\text{Re } \sigma(\omega)$ will decrease with ω , and for $q > p$ (bounce-back mechanism) $\text{Re } \sigma(\omega)$ will increase with frequency. An exponential $\psi(t)$ will also lead to frequency dependent results in multilayer assemblies.¹⁹

IV. Spatial Correlation: The Transport of a Dimer

As shown in Fig. 2, we assume that for 1D motion a dimer²⁰ can exist in a straight or a staggered configuration. The motion must alternate between these states. Hopping distribution functions $\psi_1(t) = A \exp(-At)$, and $\psi_2(t) = B \exp(-Bt)$ are assigned for making transitions from the straight and staggered configurations, respectively. Using the continuous-time random walk formalism with internal states for the dimer motion leads to

$$D(\omega) = \frac{\ell^2}{4} \frac{AB}{A+B} \left(\frac{(A+B)^2 + 2\omega^2 + i\omega(A+B)}{(A+B)^2 + \omega^2} \right) \quad (8)$$

Studies,^{2,3} suggest that the activation energies for cluster motion will be lower than for single particle motion. It is seen from Eq. (8) that $\text{Re } D(\omega)$ will increase with frequency.

V. Conclusions

It has been shown how correlations can be treated as internal states in a matrix approach to continuous-time random walks. The effect of correlations in a hopping model with a single transition rate is to make the conductivity complex and frequency dependent. The degree of disorder in the environment of the charge carrier can be incorporated¹¹ in the hopping distribution

function. An algebraic $\psi(t) \sim t^{-1-\alpha}$, $0 < \alpha < 1$, implies a large distribution of hopping rates and leads to a $D(\omega) \sim \omega^\alpha$ regime, as is seen in β -alumina.¹² To describe realistic systems the motion of ionic clusters combined with the lattice relaxation effects of caterpillar and bounce-back mechanisms with the appropriate $\psi(t)$ should be studied in 2D and 3D. Also, following Huberman and Sen,²⁰ one may wish to describe the transport above a temperature dependent cutoff frequency (i.e. at short times) by a damped harmonic oscillator driven by random forces to insure solid like behavior at low temperatures, and $\sigma(\omega) \sim \omega^{-2}$ for $\omega \rightarrow \infty$ as in the free ion model of Rice and Roth.²¹ The above considerations will be developed in the future.

Acknowledgement

The author would like to thank Dr. Harvey Scher for many interesting and useful discussions concerning random walks and models of conductivity.

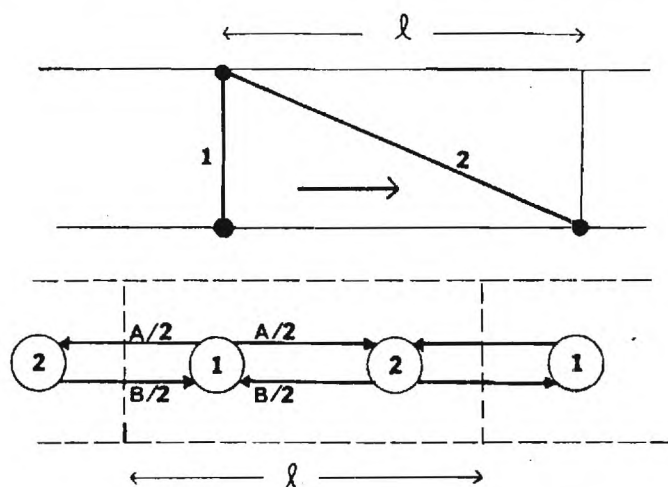


Figure 2. In 1D we allow the dimer to exist in a straight (state 1) or staggered configuration (state 2). The allowable positions of the dimer's center of mass are then mapped onto a periodic lattice with two states per unit cell. The total rate of leaving states 1 and 2 are A and B, respectively. Transitions to the right and left occur with equal probability. In the upper figure we show a transition from state 1 to state 2.

REFERENCES

1. G. D. MAHAN and W. L. ROTH, Eds, *Superionic Conductors*, Plenum Press, N.Y. (1976).
2. W. VAN GOOL AND P. H. BOTTELBERGHS, *J. Solid State Chem.* **7**, 59 (1973).
3. J. C. WANG, M. GAFFARI, and SANG-IL CHOI, *J. Chem. Phys.* **63**, 772 (1975).
4. C. R. PETERS, M. BETTMAN, J. W. MOORE, and M. D. GLICK, *Acta. Cryst. B* **27**, 1826 (1971).
5. U. STROM, P. C. TAYLOR, S. G. BISHOP, T. L. REINECKE, and K. L. NGAI, *Phys. Rev. B* **13**, 3329 (1976).
6. W. L. ROTH, *J. Solid State Chem.* **4**, 60 (1972).
7. J. B. BOYCE, T. M. HAYES, W. STUTIUS, and J. C. MIKKELSON, Jr., *Phys. Rev. Lett.* **38**, 1362 (1977).
8. C. P. FLYNN, *Point Defects and Diffusion*, Oxford U. Press, Oxford (1972).
9. D. EMIN, *Phys. Rev. B* **4**, 3639 (1971).
10. J. C. KIMBALL and L. W. ADAMS, Jr., *Phys. Rev. B* **18**, 585 (1978).
11. H. SCHER AND M. LAX, *Phys. Rev. B* **7**, 4491, 4502 (1973).
12. A. S. BARKER, JR., J. A. DITZENBERGER, and J. P. REMEIKI, *Phys. Rev. B* **14**, 4254 (1976).
13. K. FUNKE and A. JOST, *BER. BUNSENCEG.* *Phys. Chem.* **75**, 435 (1971).
14. E. W. MONTROLL and G. H. WEISS, *J. Math. Phys.* **6**, 167 (1965).
15. U. LANDMAN and M. F. SHLESINGER, *Phys. Rev. B* **19**, 6207, 6220 (1979). M. F. SHLESINGER and U. LANDMAN in *Applied Stochastic Processes*, G. ADOMIAN, Ed., Academic Press (to be published).
16. U. LANDMAN, E. W. MONTROLL AND M. F. SHLESINGER, *Phys. Rev. Lett.* **38**, 285 (1977). U. LANDMAN, E. W. MONTROLL and M. F. SHLESINGER, *Proc. Nat. Acad. Sci. (USA)* **74**, 430 (1977). U. LANDMAN and M. F. SHLESINGER, *Phys. Rev. B* **16**, 3389 (1977). U. LANDMAN and M.F. SHLESINGER, *Solid St. Commun.* **27**, 939 (1978).
17. J. K. E. TUNALEY, *Phys. Rev. Lett.* **33**, 1037 (1974).
18. M. LAX and H. SCHER, *Phys. Rev. Lett.* **39**, 781 (1977).
19. M. SUGI and S. IZIMA, *Phys. Rev. B* **15**, 574 (1977).
20. J. C. WANG, *Bull. Am. Phys. Soc.* **24**, 755 (1979).
21. B. A. HUBERMAN AND P. N. SEN, *Phys. Rev. Lett.* **33**, 1379 (1974).
22. M. J. RICE and W. L. ROTH, *J. Solid St. Chem.* **4**, 294 (1972).

SSSH1064 PRUMD,800815LM1391,1

Substrate effects on long-range order and scattering from low-dimensional systems

Charles L. Cleveland, Charles S. Brown, and Uzi Landman
 School of Physics, Georgia Institute of Technology, Atlanta, Georgia 30332
 (Received 14 December 1979)

Using solvable models it is shown that coupling one- and two-dimensional systems to substrates produces significant alterations in their long-range order and scattering characteristics, even if the coupling is very weak. Expressions for Peierls's long-range-order parameter, $\langle \delta_n^2 \rangle$, are obtained, with their asymptotic forms, and static structure factors, $S(\vec{Q})$, are evaluated.

PACS numbers: 68.60. + q, 64.60.Cn, 68.20. + t

Recent theoretical and experimental studies of systems of "less than three dimensions" have inspired a resurgence of interest in this subject. Among the systems reported to exhibit one-dimensional (1D) or quasi-1D behavior are some organic¹ and inorganic² complexes. Systems exhibiting two-dimensional (2D) or quasi-2D behavior include adsorbed layers,³ electrons trapped on a liquid helium surface⁴ and thin "soap-bubble films."⁵ Particularly intriguing are questions of ordering (degree and type) and stability in such systems.⁶⁻¹⁰ Of special interest here is their degree of long-range order in light of physical arguments,⁶ and rigorous proofs⁷ that true long-range order does not exist for strict 1D and 2D systems. Since the physical systems mentioned above are coupled to a skeletal or substrate environment, one should expect, in general, quasi-1D or quasi-2D rather than strict 1D or 2D behavior. Such coupling effects have been observed in recent neutron-scattering studies of $\text{Hg}_{3-6}\text{AsF}_6$,^{2,11} and of phases of CD_4 monolayer films on graphite¹² for which the scattered neutron line shapes could not be interpreted, even for the registered (commensurate) phase, on the basis of strict 2D theories.

Our purpose is to show that coupling to a substrate significantly affects the degree of long-range order and scattering characteristics in certain 1D and 2D model systems. To elucidate our discussion we limit our considerations to certain solvable models employing simple coupling schemes.

A measure of the long-range order in an N -particle system is provided by the function $\langle \delta_{n\vec{k}}^2 \rangle \langle (\vec{u}_n - \vec{u}_0) \cdot \vec{k} \rangle^2$ given by

$$\langle \delta_{n\vec{k}}^2 \rangle = 4(Nm)^{-1} \sum_{\vec{q}} \langle |U_{\vec{q}}^* \cdot \vec{k}|^2 \rangle \sin^2(\frac{1}{2} \vec{q} \cdot \vec{R}_n), \quad (1)$$

where \vec{u}_n is the deviation of particle n of mass m from its equilibrium position \vec{R}_n , \vec{k} is an arbitrary direction in the lattice, and $U_{\vec{q}}$ is the normal-mode amplitude. The angular brackets denote

temperature ensemble averaging. At sufficiently high temperatures, T (typically larger than the Debye temperature) equipartition can be used^{6,8} to write $\langle |U_{\vec{q}}^* \cdot \vec{k}|^2 \rangle = k_B T \omega_{\vec{q}}^{-2}$, where $\omega_{\vec{q}}$ is the normal-mode frequency.

Consider first a 1D chain of atoms of lattice spacing a and interparticle nearest-neighbor (NN) force constants K . Let it be coupled via NN and next NN force constants K_1 and K_D , respectively, to a 1D parallel substrate chain of heavy masses each a distance a , for simplicity, below a lattice site of the first chain. In the harmonic approximation, and for a stationary substrate, the longitudinal normal-mode frequency (describing motions along the chain axis) is given by $\omega_{\vec{q}}^2 = (4K/m)[R^2 + \sin^2(qa/2)]$, where $2R = K_D^2/K^2$ is a measure of the interchain relative coupling strength. Notice that this mode possesses a $q=0$ gap, equal to $4KR^2/m$. Using the high- T approximation and the above $\omega_{\vec{q}}$, transformation of the sum in Eq. (1) over \vec{q} to an integral and converting to a contour integral in the complex plane yields the following closed-form result:

$$\langle \delta_n^2 \rangle / a^2 = \sigma \left(\frac{1 - [2R^2 + 1 - 2R(R^2 + 1)^{1/2}]^n}{R(R^2 + 1)^{1/2}} \right) \equiv C_1(1 - e^{-\alpha n}), \quad (2)$$

where $\sigma = k_B T / 2Ka^2$ (typically¹¹ of the order 10^{-3} - 10^{-4}). In the limit of vanishing coupling, $R=0$, and for large n the previously known result¹¹ $\langle \delta_n^2 \rangle / a^2 \sim (2\sigma)n$ is recovered. With a criterion that long-range order exists when $\langle \delta_n^2 \rangle / a^2 < 1$ as $n \rightarrow \infty$, it follows that there is a long-range order if $R \gtrsim \sigma$, so that even weak coupling to a substrate restores long-range order. The modified behavior upon coupling is shown in Fig. 1(a).

Using the expression given in Eq. (2), the frequency-integrated dynamical structure factor $S(\vec{Q})$ (for \vec{Q} parallel to the chain) can be evaluated, yielding

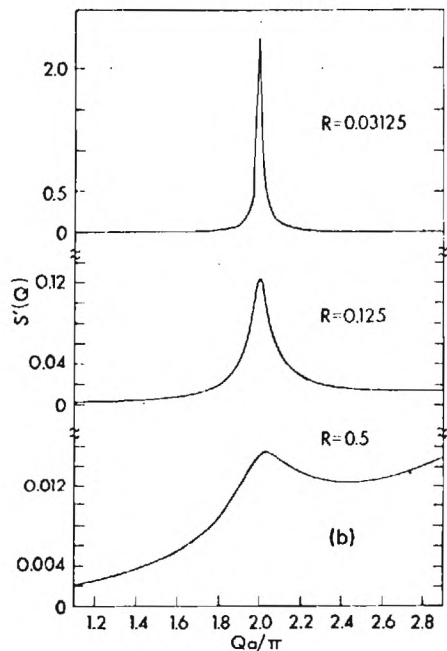
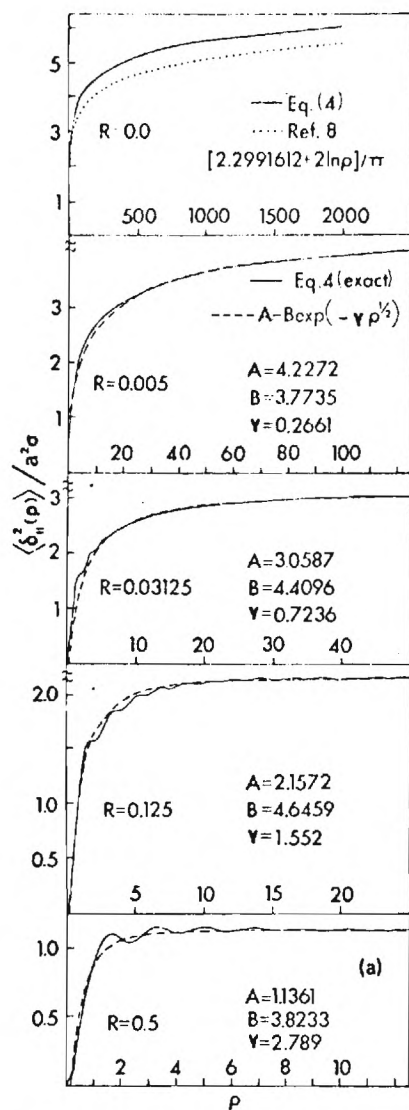


FIG. 2. 2D layer coupled to a stationary substrate layer. (a) $\langle \sigma_{\parallel}^2(\rho) \rangle$ vs $\rho = r_{\parallel}/a$ for various values of R . For $R=0$, results obtained with (dotted) and without (solid) the long-wavelength approximation are shown. For finite R values, results are shown using Eq. (4) (solid) and via the indicated fits (dashed). (b) Subtracted static structure factors, $S'(\vec{Q})$, around the (10) Bragg peak for several coupling strengths, R , $\sigma = 10^{-4}$. Note changes in scale.

$$\begin{aligned}
 S'(\vec{Q}) &= S(\vec{Q}) - \delta(\vec{Q}, \vec{G}) \exp(-A Q^2/2) \\
 &= \exp(-A Q^2/2) \left(4 \sum_{\mu=0}^{\infty} \sum_{\nu=0}^{\infty} \cos(Q_x \mu a) \cos(Q_y \nu a) [\exp(\frac{1}{2} B Q^2 e^{-\gamma(\mu^2 + \nu^2)^{1/4}}) - 1] \right. \\
 &\quad - 2 \sum_{\mu=0}^{\infty} \cos(Q_x \mu a) [\exp(\frac{1}{2} B Q^2 e^{-\gamma \mu^{1/2}}) - 1] - \sum_{\nu=0}^{\infty} \cos(Q_y \nu a) [\exp(\frac{1}{2} B Q^2 e^{-\gamma \nu^{1/2}}) - 1] \\
 &\quad \left. + \exp(\frac{1}{2} B Q^2) - 1 \right), \tag{6}
 \end{aligned}$$

where A , B , and γ are the parameters defined above and \vec{G} is a reciprocal-lattice vector of the 2D net. For a finite sample the summations in the above equation should extend up to $N_x/2$ and $N_y/2$, where $N_x a$ and $N_y a$ are the extensions of the 2D

sample in the x and y directions. Results for $S'(\vec{Q})$ around the (10) Bragg peak, for various values of R , are shown in Fig. 2(b). It is of interest to comment that for a strict 2D lattice, i.e., $R=0$, the peaks in $S(\vec{Q})$ near reciprocal-lattice vectors

$$S'(\vec{Q}) = S(\vec{Q}) - Ne^{-f^2} \delta(\vec{Q}, \vec{G}) = \sum_{l=1}^{\infty} \frac{(-f)^{2l}}{l!} Z(l), \quad (3a)$$

$$Z(l) = \sum_{j=0}^l (-1)^j \binom{l}{j} \left(\frac{e^{-\alpha j} - \cos(Qa)}{\cosh(\alpha j) - \cos(Qa)} \right), \quad (3b)$$

here $2f^2 = Q^2 C_1$ and \vec{G} is a reciprocal-lattice vector. In the limit of vanishing interchain coupling¹¹ $S'(\vec{Q})$ [and $S(\vec{Q})$] consists of a series of sharp peaks centered upon the reciprocal-lattice vectors. For nonvanishing coupling strengths a broadening of the peaks accompanied by a pronounced asymmetry occurs as shown in Fig. 1(b) (note changes in scales). Sufficient accuracy is obtained by truncating the sum over l in Eq. (3a) typically at $l=3-5$. The above could provide practical functional form for fitting purposes.

We turn next to the evaluation of $\langle \delta_{\parallel}^2(\rho) \rangle$ (where $\rho = r_{\parallel}/a$ and r_{\parallel} is an interparticle distance in an arbitrary direction) for a 2D square lattice, of lattice constant a which is coupled to a stationary square substrate layer via NN and next NN force constants K_1 and K_2 . Following arguments similar to the above, we obtain

$$\langle \delta_{\parallel}^2(\rho) \rangle / a^2 = (\sigma/2\pi) \rho^{-2} \int_0^{2\sqrt{\pi}\rho} dy y \frac{1 - J_0(y)}{R^2 + \sin^2(y/2\rho)}, \quad (4)$$

where the Debye cutoff has been employed and J_0 is the Bessel function of the first kind. For vanishing interplane coupling, $R=0$, the previously^{3,8} derived asymptotic logarithmic divergence of $\langle \delta_{\parallel}^2(\rho) \rangle$ is observed. For finite coupling asymptotic analysis yields nonlogarithmic asymptotic behavior (see Appendix).

$$\langle \delta_{\parallel}^2(\rho) \rangle / a^2 = (\sigma/\pi) \left(F(R) - \frac{\sqrt{\pi} J_1(2\pi\rho)/\rho}{R^2 + \sin^2\sqrt{\pi}} \right), \quad (5a)$$

where

$$F(R) = \int_0^{2\sqrt{\pi}} dy y (2R^2 + 1 - \cos y)^{-1}. \quad (5b)$$

Numerical evaluation of Eq. (4) for various values of R indicated that good fits to $\langle \delta_{\parallel}^2(\rho) \rangle$ are given by the form $A - B \exp(-\gamma\rho^{1/2})$ where A , B , and γ are constants dependent upon R . Sample results are shown in Fig. 2(a). Using the above form, an expression for $S'(\vec{Q})$ (for \vec{Q} parallel to the plane) can be derived, yielding

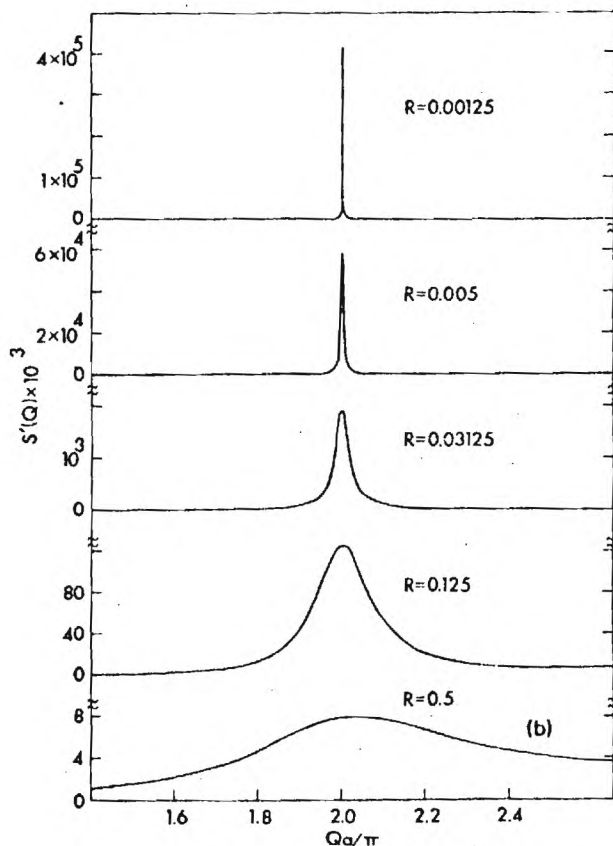
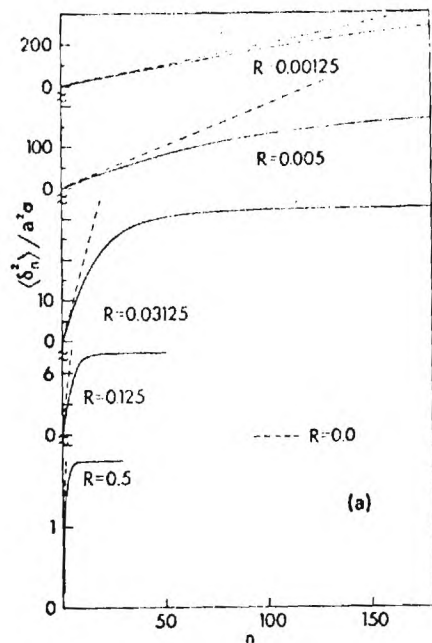


FIG. 1. 1D chain coupled to a stationary substrate chain. (a) $\langle \sigma_n^2 \rangle$ vs n , for various values of relative coupling strength R . Solid lines after Eq. (2); dashed lines correspond to the $R=0$ case. (b) Subtracted static structure factors, $S'(\vec{Q})$, around the first Bragg peak for various coupling strengths, $\sigma = 10^{-4}$. Note changes in scale.

\vec{G} are given by power-law singularities,¹⁰ $S(\vec{Q}) \sim |\vec{Q} - \vec{G}|^{-2 + \eta_{\vec{G}}(2)}$, where the bounded exponents $\eta_{\vec{G}}(T)$ are related to the elastic moduli of the lattice. We note that for both the 1D and 2D cases, the $\delta(\vec{Q}, \vec{G})$ term has been subtracted in $S'(\vec{Q})$ [e.g., Eq. (3a)]. This term which is absent in the $R=0$ limit¹¹ increases with R , i.e., increasing coherent scattering intensity at $\vec{Q} = \vec{G}$. Correspondingly, the residual $S'(\vec{Q})$ decreases in amplitude and broadens upon increased coupling to the substrate [note scales in Figs. 1(b) and 2(b)].

It is important to note that for both the 1D and 2D coupled systems the long-range-order parameters exhibit an altered asymptotic behavior, deviating significantly from the uncoupled results ($R=0$) even for small substrate coupling strengths [Figs. 1(a), 2(a)]. In fact, for both cases $\langle \delta_n^2 \rangle$ converges to a limit at microscopic distances even for small R values. Consequently, even for small couplings to the substrate strict 1D or 2D behavior is lost. This is due to the fact that by turning on the couplings to the substrate (finite R) the number of possible paths for linkage between any two atoms increases (the effective increase is related to the value of R). Thus the tendency

to maintain long-range-order increases upon coupling. These characteristics are exhibited in the integrated scattering functions [Figs. 1(b), 2(b)], which provide possible forms for the interpretation of experimental data.

While we recognize that the above model calculations employed simplifying assumptions, such as a particular geometry, range of interaction, classical description, and a stationary substrate, the essential results pertaining to the salient effects of the *dimensionality* of the system on the *degree* of long-range-order and scattering characteristics should remain valid in more general circumstances. Moreover, the first three assumptions can be easily relaxed (for commensurate arrangements) and do not modify the main conclusions. Noncommensurate configurations and couplings to extended nonstationary substrates remain the subjects of further investigations.

ACKNOWLEDGMENTS

We gratefully acknowledge discussions with H. A. Gersch, E. J. Kuster, S. K. Sinha, P. Vora, and R. A. Young. This work was supported by U. S. DOE Contract No. EG-S-05-5489.

APPENDIX

In this Appendix we outline the evaluation of the asymptotic expression for $\langle \delta_{||}^2(\rho) \rangle$ given in Eqs. (5). First, we rewrite Eq. (4) as

$$\langle \delta_{||}^2(n) \rangle / a^2 = \left(\frac{\sigma}{\pi} \right) \frac{1}{n^2} \int_0^{2n\sqrt{\pi}} dx x \frac{1 - J_0(\beta x)}{2R^2 + 1 - \cos(x/n)}, \quad (\text{A1})$$

where in terms of the lattice constant, a , the distance between two lattice sites $r_{||} (= \rho a)$ is equal to $\beta a n$ (βa is the smallest distance between lattice sites in a chosen direction, and n is an integer). Owing to the large value of n with which we are concerned, the denominator of the integral in the above equation varies much more slowly than the numerator. Therefore, we partition the integral into a sum of integrals in which the denominators are almost constant,

$$\langle \delta_{||}^2(n) \rangle / a^2 = \left(\frac{\sigma}{\pi n^2} \right) \left(\sum_{m=0}^{\tilde{n}-1} \int_{m\pi}^{(m+1)\pi} dx x \frac{1 - J_0(\beta x)}{2R^2 + 1 - \cos(x/n)} + \int_{\tilde{n}\pi}^{2n\sqrt{\pi}} dx x \frac{1 - J_0(\beta x)}{2R^2 + 1 - \cos(x/n)} \right), \quad (\text{A2})$$

where \tilde{n} is the largest integer such that $\tilde{n}\pi \leq 2\sqrt{\pi n}$. Considering the denominators in the integrands in Eq. (A2) as constant over their ranges of integration and performing the remaining integration, we obtain

$$\langle \delta_{||}^2(n) \rangle / a^2 = \frac{\sigma}{\pi n^2} \left(\sum_{m=0}^{\tilde{n}} \frac{(m + \frac{1}{2})\pi^2}{2R^2 + 1 - \cos(m\pi/n)} + \sum_{m=0}^{\tilde{n}} \frac{\cos(n\pi/n) - \cos(m+1)\pi/n}{[2R^2 + 1 - \cos(m\pi/n)][2R^2 + 1 - \cos[(m-1)\pi/n]]} \frac{m\pi J_1(\beta m\pi)}{\beta} - \frac{2n\sqrt{\pi} J_1(2\beta n\sqrt{\pi})}{\beta [2R^2 + 1 - \cos(\tilde{n}\pi/n)]} \right). \quad (\text{A3})$$

Consider the first sum in Eq. (A3). With negligible error (large n) the argument of the cosine in the denominator can be replaced by $y_m = (m + \frac{1}{2})\pi/n$. Converting to an integral we get to a good approximation the expression $n^2 F(R)$, where $F(R)$ is given

by Eq. (5b). Next, we approximate the third term in Eq. (A3) by replacing the argument of the cosine in the denominator by $2\sqrt{\pi}$ (note the above definition of \tilde{n}). Now, note that the first term in Eq. (A3) contributes a constant term, $(\sigma/\pi) F(R)$, to

the asymptotic form of $\langle \delta^2(n) \rangle / a^2$ while the third term behaves asymptotically as $n^{-3/2}$. While we have not been able to evaluate the second sum in eq. (A3) analysis of its terms for various ranges of m and R indicates that its contribution to

$\langle \delta^2(n) \rangle / a^2$ falls off asymptotically at least as fast as n^{-2} . Consequently, retaining only the contribution from the two leading terms, we arrive at the asymptotic expression given by Eq. (5).

Chemistry and Physics of One-Dimensional Metals, edited by H. J. Keller (Plenum, New York, 1977), Vol. 25B.

U. Heilmann, J. D. Axe, J. M. Hastings, G. Shiarne, A. J. Heeger and A. G. MacDiarmid, Phys. Rev. B 20, 51 (1979).

G. Dash, *Films on Solid Surfaces* (Academic, New York, 1975).

M. Platzman and H. Fukuyama, Phys. Rev. B 10, 150 (1974); C. C. Grimes and G. Adams, Phys. Rev. Lett. 42, 795 (1979).

J. Birgeneau and J. D. Lister, J. Phys. Lett. (Paris) 9, L399 (1978).

E. Peierls, Ann. Inst. Henri Poincaré 5, 177 (1935).

⁷(a) N. D. Mermin, Phys. Rev. 176, 250 (1968); (b)

B. Jancovici, Phys. Rev. Lett. 19, 20 (1967); (c)

Y. Imry and L. Gunther, Phys. Rev. B 3, 3939 (1971).

⁸J. G. Dash and M. Bretz, J. Low Temp. Phys. 9, 291 (1972).

⁹J. M. Kosterlitz and D. J. Thouless, J. Phys. C 6, 1181 (1973).

¹⁰D. R. Nelson and B. I. Halperin, Phys. Rev. B 19, 2457 (1979), and references cited therein.

¹¹V. J. Emery and J. D. Axe, Phys. Rev. Lett. 40, 1507 (1978).

¹²P. Vora, S. K. Sinha and R. K. Crawford, Phys. Rev. Lett. 43, 704 (1979), and private communications.

F. Cooper-Pairing in the Vicinity of a Localized Phonon Mode

A many-body scattering theory for the interaction of a single localized phonon with the conduction electrons of a metal is developed. Local screening is determined self-consistently by the non-linear dependence of single particle averages on dynamic two-body correlation functions. Assuming the atom executes one-dimensional harmonic oscillations only, the electronic subspace coupled to this motion is rigorously shown to be one-dimensional using the Haydock-Heine-Kelly recursion method. Two-body fluctuations off the mean one-body state are treated with one-dimensional Tomonaga-Luttinger boson techniques. A complete set of many-body eigenstates is obtained.

The study of local Cooper-Pairing ($\langle c_{1\uparrow}^+ c_{1\downarrow}^+ \rangle$) yields a simple criterion for anomalous enhancement of pairing fluctuations in the normal-metal phase. For a half-filled conduction band, neglecting screening, it is simply

$$K = \frac{32}{\pi} \left(Z \frac{e^2}{a} \right)^2 \frac{1}{a^2 W} ,$$

where K is the effective spring-constant of the vibrating impurity of charge Ze , a is its distance to the nearest electronic shell and W is the band-width. The origin of this effect is the appearance of an electron-hole scattering resonance in the long-wavelength portion of the many-body continuum.

We are concerned particularly with the question of relating the microscopic parameters which characterize a localized optic mode and its coupling to the electron gas of a metal in which it is embedded, to the effect which this interaction has on the local distribution of Cooper-pairs in the vicinity of the impurity.

Our approach is unusual. We begin by considering a microscopic model Hamiltonian for the electrostatic coupling of a charged vibrating interstitial impurity with the conduction electrons of a metal when these are in the immediate

vicinity of the impurity. The model is a charge-transfer model in the sense that the conduction electrons are not allowed to hop onto the impurity. This type of situation is expected to occur, for example, in the absorption of a single hydrogen atom by a transition metal where it is believed that the hydrogen's electron settles in low-lying, hybridized, hydrogen-metal bonding states. This charge-transfer assumption is dispensable, however, and is introduced to minimize the ensuing complexities. With little modification this theory may also be applied to the study of a substitutional rather than an interstitial defect.

A complete set of approximate many-body eigenstates will be obtained for this Hamiltonian using a self-consistent procedure, termed Self-Consistent Lattice Bosons (S.L.B.) which has recently been applied to the study of a magnetic impurity problem, the Wolff model.

The S.L.B. method is an unambiguous procedure which yields an approximate set of self-consistent many-body eigenstates for a class of impurity problems in metals and alloys. The class of problems for which it is most naturally suited satisfy two basic conditions:

Condition 1. They are "Weak-Coupling" problems in the sense that a self-consistent Hartree-Fock (H.F.) analysis of them yields a single non-degenerate H.F. - ground state. That is, the mean-field ground state is unique. In general, this requirement translates into a restriction on the magnitude of the parameters appearing in the microscopic Hamiltonian. Only in this restricted region may one hope to achieve a straightforward S.L.B. diagonalization of the problem.

(Figure 1). Bonding of the impurity to the metal and its interaction with core electrons is assumed to be accounted for by $K'_0 > 0$ of (3). A single band of conduction electrons which hop itinerantly by the action of (2) is assumed. For technical reasons it is necessary to assume that the impurity (of mass M_0) executes oscillations along a single spatial direction, the x-direction. Coupling of the conduction electrons to the impurity is electrostatic in origin. The impurity of charge Ze (either positive or negative) couples to the total (proton + electrons) charge assumed localized on the two sites at $\pm ax$. The F.C.C. lattice constant is $2a$ (Figure 1). In (4), $0 \leq \rho \leq 2$ parametrizes the valency of the metal ions with $\rho = 1$ for a 1/2-filled conduction band. Finally ΔU in (5) describes correlation effects in the conduction band. Concerning the origin of this term, two points of view are possible. The first presumes the Hamiltonian (1) to describe the interaction of the impurity with a band of real electrons in which case $\Delta U > 0$ parametrizes local correlation effects while distant correlations are neglected. The alternate view interprets (1) as describing the coupling of the impurity to a band of non-interacting quasi-electrons resulting from a partial diagonalization of a (weakly-correlated) electronic Hamiltonian over sites not neighbouring the impurity. In this case (5) results from the impurity's destruction of translational invariance. ΔU parametrizes a residual correlation between quasi-electrons and could be negative though it is generally expected to be positive. This latter interpretation has recently been applied to a self-consistent theory of metallic magnetism.

Implementation of the S.L.B. method may be achieved in 7 steps:

Step 1. Separation of the one-body (mean-field) terms from the many-body-fluctuations contribution to the impurity Hamiltonian and approxi-

mation of the latter by their leading-order two-body processes to include: terms at most bi-quadratic in fermion creation and destruction operators; terms linear in bosons and quadratic in fermions; terms quadratic in bosons.

- Step 2. Re-expression of the local two-body-fluctuation terms as a sum of bi-linear products of eigenoperators of an element of the symmetry group of the kinetic energy operator.
- Step 3. Application of the Haydock-Heine-Kelly (H.H.K.) recursion method to obtain the one-dimensional kinetic manifold which couples to each of the local fluctuation operators identified in Step 2. Symmetry ensures that the one-dimensional subspaces obtained will be orthogonal and dynamically independent.
- Step 4. Self-consistent Hartree-Fock diagonalization of all the independent one-body Hamiltonians obtained in Step 3. In general, these Hartree-Fock problems will be parametrized by two-body correlation functions over the fluctuation variables which are yet to be determined. Also this step will generally necessitate some approximation to the near-defect one-dimensional kinetic energy matrix elements.
- Step 5. Transformation of the two-body Hamiltonian terms by the unitary operations which removed one-body terms in Step 4. This introduces an important mean-field renormalization of one-electron wave functions.
- Step 6. Approximation of the renormalized one-electron wave function by their fermi-level value and factorization of these from the band-sum representations of the symmetry-resolved fluctuation operators. In this manner a mean-field renormalization of two-body coupling constant is achieved.

Step 7. Application of one-dimensional Tomonaga-Luttinger (T.L.) bosonization methods to the diagonalization of the resulting multichannel scattering problem. A complete set of (boson) eigenoperators of the defect Hamiltonian are obtained.

Details of the application of the above procedure to the Hamiltonian given in Eqs. (1-6) will be reported in due course. Once the approximate set of many-body eigenstates is found an approximate representation of the local Fermion operators is constructed and the local Cooper-pair enhancement factor

$$R = \frac{\langle C_{1\uparrow}^+ C_{1\downarrow}^+ \rangle (z)}{\langle C_{1\uparrow}^+ C_{1\downarrow}^+ \rangle (z=0)}$$

analyzed. It is shown to diverge subject to the criteria mentioned above.

Analysis of the influence of adsorbate (or impurity) local modes at surfaces on local Cooper-pairing enhancement is currently being pursued.

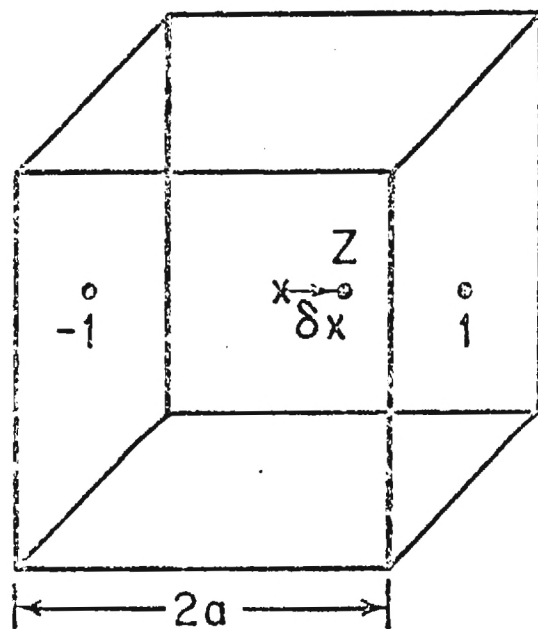


Figure 1. We obtain approximate many-body eigenstates for the electrostatic interaction of a single vibrating impurity of mass M_0 and effective charge Ze with the conduction electrons of an F.C.C. metal. The impurity, whose stable position is the octohedral site of the central cell, is assumed to execute one-dimensional harmonic oscillations along the x-axis, only. It interacts with conduction electrons when they are located at sites labeled $j = \pm 1$. $2a$ is the F.C.C. lattice constant.

G. LOCAL ELECTRONIC PROPERTIES: Si

1. INTRODUCTION

A. The Nature of Cluster Calculations

Increased resolution and sensitivity of experimental bulk and surface analytical probes in the last two decades have produced results well correlated with the microscopic properties of solids. However, the conventional band theories of solids, primarily developed to understand bulk properties of crystalline solids, have undergone extensive modifications in efforts to accommodate phenomena such as impurities, vacancies, surfaces, interfaces, and other defects. These phenomena generally enter the theoretical framework as perturbations on the long-range order of a crystalline solid system. Conventional condensed matter theories apparently cannot handle with ease such problems as lattice distortions, isolated defect charge states, interstitials, polycrystalline matter, and amorphous matter.

Acting on the premise that the details of the local geometry and the electronic microstructure, in terms of local bonding directionality and inhomogeneous charge distribution, may be more important in certain cases than extended condensed matter properties, one is led to consider clusters of atoms as a preliminary model. The obvious treatment for the first attempting to model local properties of condensed matter systems is to define one cluster of atoms in an arbitrary geometrical arrangement and model it's environment, which represents the remainder of the solid, in a realistic way. In contrast, then, to conventional theories of solids, the local region is perturbed by the environment. The advantage of the cluster concept is that it can be used to study in detail phenomena at least of short-range nature, incorporating flexibility in the specification of geometry, atomic species and electronic

configuration. Perhaps concepts involving multiple clusters could also be developed for polycrystalline or amorphous studies.

Quantum chemistry methods have presently evolved to the point of handling "large" clusters of 10-30 atoms based on ab-initio theories of electronic structure. The use of a rigorous theory, based on fundamental principles, for the calculation of the local electronic microstructure of a cluster with the inclusion of environmental effects in some manner represents an alternative approach to the traditional theoretical description of condensed matter.

The size of the cluster necessary to simulate an imperfect local region may be qualitatively determined by considering the range of interaction of the imperfection. One prerequisite for a valid cluster calculation, then, is that an imperfection must be well screened within the confines of a cluster boundary. Another consideration, not often mentioned, is that the cluster size should not be chosen very large because of the well known deficiencies of the fundamental theories, for example, Hartree-Fock, when they are applied to extended systems.

The development of a model to include the environmental effects of a cluster and, hence, the remainder of the solid, which is coupled to the cluster is a largely unexplored area. The best attempts appear to be that of Grimley and Pisani in the context of local chemisorption. In many cluster calculations, claiming to be representative of solids in terms of localized properties, environmental effects are totally ignored. This appears to be generally the case for metal substrates. For the case of host systems with covalent bonds, the neglect of environmental effects is more serious due to unpaired electrons at the cluster boundary, so-called "dangling bonds". For homopolar semiconductors, these unpaired electrons are associated with cluster surface states and manifest themselves within the forbidden energy gap. First attempts at

modeling the environment of such systems have relied on adding atoms to the cluster proper in the context of "bond saturators". Since the saturators are actually part of the cluster, they are self-consistently connected to the local cluster of interest. This model has the disadvantage of not providing an absolute reference between systems when the cluster of interest is changed. The development of a good environmental model must have the requirements that in the limit that the local cluster is "perfect", bulk results are obtained, and that when the local cluster is imperfect, results must be related to bulk results (i.e., band edges, charge densities, local densities of states, etc.). The comparison of results of a good cluster/environmental model to cluster models neglecting the environment or modeling it by "saturators" may, in addition, define better the range of problems accessible by the less sophisticated models. The development of a hybrid cluster/environment scheme is currently in progress by the authors.

B. Hydrogen-Bounded Silicon Clusters

In an effort to assess the quality of using 12 hydrogen "saturators" for environmental modeling of a cluster of 5 silicon atoms arranged geometrically in tetrahedral coordination, ab-initio calculations have been performed variationally and self-consistently to determine the electronic microstructure.

As our method of calculation we use the unrestricted Hartree-Fock (UHF-SCF) procedure. In general, the calculations are done using an ab-initio effective core potential for the 10 core electrons on each silicon center. However, test calculations have been done which include all electrons on a silicon center.

The UHF method, coupled with the frozen HF effective core and symmetry projection, provides a first-principles testing ground for medium size clusters (10 ~ 20 atoms) limited primarily by current computational facilities. As with all cluster models, based on HF theory or derivatives thereof, the "range of

application and flexibility" should be qualified relative to the basic approximations used.

Atomic silicon and several different geometries of hydrogen-bounded and unbounded silicon clusters have been studied primarily directed at establishing the validity of the Si_5H_{12} cluster in terms of the selection of an appropriate basis set. The cluster species studied include: Si^{ae} , Si , $\text{Si}^{\text{ae}}\text{H}_3$, SiH_3 , $\text{Si}^{\text{ae}}\text{H}_4$, SiH_4 , Si_2H_6 , Si_5 , $\text{Si}^{\text{ae}}\text{H}_{12}$, Si_5H_{12} , and Si_8 , where the superscript "ae" designates a silicon center including all electrons. In the cases where "saturating" hydrogen atoms are used, the Si-H bond lengths have been varied over the range 1.332 \AA to 2.6 \AA , retaining tetrahedral coordination, in order to assess the "saturation" placement with respect to the silicon core.

2. CLUSTER GEOMETRIES AND BASIS SETS

Figure 1 illustrates the geometrical arrangement chosen for the 17 atom cluster Si_5H_{12} . A central silicon atom is at the origin, surrounded by four silicon nearest neighbors in tetrahedral coordination with Si-Si bond lengths of $b_{\text{Si}} = \frac{\sqrt{3}}{4} a = 2.3517 \text{ \AA}$, where a is the lattice constant of bulk silicon. Surrounding the shell of nearest neighbors are hydrogen atoms (or saturators) in tetrahedral coordination with the central Si_5 complex. In this study, the 12 Si-H bond lengths, b_{H} , have been varied simultaneously, retaining the underlying tetrahedral (T_d) symmetry. The Si-H bond lengths have been varied over the range 1.332 \AA to 2.6 \AA encompassing the experimental bond lengths of 1.48 \AA in silane (SiH_4) and the Si-Si distance of 2.3517 \AA in bulk silicon. The values of b_{H} chosen are 1.332 , 1.48 , 1.776 , 2.1 , 2.3517 , and 2.6 \AA .

Defining the quantities:

$$\alpha = \frac{a}{4} = \frac{b_{\text{Si}}}{\sqrt{3}}$$

$$\beta = \frac{b_{\text{H}}}{\sqrt{3}}$$

$$\delta = \alpha + \beta$$

$$\sigma = \alpha - \beta ,$$

the coordinates of Si_5H_{12} are tabulated in Table 1.

The 8 atom clusters Si_2H_6 and Si_8 , used for supporting studies, retain the tetrahedral bonding angles and have C_{3v} symmetry (no inversion symmetry). All Si-Si bonds are fixed at the b_{Si} value and in the case of Si_2H_6 , the Si-H bond lengths have been varied.

3. RESULTS AND DISCUSSION

A. Groundstate and Excited State Calculations

The Si_5H_{12} cluster has a singlet groundstate with a closed-shell configuration of 32 electrons. By virtue of its tetrahedral point group symmetry (T_d), the electronic eigenfunctions may be classified according to 5 irreducible representations: a_1 , a_2 , e , t_1 , and t_2 (singly, doubly, and triply degenerate).

Figure 2 illustrates the change in total energy as a function of all twelve hydrogen "saturators" being placed at one of the six bond lengths (1.332, 1.48, 1.776, 2.1, 2.3517, or 2.6 Å), but still in tetrahedral coordination with the fixed cluster core of 5 silicon atoms. The minimum of the groundstate curve lies at 1.48 Å, which is expected, since this is the experimental Si-H bond length in silane (SiH_4) where sp^3 -s bonds are also found. The minimization of total energy, based on variational self-consistent techniques, for predicting geometry is well established for molecular systems. However, there is no a-priori reason for using the equilibrium Si-H distance when the hydrogens are used as "saturators" for the simulation of silicon.

In addition, Figure 2 illustrates the total energies for an excited state configuration where an electron is forced from an orbital of $3t_2$ symmetry to occupy an orbital of $3a_1$ symmetry. A dynamic symmetry searching procedure has been implemented during each iteration to insure the desired occupation numbers for the orbitals due to the fact that energetically close-lying orbitals of different symmetries often switch positions. Figure 3 illustrates the energy switching for the groundstate $1t_1$ symmetry's orbital energy as a function of Si-H bond lengths.

In Figure 3, the orbitals with symmetries $1a_1$, $2a_1$, $1e$, $1t_2$, $2t_2$, $3t_2$, and $1t_1$ are all fully occupied with 32 electrons and the orbitals $3a_1$, $4t_2$, and $2e$ are the first 3 unoccupied symmetries. Since Si_5H_{12} is closed-shell, the

spin up and spin down electrons are degenerate. By analysis of the basis function coefficients and the charge densities of the $1t_1$ and $2e$ symmetry orbitals, it is found that they contribute minimally to the bonding of the central silicon atom and are delocalized in the outlying region of the cluster, contributing to the Si-H bonds. In contrast, the orbitals of symmetry a_1 and t_2 are found to contribute predominately to the bonding region about the central silicon with moderate contributions from the outlying hydrogens. Since the central core of 5 silicons has been geometrically fixed in the calculations, Figure 3 illustrates, in particular, the rapid movement of the $1t_1$ and $1e$ states with respect to the others in the valence band based on hydrogen placement. One importance consequence of "saturator" placement is that, in effect, the levels associated with the "saturators", and hence the environment can be moved to anywhere desired with respect to levels localized in the central cluster region. The Si-H bond length then could be considered as an adjustable parameter and is perhaps analogous to surrounding the cluster with a directional self-consistent potential. The SCF-X α -SW silicon calculations generally include the directional hydrogen spheres but also include a Watson sphere surrounding the entire cluster with an adjustable charge. Fazio has suggested that the Watson sphere by itself, with a fixed charge equal to that of the unpaired electrons, is a successful model of the semiconductor environment. It is unclear what effect the loss of bonding directionality by the uniform distribution of charge on the Watson sphere has on Si-Si bonds within the cluster.

If the assumption is made that the $1t_1$ symmetry is representative of the bulk valence band edge, some credence can be given to the selection of the 2.3517 \AA^0 Si-H bond length based on the observation in Figure 3 that the $1t_1$ and $3t_2$ states are nearly degenerate. It is observed that the $1t_1$ and $3t_2$ levels become degenerate at the distance of $\sim 2.30 \text{ \AA}^0$. Since the central atom

is a silicon and the $3t_2$ state is associated with the central region, the (near) degeneracy can be associated with a self-consistent match of the central cluster to the "saturators", i.e. environment. Cartling, using SCF-X α -SW with the same geometry, points out that "the high location of the $1t_1$ level [with respect to the $3t_2$ level] is probably due to the model inequivalence of equal atoms". In the UHF cluster, the same symmetry ordering is obtained, and in addition to the above remark, we conclude that the $1t_1$ level can be adjusted based on the "saturator" placement. Since the $3t_2$ orbital is predominantly representative of the central silicon atom bonding, it is perhaps more representative of the valence band edge in the local region, in agreement with Cartling. Any localized excitations from the top of the valence band should be performed with this symmetry.

It is observed in Figure 3 that for Si-H bond lengths less than 2.30 Å, the $1t_1$ and $1e$ levels become further depressed in the valence band. If the $1t_1$ and $1e$ symmetry states are associated with unwanted cluster surface states, as in the Si_5 cluster, the addition of hydrogens at distances near the Si-H equilibrium distance results in the transferral of these states deep into the valence band.

The selection of either the 1.48 Å or 2.3517 Å "saturator" distance used by different authors, is shown by UHF to have significantly different electronic character based on the total energies and orbital symmetry order. Furthermore, the results for the two different distances question as to what role the "saturators" should actually play - that of modeling the environment or that of just eliminating unwanted states from the forbidden energy gap.

B. Cluster Band Gap Calculations

The "cluster band gap" is now defined as the energy difference required for a localized excitation of an electron from the highest occupied cluster orbital to the lowest unoccupied cluster orbital where the orbitals are primarily localized in the central region. This last qualifying statement prohibits, for example, the participation of e and t_1 symmetry orbitals. As remarked previously, the $3t_2$ symmetry orbital is representative of the central silicon bonding region and is shown, in Figure 2, to be at the top or just beneath the $1t_1$ symmetry level in the energetic order of occupied states. In addition, the $3t_2$ orbital is predominately p character and can be associated with the Γ'_{25} ($\vec{k} = 0$) point at the top of the valence band in bulk silicon. The lowest unoccupied states in the clusters are of $3a_1$ symmetry and are also found to be primarily located in the central region of the cluster but possess predominantly s character. The $3a_1$ state might be associated with the Γ'_2 ($\vec{k} = 0$) conduction band state which is known to be of s character, but is not the conduction band minimum. The association of the $3a_1$ orbital with other non-zero \vec{k} points in the Brillouin zone, such as the conduction band minimum at $\vec{k} \approx 0.8 X_1$, is questionable since classification based on an atomic orbital model is known to be deficient. Nevertheless, if the cluster model does represent silicon in some manner, the transition of an electron from $3t_2$ to $3a_1$ symmetry should represent some localized low-energy transition and is favored by selection rules. Whether such a cluster model can represent the true energy band gap to any degree of accuracy, since this is an intrinsically extended bulk property of a semiconductor, is questionable. In fact, Phillips points out that in a bond model for semiconductors, the difference between averages of antibonding and bonding energies, called the "bond energy gap", is in general much greater than the conventional energy band gap defined by the maximum valence and minimum

conduction band edges. For silicon, the bond energy gap is 4.77 eV and the band energy gap is 1.1 eV at room temperature. For the lowest cluster excitation ($3t_2-3a_1$), one should expect the transition energy to be in this range if the model is appropriate at all.

Figure 4 illustrates the calculation of the cluster band gap for the various Si-H bond lengths. Curve (a) is the difference between the ground-state $3t_2$ and $3a_1$ orbitals energies, interpreted by Koopmans' theorem, which includes no hole electronic relaxation. In contrast, curve (b) utilizes a Δ SCF approach, by taking the difference between the total energies of the excited state and groundstate calculations, and, hence, includes the electronic relaxation due to the presence of a "valence band" hole. The difference of the two curves in Figure 4 is a measure of the hole electronic relaxation and can be considered significant compared to the expected transition energy range of 1.1 - 4.8 eV. The relaxing of symmetry in the UHF method could even increase this electronic relaxation. One might question the results of the SCF- $X\alpha$ -SW calculations for silicon when they are based on a Koopmans' theorem analysis and even when a "transition-state" procedure is used where the occupation of an electron is split between the levels of interest. The curious rise in the Koopmans' theorem curve at 2.3517 \AA is due to the switching of the $3t_2$ and $1t_1$ orbital energies. Based on Figure 3, the calculation of intermediate distances apparently would show the local minimum of this curve to be around 2.3 \AA , where the degeneracy occurs. Note that the Δ SCF curve, however, continues its downward trend. Based on the expected transition energy range, bounded by the bond and band energy gaps on Figure 4, one notes that "saturation" distances at least greater than 2.1 \AA should probably be used.

C. Charge Densities

In addition to the energetic properties discussed previously, charge densities are analyzed in this section to characterize more fully the details of the electronic microstructure. Figure 5a illustrates the groundstate charge density of the $[\bar{1},1,1]$ plane in the cluster and includes the central silicon atom, two nearest silicon neighbors, and two hydrogens located at the boundary. It is observed that the central silicon forms covalent bonds with the nearest neighbors and that partially ionic Si-H bonds are found with charge piled up on the hydrogens. Figure 5b focuses in on the central silicon and two of its bonds. Figure 5c is a further magnification of one Si-Si bond, with the central silicon at the bottom and the next-nearest neighbor near the top. Qualitatively and quantitatively, the charge density results for all of the Si-H bond lengths studied are remarkably similar in the cluster core region-described in this plane by the three silicon atoms. Three important points are noticed concerning the Si-Si bond in Figure 5c. First, the charge density is symmetric about both the bond axis and a line perpendicular to the bond axis through the bond midpoint. Secondly, the Si-Si bond is elongated along the bond axis. Thirdly, there apparently exists two areas of maximum electron concentration along the bonding direction giving rise to the hourglass appearance of the contours.

Symmetry, parallel and perpendicular to the bond, is naturally expected for the bonds appearing in the bulk system, but not expected a priori in the hydrogen-bounded Si cluster where the central and nearest-neighbor atoms are inequivalent in terms of bonding. The fact that symmetry perpendicular to the bond does exist and that the hydrogens are not the dominant contributors in this region suggests that the cluster model with a "saturated" boundary may

represent with accuracy some details of bulk silicon. Figure 6 shows a line scan of the charge density along the bond axis. One observes that some asymmetry begins to become evident at the smaller Si-H distances.

The result that the Si-Si bond is elongated in the direction of the bond axis is in agreement with experimental x-ray diffraction results and non-local pseudopotential calculations, as illustrated in Figure 7a and 7b. Earlier local pseudopotential results, shown in Figure 7c, show elongation perpendicular to the bond.

In disagreement with the experimental x-ray diffraction and pseudopotential results, the UHF cluster does not yield the maximum charge density at the midpoint of the bond. Instead the charge density has two maxima symmetrically located, as shown in Figures 5c and 6, with a small depression in the midpoint region. Figure 6 also illustrates the charge densities along a Si-Si bond for the x-ray and non-local pseudopotential results for a comparison of absolute magnitudes. It is observed that the magnitude and slope of the cluster charge densities outside of the midpoint region compare relatively closely. It is perhaps remarkable that such a small cluster, computed with ab-initio methods can yield, at least, comparable results to bulk silicon. It is also worthwhile to observe that the experimental x-ray results, in Figure 7a, shows evidence of the bond being more elongated and charge pulled more towards the atomic sites - resulting in a "pinched" appearance of contours at the outskirts of the bond. These details are not apparent in the pseudopotential results, shown in Figure 7b, where the contours are essentially elliptical and not very elongated.

In order to assess the quality of the charge densities for Si_5H_{12} , supporting studies have been performed on $\text{Si}^{\text{ae}}\text{Si}_4\text{H}_{12}$, Si_2H_6 , and Si_8 clusters.

The $\text{Si}^{\text{ae}}\text{Si}_4\text{H}_{12}$ cluster possesses all of the electrons on the central silicon and was used to assess the quality of the effective core potential. Energetically the system exhibits valence orbital energies very close to the Si_5H_{12} results establishing the adequacy of the core potential. Figure 8 illustrates the Si-Si region, with only the valence orbitals included in the charge density. Qualitatively the hourglass appearance is similar, however, some asymmetry is noted. A line scan along the bond shows good quantitative agreement with the previous results.

Figure 9 illustrates the charge density results, in a plane with a Si-Si bond and two hydrogens, of an Si_2H_6 cluster. Gaussian type p-functions were optimized on the silicon atoms and p-functions added on the hydrogens in order to test for basis set deficiencies. Results showed little change in the energetics and essentially no change in the qualitative appearance of the Si-Si bonding region.

An Si_8 cluster was studied to see if next-nearest neighbor effects or hydrogen bonding effects might produce "detrimental" results for the Si_5H_{12} cluster. Figure 10 illustrates the charge density in a region containing 4 silicon atoms. Each "central" silicon has four nearest neighbors and three next-nearest neighbors. Qualitatively, the central Si-Si bond also exhibits the double maxima and hourglass appearance characteristic of the other clusters. Due to the lack of any environment, one notices the asymmetry in the outlying covalent Si-Si bonds. The Si_8 result illustrates that the hydrogens possibly have very little effect on the charge density of the central bonding region.

Based on supporting studies including basis set analyses, hydrogen bonding effects, next-nearest neighbor effects, and core potential effects, we conclude that the inability to represent accurately the precise charge density in the central bonding region might be the lack of correlation or relativistic corrections

to UHF. In addition, charge densities of the $3t_2 \rightarrow 3a_1$ excited system have been studied giving similar qualitative results.

The overall analysis of charge density results suggest that the environmental effects have very little effect on the central bonding region of the Si_5H_{12} cluster.

The variation of Si-H bond lengths and even the use of silicons as next-nearest neighbors has been shown to affect the central charge distribution minimally. However, the effect on the energetics of the cluster has been shown to be dramatic, in terms the "cluster band gap", the total energies, the $1t_1$ and $1e$ orbital energies, and the occupation of electronic states.

LIST OF FIGURES

1. Geometry of an Si_5H_{12} Cluster.
2. Variation of Total Energy with All Si-H Bond Lengths for a Si_5H_{12} Cluster,
 - a. groundstate
 - b. excited state ($3t_2 \rightarrow 3a_1$).
3. Groundstate Orbital Energies for Different Si-H Bond Lengths.
4. Cluster Band Gap ($3t_2 - 3a_1$) for Different Si-H Bond Lengths,
 - a. Koopmans' theorem
 - b. ΔSCF
5. Si_5H_{12} Groundstate Charge Density in the $[\bar{1},1,1]$ plane, Si-H Bond Lengths: 2.3517 Å, units of $(\frac{e}{\Omega_c})$.
 - a. Entire cluster region.
 - b. Si-Si-Si region.
 - c. Si-Si region.
6. Charge Density Line Scans Along Si-Si Bond Axis.
7. Bulk Silicon Charge Density.
 - a. Experimental
 - b. Local Pseudopotential
 - c. Non-local Pseudopotential
8. $\text{Si}^{\text{ae}} \text{Si}_4\text{H}_{12}$ Groundstate Valence Charge Density in the $[\bar{1},1,1]$ plane, Si-H Bond Lengths: 2.3517 Å, units of $(\frac{e}{\Omega_c})$.
9. Si_2H_6 Groundstate Charge Density in the Si-Si Bonding Plane including 2 Hydrogens; Si-H Bond Lengths: 1.480 Å, units of $(\frac{e}{\Omega_c})$.
10. Si_8 Groundstate Charge Density in the $[\bar{1},1,1]$ plane, all Si-Si Bond Lengths are 2.3517 Å, units of $(\frac{e}{\Omega_c})$.

LIST OF TABLES

1. Coordinates of an Si_5H_{12} Cluster (T_d symmetry).
2. Effective Core Potential for Silicon.
3. Contracted Valence Basis Set for Silicon (2s/2p).

TABLE 1

Coordinates of an Si_5H_{12} cluster (T_d symmetry).

(1)	Si	(0,0,0)	Central
(2)	Si	$(-\alpha, -\alpha, -\alpha)$	} Nearest Neighbors to (1)
(3)	Si	$(\alpha, \alpha, -\alpha)$	
(4)	Si	$(\alpha, -\alpha, \alpha)$	
(5)	Si	$(-\alpha, \alpha, \alpha)$	
			Next-Nearest Neighbors
(6)	H	$(-\sigma, -\sigma, -\delta)$	} to (1) through Si(n)
(7)	H	$(-\sigma, -\delta, \sigma)$	
(8)	H	$(-\delta, -\sigma, -\sigma)$	} n=3
(9)	H	$(\sigma, \sigma, -\delta)$	
(10)	H	$(\delta, \sigma, -\sigma)$	
(11)	H	$(\sigma, \delta, -\sigma)$	} n=4
(12)	H	$(\sigma, -\delta, \sigma)$	
(13)	H	$(\sigma, -\sigma, \delta)$	
(14)	H	$(\delta, -\sigma, \sigma)$	
(15)	H	$(-\delta, \sigma, \sigma)$	} n=5
(16)	H	$(-\sigma, \sigma, \delta)$	
(17)	H	$(-\sigma, \delta, \sigma)$	

TABLE 2

Effective core potential for Silicon.

$L = 2 = d$	k	$n_{k\ell}$	$\alpha_{k\ell}$	$c_{k\ell}$
$r^2 \left[\hat{U}_d(r) - \frac{10}{r} \right]$	1	1	80.0	-10.0
	2	2	0.03010	-0.00071
	3	2	0.36711	-0.10869
	4	2	4.72826	-12.76985
$r^2 \left[\hat{U}_p - \hat{U}_d(r) \right]$	1	0	0.40235	0.97766
	2	0	1.99278	2.63443
	3	2	0.81559	0.35334
$r^2 \left[\hat{U}_s - \hat{U}_d(r) \right]$	1	0	12.49710	-0.43633
	2	0	0.58244	2.54384
	3	2	5.80343	25.82973

TABLE 3

Contracted Valence Basis Set for Silicon (2s/2p).

	Exponents	Coefficients
S-1	2.01139	-0.157747
	0.19160	0.86492965
S-2	0.04268	1.0
P-1	6.17212	0.0120628
	0.40375	-0.314719
	0.14448	-0.584655
	0.04925	-0.23348
P-2	0.1	1.0

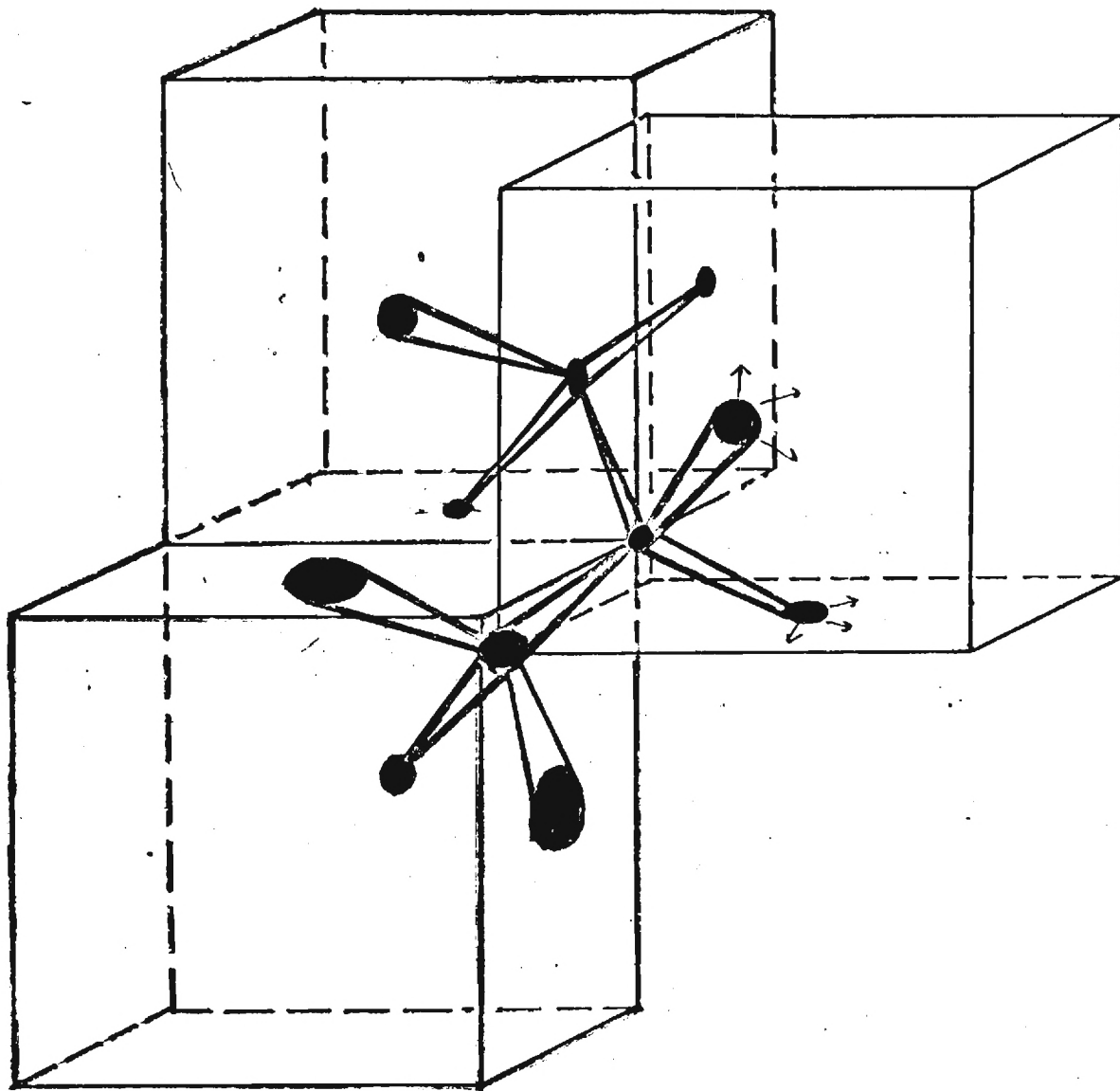


Figure 1

TRANSPAREX

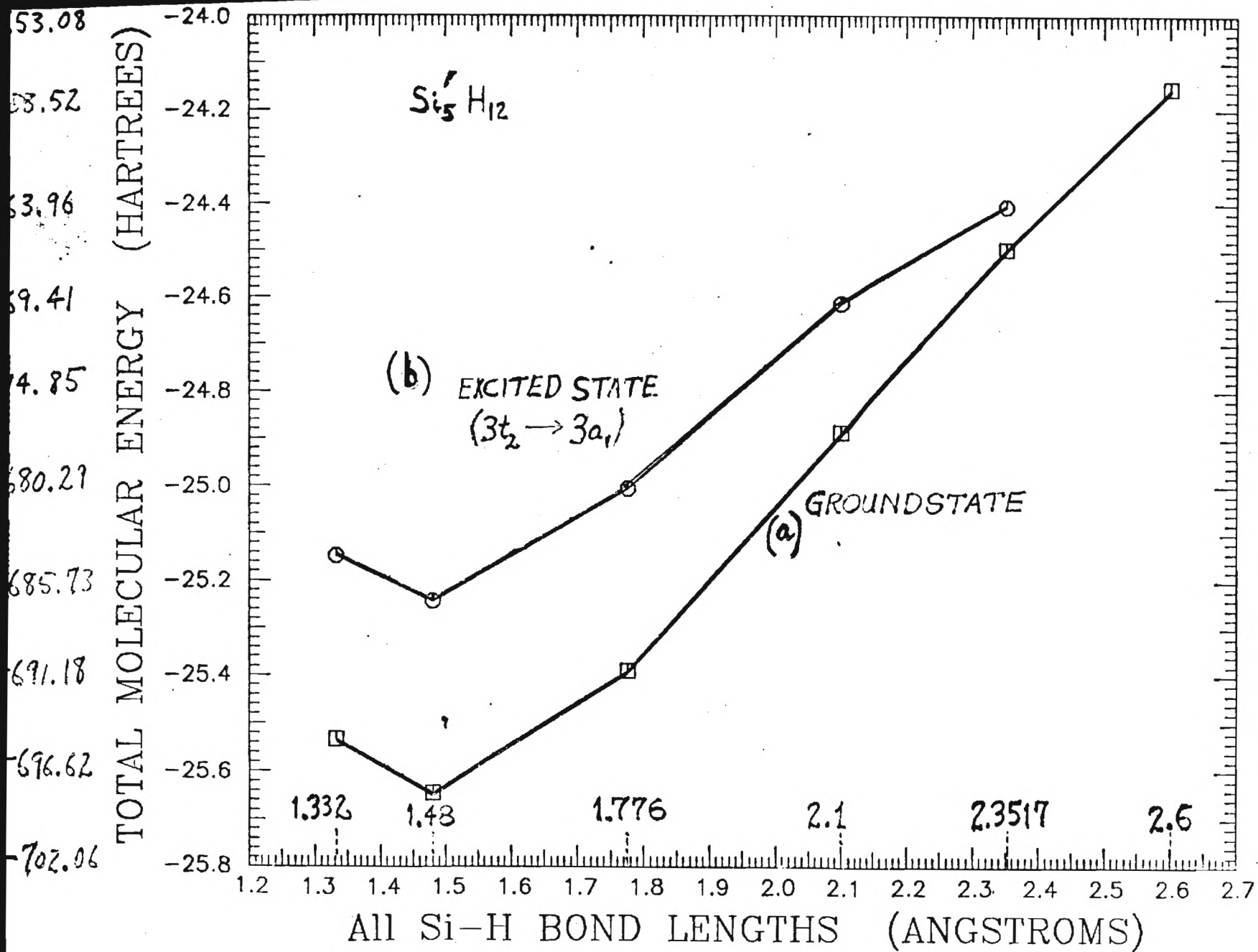


Figure 2

TRANSPAREX

GROUNDSTATE ORBITAL ENERGIES (HARTREES)

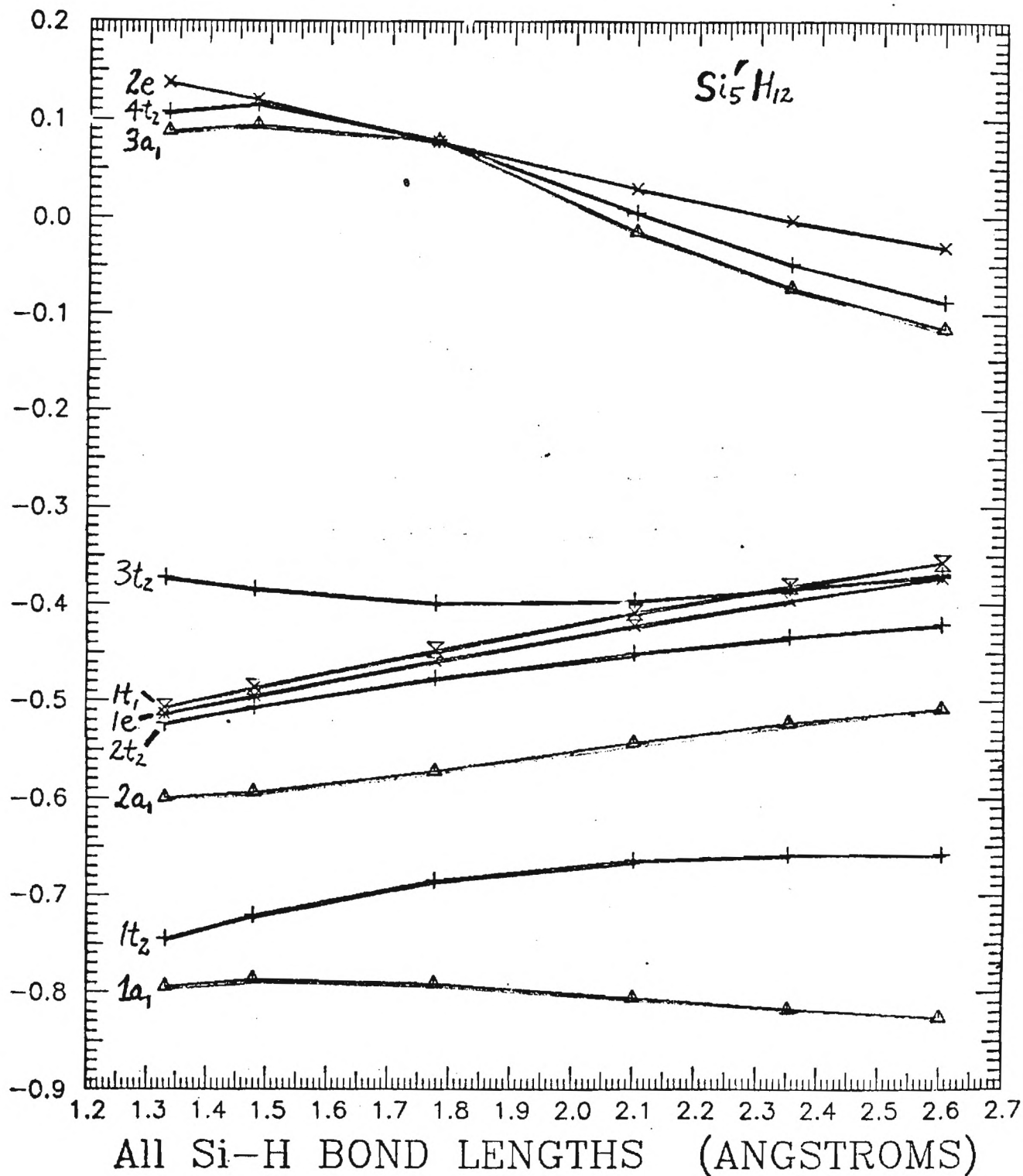


Figure 3

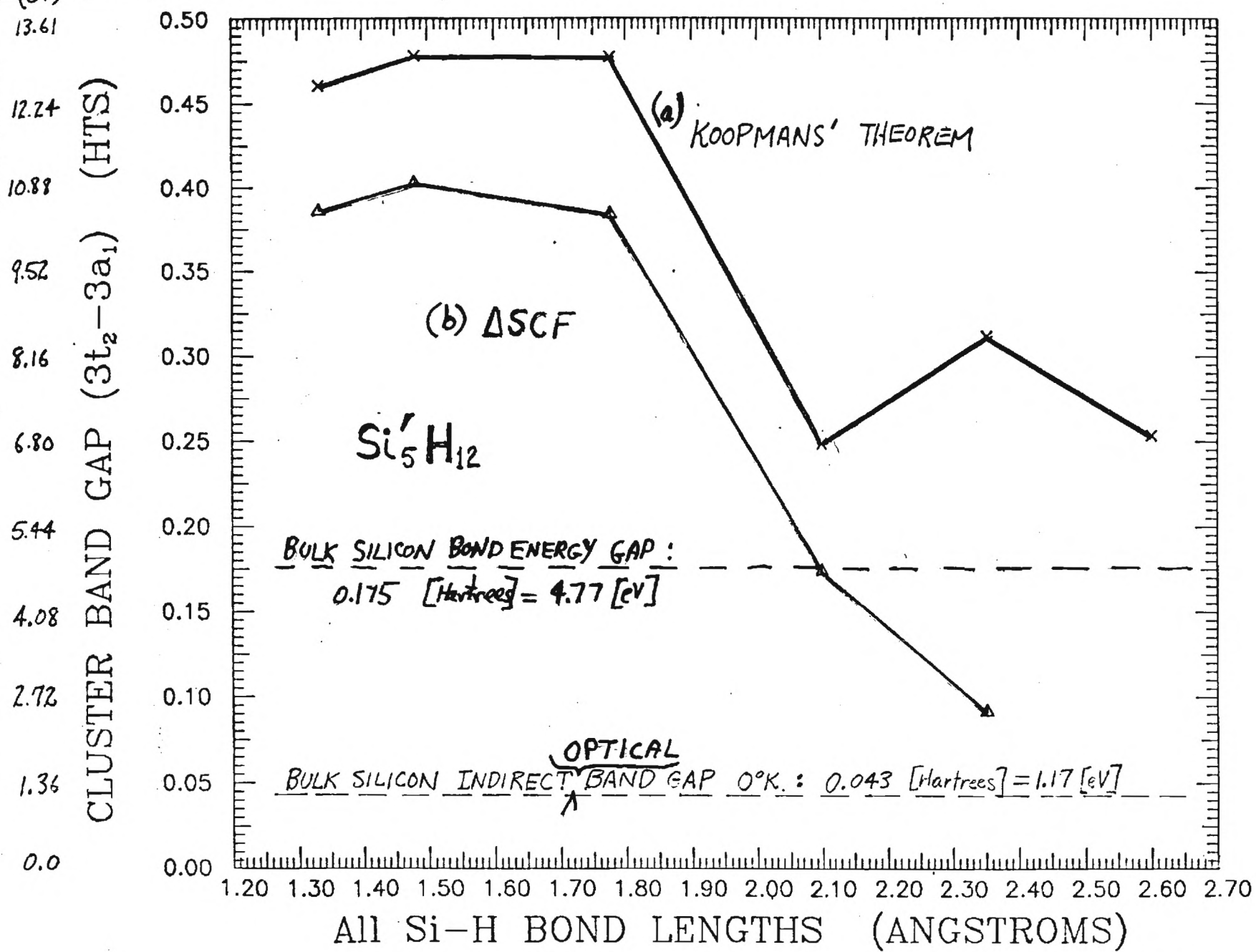
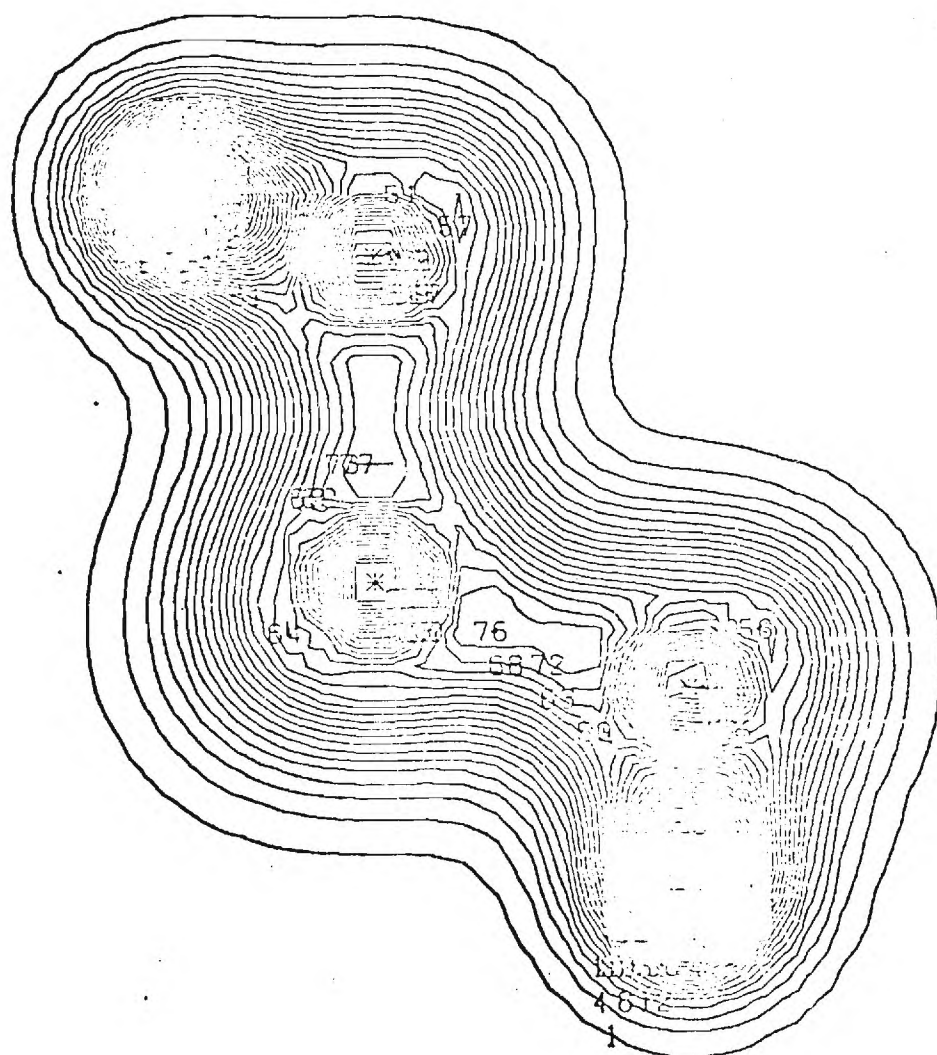


Figure 4

TRANSPAREX

SI5H12 CLUSTER 1.480 ANGSTROM
GROUNDSTATE



9.0

0.0

(A)

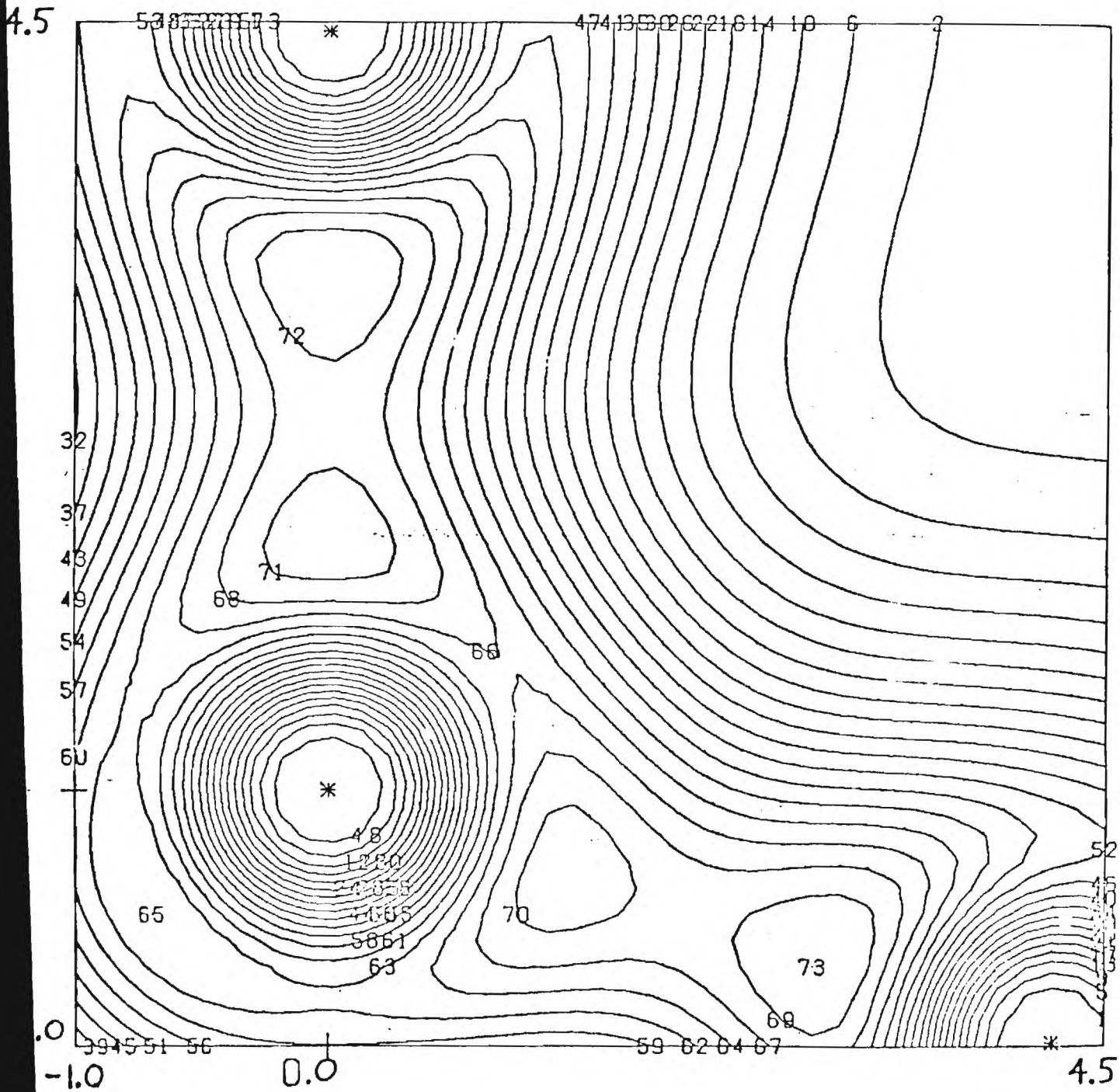
9.0

IN [-1, 1, 1] PLANE

FIGURE 5a

TRANSPAREX

SI5H12 CLUSTER 2.3517
ANGSTROMS GROUNDSTATE



IN [-1, 1, 1] PLANE

FIGURE 5b

SI5H12 CLUSTER 2.3517
ANGSTROMS GROUNDSTATE

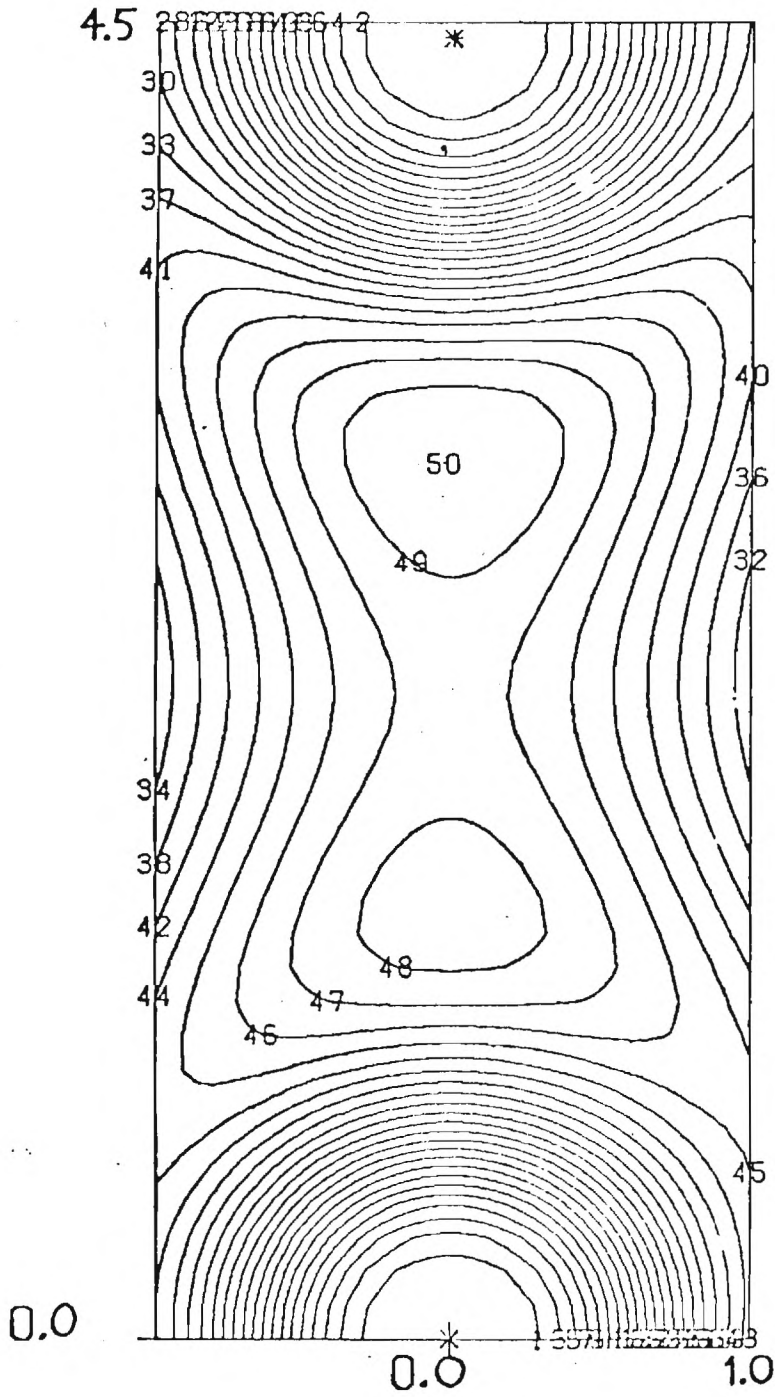


FIGURE 5C IN $[-1, 1, 1]$ PLANE

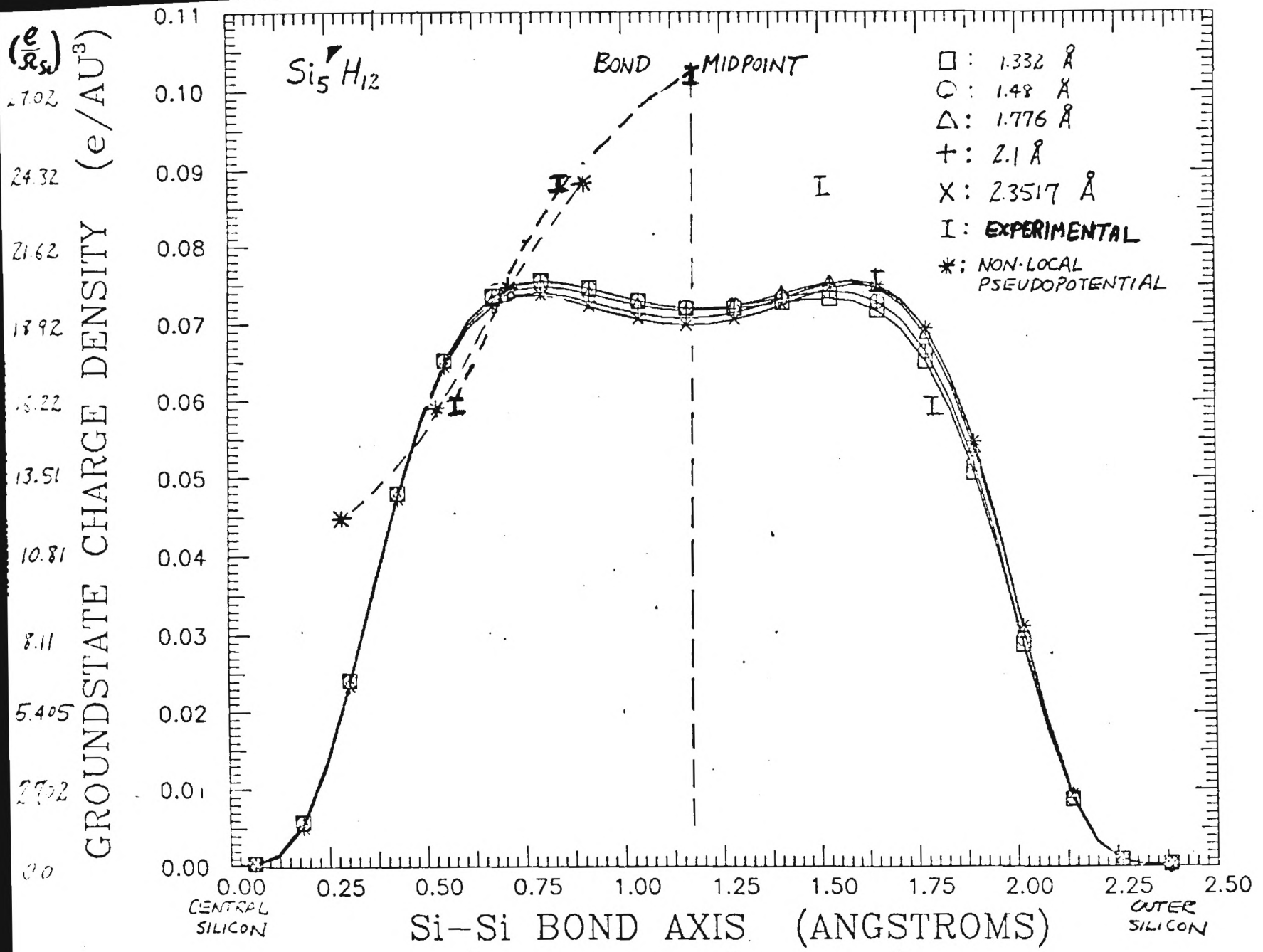
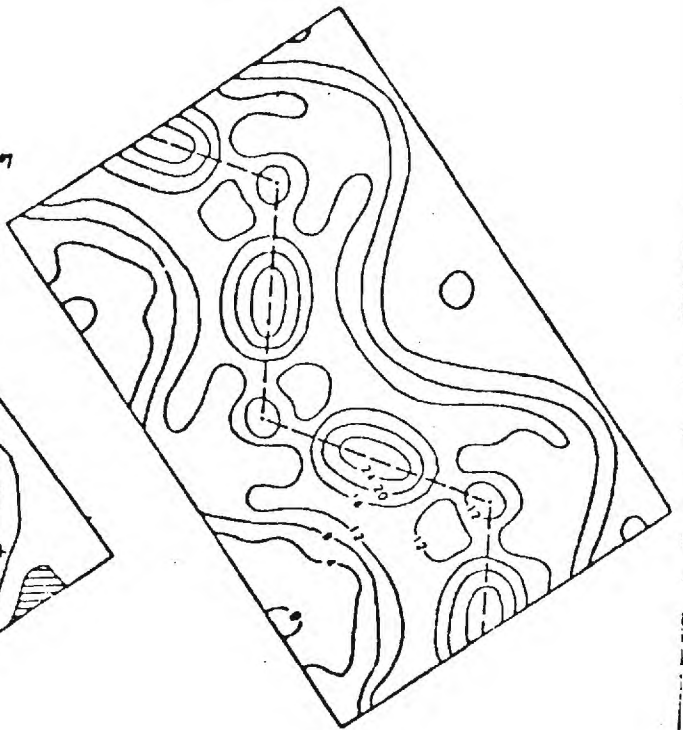
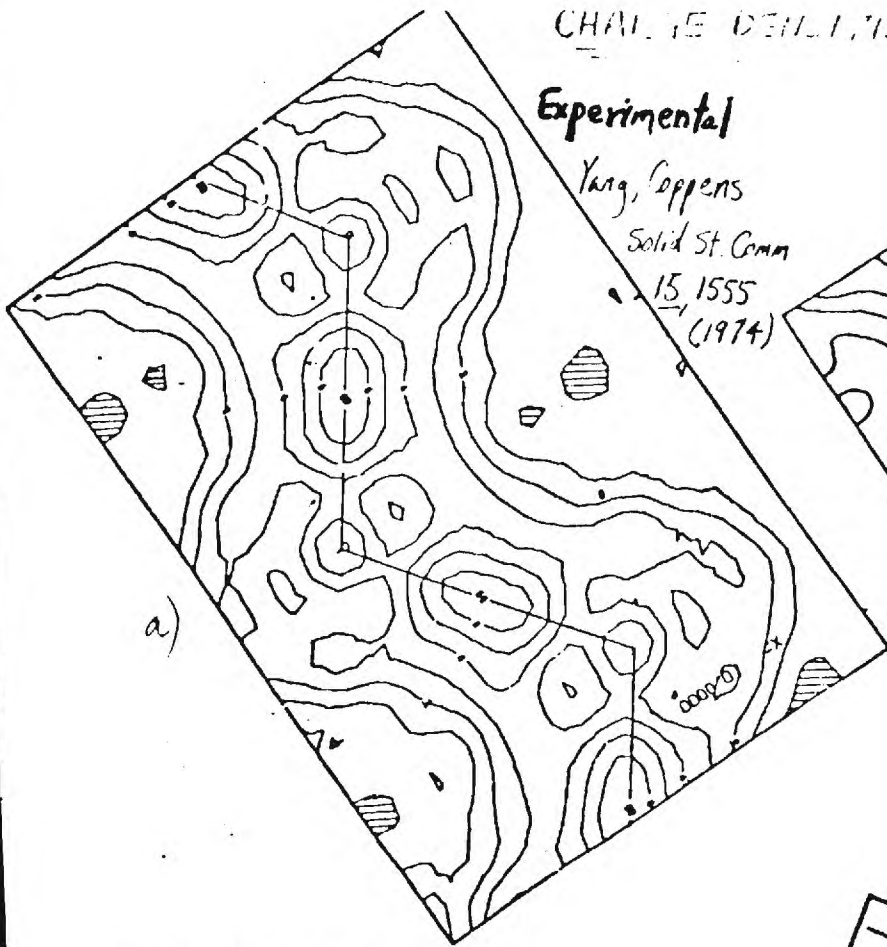


FIGURE 6

CHARGE DENSITIES IN SILICON

Experimental

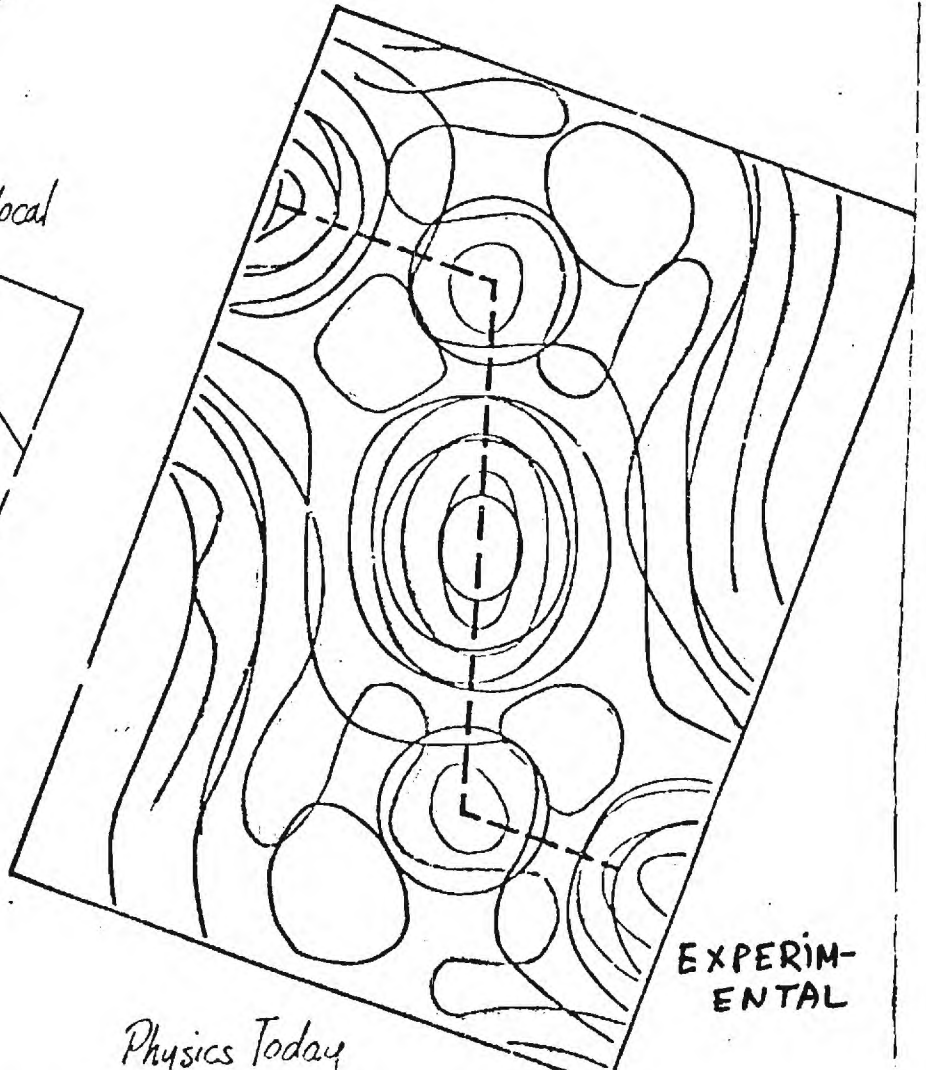
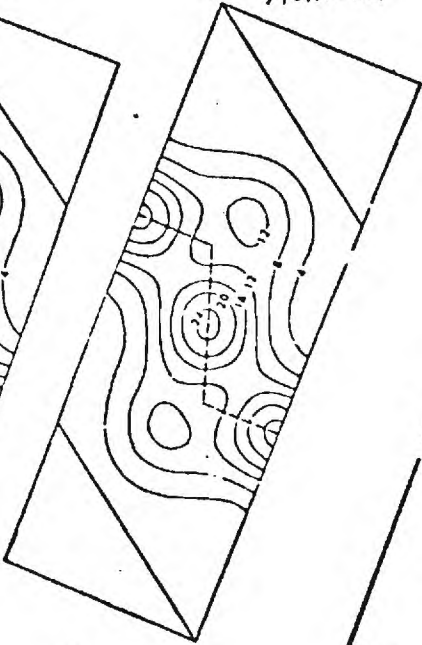
Yang, Coppens
Solid St. Comm
15, 1555
(1974)



Pseudopotential Method

Local

b) Nonlocal



EXPERIMENTAL

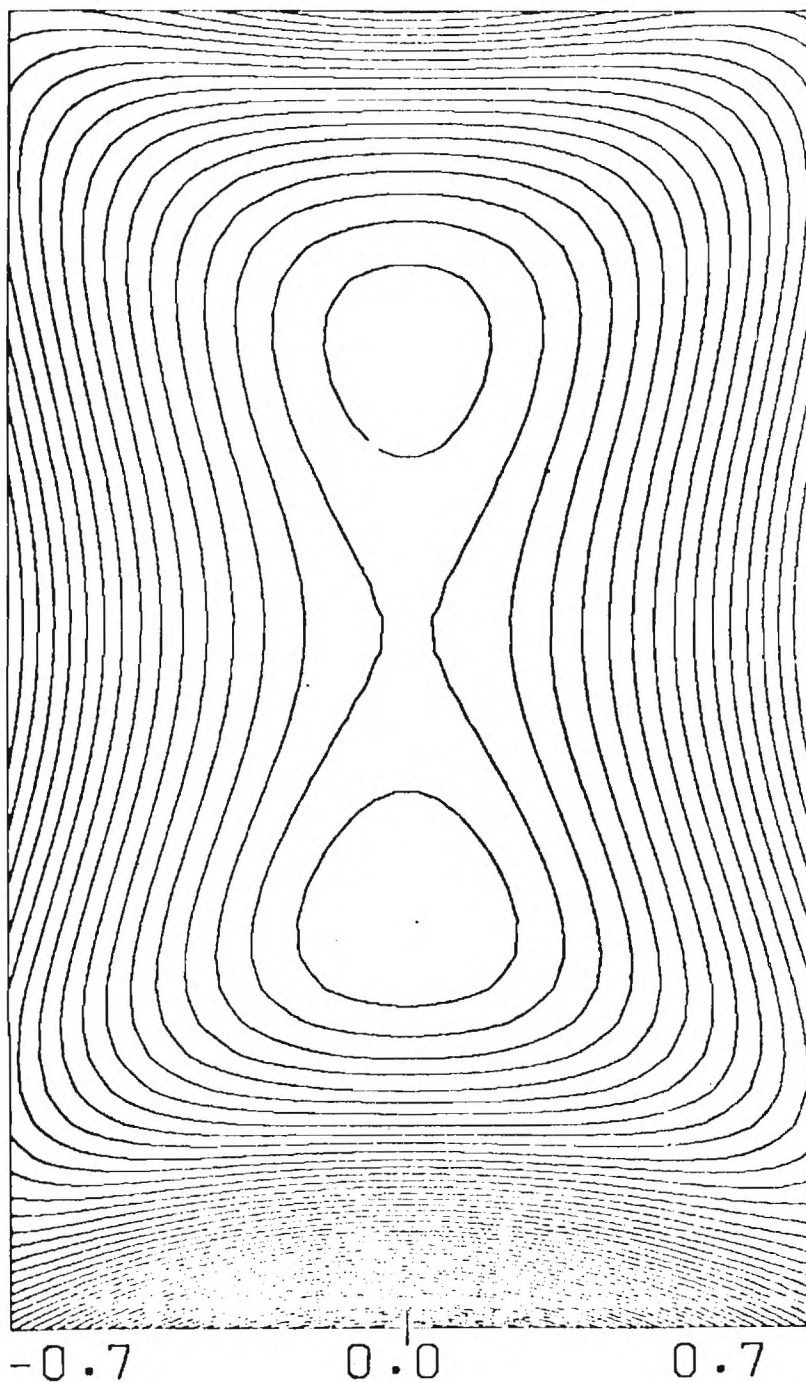
Chelikowsky, M.L. Cohen
Rev. B 10, 5095 (1974)
Rev. B 14, 556 (1976)

Physics Today

FIGURE 7

ALL E CENTRAL SI SI5H12
ANGS GS *ALL VALENCE*

3.5



IN $[-1, 1, 1]$ PLANE

FIGURE 8

SI2H6 CLUSTER 1.480 ANGSTROMS
GROUNDSTATE (P-2 EXP=0.1)

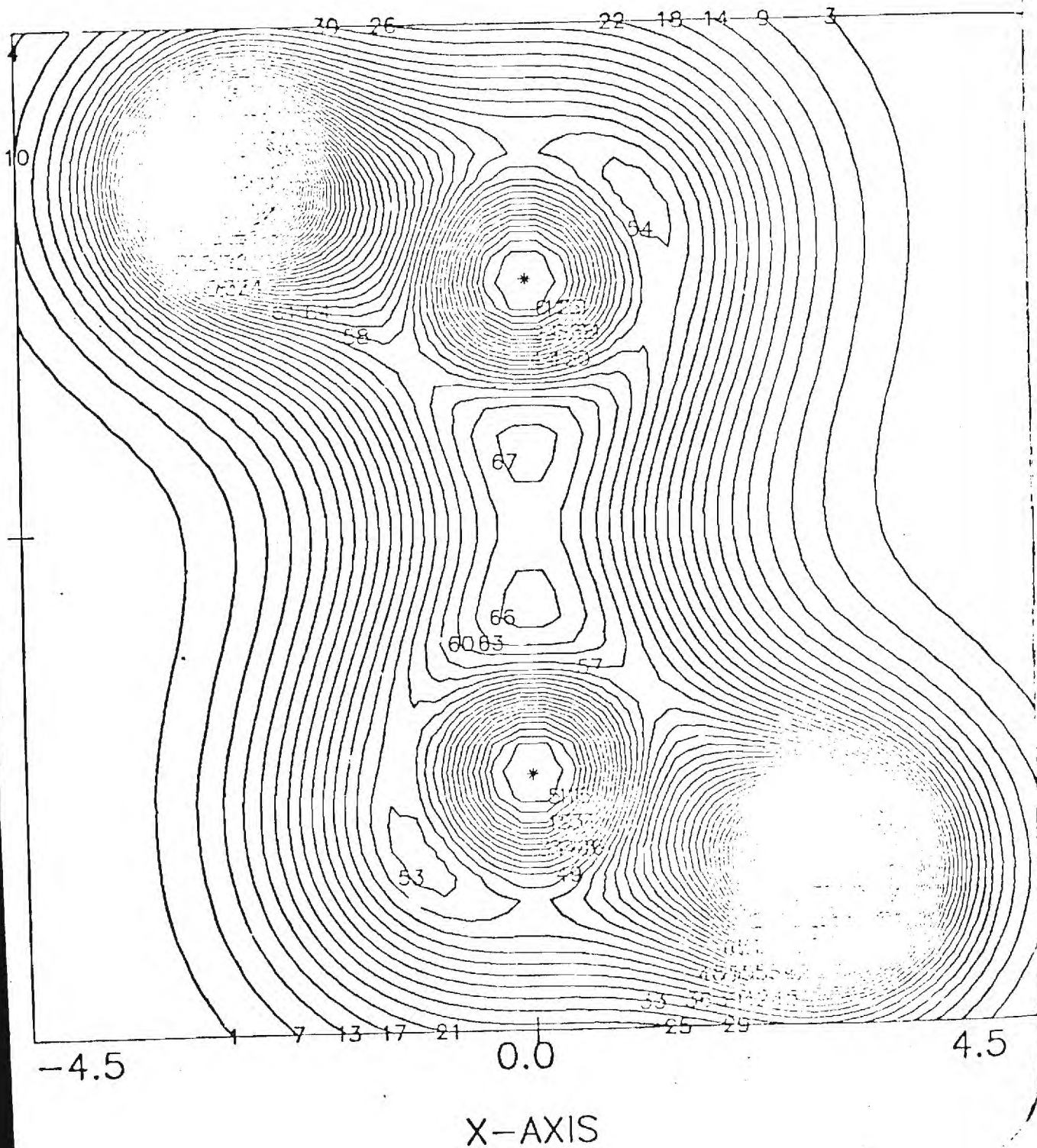
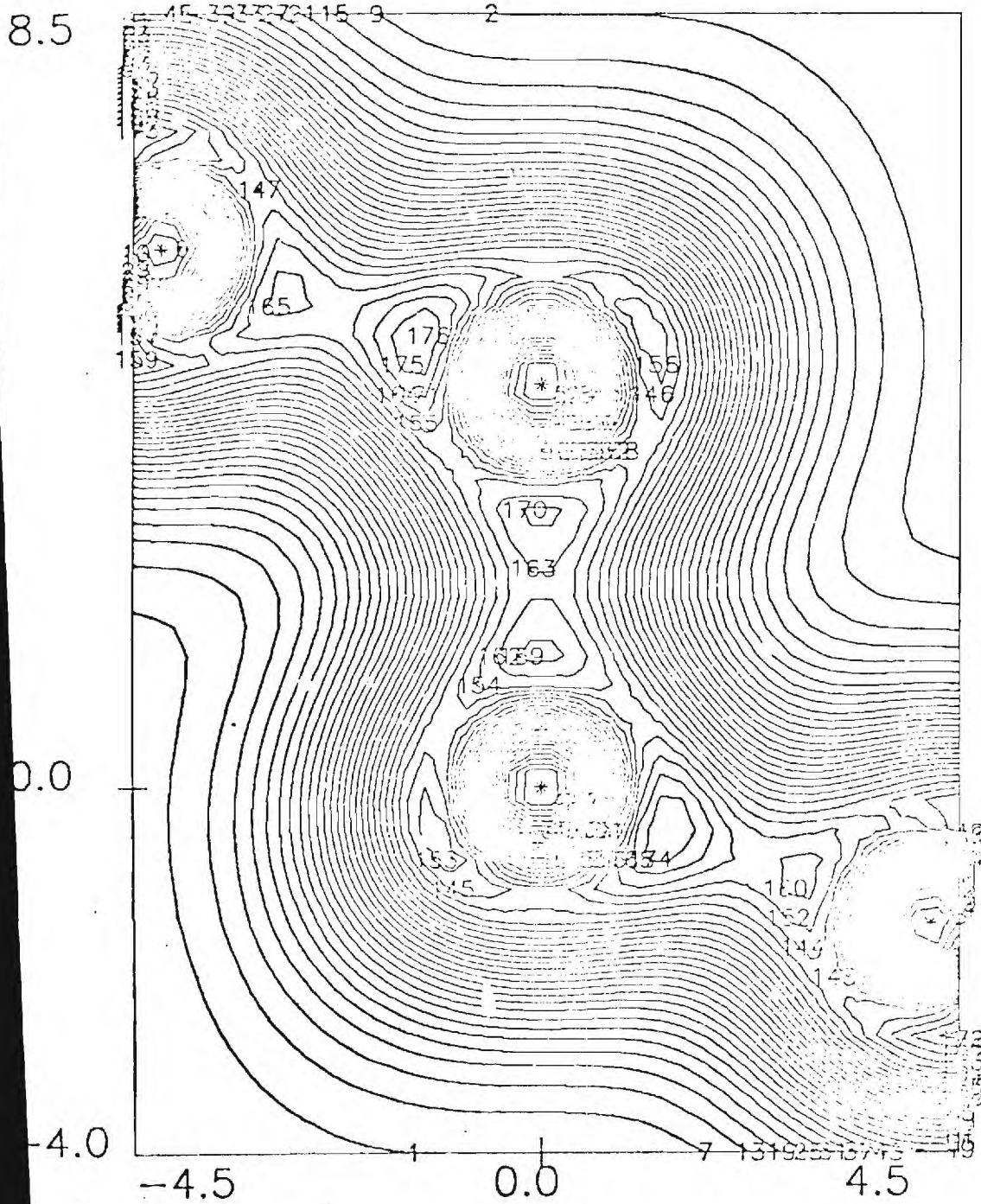


FIGURE 9

S18 CLUSTER 2.3517 ANGSTROMS
GROUNDSTATE



IN -1,1,1 PLANE

FIGURE 10

H. Vacancy Formation and Migration at Metallic Surfaces

The pseudopotential method has been employed successfully to study properties of simple metals and of bulk defects in these metals. In particular, the method yields adequate results for bulk vacancy formation and motion energies. Since the electron distribution at a metal surface differs from that of the bulk it is to be expected that the screening of bare-ion pseudopotential in the surface region will be significantly modified from the corresponding bulk pseudopotentials. Consequently, the values of the above energies will be different. Vacancy mechanisms play a dominant role in a number of surface and interface phenomena, such as surface self-diffusion, damage annealing, and surface phase transformations (surface premelting). Thus, it is of importance to develop theoretical models which would allow a systematic study of the energetics of point defects at surfaces and provide an estimate of the pertinent quantities.

The investigation of surface vacancy formation and motion energies involves a calculation of the total energy of a semi-infinite metal,

$$E_{TOT} = E_{fe} + E_{bs} + E_{es} ,$$

where E_{fe} is the free-electron energy, E_{bs} is the band-structure energy and E_{es} is the electrostatic (Madelung) energy. Having obtained an expression for E_{TOT} for an ideal semi-infinite crystal (E_{TOT}^O) and that of a defective one (E_{TOT}'), the required energies are expressed as

$$\Delta = E_{TOT}^O - E_{TOT}' .$$

The first step in our calculation is to express E_{bs} for a semi-infinite solid in terms of its 2D Fourier decomposition parallel to the surface plane (\vec{Q}) and a sum over layers. Using second-order perturbation theory, and basis

set wave functions appropriate for the semi-infinite free-electron metal (infinite barrier or finite barrier models) an expression for E_{bs} is developed. In course of deriving the above, expressions for the matrix elements of the screened bare pseudopotentials in the surface region have been obtained. In general, the matrix element of the total pseudopotential, W , is given by the expression

$$\langle \vec{k} + \vec{Q}, k + q | W | \vec{K}, k \rangle = \sum_n S_n(\vec{Q}) \frac{1}{A_0} \int d^3r \phi_{k+q}(z+z_n) \times \\ e^{-i(\vec{K}+\vec{Q}) \cdot \vec{R}} w(\vec{r}) \phi_k(z+z_n) e^{i\vec{k} \cdot \vec{R}}$$

where the layer structure factor $S_n(\vec{Q})$ is given by

$$S_n(\vec{Q}) = \frac{1}{N} \sum_{R_i^n} e^{-i\vec{Q} \cdot R_i^n} .$$

N is the number of surface unit cells, \vec{R}_i^n is the position vector of the i -th ion in layer n , z_n is the distance of layer n from the surface and w is the screened atomic pseudo-potential. For a local pseudopotential a self-consistent treatment (in RPA sense) yields an integral equation for the atomic pseudo-potential matrix elements. Upon solution of the integral equation the differences in the band structure energies depend only on the structure factors. These together with the free-electron and electrostatic contribution can be used in the evaluation of the defect energies, Δ . Analysis of the results as a function of the location of the defect would allow an estimate of the surface effect on the energetics of transport processes near surfaces.

QUANTUM MODELS WITH VARIABLE BOUNDARY CONDITIONS*

- I. THE HYDROGEN-IMPENETRABLE WALL SYSTEM AS A MODEL OF PHYSISORPTION

- II. SHALLOW DONOR IMPURITIES NEAR SEMICONDUCTOR INTERFACES: Si, Ge.

by

Donald B. MacMillen and Uzi Landman

School of Physics

Georgia Institute of Technology

Atlanta, Ga. 30332

*Work Supported by D.O.E. Contract No. EG-77-S-05-5489.

CONTENTS

	Page
INTRODUCTION	1-5
I. THE EFFECT OF CHANGING BOUNDARY CONDITIONS ON SIMPLE QUANTUM SYSTEMS	
1.1 A Variational Solution to a Change in Boundary Conditions	6-11
1.2 The Basis Set, Matrix Elements, and the Matrix Equations	11-19
1.3 Solution of the Matrix Equations: Energy Levels and Properties of the Hydrogen/Impenetrable Wall System	19-41
1.4 Image Charges and a Model of the Physical Adsorption of Atomic Hydrogen	41-53
II. SHALLOW DONOR IMPURITIES NEAR SEMICONDUCTOR INTERFACES	
2.1 The Effective Mass Hamiltonian	55-63
2.2 Ellipsoidal Conduction Bands and the Boundary Condition Near a Surface	63-71
2.3 Donor Impurities Near the Silicon (001)/Vacuum and the Germanium (111)/Vacuum Interfaces	71-85
2.4 A Donor Impurity Near the Si/SiO ₂ Interface of a M.O.S. Field Effect Transistor	85-101
APPENDIX A ENERGIES FOR SOME EXCITED STATES OF THE HYDROGEN/IMPENETRABLE WALL SYSTEM	102-103
REFERENCES	104-105

TABLES

	Page	
1.1	Convergence of the ground state energy for the hydrogen/impenetrable wall system at several distances	21
1.2	Ground state properties of the hydrogen/impenetrable wall system	23
1.3	Properties of the first excited state of the hydrogen/impenetrable wall system	24
1.4	Properties of the second excited state of the hydrogen/impenetrable wall system	25
1.5	Properties of the third excited state of the hydrogen/impenetrable wall system	26
1.6	Ground state properties for the hydrogen/perfectly imaging substrate system	44
1.7	Properties of the first excited state of the hydrogen/perfectly imaging substrate system	45
1.8	Properties of the second excited state of the hydrogen/perfectly imaging substrate system	46
2.1	Ground state properties of a shallow donor near the surface of a symmetric ($\gamma=1$) silicon	74
2.2	Ground state properties of a shallow donor near the (001) surface of silicon	75
2.3	Ground state properties of a shallow donor near the (111) surface of germanium	76
2.4	Binding energy as a function of impurity distance into the oxide layer for several values of the electric field strength	98

LIST OF FIGURES

	Page
1.1 The coordinate system of Eq. (5.1) centered at proton and the boundary surface at $Z = R = r \cos \theta$	8
1.2 Ground state energy as a function of distance of the hydrogen/impenetrable wall system	28
1.3 The first 13 excited states of the hydrogen/impenetrable wall system	29
1.4 Ground state wave function when proton is $1.4 a_0$ away from plane	32
1.5 Ground state wave function when proton is $1.0 a_0$ away from plane	33
1.6 Ground state wave function when proton is $0.6 a_0$ away from plane	34
1.7 Ground state wave function when proton is $0.2 a_0$ away from plane	35
1.8 Ground state wave function when proton is on the plane	36
1.9 Force on the proton when the electron is in its ground state	40
1.10 Ground state energy as a function of proton distance from the plane for the perfectly imaging substrate system	47
1.11 The 'holding potential' of Bruch and Ruijgrok in which the image electron-proton interaction has not been included	50
1.12 The various contributions to the interaction potential	52
2.1 Ground state energy of a shallow donor impurity near the (001) surface of silicon	79
2.2 Ground state energy of a shallow donor impurity near the (111) surface of germanium	80
2.3 Excited states of a shallow donor impurity near the (001) surface of silicon	82
2.4 Excited states of a shallow donor impurity near the (111) surface of germanium	83

	Page
2.5 Interaction energy of a shallow donor impurity with the surface of a semiconductor for three different systems	84
2.6 Schematic of a metal-oxide-semiconductor field effect transistor	86
2.7 The experimental results of Hartstein and Fowler ⁸⁹ for the channel conductivity of a MOS field effect transistor	88
2.8 Binding energy of an electron to a donor impurity located on the interface between the silicon and silicon dioxide as a function of electric field	94
2.9 Binding energy at zero field as a function of impurity distance into the silicon (semiconductor) layer	95
2.10 Binding energy at zero field as a function of impurity distance into the silicon dioxide layer	96
2.11 Binding energy at several field strengths as a function of impurity distance into the silicon dioxide layer	100

INTRODUCTION

Boundary conditions, as utilized in Quantum Mechanics, are usually dictated by the requirements of *physical admissibility*. For example, when considering bound states the requirement that the normalization integral converge leads to the consideration of only those solutions which are regular at the origin and are zero at infinity. For scattering states a wave function which tends to infinity as r goes to infinity corresponds to a state that has no physical meaning and must be discarded. More generally it is known that a partial differential equation possesses several arbitrary constants and it is the specification of the value of the solution, or its normal derivative, on the boundary that yields the values of these constants.

One of the first uses of a boundary perturbation, that is a change in the boundary conditions, to *model* a physical situation was a calculation of the energy levels of a compressed hydrogen atom.^{1,2} In this calculation the effect of very high pressure on atomic hydrogen is taken into account by requiring that the wavefunction vanish - on a sphere at some finite distance from the proton. This type of calculation is, of course, only an approximate one for it only indicates the effect of repulsive forces at very high densities; but of course this is the main attraction of such an approximation in that it replaces the complicated set of interactions with only a change in the boundary conditions, which in this case is exactly solvable.³

By changing the new boundary surface from the sphere of the previous example to an infinite plane surface, there results a situation that has been used to model several physical systems. The requirement of a vanishing wavefunction on a plane has been used⁴ to represent the exchange repulsion of atomic hydrogen physically adsorbed onto a metal surface. As shall be shown, this model of physical adsorption of atomic hydrogen, when consistently interpreted, yields no potential well and thus no adsorption.

Perhaps a more realistic use of this boundary condition in the modelling of a physical problem arises in the effective mass theory of shallow donor impurities near the surface of a semiconductor. Because the binding energy of a shallow donor is of the order of a few milli-electron volts and the height of the surface barrier is several electron volts, the surface is essentially an infinite potential barrier and the envelope function of the donor impurity must be required to vanish on the surface. This condition on shallow impurities near semiconductor surfaces was first pointed out by Levine.⁵

It is the last two examples of modelling a physical problem with the use of boundary conditions that will be addressed in this report. The boundary perturbation in each case involves a change in the shape of the boundary surface while still requiring that homogeneous Dirichlet conditions be satisfied. (Recall that the isolated hydrogen atom wavefunction is required to be zero on the sphere at infinity.)

When the surface on which the boundary conditions are to be specified is no longer a surface in a coordinate system in which the partial differential equation separates, the problem is non-separable. This is due to the fact that even though it may be possible to separate the equation, there is no way to satisfy the boundary conditions on a surface which depends upon at least two independent variables. Because of this nonseparability, some type of approximation method must be used.

One of the first approaches to the boundary perturbation problem was made by Brillouin.⁶ By considering a displacement operator acting on the boundary he was able to construct a method that is formally similar to the standard perturbation series. However the expansion parameter in this case is the magnitude by which the boundary surface is displaced and this parameter is assumed to be small. This is clearly not satisfied by the problem we wish to solve. Other methods of treating boundary perturbations have been developed^{7,8} but they all have the same restriction. That is, they can only be used when the domain of the PDE is finite and the change in the boundaries is finite. In addition to these methods, a perturbation method using Green's functions has been developed by Feshbach⁹ and also presented in Morse and Feshbach.¹⁰ However, the method is mathematically complicated and for the problem of a change in the boundary shape while requiring homogeneous Dirichlet conditions to hold, the method cannot be used to find corrections to the energy beyond the second order.

These considerations lead to the conviction that the variational method will yield the best approximate solutions to this type of boundary perturbation problem.

In Chapter I a variational solution to the problem of a hydrogen atom in the presence of a planar infinite-potential wall is given. The effect of this boundary perturbation on the spectrum of the hydrogen atom is discussed. At a large distance from the plane, the isolated hydrogen atom levels are regained. When the proton lies on the boundary plane the problem is again exactly solvable and these solutions are recovered by the variational solution. Between these two limits the energy levels vary smoothly and exhibit several interesting level crossings. By using these methods, the Bruch and Ruijgrok⁴ model of the physical adsorption of atomic hydrogen is re-examined. When an interaction term that they neglect, but is required for a consistent treatment, is included, the shallow well in the interaction energy that these authors found disappears.

Chapter II addresses the problem of a shallow donor impurity near a semiconductor surface or interface. Modifications in the variational solution due to the effect of an anisotropic effective mass are presented. The resulting energy levels of shallow donors near the surface of silicon and germanium are calculated and presented. An interesting result of this model is that the total interaction energy of a shallow donor with the semiconductor surface possesses a minimum and this suggests a possible clustering of these impurities near the surface. Finally, the binding energy of

a shallow donor impurity associated with an n-type inversion layer of a metal-oxide-semiconductor field effect transistor is calculated and compared with other recent theoretical treatments.

CHAPTER I

THE EFFECT OF CHANGING BOUNDARY CONDITIONS ON SIMPLE QUANTUM SYSTEMS

In this chapter we shall be concerned with solving the problem of a hydrogen atom in the presence of a plane on which the potential is infinite. As noted in the introduction boundary perturbation methods are inadequate when the change of the location of the boundary surface is from infinity to some finite distance from the proton. Here a variational solution to the problem is given; the matrix equations and the matrix elements for a particular choice of basis functions are exhibited. The resulting energy levels and properties of this system are presented. Finally, with the introduction of image charges, the results for Bruch and Ruijgrok's⁴ model of the physical adsorption of atomic hydrogen, when *all* interactions are taken into account, are shown to lead to no potential well in the interaction energy.

1.1 A Variational Solution to a Change in Boundary Conditions

The problem that is to be solved is that of a hydrogen atom which is at some finite distance, say R , from an infinite plane surface upon which the potential is taken to be infinite. This infinite potential manifests itself by the requirement that ψ , the wavefunction

of the electron, must vanish on the plane and in the half-space not containing the proton¹¹. In our treatment of the model, the Born-Oppenheimer approximation shall be used, inasmuch as the proton will be taken as being located at a fixed distance from the plane, so that there is no coupling between the nuclear and electronic motions.

The Hamiltonian of the problem is given by the usual hydrogen atom Hamiltonian

$$\mathcal{H} = -\frac{\hbar^2}{2m} \nabla^2 - \frac{e^2}{r} \quad (1.1)$$

but now the boundary condition is that ψ must be equal to zero on the plane $z = R$ (see Fig. 1.1). This choice of orientation of the plane and coordinate system, which is centered on the proton, is made to simplify the following calculations.

The variational principle for eigenvalues¹² is

$$\delta[E] = \delta \left[\frac{\int \psi^\dagger \mathcal{H} \psi dV}{\int \psi^\dagger \psi dV} \right] = 0 \quad (1.2)$$

where H is an arbitrary Hermitian operator, and this leads to the eigenvalue equation

$$\mathcal{H} \psi = E \psi \quad (1.3)$$

only when the function ψ in (1.2) obeys the same boundary conditions that are to be imposed upon the solutions of Eq. (1.3). In practical applications of the variational method, this means that the trial

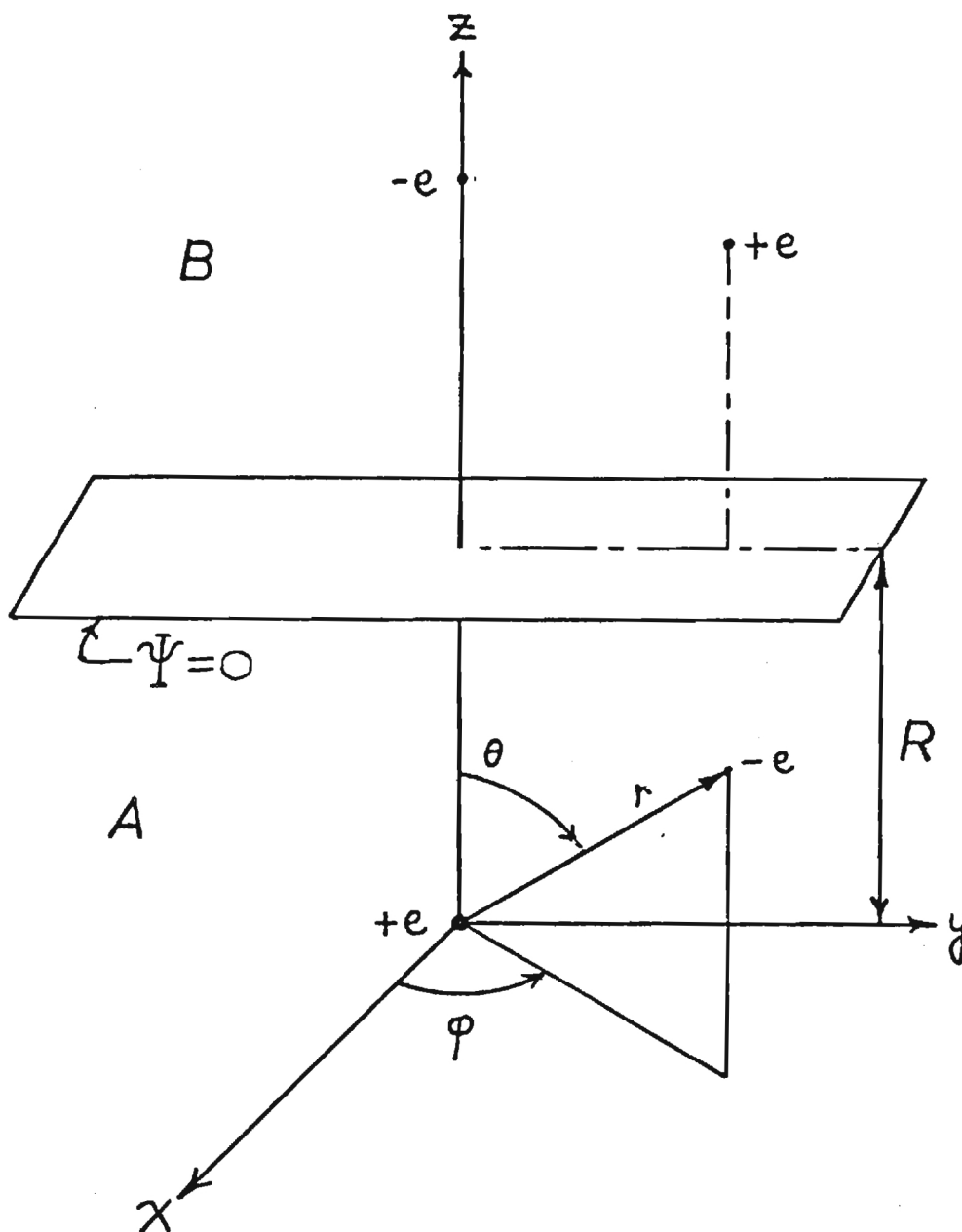


Fig. 1.1 The co-ordinate system of Eq. (1.1) centered at the proton and the boundary surface at $z = R = r \cos \theta$.

functions must obey the correct boundary values, independent of the choice of values of whatever variational parameters the trial function may contain. When this condition is satisfied, the trial function is said to be admissible.¹³

This requirement usually poses no problems and its importance is not often emphasized. However, in the present case when the location of the boundary surface is to be varied, and more generally when the boundary surface and conditions will be considered to be input variables, the construction of admissible trial functions can become quite cumbersome. To avoid this complication in the construction of a set of trial functions for the linear variation problem one can form the combination

$$\Psi(\vec{r}) = G(\vec{r}) \sum_n A_n \phi_n(\vec{r}) + F(\vec{r}) \quad (1.4)$$

Here the A_n are of course the linear variation parameters and the set $\phi_n(r)$ is to satisfy the boundary conditions of the unperturbed problem. The n 's are taken to stand for all the quantum numbers which characterize the basis set of the system. The function $G(r)$ is such that $G(\vec{r} \text{ on } S) = 0$ where S denotes the boundary surface. The function $F(\vec{r})$ is to satisfy $F(\vec{r} \text{ on } S) = X_1(S)$ for Dirichlet conditions, or $\frac{\partial F}{\partial n}(\vec{r} \text{ on } S) = X_2(S)$ for Neumann conditions. In the present instance we are concerned only with homogeneous Dirichlet conditions and therefore need only consider, taking into account the coordinate system of Fig. 1.1 and the fact that the additional boundary surface is a plane, the combination

$$\Psi(\vec{r}) = G(z) \sum_n A_n \phi_n \quad (1.5)$$

where $G(R) = 0$.

When the boundary surfaces are changed, there arises one more modification of the variational principle of Eq. (1.2). The range of the integrations in Eq. (1.2) is over the domain of the Eq. (1.3) and that domain is defined as the inside of the closed boundary surface on which the boundary conditions are to be satisfied. The fact that the surface is closed follows from the elliptic character of the time-independent Schrödinger equation. This means that the limits of integration in Eq. (1.2) will become dependent upon the position of the boundary surface.

Taking into account all of these considerations and using the trial function of Eq. (1.5) the energy of the system can be written as

$$[E] = \frac{\int_T [G(Z) \sum_n A_n \phi_n]^\dagger \mathcal{H} [G(Z) \sum_n A_n \phi_n] dV}{\int_T [G(Z) \sum_m A_m \phi_m]^\dagger [G(Z) \sum_m A_m \phi_m] dV} \quad (1.6)$$

where the subscript T on the integrals indicates that the integration is over a truncated space and H is given by Eq. (1.1). The basis set used to expand the trial function will not in general be orthogonal, because of the factor G(Z) and the integration is over a truncated space, so that the variation of the linear parameters A_n will lead to a generalized matrix eigenvalue problem

$$\mathcal{H} \underline{A} = E \underline{N} \underline{A} \quad (1.7)$$

where there now appears the overlap matrix \underline{N} . More specifically the matrix elements are given by

$$(\underline{H})_{n'n} = \int_{\tau} [G(\underline{z}) \phi_{n'}]^\dagger \mathcal{H} [G(\underline{z}) \phi_n] dV \quad (1.8)$$

and

$$(\underline{N})_{n'n} = \int_{\tau} [G(\underline{z}) \phi_{n'}]^\dagger [G(\underline{z}) \phi_n] dV \quad (1.9)$$

Since both \underline{H} and \underline{N} are hermitian, which will be demonstrated later for a particular choice of the ϕ_n 's, the usual properties of hermitian matrices are present; except that the orthonormality of the vectors \underline{A}_n is expressed as¹⁴

$$\underline{A}_n^\dagger \underline{N} \underline{A}_{n'} = \delta_{nn'} \quad (1.10)$$

1.2 The Basis Set, Matrix Elements, and the Matrix Equations

Before the choice of the set ϕ_n is presented, the specific form of $G(\underline{z})$ which is zero on the boundary surface will be given. The most convenient choice is simply to set

$$G(\underline{z}) = R - z = R - r \cos \theta \quad (1.11)$$

Then the development of the Laplacian of the Hamiltonian (1.1) is

$$\nabla^2 [(R - r \cos \theta) \phi_n] = (R - r \cos \theta) \nabla^2 \phi_n - 2 \hat{k} \cdot \nabla \phi_n$$

since, on noting that \hat{k} is the unit vector in the z-direction,

$$\nabla(R - r \cos \theta) = -\hat{k}$$

and

$$\nabla^2(R - r \cos \theta) = 0$$

It is interesting to note that this choice yields an expression that is similar to the variational principle for unrestricted trial functions (i.e. they do not obey the boundary conditions) given by Morse and Feshbach¹². Both forms involve the derivative of ϕ_n that is normal to the boundary surface; however in the present instance the integration is over the entire volume and not only over the new boundary surface.

The basis set $\phi_n(\vec{r})$, which must satisfy only the isolated hydrogen atom boundary conditions, i.e. $\psi \rightarrow 0$ as $r \rightarrow \infty$, is chosen to be

$$\begin{aligned} \phi_n = \phi_{n\ell m}(\vec{r}, \beta) &= (2\beta)^{3/2} / \sqrt{2n} \left[(n-\ell-1)! / [(n+\ell)!]^3 \right]^{1/2} \\ &\times (2\beta r)^\ell L_{n-\ell-1}^{2\ell+1}(2\beta r) e^{-\beta r} Y_\ell^m(\theta, \varphi) \end{aligned} \quad (1.12)$$

In Eq. (5.12) the Y_ℓ^m are the usual spherical harmonics, the L_p^k are the associated Laguerre polynomials and r is taken to be in units of Bohr radii, a_0 ($a_0 = \hbar^2/me^2$). This corresponds to a scaling of the Hamiltonian (1.1) to

$$\left(-\nabla^2 - \frac{2}{r}\right) \Psi = E \Psi$$

where E is given in units of Rydbergs ($e^2/2a_0$).

The difference between the set of functions given by Eq. (1.12) and the isolated hydrogen atom eigenfunctions is the appearance of the combination βr , where β is an additional variational parameter independent of any quantum number, rather than the combination r/n which depends upon the particular state under consideration. The advantages of this choice are twofold. First the isolated hydrogen atom orbitals do not form a complete set without the inclusion of the continuum states¹⁵. Use of the set given by (5.12) has been shown to include contributions from these states¹⁶. Second, the virial theorem is automatically satisfied for any quantum mechanical system whose potential is a homogeneous function of the coordinates if a scale factor is introduced into the approximate wave function and varied so as to give the lowest energy^{17,14}. The parameter β is such a scale factor and because its optimum value will be found, the properties of the states found with the approximate wave functions of Eq. (1.5) will be better than those which do not contain such a scaling.

Since the boundary surface was chosen to be a plane perpendicular to the z -axis, there are no changes in the limits of integration over the variable ϕ . Consequently the m -quantum number remains good. This means that we can separate the problem according to the m -value of the particular level that we are interested in solving. Moreover, since the degeneracy of the two states $[n, \ell, \pm m]$ is not lifted we need consider only the positive m values. The original matrix problem of Eq. (1.7) then reduces to the set of matrix problems for which $m = 0, 1, 2, \dots$. That is

$$\underline{\mathcal{H}}^{(m)} \underline{A}^{(m)} = E \underline{N}^{(m)} \underline{A}^{(m)} \quad (1.13)$$

In the calculation of the matrix elements for these separate problems, the integration over the variable ϕ can now be replaced by multiplication with the factor $2\pi\delta_{m',m}$.

The calculation of the Hamiltonian matrix elements now proceeds as follows. The limits of integration, in taking account of the truncation of the region along with the above considerations, become

$$2\pi \left\{ \int_0^R \int_0^\pi \mathcal{H}_{n'h}^{(m)} \sin\theta d\theta r^2 dr + \int_R^\infty \int_{\cos^{-1}(R/r)}^\pi \mathcal{H}_{n'n}^{(m)} \sin\theta d\theta r^2 dr \right\} \quad (1.14)$$

It is here, in the lower limit of the θ -integration of the second term, that the non-separability of the problem becomes apparent with the appearance of the term $\cos^{-1}(R/r)$. For future convenience we shall denote this integration as

$$\int_T \mathcal{H}_{n'n}^{(m)} dV.$$

The matrix elements of the Hamiltonian are now expressible as

$$\begin{aligned} \mathcal{H}_{n'a',n\ell}^{(m)} &= \int_T (R-r\cos\theta) \phi_{n'a'm}(\vec{r},\beta) \left\{ (R-r\cos\theta) \right. \\ &\times \left[-\nabla^2 - \frac{2}{r} \right] \phi_{n\ell m}(\vec{r},\beta) - 2\hat{k} \cdot \nabla \phi_{n\ell m}(\vec{r},\beta) \left. \right\} dV \quad (1.15) \end{aligned}$$

It is easy to show that

$$\left(-\nabla^2 - \frac{2}{r}\right) \phi_{n\ell m}(\vec{r}, \beta) = \left\{-\beta^2 + \frac{2(\beta n - 1)}{r}\right\} \phi_{n\ell m}(\vec{r}, \beta) \quad (1.16)$$

While the expression for $-\hat{k} \cdot \nabla \phi_{n\ell m}(\vec{r}, \beta)$ is slightly more complicated, its calculation is straightforward. First

$$\hat{k} \cdot \nabla \phi_{n\ell m}(\vec{r}, \beta) = \cos\theta \frac{\partial \phi_{n\ell m}}{\partial r} - \frac{\sin\theta}{r} \frac{\partial \phi_{n\ell m}}{\partial \theta} \quad (1.17)$$

which yields, upon collecting constants in $C_{n\ell m}(\beta)$,

$$\begin{aligned} \hat{k} \cdot \nabla \phi_{n\ell m} &= C_{n\ell m}(\beta) \left\{ -2(2\beta r)^\ell L_{n-\ell-2}^{2\ell+2}(2\beta r) e^{-\beta r} \right. \\ &* P_\ell^m(\cos\theta) \cos\theta - (2\beta r)^\ell L_{n-\ell-1}^{2\ell+1}(2\beta r) e^{-\beta r} P_\ell^m(\cos\theta) \cos\theta \\ &\left. + 2(2\beta r)^{\ell-1} L_{n-\ell-1}^{2\ell+1}(2\beta r) e^{-\beta r} (\ell+m) P_{\ell-1}^m(\cos\theta) \right\}. \end{aligned} \quad (1.18)$$

The expression for the overlap matrix is given simply by

$$\begin{aligned} N_{n'a', n\ell}^{(m)}(R) &= \int_{\mathcal{T}} \left\{ (R - r \cos\theta)^2 \right. \\ &\left. * \phi_{n'a'm}(\vec{r}, \beta) \phi_{n\ell m}(\vec{r}, \beta) \right\} dV \end{aligned} \quad (1.19)$$

The integration of the expressions given by Eq. (1.15) and Eq. (1.19) is straightforward; however it is quite lengthy. It is easy to see from the limits of the integrations given in Eq. (1.14) that all of the matrix elements for both $\underline{H}^{(m)}$ and $\underline{N}^{(m)}$ will be dependent

upon R , the perpendicular distance of the proton from the boundary plane. By way of illustration one term of the normalization matrix is presented here.

The squared term in Eq. (1.19) can be expanded to yield three integrals. Denoting these as $N_{nl, n'l}^{(m)i}$, where $i=1,2,3$, we can write

$$N_{n'l, n'l}^{(m)}(R) = R^2 N_{n'l, n'l}^{(m)1}(R) - 2R N_{n'l, n'l}^{(m)2}(R) + N_{n'l, n'l}^{(m)3}(R) \quad (1.20)$$

The last of these is given by the rather lengthy expression

$$N_{n'l, n'l}^{(m)3}(R) = \frac{(2\beta)^{l+l'+3}}{\sqrt{nn'}} \left[(n'+l'-1)! (n'+l')! (n-l-1)! (n+l)! \right]^{1/2}$$

$$\times \left[\frac{(2l'+1)(l'-m)! (2l+1)(l-m)!}{(l'+m)! (l+m)!} \right]^{1/2} \sum_{s=0}^{n'-l'-1} \frac{(-2\beta)^s}{(n-l-1-s)! (2l'+1+s)! s!}$$

$$\times \sum_{t=0}^{n-l-1} \frac{(-2\beta)^t}{(n-l-1-t)! (2l+1+t)! t!} \frac{LST! 2^{l+l'+1}}{(2\beta)^{LST+1} (2l+1)}$$

$$\times \left\{ \frac{(l+1-m)(l+2-m)(l+2+m)!}{(2l+3)(2l+5)(l+2-m)!} \delta_{l', l+2} + \right.$$

$$\left[\frac{(l+1-m)(l+1+m)}{(2l+1)(2l+3)} + \frac{(l+m)(l-m)}{(2l-1)(2l+1)} \right] \frac{(l+m)!}{(l-m)!} \delta_{l, l'}$$

$$\left. + \frac{(l+m)(l-1+m)(l-2+m)!}{(2l-1)(2l-3)(l-2-m)!} \delta_{l', l-2} \right\}$$

$$- \sum_{k=0}^{LST} \frac{LST!}{(LST-k)! (2\beta)^{k+1}} \sum_{r=0}^{\lfloor \frac{l'-m}{2} \rfloor} \frac{(-)^r (2l'-2r)!}{r! (l'-r)! (l'-2r-m)!}$$

$$* \sum_{g=0}^{\lfloor \frac{l-m}{2} \rfloor} \frac{(-)^g (2l-2g)!}{g! (l-g)! (l-2g-m)!} \sum_{h=0}^m \frac{(-)^h m!}{(m-h)! h!}$$

$$\left. \begin{array}{l} \sum_{g=0}^p \frac{p! R^{LST-k-g-1}}{(p-g)! (2\beta)^{g+1}} \quad \text{if } p \geq 0 \\ 0 \quad \text{if } p = -1 \\ \sum_{g=1}^{-p-1} \frac{(-p-1-g)! (-2\beta)^{g-1} R^{LST-k+g+1}}{(-p-1)!} \quad \text{if } p \leq -2 \end{array} \right\} e^{-2\beta R} \quad (1.21)$$

where we have used the definitions

$$LST = l + l' + s + t + 4$$

$$p = s + t + 2r + 2g + 2m - k - 2h \quad (1.22)$$

Most generally, it is the combination of an operator and the boundary conditions of the functions on which it operates which determines the property of hermiticity. In the present situation where only the boundary surface has been changed we expect that the matrices $\underline{\underline{H}}^{(m)}$ and $\underline{\underline{N}}^{(m)}$ defined by Equations (1.15) and (1.19), to be hermitian. It is obvious from Eq. (1.19) that not only is $\underline{\underline{N}}^{(m)}$ hermitian, it is real and symmetric. This property is not so obvious for the matrix $\underline{\underline{H}}^{(m)}$. The matrix $\underline{\underline{H}}^{(m)}$ will be hermitian if (see Eqns. (1.15) and (1.16)).

$$\int_{\mathcal{T}} \left\{ \beta n \frac{(R-r\cos\theta)^2}{r} \phi_n \phi_{n'} + (R-r\cos\theta) \phi_{n'} \hat{\mathbf{k}} \cdot \nabla \phi_n \right\} dV$$

$$= \int_{\mathcal{T}} \left\{ \beta n' \frac{(R-r\cos\theta)^2}{r} \phi_{n'} \phi_n + (R-r\cos\theta) \phi_n \hat{\mathbf{k}} \cdot \nabla \phi_{n'} \right\} dV \quad (1.23a)$$

Rearranging, this yields

$$\beta (n'-n) \int_{\mathcal{T}} \frac{(R-r\cos\theta)^2}{r} \phi_{n'} \phi_n dV$$

$$= \int_{\mathcal{T}} (R-r\cos\theta) \hat{\mathbf{k}} \cdot (\phi_{n'} \nabla \phi_n - \phi_n \nabla \phi_{n'}) dV \quad (1.23b)$$

To obtain this result, first note that by the divergence theorem and the boundary conditions obeyed by $\phi_n, \phi_{n'}$ and the factor $(R-r\cos\theta)$ we have

$$\int_{\mathcal{T}} \nabla \cdot \left[(R-r\cos\theta)^2 \left\{ \phi_{n'} \nabla \phi_n - \phi_n \nabla \phi_{n'} \right\} \right] dV$$

$$= \oint_S \hat{\mathbf{n}} \cdot \left[(R-r\cos\theta)^2 \left\{ \phi_{n'} \nabla \phi_n - \phi_n \nabla \phi_{n'} \right\} \right] dS$$

$$= 0 \quad (1.24)$$

On developing the left hand side of Eq. (1.24)

$$\begin{aligned} & \int_{\tau} 2(R-r\cos\theta)(-\hat{k}) \cdot \{ \phi_{n'} \nabla \phi_n - \phi_n \nabla \phi_{n'} \} dV \\ &= - \int (R-r\cos\theta)^2 \{ \phi_{n'} \nabla^2 \phi_n - \phi_n \nabla^2 \phi_{n'} \} dV \end{aligned} \quad (1.25)$$

Using the identity (1.16) on the right hand side of Eq. (1.25) we obtain

$$\begin{aligned} & -2 \int_{\tau} (R-r\cos\theta) \hat{k} \cdot \{ \phi_{n'} \nabla \phi_n - \phi_n \nabla \phi_{n'} \} dV \\ &= -2\beta(n'-n) \int_{\tau} \frac{(R-r\cos\theta)^2}{r} \phi_{n'} \phi_n dV \end{aligned} \quad (1.26)$$

Equation (1.26) is exactly the same as Eq. (1.23) thus showing the hermitian character of $H_{\equiv}^{(m)}$. In the next section the solution and results of the matrix equations (1.13) are presented.

1.3 Solution of the Matrix Equations: Energy Levels and Properties of the Hydrogen/Impenetrable Wall System

The numerical solution of the matrix equation (1.13) is a two step process. Because of the complicated dependence of the matrices and the associated eigenvalues on the parameter beta, it is impractical to develop the variational condition $\partial[E]/\partial\beta = 0$. Therefore, at a specific distance a value of beta must be assumed and then the linear problem of Eq. (1.13) can be solved, yielding the eigenvalues and eigenvectors. At this point the value of beta can be varied, the

matrix elements calculated, and the matrix equation (1.13) is again solved. In this way one can search for the value of beta that gives the best upper bound on the eigenvalue.

Before the above procedure can be applied, it must first be decided to what extent the basis set of Eq. (1.12) will be extended in the expansion of the trial function. This determines the order of the matrix equation to be solved. Since only the positive m values, one at a time, need be considered the expansion of the trial function can be written as

$$\Psi_m(\vec{r}) = (R-r\cos\theta) \sum_{j=1}^N \sum_{k=0}^{j-1} A_{j+k}^{(m)}(m+j, m+k, m) \quad (1.27)$$

where m is fixed and (n, ℓ, m) denotes the function of those parameters given by Eq. (1.12). Once N is chosen the size of basis set, and of the matrices $H^{(m)}$ and $N^{(m)}$, is easily seen to be

$$\text{MATRIX SIZE} = \sum_{i=1}^N i = \frac{N(N+1)}{2} \quad (1.28)$$

Increasing N is analogous to increasing the value of the principal quantum number n that is included in the expansion of the trial function, but care has to be taken in this interpretation since the set of functions of Eq. (1.12) are not the isolated hydrogen atom wavefunctions.

The procedure of the calculation is now given by the following. First, the value of the m quantum number, which is still a good quantum number, is decided upon. Second, the eigenvalue's position in

TABLE 1.1

Convergence of the ground state energy for the hydrogen/impenetrable wall system at several distances. Distance is given in units of Bohr radii and energy is in units of Rydbergs.

	R	0.0	0.2	0.8	4.0
	3 × 3	-.2500	-.2448	-.4849	-.9888
	6 × 6	-.2500	-.2735	-.5012	-.9955
	10 × 10	-.2500	-.2786	-.5042	-.9969
	15 × 15	...	-.2800	-.5058	-.9972
	21 × 21	...	-.2801	-.5064	-.9973
	28 × 28	...	-.2802	-.5065	-.9974

the ordered set $E_i^{(m)}(R)$ $i=1,2,3,\dots$ is chosen. This is done because the optimum value of beta is dependent upon exactly which eigenvalue is to be minimized. Now the value of N of Eq. (1.27) is set and the optimum value of beta and the associated eigenvalue at that matrix size are calculated. Next the value of N is increased by 1, which increases the matrix size by $N + 1$, and again the eigenvalue is minimized with respect to beta. This process is repeated until the values of the minimized energy at two successive matrix sizes agree to a certain number of significant figures. In this report most of the results presented are calculated to four significant figures, recall that the energy is in units of Rydbergs, and this was obtained by going to matrix sizes of (28×28) . An example of convergence of the ground state for several distances is given in Table 5.1.

The results of the calculation for the first five states are given in Tables 1.2 to 1.5. There we have tabulated the optimum value of beta and the energy for a range of distances of the proton from the plane. Also included are several properties of these states that shall be discussed later. In these tables we have labelled the states by their m -quantum number and their position in the spectrum of the reduced problem, that is the spectrum of levels with all the same m -value. Tables of results for some of the higher excited states are presented in Appendix G.

The results of the ground state energy can be compared to those obtained by Bruch and Ruijgrok⁴ These authors were mainly interested in the imaging system as a model of physical adsorption (see next section); however the results for a change of the boundary

TABLE 1.2

Ground state properties of the hydrogen/impenetrable wall system ($m=0$, $p=1$). Energies are in units of Rydbergs, the dipole values are given in units of $\frac{ea_0}{2}$ ($=1.271$ debye), and the distances are given in terms of Bohr radii ($a_0 = 0.529 \text{ \AA}$).

R	β	E_0	$\bar{\mu}_z$	\bar{T}	\bar{V}
0.0	1.000	-0.2500	-	0.2500	-0.5000
0.2	1.001	-0.2802	-6.383	0.3170	-0.5972
0.4	1.077	-0.3272	-5.099	0.4458	-0.7730
0.6	1.321	-0.4027	-3.735	0.6774	-1.0801
0.8	1.537	-0.5065	-2.617	0.9527	-1.4592
1.0	1.696	-0.6172	-1.877	1.1480	-1.7652
1.2	1.795	-0.7144	-1.407	1.2375	-1.9519
1.4	1.850	-0.7912	-1.092	1.2576	-2.0488
1.6	1.872	-0.8488	-0.865	1.2429	-2.0917
1.8	1.876	-0.8911	-0.693	1.2139	-2.1049
2.0	1.870	-0.9217	-0.559	1.1811	-2.1028
3.0	1.603	-0.9855	-0.186	1.0599	-2.0452
4.0	1.183	-0.9974	-0.055	1.0157	-2.0131

TABLE 1.3

Properties of the first excited state of the hydrogen/impenetrable wall system ($m=0, p=2$). Units as in Table 1.2

R	β	$E(0,2)$	$\bar{\mu}_z$	\bar{T}	\bar{V}
0.0	0.500	-0.1111	-	0.1111	-0.2222
0.2	0.506	-0.1198	-17.171	0.1300	-0.2498
0.4	0.636	-0.1321	-15.231	0.1623	-0.2944
0.6	0.728	-0.1493	-13.148	0.2074	-0.3568
0.8	0.793	-0.1687	-11.408	0.2436	-0.4123
1.0	0.848	-0.1856	-10.172	0.2610	-0.4466
1.2	0.855	-0.1988	- 9.353	0.2669	-0.4657
1.4	0.865	-0.2087	- 8.761	0.2594	-0.4781
1.6	0.866	-0.2164	- 8.320	0.2702	-0.4866
1.8	0.868	-0.2224	- 7.974	0.2704	-0.4928
2.0	0.869	-0.2272	- 7.695	0.2700	-0.4972
3.0	0.849	-0.2408	- 6.840	0.2651	-0.5058
4.0	0.823	-0.2462	- 6.417	0.2595	-0.5056
5.0	0.793	-0.2484	- 6.193	0.2554	-0.5038

TABLE 1.4

Properties of the second excited state ($m=1, p=1$) of the hydrogen/
impenetrable wall system.

R	β	$E(1,1)$	$\bar{\mu}_z$	\bar{T}	\bar{V}
0.0	0.412	-0.1111	-	0.1111	-0.2222
0.2	0.449	-0.1150	-12.358	0.1190	-0.2340
0.4	0.486	-0.1192	-11.580	0.1282	-0.2474
0.6	0.519	-0.1239	-10.792	0.1387	-0.2626
0.8	0.559	-0.1291	- 9.999	0.1507	-0.2798
1.0	0.590	-0.1347	- 9.206	0.1643	-0.2991
1.2	0.625	-0.1409	- 8.425	0.1794	-0.3203
1.4	0.656	-0.1476	- 7.668	0.1956	-0.3431
1.6	0.687	-0.1545	- 6.948	0.2121	-0.3667
1.8	0.713	-0.1619	- 6.278	0.2282	-0.3900
2.0	0.738	-0.1693	- 5.663	0.2430	-0.4123
3.0	0.822	-0.2027	- 3.426	0.2871	-0.4898
4.0	0.851	-0.2248	- 2.147	0.2911	-0.5159
5.0	0.849	-0.2372	- 1.356	0.2815	-0.5187

TABLE 1.5

Properties of the third excited state ($m=0, p=3$) of the hydrogen/ impenetrable wall system. Note the discontinuity of the properties $\bar{\mu}_z$, \bar{T} and \bar{V} between the distances of $3.4a_0$ - $3.6a_0$ which indicates a level crossing.

R	β	$E(0,3)$	$\bar{\mu}_z$	\bar{T}	\bar{V}
0.0	0.268	-0.0625	-	0.0625	-0.1250
0.2	0.311	-0.0661	-32.516	0.0701	-0.1362
0.4	0.352	-0.0709	-30.202	0.0812	-0.1521
0.6	0.398	-0.0772	-27.665	0.0949	-0.1720
0.8	0.441	-0.0838	-25.323	0.1056	-0.1895
1.0	0.472	-0.0895	-23.551	0.1110	-0.2005
1.2	0.491	-0.0938	-22.314	0.1133	-0.2071
1.4	0.502	-0.0970	-21.444	0.1143	-0.2113
1.6	0.509	-0.0994	-20.804	0.1149	-0.2143
1.8	0.513	-0.1013	-20.317	0.1152	-0.2164
2.0	0.515	-0.1028	-19.932	0.1153	-0.2181
3.0	0.515	-0.1072	-18.809	0.1150	-0.2221
3.2	0.510	-0.1077	-18.676	0.1148	-0.2225
3.4	0.508	-0.1081	-18.558	0.1146	-0.2227
3.6	0.423	-0.1087	- 5.856	0.2206	-0.3294
3.8	0.449	-0.1154	- 4.709	0.2494	-0.3648
4.0	0.496	-0.1228	- 3.590	0.2791	-0.4019
5.0	0.650	-0.1656	+ 0.383	0.3736	-0.5391

surface only are given for the ground state. Their approach to the problem is a variational one that is similar in spirit to the present one. The difference is that the problem is cast in confocal elliptic coordinates with the foci at the proton and the image proton. The trial function is then chosen as

$$\psi_t = \exp(-\alpha \xi/2) \sinh(\beta \eta/2) \sum_{k,l} C_{k,l} \xi^k \eta^l \quad (1.29)$$

In Eq. (1.29) ξ and η are the coordinates in the confocal elliptic system, α and β are non-linear variational parameters, and the set $C_{k,l}$ constitute the linear variational parameters. The important feature of the trial function (1.29) is that the boundary value of $\psi_t = 0$ on the plane is satisfied by the $\sinh(\beta \eta/2)$ term. After converting their results to Rydbergs, the two calculations agree to as many significant figures as are reported in that paper. For example, at a distance of 1.2 Bohr radii from the plane both methods yield a ground state energy of -0.7144 Ry.

However the results of Bruch and Ruijgrok are given only for the ground state so that there is no information on the manner in which the spectrum of a hydrogen atom changes as an infinite plane potential moves in from infinity. This information is easier to interpret when it is presented as a graph showing the energy as a function of the distance of the proton from the plane. These graphs are presented in Figures 1.2 and 1.3.

It is evident from Figure 1.2 that when the proton is located

Fig. 1.2 Ground state energy as a function of distance of the hydrogen/impenetrable wall system. In this, and the following figures energy is in units of Rydbergs and distance is in units of Bohr radii.

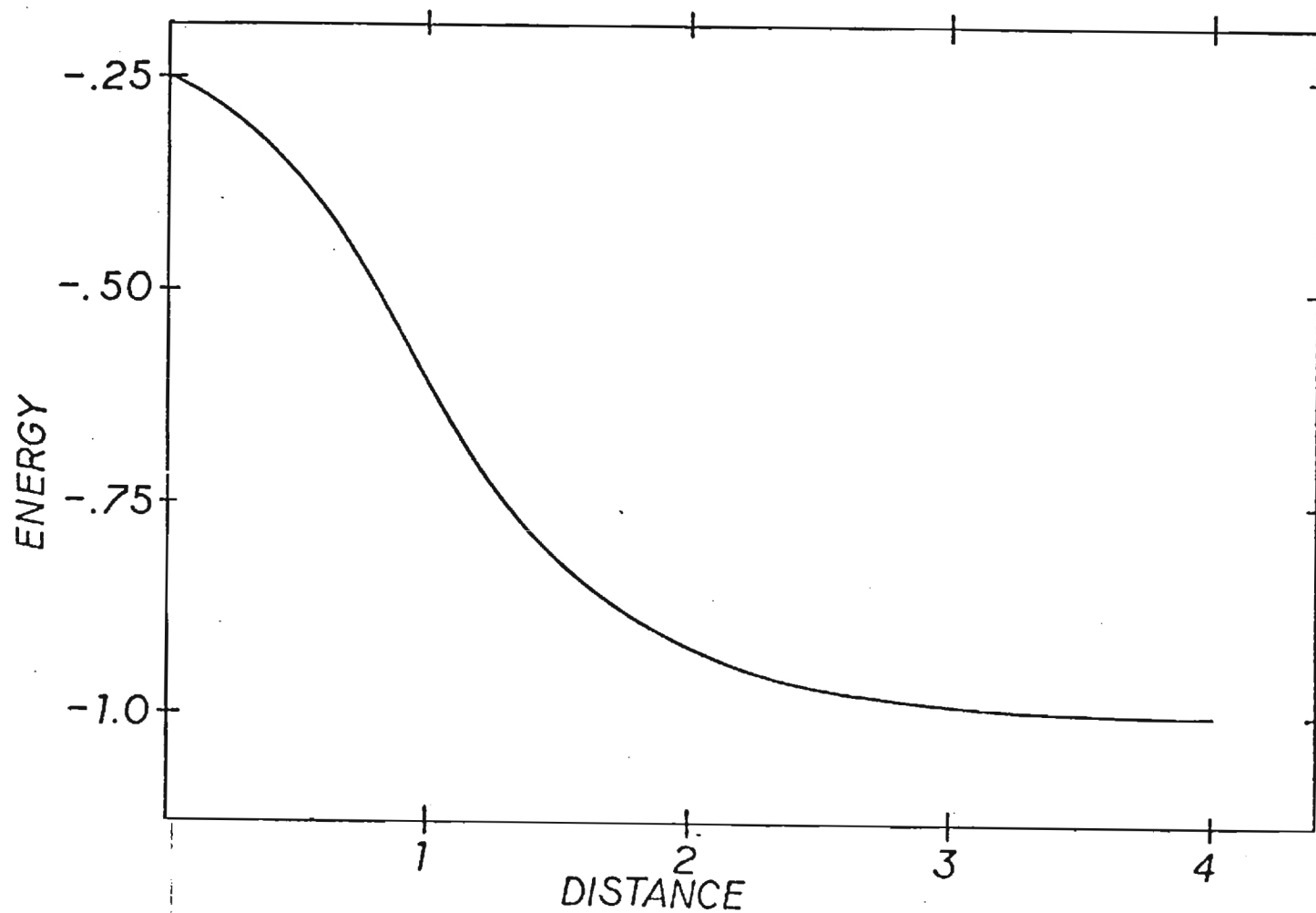
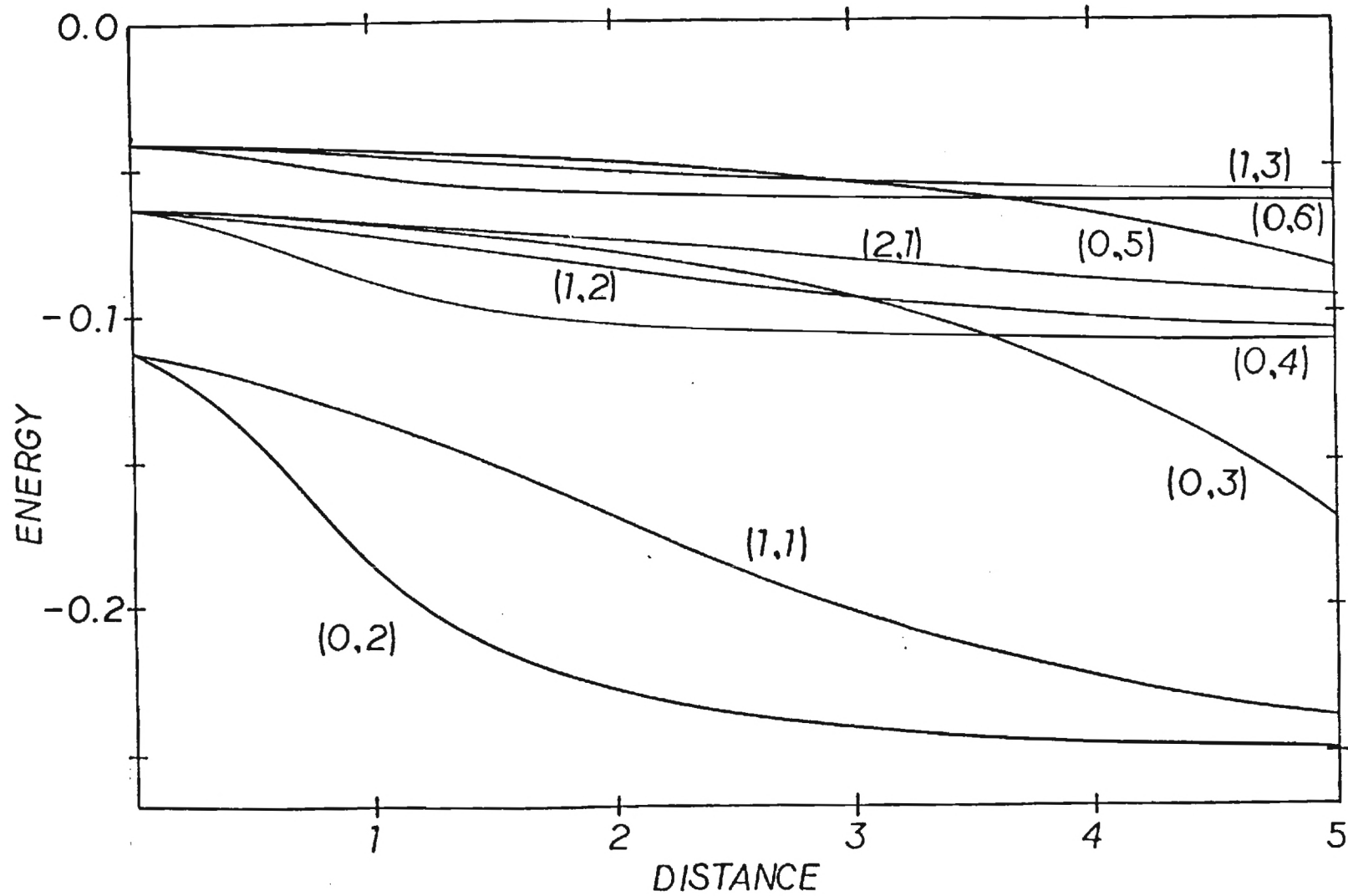


Fig. 1.3 The first 13 excited states of the hydrogen/impenetrable wall system.



four Bohr radii away from the plane there is very little change in the ground state energy. As the distance from the plane decreases the energy increases until, at $R=0$, it is equal to $-.25 \text{ Ry}$. This result is expected for the following reason. When the proton is located on the plane the boundary surface becomes a constant surface of a coordinate in a system in which the Hamiltonian is separable. Specifically, the plane can now be specified by $\theta = \pi/2$ and this means that the problem is again exactly solvable. The solutions are the isolated hydrogen atom eigenfunctions restricted by the selection rule

$$|\ell - m| = \text{odd} \quad (1.30)$$

This can be easily deduced from the value of the associated Legendre polynomials at zero argument. This result was first pointed out by Levine⁵, who noted its importance for a shallow donor impurity located at a surface.

The correct values of the $R=0$ limit are displayed by the excited states in Fig. 1.3. In that figure the states are labelled by their m value and their position in the matrix by the notation (m,p) . There are several interesting features exhibited by the spectrum presented in Figure 1.3. At $R = \infty$ there exists two states with $n = 2$ and $m = 0$, i.e. the $2S$ and $2p_0$ states. However, at $R=0$ there exists only one state with $n = 3$ and $m = 0$ because of the selection rule (1.30) and that is the $3p_0$ state. Therefore one of the states with $n = 2, m = 0$ at $R = \infty$ must map onto a state with $n = 4$ at $R = 0$. At $R = 5 a_0$ the state which does this is labelled by $(0,3)$. As R decreases the energy

of state (0,3) increases until it crosses the state (0,4). These two states possess the same azimuthal quantum number m and are therefore eigenvalues of the same matrix problem. This appears to be a true crossing for two reasons. First, the eigenvalues become equal, to four figure accuracy which is the limit of accuracy in the present calculations, at a distance from the plane of approximately $3.58 a_0$. Second, the properties derived from the wavefunctions of these two states only have a consistent interpretation if such a crossing takes place. That is, the dipole in the z -direction, the average kinetic energy and the average potential energy should be continuous functions of the distance from the plane and this would not be the case if such a crossing did not occur. The symmetry that this degeneracy might imply has not yet been determined. As the distance to the plane is decreased even further there takes place another crossing. However this crossing is for states of differing azimuthal symmetry so there is no reason to suspect another symmetry of the system at this distance.

Turning now from the energies of these states to some of their properties, the set of Figures 1.4 to 1.8 exhibit the changes in the ground state wavefunction as the proton moves closer to the plane on which $\psi = 0$. What is shown in these perspective plots is the value of the wavefunction on a plane that contains the proton and is perpendicular to the boundary plane. The location of the proton is at the intersection of the grid lines marked by the arrows, and the boundary plane intersection is marked by a dark line. These figures exhibit the smooth change of the ground state from a $1s$ state

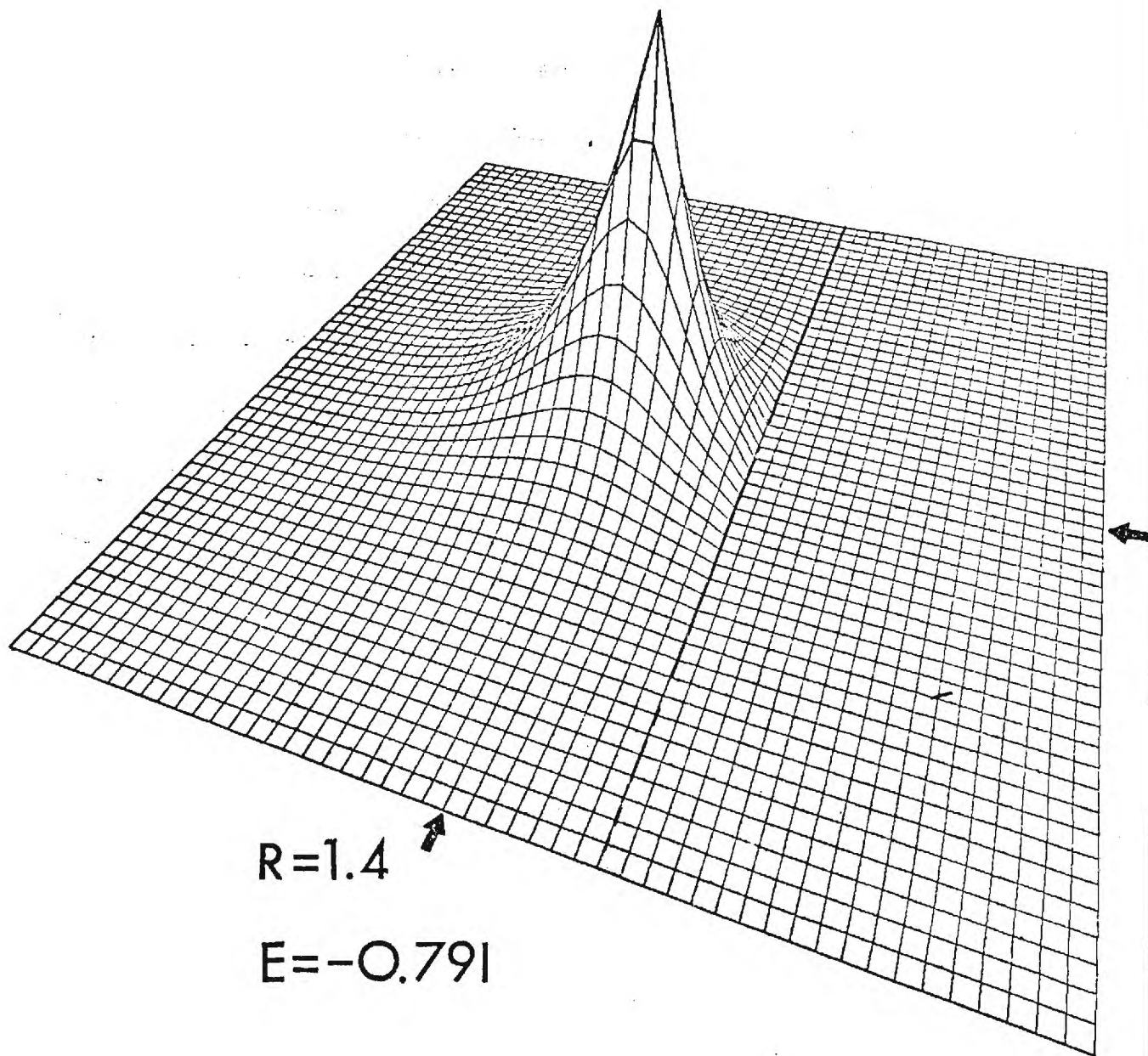


Fig. 1.4 Ground state wavefunction when proton is $1.4 a_0$ away from plane. (See text above Eq. (1.31).)

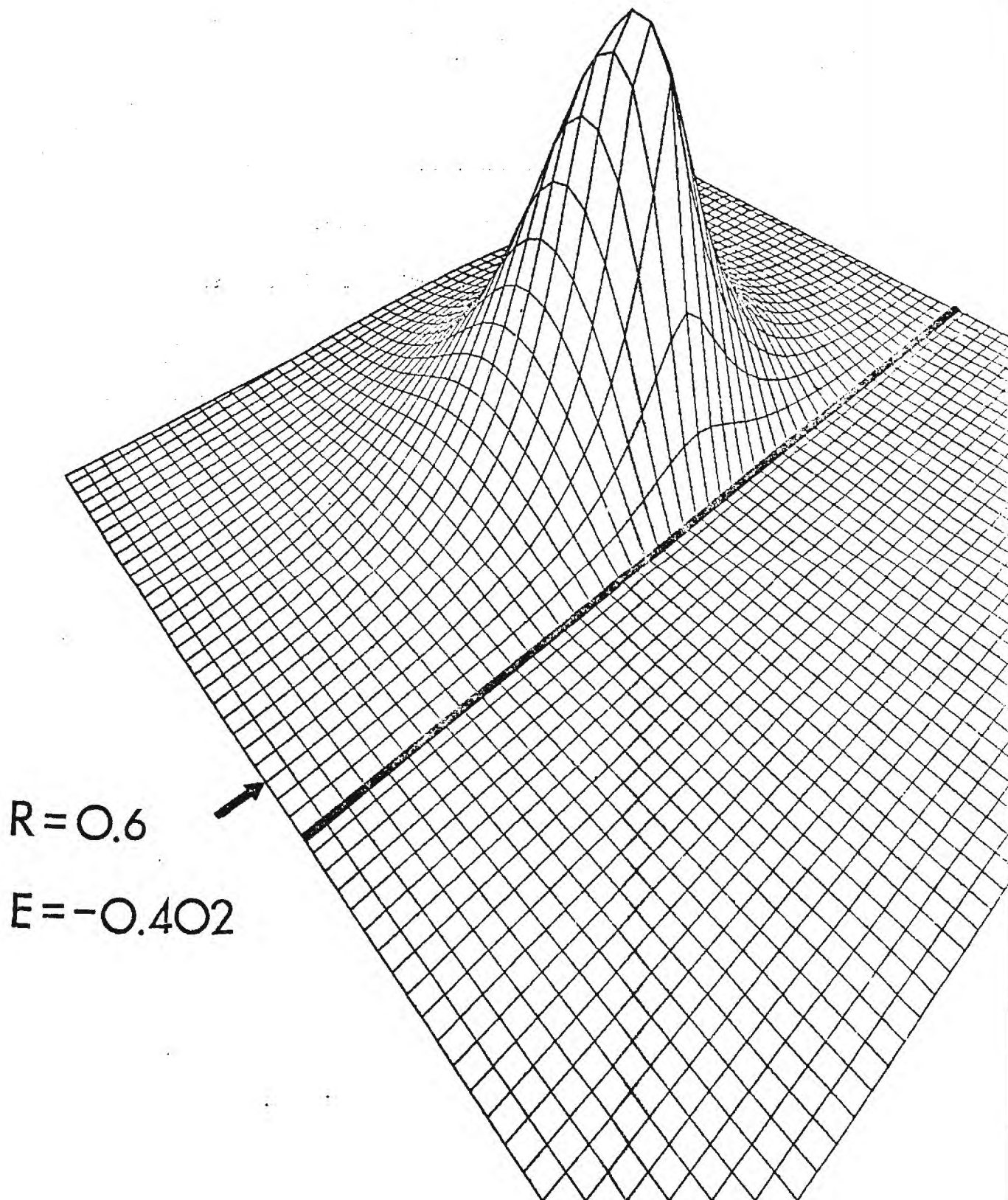


Fig. 1.6 Ground state wavefunction when proton is $0.6 a_0$ away from plane.

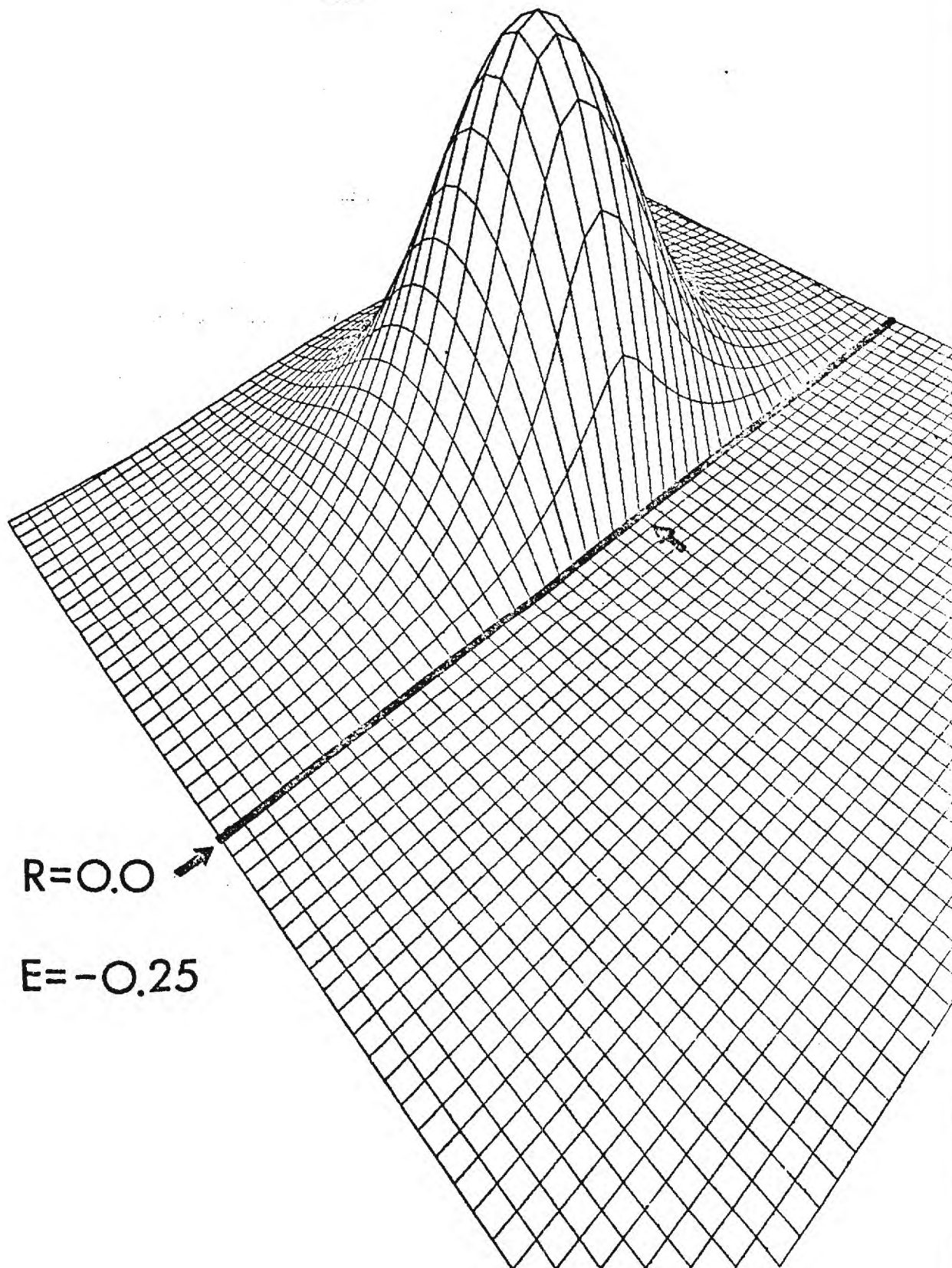


Fig. 1.7 Ground state wavefunction when proton is on the plane.

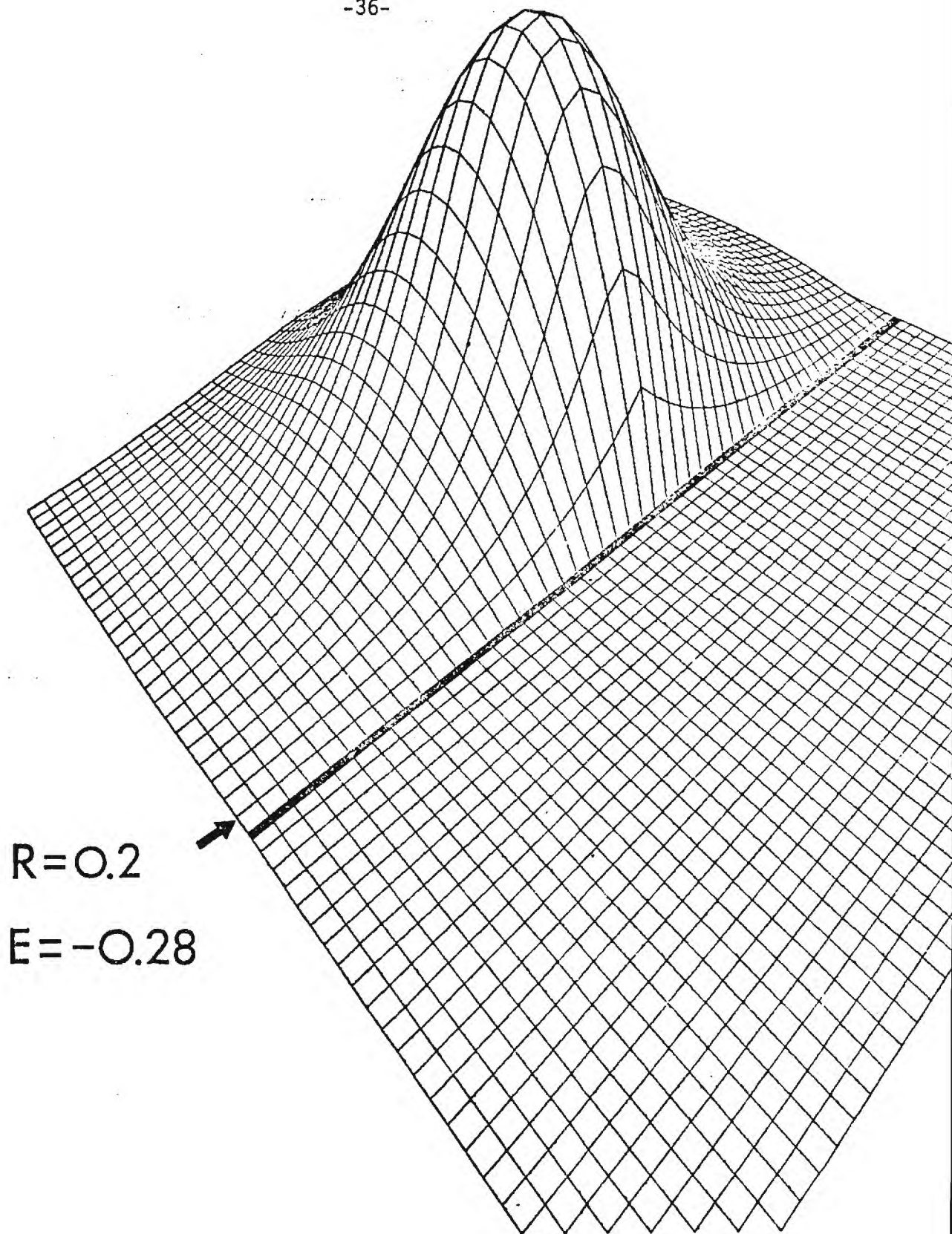


Fig. 1.8 Ground state wavefunction when proton is $0.2 a_0$ away from plane.

at large R to the $2p_0$ state at $R = 0$.

The ground state of an isolated hydrogen atom does not possess a net dipole moment. However when the charge distribution is changed by the presence of the boundary plane this is no longer true. Because of the azimuthal symmetry, the dipole moment of the ground state will be in the z-direction and the dipole moment operator can be written as⁴

$$\mu \equiv Z = r \cos \theta. \quad (1.31)$$

A positive dipole moment is directed away from the boundary plane.

The convention used here is that the dipole points from the negative to the positive charge.

The manner in which the average value of μ is calculated is modified slightly due to the non-orthogonality previously discussed.

First the matrix $\underline{D}^{(m)}$ is calculated, where

$$\left(\underline{D}^{(m)} \right)_{h'l', h'l} = \int_T \phi_{h'l'm} \mu \phi_{h'l'm} dV, \quad (1.32)$$

and the optimized value of β is used. The expectation value of μ for a state labelled by (m,k) is then given by

$$\langle \mu \rangle_k^{(m)} = \frac{A_k^{(m)T} \underline{D}^{(m)} A_k^{(m)}}{A_k^{(m)T} \underline{N}^{(m)} A_k^{(m)}} \quad (1.33)$$

where $\underline{A}_k^{(m)}$ is the optimized k-th eigenvector of Eq. (1.13) and $\underline{N}^{(m)}$ is the overlap matrix.

These average values have been calculated and they appear in Tables 1.2 through 1.5 and in Appendix A. As expected, and shown previously in the perspective plots, the action of the boundary plane is to push the electronic charge distribution away so that its 'center of gravity' lies behind the proton and yields negative $\langle \mu \rangle$. Note also that the dipole moments fall off much less rapidly as a function of R for the excited states. This is due to the fact that the excited states, because of their greater spatial extent, 'feel' the presence of the plane for a further distance than does the ground state.

The average kinetic and potential energies can be calculated in a manner similar to that for the dipole. But now it is not necessary to calculate any additional matrices, for $\underline{T}^{(m)}$ and $\underline{V}^{(m)}$ are already available from the calculation of $\underline{H}^{(m)}$. These expectation values have also been computed and appear in the same tables as the energies and dipole moments.

In examining the expectation values of the kinetic and potential energies of the electron given in these tables it is apparent that the relation

$$2\bar{T} = -\bar{V} \quad (1.34)$$

is no longer satisfied. Equation (5.34) is of course the statement of the virial theorem for an isolated system with a coulomb interaction. When the system depends upon a parameter which is assumed to be fixed, which for example can be the internuclear coordinates of a

diatomic molecule in the Born-Oppenheimer approximation or the distance to the plane in the present problem, the virial theorem must be modified from the form given in Eq. (1.34). This is due to the fact that the quantity known as the 'virial'

$$-\frac{1}{2} \sum_i \overline{r_i F_i}$$

must include *all* of the forces acting on the system. This means that since the proton is assumed to be in a fixed position some external force must be acting on it so that it remains stationary. When this external force is taken into account the correct form of the virial theorem is given by

$$2\overline{T} = -\overline{V} - R \frac{\partial E}{\partial R} \quad (1.35)$$

The force acting on the proton is therefore given by the quantity $\partial E/\partial R$. Note that in the present case the Hellman-Feynman theorem is no longer valid^{4,18}. That is

$$\frac{\partial E}{\partial R} \neq \left\langle \frac{\partial H}{\partial R} \right\rangle$$

because the region of integration of the matrix elements is dependent upon R. This points out the importance of the virial theorem, and the choice of the basis set, if the force on the proton is to be found.

The results presented in Table 1.2 have been used, with the aid of Eq. (1.35), to calculate the force on the proton when the atom is

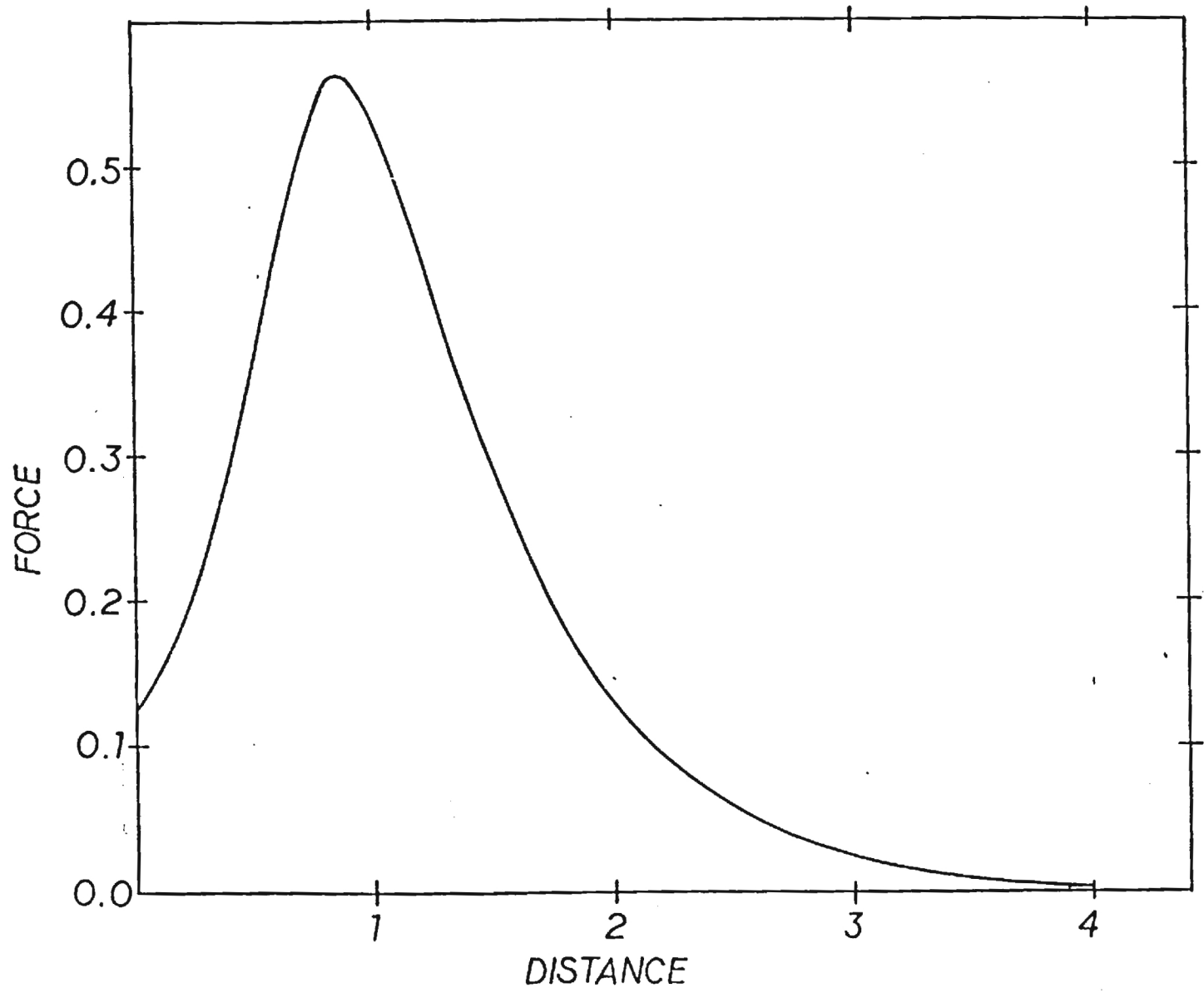


Fig. 1.9 Force on the proton when the electron is in its ground state.

in its ground state as a function of distance. This force is presented graphically in Figure 1.9. The interesting features of this force is that it has a maximum at approximately $0.9 a_0$ and that it is nonzero at $R = 0$. At $R = \infty$ the force is zero and at $R = -\infty$ it must also be zero for then the electron and proton have been completely separated. Therefore a maximum must exist between these two limits.

1.4 Image Charges and a Model of the Physical Adsorption of Atomic Hydrogen

When a gas adsorbs onto a solid surface, depending upon the binding energy, it is usually said to be chemisorbed or physically adsorbed. The binding energy that is ascribed to chemical adsorption can be several electron volts while the weaker physical adsorption is several orders of magnitude less. The difference in binding energy is a reflection of the different processes which are believed to occur in the two types of adsorption; in chemical adsorption a bond is formed between the adsorbed molecule or atom and the surface while in physical adsorption significant charge rearrangement is absent.

Physical adsorption is usually thought to be due to a potential that is made up of an attractive long-range Van der Waals (or dispersion) potential and a short-range repulsive potential due to the overlap of the electrons of the ad-atom with those of the metal. The problem is a many electron one and has been the subject of much recent work¹⁹. However, in the case of atomic hydrogen an idealized model can be constructed, as presented by Bruch and Ruijgrok, which

reduces to a one electron problem.

The model is given by the following. The metal is replaced by a perfectly imaging medium with instantaneous coulomb interactions. The effect of the exchange repulsion is modelled by the condition that the atomic electron is excluded from the metal and that its wavefunction vanish on the surface. The potential that the proton then experiences, what is called by Bruch and Ruijgrok the 'holding potential', is given by the change in the ground state electronic energy plus the interaction of the proton with the various images in the metal.

Solving the problem of the ground state electronic energy of this system is the first step in obtaining the 'holding potential' of the atomic hydrogen. Taking into account the possibility of finite dielectric constant for Region B of Fig. 1.1, the Hamiltonian for the electron can be written as

$$\mathcal{H} = \frac{-\hbar^2}{2m} \nabla^2 - \frac{e^2}{r} + \frac{(\epsilon-1)}{(\epsilon+1)} \frac{e^2}{[r^2 + 4R^2 - 4rR\cos\theta]^{1/2}} - \frac{(\epsilon-1)}{4(\epsilon+1)} \frac{e^2}{(R-r\cos\theta)} \quad (1.36)$$

Equation (1.36) must, of course, be solved subject to the boundary condition that $\psi = 0$ on the surface $z = R$. The coordinate system of Eq. (1.36) is that indicated in Figure 1.1 and ϵ denotes the static dielectric constant of region B. We shall be interested mainly in the 'metallic' limit, that is $\epsilon \rightarrow \infty$. The last two terms in Eq. (1.36)

are, respectively, the interaction of the electron with the image of the proton and the interaction of the electron with its own image, and hence the extra factor of $1/2$ (energy of assembly).

The calculation of the energy eigenvalues and properties of these states proceeds exactly as previously outlined. Now, however, there are the two additional matrix elements to be included in the matrix equations. The electron-image electron term is not hard to calculate analytically but this is not true of the electron-image proton interaction given by the third term of Eq. (1.36). Because of the law of cosines denominator and the restricted region of integration given by Eq. (1.14), it has not been possible to find a closed form expression for that matrix element.

There are two ways of calculating the electron-image proton matrix element. One can either use a numerical approach or, by expanding the denominator of the electron-image proton potential in the standard series of Legendre polynomials, integrate term by term. The former method was chosen because the expressions and summation of the latter method consumed a much greater amount of computer time than a straightforward numerical integration of the matrix elements by the Gauss-Legendre and Gauss-Laguerre methods.

The results of this calculation are given in Tables 1.6 through 1.9 for the first 5 states. (Recall that $m \neq 0$ states are doubly degenerate.) The ground state of this system is shown graphically in Figure 1.10 where the ground state of the non-imaging case has been repeated for comparison. As is apparent from this figure, and shown

TABLE 1.6

Ground state properties of the hydrogen/perfectly imaging substrate system. \bar{V}_1 , \bar{V}_2 and \bar{V}_3 denote the average values of the last three interaction terms in the Hamiltonian of Eq. (1.36).

R	β	$E(0,1)$	$\bar{\mu}_z$	\bar{T}	\bar{V}_1	\bar{V}_2	\bar{V}_3
0.2	0.174	-0.0633	-11.408	0.0673	-0.1470	-0.1267	0.1440
0.4	0.399	-0.0726	- 9.597	0.1055	-0.2995	-0.1450	0.2664
0.6	0.753	-0.1039	- 6.482	0.2578	-0.5789	-0.2002	0.4174
0.8	1.142	-0.1839	- 3.671	0.6107	-1.0821	-0.2841	0.5717
1.0	1.439	-0.3049	- 2.237	0.9413	-1.5444	-0.3326	0.6308
1.2	1.621	-0.4274	- 1.532	1.1139	-1.8209	-0.3409	0.6205
1.4	1.725	-0.5309	- 1.125	1.1758	-1.9612	-0.3295	0.5848
1.6	1.780	-0.6123	- 0.856	1.1821	-2.0270	-0.3105	0.5430
1.8	1.806	-0.6748	- 0.662	1.1641	-2.0518	-0.2893	0.5024
2.0	1.813	-0.7224	- 0.514	1.1376	-2.0564	-0.2684	0.4648
3.0	1.539	-0.8405	- 0.125	1.0296	-2.0135	-0.1853	0.3287
4.0	1.228	-0.8825	- 0.009	0.9959	-1.9927	-0.1353	0.2497
5.0	1.033	-0.9046	+ 0.013	0.9922	-1.9915	-0.1053	0.2001
6.0	0.912	-0.9193	+ 0.011	0.9943	-1.9942	-0.0862	0.1667

TABLE 1.7

Properties of the first excited state ($m=1, p=1$) of the hydrogen/
impenetrable wall system.

R	β	$E(1,1)$	$\bar{\mu}_z$	\bar{T}	\bar{V}_1	\bar{V}_2	\bar{V}_3
0.2	0.149	-0.0602	-11.906	0.0606	-0.0506	-0.1207	0.0505
0.4	0.150	-0.0604	-11.486	0.0609	-0.0530	-0.1210	0.0527
0.6	0.152	-0.0605	-11.059	0.0614	-0.0565	-0.1213	0.0558
0.8	0.156	-0.0608	-10.624	0.0621	-0.0620	-0.1217	0.0608
1.0	0.162	-0.0611	-10.170	0.0636	-0.0717	-0.1223	0.0694
1.2	0.177	-0.0617	- 9.676	0.0671	-0.0915	-0.1234	0.0860
1.4	0.216	-0.0630	- 9.077	0.0759	-0.1287	-0.1253	0.1152
1.6	0.286	-0.0656	- 8.299	0.0920	-0.1766	-0.1288	0.1478
1.8	0.363	-0.0697	- 7.407	0.1133	-0.2234	-0.1335	0.1740
2.0	0.434	-0.0752	- 6.503	0.1372	-0.2675	-0.1386	0.1936
3.0	0.660	-0.1138	- 3.207	0.2322	-0.4205	-0.1490	0.2235
4.0	0.745	-0.1476	- 1.587	0.2575	-0.4732	-0.1369	0.2050
5.0	0.757	-0.1695	- 0.669	0.2544	-0.4847	-0.1191	0.1799
6.0	0.722	-0.1830	- 0.116	0.2463	-0.4848	-0.1019	0.1574

TABLE 1.8

Properties of the second excited state of the hydrogen/perfectly imaging substrate system.

R	β	$E(0,2)$	$\bar{\mu}_z$	\bar{T}	\bar{V}_1	\bar{V}_2	\bar{V}_3
0.2	0.135	-0.0590	-12.162	0.0615	-0.0773	-0.1184	0.0756
0.4	0.144	-0.0602	-11.526	0.0622	-0.0590	-0.1207	0.0573
0.6	0.154	-0.0608	-11.052	0.0630	-0.0623	-0.1219	0.0604
0.8	0.191	-0.0616	-10.669	0.0663	-0.0836	-0.1229	0.0786
1.0	0.423	-0.0656	-10.648	0.0983	-0.2011	-0.1213	0.1586
1.2	0.537	-0.0733	-10.036	0.1239	-0.2692	-0.1207	0.1927
1.4	0.596	-0.0819	- 9.344	0.1430	-0.3128	-0.1207	0.2086
1.6	0.635	-0.0906	- 8.736	0.1587	-0.3451	-0.1203	0.2161
1.8	0.662	-0.0989	- 8.228	0.1716	-0.3700	-0.1193	0.2187
2.0	0.681	-0.1068	- 7.806	0.1822	-0.3897	-0.1176	0.2183
3.0	0.727	-0.1378	- 6.508	0.2119	-0.4430	-0.1045	0.1977
4.0	0.720	-0.1580	- 5.885	0.2230	-0.4631	-0.0899	0.1720
5.0	0.678	-0.1716	- 5.497	0.2291	-0.4730	-0.0779	0.1501
6.0	0.609	-0.1818	- 4.762	0.2368	-0.4806	-0.0722	0.1343

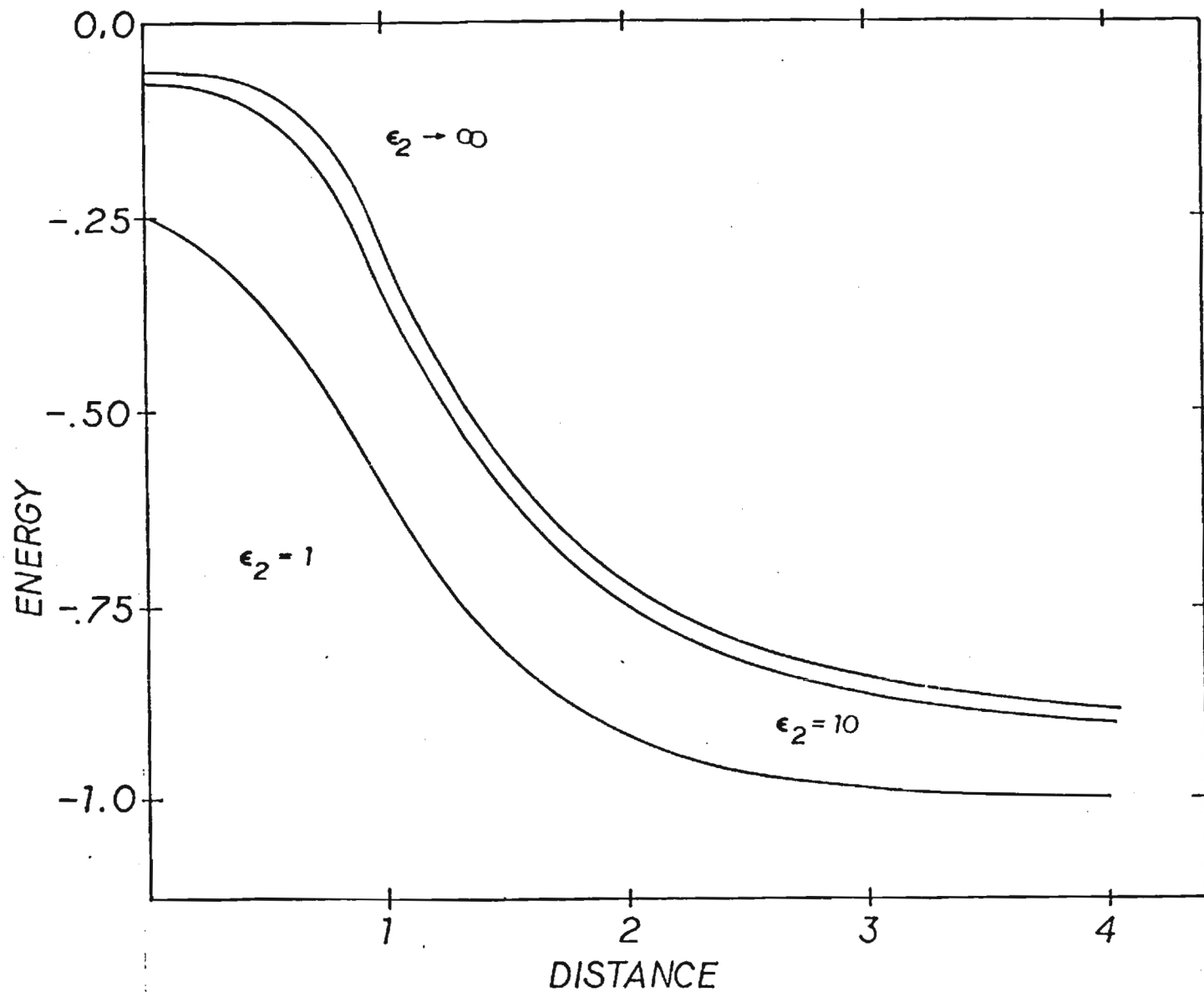


Fig. 1.10 Ground state energy as a function of proton distance from the plane for the perfectly imaging substrate ($\epsilon_2 \rightarrow \infty$) system.

explicitly in Table 1.6 where all the energy contributions are tabulated, the interaction of the electron with the image of the proton, which is repulsive, dominates the electron-image electron interaction which is attractive. In this instance also the $R = 0$ value is an expected one. When $R = 0$, and the system is perfectly imaging, the proton and image proton charges cancel each other (at least as far as the electron is concerned) and the problem is now that of an electron bound by its image, that is, a one-dimensional coulomb problem. Therefore at $R = 0$ the problem becomes the exactly solvable^{20,21} one dimensional coulomb problem with a ground state energy of -0.0625 Ry.

Now that the electronic part of the problem is solved, it is possible to construct the 'holding potential' of the atomic hydrogen. The potential field that the proton experiences has three contributions. First, still in the Born-Oppenheimer approximation, is the change in the ground state energy of the system as a function of distance. The second is the proton-image proton interaction which is attractive in nature. Thirdly, the potential at the site of the real proton due to the presence of the image electron must be calculated. However, and this is a crucial point, the electronic problem alone must first be solved before this last interaction can be calculated. Since the proton is considered as being fixed while the electron is not, the ground state *wavefunction* at that distance must be calculated and the corresponding charge density formed to obtain an *image charge density*. The coulomb interaction between the image charge density and the real proton is then integrated over the domain of the image

charge density to finally yield the third interaction term of the holding potential. This last quantity is exactly given by the average value of the third term in Eq. (1.36), the electron-image proton term. This is due simply because the charge products and distances involved are exactly the same. To repeat for the sake of clarity, this third interaction term is not to be added to the Hamiltonian of Eq. (1.36) for it has nothing to do with the potential the electron experiences, but it is rather associated with the potential the proton experiences and it cannot be calculated until the image charge density is known, i.e. the ground state wave function of the Hamiltonian of Eq. (1.36).

This last term in the interaction energy *has not* been included in the calculation of Bruch and Ruijgrok. This is evident in their equations (2.8) through (2.12) which are the defining equations of their model. To demonstrate this numerically we take the energy values presented in our Table 1.6, subtract out the ground state energy at $R = \infty$ (-1.0 Ry) and add the proton-proton image interaction energy of $-1/2R$ Ry. There results the same values as given by Table 1 of Bruch and Ruijgrok. For comparison, converting their value into an electronic ground state energy by the reverse of the above process, their result at $R = 2.0 a_0$ is $-.7223$ Ry while that of the present calculation is $-.7224$ Ry.

When the 'holding potential' is calculated in this way, that is the proton-image electron interaction is neglected, there results a potential well at approximately $R = 3.44 a_0$ and a depth of $\sim 8.6 \times 10^{-3}$ Ry. This is shown graphically in Fig. 1.11. The various contributions

Fig. 1.11 The 'holding potential' of Bruch and Ruijgiok in which the image electron-proton interaction has not been included.

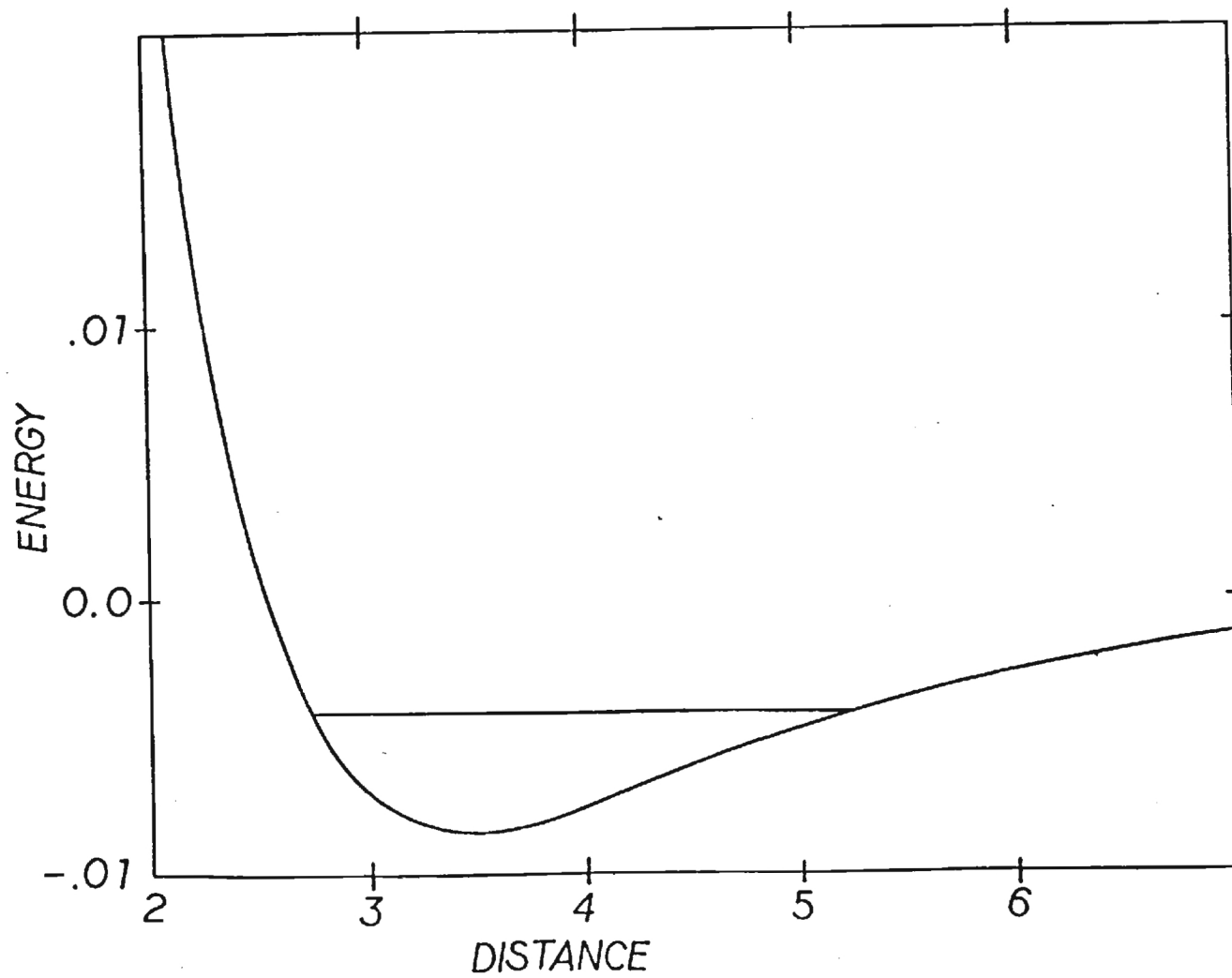
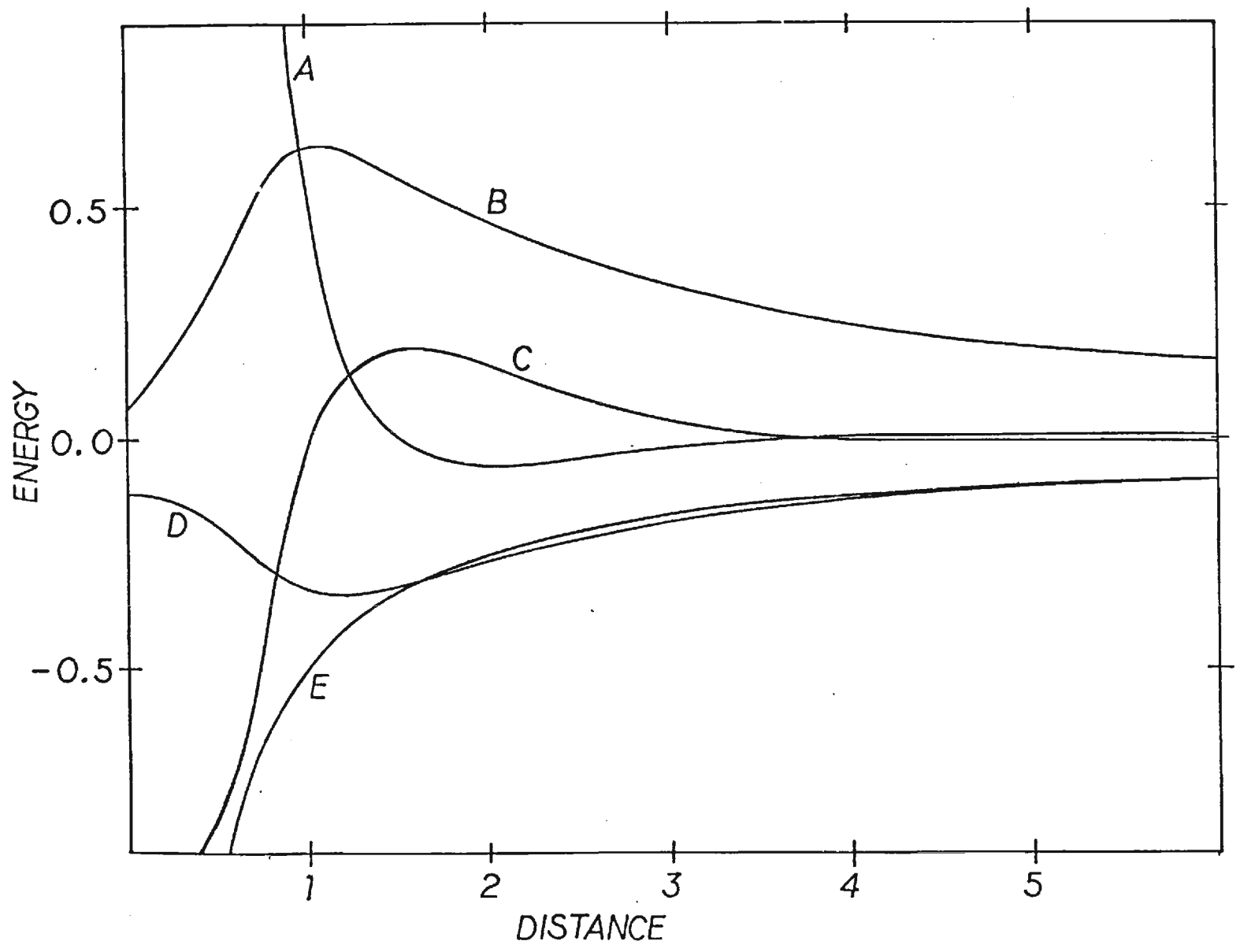


Fig. 1.12 The various contributions to the interaction potential. The curve A represents the change in the expectation value of the electron-proton interaction from its value for the isolated hydrogen atom. The curve B is the average value of the electron-image proton interaction ($\bar{V}_e - \text{Imp}$). The curve C is the change in the electron's average kinetic energy. The curve D represents the average value of the electron-image electron interaction ($\bar{V}_e - \text{Ime}$). The curve E is the proton-image proton interaction ($-1/2R$).



to this 'holding potential' are shown in Fig. 1.12. The $R = \infty$ values of the kinetic and potential (real electron-real proton) energies have been subtracted from those terms and the electron-image proton average interaction is denoted by V_{e-IMP} and that of the electron-image electron by \bar{V}_{e-IME} . The proton-image proton interaction is denoted by $-1/2R$. The sum of the curves in Fig. 1.12 is then simply the potential curve presented in Fig. 1.11.

This situation changes drastically when the proton-image electron interaction is added. As noted before, this is identical to the average value of the electron-image proton interaction which is listed in Table 1.5 and shown in Fig. 1.12 by the curve labelled \bar{V}_{e-IMP} . When this term is added the shallow potential well shown in Fig. 1.11 is completely lost and the 'holding potential' simply doesn't hold. Therefore it is seen that when all the interactions are taken into account, the model of physical adsorption of atomic hydrogen presented by Bruch and Ruijgrok yields no binding between a hydrogen atom in its ground state and the model surface.

CHAPTER II

SHALLOW DONOR IMPURITIES NEAR SEMICONDUCTOR INTERFACES

The methods presented in the preceding chapter will be used in the present chapter to solve the effective mass Hamiltonian for a shallow donor impurity when it is near the interface of a semiconductor. The boundary condition of $\psi = 0$ on a plane is used because the increase in the potential energy of the electron upon leaving the semiconductor is usually on the order of several electron volts, which is several orders of magnitude larger than the binding energy of the electron to the impurity center. First a brief discussion of the effective mass Hamiltonian and its derivation is presented. For materials with spherical conduction bands the methods of Section 1.4 can be used without modification. However, when materials with ellipsoidal conduction bands like silicon and germanium are considered, the anisotropic effective mass must be taken into account in the effective mass Hamiltonian and in the trial function. After this is done, results for the binding energies of shallow donors near the Si (001) surface and the Ge (111) surface are presented. Finally, with the inclusion of an additional matrix element, the effect of a Si/SiO₂ interface and the applied field in a MOS (Metal-Oxide-Semiconductor) Field effect transistor is studied.

2.1 The Effective Mass Hamiltonian

Consider the introduction of a Group V atom into a Group IV elemental semiconductor, or of Group VI impurity in a III-V semiconductor²². In both cases we assume that the impurity location is a substitutional one and in the second case it is the Group V atom that has been replaced. Because of the impurity, the periodicity of the perfect lattice is lost and we wish to investigate the consequences of this.

Purely as a gedanken exercise assume that such an impurity atom has been introduced minus one electron, so that it contains the same number of valence electrons as that of the replaced atom. The impurity potential arising from such a substitution is then analogous to placing an extra positive charge at one of the lattice positions and this leads to a Coulombic potential that is reduced by the static dielectric constant, ϵ , of the pure material, that is

$$V_i(r) = \frac{-e^2}{\epsilon r}. \quad (2.1)$$

For semiconductors to which this analysis is applied, typical values of ϵ range from about 10 to 16. When the electron is added to this system it must enter the conduction band (we assume $T=0$ so that the valence band is completely filled) and its motion is governed by the band structure and the action of the impurity potential. Because the electron enters an empty conduction band we can perform a Taylor series expansion about the minimum of the energy band to obtain

$$E(\vec{k}) - E_c = \frac{\hbar^2}{2} (\vec{k} - \vec{k}_0) \cdot \overleftrightarrow{m}^{*-1} \cdot (\vec{k} - \vec{k}_0), \quad (2.2)$$

where E_c denotes the conduction band edge and

$$\frac{1}{m_{ij}^*} = \left. \frac{\partial^2 E(\vec{k})}{\partial k_i \partial k_j} \right|_{\vec{k} = \vec{k}_0}, \quad (2.3)$$

where the quantity \overleftrightarrow{m}^* is known as the effective mass tensor. In coordinate space this yields an effective one-electron Hamiltonian, when the effective mass tensor has only equal diagonal components, given by

$$\mathcal{H} = \frac{-\hbar^2}{2m^*} \nabla^2 - \frac{e^2}{\epsilon r}. \quad (2.4)$$

It is through the use of an effective mass, m^* , that the action of the periodic potential of the crystal is taken into account in a one-electron Hamiltonian.

The use of the Coulombic potential that is reduced by the static dielectric constant, can only be justified if the distances involved are much larger than the lattice spacing. To investigate this point note that Eq. (2.4) is just that of a hydrogen atom in a dielectric medium and that the eigenvalues are given by²²

$$E_n = -13.6 \frac{1}{n^2} \left(\frac{m^*}{m} \right) \left(\frac{1}{\epsilon^2} \right) \text{ eV}. \quad (2.5)$$

The radius of the minimum Bohr orbit of the electron about the impurity is

$$a_0^* = \frac{\hbar^2 \epsilon}{m^* e^2} = 0.529 \left(\frac{\epsilon m}{m^*} \right) \text{Å}. \quad (2.6)$$

For GaAs where $(m^*/m) = 0.07$ and $\epsilon = 11.6$, the ground state energy is $E = -.006 \text{ eV} = 6 \text{ meV}$. The orbit size is about 90 Å and this indicates that the use of the impurity potential of Eq. (2.1) is not inconsistent.

The derivation of an effective mass Hamiltonian has a more formal nature than the foregoing discussion suggests. In the original work of Kohn and Luttinger^{23a} and in the review article by Kohn^{23b} it is shown how to derive, and variationally solve, effective mass Hamiltonians for silicon and germanium. In the following we shall follow the derivation given by Pantelides in a recent review article²⁴.

One starts with the one-electron Hamiltonian for the imperfect crystal

$$\mathcal{H} \psi_{\nu} = E_{\nu} \psi_{\nu}, \quad (2.7)$$

and then expands ψ_{ν} in terms of the Bloch functions of the unperturbed crystal

$$\psi_{\nu}(\vec{r}) = \sum_{n, \vec{k}} F_n(\vec{k}) \psi_{n\vec{k}}^{\circ}(\vec{r}) \quad (2.8)$$

Here n denotes the band index, \vec{k} the wave vector and the $F_n(\vec{k})$ are the expansion coefficients. Upon writing $H = H_0 + U$, where U is the

impurity potential; and using the expansion (2.8) in Eq. (2.7) the following equation is obtained

$$\begin{aligned} (\mathcal{H}_0 + U) \sum_{n\vec{k}} F_n(\vec{k}) \psi_{n\vec{k}}^0(\vec{r}) &= \sum_{n\vec{k}} (E_n^0(\vec{k}) + U) F_n(\vec{k}) \psi_{n\vec{k}}^0(\vec{r}) \\ &= E_{\mathcal{V}} \sum_{n\vec{k}} F_n(\vec{k}) \psi_{n\vec{k}}^0(\vec{r}) \end{aligned} \quad (2.9)$$

After multiplying on the left by $\psi_{n'\vec{k}'}$, integrating over all space and using the ortho-normality of the Bloch functions, i.e.

$$\langle \psi_{n'\vec{k}'}^0 | \psi_{n\vec{k}}^0 \rangle = \delta_{n'n} \delta_{\vec{k}'\vec{k}}, \quad (2.10)$$

there results after switching primed and unprimed symbols, the equation

$$E_n^0(\vec{k}) F_n(\vec{k}) + \sum_{n'\vec{k}'} \langle \psi_{n\vec{k}}^0 | U | \psi_{n'\vec{k}'}^0 \rangle F_{n'}(\vec{k}') = E_{\mathcal{V}} F_n(\vec{k}) \quad (2.11)$$

One form of Bloch's Theorem states that the perfect crystal wave functions, $\psi_{n\vec{k}}^0(\vec{r})$, can be written as

$$\psi_{n\vec{k}}^0(\vec{r}) = e^{i\vec{k}\cdot\vec{r}} u_{n\vec{k}}^0(\vec{r}) \quad (2.12)$$

where $u_{n\vec{k}}^0(\vec{r})$ possess the periodicity of the crystal lattice. That is

$$u_{n\vec{k}}^0(\vec{r} + \vec{l}) = u_{n\vec{k}}^0(\vec{r}) \quad (2.13)$$

where \vec{l} is a crystal lattice vector. If the form of Eq.(2.12) is used in (2.11), the product $u_{n\vec{k}}^{0*}(\vec{r}) u_{n\vec{k}}^0(\vec{r})$ can be expanded as

$$u_{n\vec{k}}^{\circ*}(\vec{r}) u_{n'\vec{k}'}^{\circ}(\vec{r}) = \sum_{\vec{p}} C_{\vec{k}\vec{k}'}^{nn'}(\vec{K}_p) e^{i\vec{K}_p \cdot \vec{r}} \quad (2.14)$$

In Eq. (2.14) the \vec{K}_p 's are the reciprocal lattice vectors and they yield the only contribution to the sum because of the periodicity condition given by Eq. (2.12). The matrix element in Eq. (2.11) can now be written as

$$\langle \psi_{n\vec{k}}^{\circ} | U | \psi_{n'\vec{k}'}^{\circ} \rangle = \sum_{\vec{p}} C_{\vec{k}\vec{k}'}^{nn'}(\vec{K}_p) U(\vec{k} - \vec{k}' - \vec{K}_p) \quad (2.15)$$

where $U(\vec{q})$ denotes the Fourier transform of $U(\vec{r})$

$$U(\vec{q}) = \int d^3r U(\vec{r}) e^{i\vec{q} \cdot \vec{r}} \quad (2.16)$$

When the relation given by Eq. (2.15) is substituted into Eq. (2.11) there results

$$E_n^{\circ}(\vec{k}) F_n(\vec{k}) + \sum_{n'\vec{k}'} \sum_{\vec{p}} C_{\vec{k}\vec{k}'}^{nn'}(\vec{K}_p) U(\vec{k} - \vec{k}' - \vec{K}_p) F_{n'}(\vec{k}') = E_{\gamma} F_n(\vec{k}) \quad (2.17)$$

Within the framework of one electron theory Eq. (2.17) is still exact. At this point we should mention that the potential $U(\vec{r})$ shall be taken to be the hydrogenic one given by Eq. (2.1). Its Fourier transform is given by

$$U_H(\vec{q}) = \frac{-4\pi e^2}{\epsilon q^2} \quad (2.18)$$

To solve Eq. (2.17) a series of approximations must now be

introduced. First only one band is assumed to contribute to the sum in Eq. (2.17) so the band index n can be dropped. The solutions $F(\vec{k})$ are anticipated to be localized around $\vec{k} = 0$ so that

$$|\vec{k} - \vec{k}'| \ll K_p \quad (2.19)$$

This leads to dropping the $K_p \neq 0$ terms because of the form of the Fourier transform of the potential given by Eq. (2.18). Furthermore, since

$$C_{\vec{k}\vec{k}'}^{nn'}(\vec{K}_p) = \int d^3r u_{n\vec{k}}^{o*}(\vec{r}) u_{n'\vec{k}'}^o(\vec{r}) e^{-i\vec{K}_p \cdot \vec{r}} \quad (2.20)$$

The term $C_{\vec{k}\vec{k}'}^{nn'}(0)$ is approximated by $C_{\vec{k}\vec{k}}^{nn}(0)$ which is equal to one by Eq. (2.20) and the orthonormality relation of Eq. (2.10). The sum over \vec{k}' is now converted into an integral over all \vec{k}' space. Finally, the unperturbed band energy $E_n^0(\vec{k})$ is expanded to order k^2 about its extremum, i.e.

$$E_n^0(\vec{k}) \cong E_c^0 + \frac{\hbar^2 \vec{k}^2}{2m^*} \quad (2.21)$$

As noted earlier m^* is the effective mass and is given by Eq.

With these approximations Eq. (2.17) becomes

$$\frac{\hbar^2 \vec{k}^2}{2m^*} F(\vec{k}) + \int d^3k' U(\vec{k} - \vec{k}') F(\vec{k}') = E_b F(\vec{k}) \quad (2.22)$$

where E_b , the binding energy of the electron, is given by

$$E_b = E_{\gamma} - E_c^{\circ} \quad (2.23)$$

That is, it represents a binding energy of the impurity electron to the impurity center relative to the bottom of the conduction band.

It is immediately obvious that Eq. (2.22) is equivalent to the Schrödinger equation in momentum space of a particle in the presence of a potential U and possessing a mass of m^* . This can be transformed to coordinate space by defining

$$F(\vec{r}) = \int d^3k F(\vec{k}) e^{i\vec{k}\cdot\vec{r}} \quad (2.24)$$

The resulting equation is given by

$$\left\{ \frac{-\hbar^2}{2m^*} \nabla^2 + \frac{e^2}{\epsilon r} \right\} F(\vec{r}) = E_b F(\vec{r}) \quad (2.25)$$

It is now apparent that the 'wavefunction' of the effective mass Hamiltonian is the Fourier transform of the expansion coefficients of Eq. (2.8). The function $F(\vec{r})$ is known technically as the envelope function.

When the band minima are not located at $\vec{k} = 0$, the function $F(\vec{k})$ is written as

$$F(\vec{k}) = \sum_{i=1}^N \alpha_i F^{(i)}(\vec{k})$$

where the $F^{(i)}(\vec{k})$ is localized about the i -th minima. This form of the envelope function leads to what are known as intervalley terms that couple wave vectors that lie near different extrema. These

terms are usually neglected due to the expectation that the different $F^{(i)}(\vec{k})$'s have negligible overlap. The result^{23b} of this treatment yields a hydrogen-like effective mass equation, except that the kinetic energy term is anisotropic. These extrema usually lie along a crystallographic direction and when this is the case that direction can be defined as the z-direction. Expanding $E^0(\vec{k})$ about this extrema yields

$$E^0(\vec{k}) \simeq E_c^0 + \frac{\hbar^2}{2} \left(\frac{1}{m_t^*} (k_x^2 + k_y^2) + \frac{k_z^2}{m_l^*} \right) \quad (2.26)$$

where m_t^* and m_l^* are the transverse and longitudinal effective masses. The resulting one valley effective mass equation is then given by

$$\left\{ -\frac{\hbar^2}{2m_t^*} \left(\frac{\partial^2}{\partial x^2} + \frac{\partial^2}{\partial y^2} \right) - \frac{\hbar^2}{2m_l^*} \frac{\partial^2}{\partial z^2} - \frac{e^2}{\epsilon r} \right\} F^{(j)}(\vec{r}) = E_b F^{(j)}(\vec{r}) \quad (2.27)$$

The effective masses m_t^* and m_l^* can be determined by cyclotron resonance experiments. For silicon²⁵ these parameters are given by

$$\begin{aligned} m_t^*/m_0 &= 0.1905 \\ m_l^*/m_0 &= 0.9163 \\ \gamma &= m_t^*/m_l^* = 0.2079 \end{aligned} \quad (2.28a)$$

while for germanium²⁶

$$\begin{aligned} m_t^*/m_0 &= 0.08152 \\ m_l^*/m_0 &= 1.588 \\ \gamma &= 0.05134 \end{aligned} \quad (2.28b)$$

Because of the anisotropic effective mass, Eq. (2.28) is no longer separable and some approximation method must be used. Kohn and Luttinger have used a trial function of the form

$$F(\vec{r}) = (\pi a^2 b)^{-1/2} \exp\left(-\sqrt{\frac{x^2 + y^2}{a^2} + \frac{z^2}{b^2}}\right) \quad (2.29)$$

where a and b are variational parameters, to obtain approximate binding energies of shallow donors in silicon and germanium. The results of a more complete calculation given by Faulkner²⁷ show that the energies obtained by the variational form of Eq.(2.29) yield remarkably good binding energies.

2.2 Ellipsoidal Conduction Bands and the Boundary Condition Near a Surface

As was mentioned earlier, it was first pointed out by Levine²⁵ that since the height of the surface barrier can be several electron volts and since the binding energy of shallow donor impurities is on the order of milli electron volts, the surface can be assumed to be an infinite potential barrier. Levine then showed that in the absence of image charges the allowed states are the hydrogenic ones for which $|l-m| = \text{odd}$. This result assumes that the impurity lies exactly at the surface.

Since that time there have been several investigations of the energies and properties of these states. Bell²⁸ et.al. used the selection rules of Levine and the bulk energies of silicon and

germanium to calculate transition energies. Petukhov²⁹ et.al. included image charges in the effective mass Hamiltonian and performed a perturbation calculation on that system. Karpushin³⁰ extended that perturbative treatment with the inclusion of linear band bending near the surface. In a later article Karpushin³¹ used a variational method to calculate the binding energies of donors on silicon and germanium surfaces. It is important to note that all of these authors constrained the impurity to lie exactly on the surface.

The restriction of the impurity to the surface plane shall not be assumed in the following. However, there are a number of simplifying assumptions which shall be made. First, because of the multiple minima of the conduction band in k-space, the crystallographic orientation of the surface becomes important. When considering the (001) plane of silicon or the (111) plane of germanium there exists³² two kinds of constant energy ellipsoids; those with their major axis parallel to the surface and those with their major axis perpendicular. One of the results of Karpushin³¹ is that the ellipsoids with their major axes perpendicular give rise to a series of states which lie lower in energy than those with their major axis parallel to the surface. Consequently only these types of ellipsoids will be considered, because this allows a simplification in the requirements of the boundary condition $\psi = 0$ on the surface plane. In addition we shall assume that there is no change in the band structure near the surface, such as the formation of a space charge layer, so that there is no band bending near the surface. Finally, we shall be

working in the one-valley effective mass approximation³³.

The preceding considerations lead to an effective mass equation given by

$$\left\{ \begin{aligned} & -\frac{\hbar^2}{2m_t^*} \left(\frac{\partial^2}{\partial x^2} + \frac{\partial^2}{\partial y^2} \right) - \frac{\hbar^2}{2m_l^*} \frac{\partial^2}{\partial z^2} - \frac{e^2}{\epsilon_1 r} \\ & + \frac{(\epsilon_2 - \epsilon_1)}{\epsilon_1(\epsilon_1 + \epsilon_2)} \frac{e^2}{[r^2 + 4R^2 - 4rR \cos\theta]^{1/2}} \\ & - \frac{(\epsilon_2 - \epsilon_1)e^2}{4\epsilon_1(\epsilon_1 + \epsilon_2)(R - r \cos\theta)} \end{aligned} \right\} F(\vec{r}) = E F(\vec{r}) \quad (2.30)$$

This equation must be solved subject to the boundary condition

$$F(\vec{r}) = 0 \quad \text{when} \quad r \cos\theta = R \quad (2.31)$$

Note that this last equation follows from the choice of the (001) surface for silicon or the (111) surface for germanium. In Eq.(2.30) m_t^* and m_l^* are the transverse and longitudinal effective masses, ϵ_1 denotes the static dielectric constant of the region containing the impurity, and in this case that is the semiconductor. The static dielectric constant of region B (see Fig. 1.1) is denoted by ϵ_2 . This leaves open the option of solving for a semiconductor/insulator interface or a semiconductor/vacuum interface. From Eqs. (2.30) and (1.36) it is apparent that the methods of the previous chapter are applicable when $m_t^* = m_l^*$. The last two terms on the right hand side of Eq. (2.30) are of course, the electron-image proton and the

electron-image electron terms respectively.

In the following we shall be concerned with solving a scaled version of Eq. (2.30). All distances, including R , the distance of the impurity from the surface plane, are scaled to units of effective Bohr radii given by

$$a_0^* = \frac{\hbar^2 \epsilon_1}{m_t^* e^2} = 0.529 \left(\frac{\epsilon_1 m}{m_t^*} \right) \text{\AA}, \quad (2.32)$$

and the energy is in units of effective Rydbergs

$$Ry^* = \frac{m_t^* e^4}{2 \hbar^2 \epsilon_1^2} = 13.6 \left(\frac{m_t^*}{m} \frac{1}{\epsilon_1^2} \right) \text{eV}. \quad (2.33)$$

The scaled version of Eq. (2.30) is then given by

$$\left\{ - \left(\frac{\partial^2}{\partial x^2} + \frac{\partial^2}{\partial y^2} + \gamma \frac{\partial^2}{\partial z^2} \right) - \frac{2}{r} + \frac{2Q}{[r + 4R^2 - 4rR \cos \theta]^{1/2}} - \frac{Q}{2[R - r \cos \theta]} \right\} F(\vec{r}) = E_b F(\vec{r}), \quad (2.34)$$

where Q is given by

$$Q = \frac{(\epsilon_2 - \epsilon_1)}{(\epsilon_2 + \epsilon_1)},$$

and γ is the effective mass ratio defined in Eq. (2.28). We note in passing that the effective mass equation has been scaled to the bulk semiconductor parameters rather than the surface units defined by Stern and Howard³². This scaling has been chosen for easier comparison to the bulk limit ($R \rightarrow$ large) and because this choice

yields the factor $(\epsilon_2 - \epsilon_1)/(\epsilon_1 + \epsilon_2)$. This factor always lies between -1 and 1 whereas this is not the case for surface units. This feature is a practical one since large constants multiplying matrix elements are undesirable in the solution of the matrix equations.

In the solution of Eq. (2.34), subject to the boundary conditions of Eq. (2.31), a strategy that is a combination of the methods of Chapter 1 with a method presented by Faulkner²⁷ is used. Since the change in the Hamiltonian of Eq. (2.34) from that of the last chapter is in the z-dependence only, all the symmetry properties previously discussed are valid here. In particular m remains a good quantum number while n and ℓ do not. The difference from the $R \rightarrow \infty$ case in this situation is slightly different from that of the last chapter. This is due to the symmetry properties of Eq. (2.34) without the boundary condition (2.31). The effective mass Hamiltonian is invariant under operations of parity and rotation about the z-axis. This means that for the bulk impurity n and ℓ are no longer good quantum numbers while m is; however states of even and odd ℓ are not mixed. This means that the effect of the boundary condition in this situation is to mix states of differing parity.

Since m remains a good quantum number the problem can again be reduced to the set of independent ones characterized by their m values. Using this we can write

$$F_m(\vec{r}) = (R-r\cos\theta) \sum_{n\ell} A_{n\ell} \chi_{n\ell m}(\vec{r}) \quad (2.35)$$

where the choice of $G(z)$ is as before. Now the $\chi_{n\ell m}$'s are chosen as

$$\chi_{n\ell m}(x, y, z) = \left(\frac{\alpha}{\gamma}\right)^{1/4} \phi_{n\ell m}\left(x, y, \left(\frac{\alpha}{\gamma}\right)^{1/2} z, \beta\right) \quad (2.36)$$

where γ is the effective mass ratio and α is another non-linear variational parameter. The $\phi_{n\ell m}(\vec{r}, \beta)$'s are given by Eq. (1.12) and β is the variational parameter that is discussed in Section 1.2. The parameter α is a measure of the asymmetry induced in the wavefunction due to the asymmetric effective mass. The choice of the functions given by Eq. (2.36) was inspired by the success of the Kohn-Luttinger form of Eq. (2.29); for upon setting $\beta = 1/a$ and $\alpha = a^2\gamma/b^2$, $\chi_{1,0,0}(x,y,z)$ is given *exactly* by Eq. (2.29). This basis set differs from that used by Faulkner inasmuch as we use the combination βr rather than $\beta r/n$ in the radial function where n is the principal quantum number. This means that for the calculation presented here there are only two nonlinear variational parameters whereas Faulkner must use a set of such parameters; the number of which depends upon the size of the basis set used in the expansion of the trial function. Of course, this means that we must calculate an overlap matrix, but as it has been shown this is not a great handicap.

As before, the substitution of Eq. (2.35) into Eq. (2.34) will lead to a generalized eigenvalue problem of the form of Eq. (1.7). There is a transformation that facilitates the calculation of the Hamiltonian matrix elements. These matrix elements are given by

$$\begin{aligned} \langle n'l' | \mathcal{H}^{(m)} | nl \rangle &= \int_{\tau} \left(\frac{\alpha}{r}\right)^{1/2} (R - r \cos \theta) \phi_{n'l'm}^* (x, y, \left(\frac{\alpha}{r}\right)^{1/2} z, \beta) \\ &\times \left\{ - \left(\frac{\partial^2}{\partial x^2} + \frac{\partial^2}{\partial y^2} + r \frac{\partial^2}{\partial z^2} \right) - \frac{2}{r} + \frac{2Q}{[r^2 + 4R^2 - 4rR \cos \theta]^{1/2}} \right. \\ &\left. + \frac{Q}{2(R - r \cos \theta)} \right\} (R - r \cos \theta) \phi_{n'l'm} (x, y, \left(\frac{\alpha}{r}\right)^{1/2} z, \beta) dV \quad (2.37) \end{aligned}$$

Making the substitution

$$\left(\frac{\alpha}{r}\right)^{1/2} z' = z$$

yields

$$\begin{aligned} \langle n'l' | \mathcal{H}^{(m)} | nl \rangle &= \int_{\tau'} (R - \left(\frac{r}{\alpha}\right)^{1/2} r \cos \theta) \phi_{n'l'm} (x, y, z, \beta) \\ &\left\{ - \left(\frac{\partial^2}{\partial x^2} + \frac{\partial^2}{\partial y^2} + r \frac{\partial^2}{\partial z^2} \right) + (1-\alpha) \frac{\partial^2}{\partial z'^2} - \frac{2}{[x^2 + y^2 + \frac{r}{\alpha} z'^2]^{1/2}} \right. \\ &\left. + \frac{2Q}{[x^2 + y^2 + \frac{r}{\alpha} z'^2 + 4R^2 - 4\left(\frac{r}{\alpha}\right)^{1/2} r R \cos \theta]^{1/2}} \right. \\ &\left. - \frac{Q}{2(R - \left(\frac{r}{\alpha}\right)^{1/2} r \cos \theta)} \right\} \left[(R - \left(\frac{r}{\alpha}\right)^{1/2} r \cos \theta) \phi_{n'l'm} (x, y, z, \beta) \right] dV \quad (2.38) \end{aligned}$$

The overlap matrix elements are given by

$$\langle n'l' | n'l \rangle = \int_{T'} \left(R - \left(\frac{r}{\alpha} \right)^{1/2} r \cos \theta \right)^2 \phi_{n'l'm}(\vec{r}, \beta) \phi_{n'l'm}(\vec{r}, \beta) dV \quad (2.39)$$

The subscript T and T' on Eqs. (2.37) and (2.38) indicates truncated regions of integration. The effect of the transformation is seen to be a simplification of the expansion functions at the expense of dealing with more complicated operators.

The generalized matrix equation whose elements are given by Eqs. (2.38) and (2.39) shall be solved numerically. The first step in this direction is the calculation of the quantities

$$-\nabla^2 \left\{ \left(R - \left(\frac{r}{\alpha} \right)^{1/2} r \cos \theta \right) \phi_{n'l'm}(\vec{r}, \beta) \right\} \quad (2.40)$$

and

$$(1-\alpha) \frac{d^2}{dz^2} \left[\left(R - \left(\frac{r}{\alpha} \right)^{1/2} r \cos \theta \right) \phi_{n'l'm}(\vec{r}, \beta) \right] \quad (2.41)$$

The first of these expressions (Eq. (2.40)) has already been calculated (see Eqs. (1.11) and (1.16)). The second yields a somewhat complicated sum of terms involving the Legendre and Laguerre functions of various orders and will not be repeated here. Most of these terms can be integrated in closed form. However, for the third and fourth terms in Eq. (2.38) this was not found to be the case. Consequently these terms were numerically integrated as previously described.

The general method of the numerical solution of the matrix equations is the same as described in the previous chapter. However, there is now an additional parameter, namely α , which must be varied

to yield an optimized energy. In practice the energy is a relatively slowly varying function of α near the optimum values of these quantities and this feature eases the problems associated with locating a minimum in a two parameter space.

2.3 Donor Impurities Near the Silicon (001)/Vacuum and the Germanium (111)/Vacuum Interfaces

Before discussing the results of this section, all of which are presented in effective units, the various physical constants of silicon and germanium that are relevant to this problem are presented. The effective masses have already been given in Eqs. (2.28b) and (2.28c) and from Eq. (2.30) the other parameters needed are seen to be the static dielectric constants of silicon and germanium. Faulkner²⁷ has determined low temperature values of these dielectric constants by requiring that the donor spectrum calculated in the effective mass approximation have an optimum fit to the experimentally determined donor level spacing. These values are given by

$$\epsilon_{Si} = 11.4 \quad (2.42a)$$

$$\epsilon_{Ge} = 15.36 \quad (2.42b)$$

Using these values and those of (2.28) the effective units for silicon are given by

$$a_{0Si}^* = \frac{\hbar^2 \epsilon_{Si}}{m_{zSi}^* e^2} = 31.7 \text{ \AA} \quad (2.43a)$$

$$Ry_{Si}^* = \frac{m_{tSi}^* e^4}{2 \hbar^2 \epsilon_{Si}^2} = 1.99 \times 10^{-2} \text{ eV} \quad (2.43b)$$

while those for germanium are

$$a_{oGe}^* = 99.7 \text{ \AA} \quad (2.43c)$$

$$Ry_{Ge}^* = 4.70 \times 10^{-3} \text{ eV.} \quad (2.43d)$$

To convert the following results to measurable units one needs only to multiply by the appropriate member of Eqs. (2.43).

Besides the introduction of an anisotropic effective mass, the major difference from the problem of the preceding chapter is that the 'hydrogen atom' is now imbedded in a dielectric media and is near an interface with a media possessing a lower dielectric constant. This means that the image charges possess the same sign (positive or negative) as the charges that induce them. This can be seen from the form of the dielectric quotient given by $(\epsilon_2 - \epsilon_1) / (\epsilon_1 + \epsilon_2)$. This results in a repulsive electron-image electron interaction, while the electron-image proton interaction now becomes attractive.

The results of the 'perfectly imaging' plane show that, at least for the ground state, the absolute value of the expectation value of the electron-image proton interaction is greater than the expectation value of the electron-image electron interaction. Since the former of these quantities is negative, at a large enough distance from the surface the ground state electronic energy is expected

to be lower than the $R = \infty$ limit when there is no image charge contribution. As the impurity is moved closer to the surface, the change in the energy due to the exclusion of the electron from the half-space $r \cos \theta \geq R$ will begin to dominate and begin to raise (as a function of the impurity distance from the surface) the ground state energy. Therefore, we expect to see the formation of a minimum in the ground state electronic energy.

The results presented in Tables 2.1 through 2.3 show that this is precisely what takes place. Table 2.1 presents the ground state energy of an impurity near a silicon surface for $\gamma = 1.0$; that is, as if silicon possessed a spherical conduction band. The bulk limit in this case is given by the hydrogenic -1.0 Ry^* . Tables 2.2 and 2.3 give the ground state properties of a donor impurity near the (001) silicon surface and the (111) germanium surface respectively. The bulk values for these two systems, in effective Rydbergs, are given by²⁷

$$E_0^{Si}(R \rightarrow \infty) = -1.568 \text{ Ry}_{Si}^* \quad (2.44a)$$

$$E_0^{Ge}(R \rightarrow \infty) = -2.087 \text{ Ry}_{Ge}^* \quad (2.44b)$$

As a calculational check, the energies of these ground states were computed at a distance from the surface of $100 a_0^*$, yielding,

$$E_0^{Si}(R = 100 a_{0Si}^*) = -1.571 \text{ Ry}_{Si}^* \quad (2.44c)$$

$$E_0^{Ge}(R = 100 a_{0Ge}^*) = -2.094 \text{ Ry}_{Ge}^* \quad (2.44d)$$

which is in agreement with the bulk values.

TABLE 2.1

Ground state properties of a shallow donor near the surface of a symmetric ($\gamma=1$) silicon. All quantities are given in bulk units defined by Eqs. (2.32) and (2.33). E_0 denotes the ground state energy, \bar{T} the average kinetic energy and \bar{V}_1 , \bar{V}_2 , \bar{V}_3 are the average values of the three potential terms in Eq. (2.34) respectively.

R	E_0	\bar{T}	\bar{V}_1	\bar{V}_2	\bar{V}_3
0.2	-0.6064	0.6373	-0.8658	0.2380	-0.6159
0.4	-0.6507	0.7670	-1.0594	0.2586	-0.6169
0.6	-0.7221	0.9696	-1.3522	0.2841	-0.6237
0.8	-0.8098	1.1662	-1.6626	0.3001	-0.6135
1.0	-0.8945	1.2853	-1.8972	0.3000	-0.5825
1.2	-0.9640	1.3268	-2.0379	0.2882	-0.5410
1.4	-1.0158	1.3204	-2.1092	0.2708	-0.4978
1.6	-1.0521	1.2912	-2.1381	0.2519	-0.4571
1.8	-1.0767	1.2539	-2.1434	0.2332	-0.4204
2.0	-1.0925	1.2160	-2.1364	0.2157	-0.3878
3.0	-1.1086	1.0827	-2.0674	0.1498	-0.2736
4.0	-1.0944	1.0302	-2.0273	0.1111	-0.2084
5.0	-1.0794	1.0121	-2.0115	0.0875	-0.1674
6.0	-1.0676	1.0057	-2.0056	0.0720	-0.1397

TABLE 2.2

Ground state properties of a shallow donor near the (001) surface of silicon. ($\gamma = 0.2079$, entries and units are as in Table 2.1.)

R	E	\bar{T}	\bar{V}_1	\bar{V}_2	\bar{V}_3
0.2	-1.3601	1.3555	-2.0850	0.6374	-1.2679
0.4	-1.5927	1.6827	-2.7632	0.6695	-1.1817
0.6	-1.7496	1.8436	-3.1709	0.6084	-1.0307
0.8	-1.8133	1.8267	-3.2815	0.5165	-0.8750
1.0	-1.8278	1.7695	-3.2845	0.4345	-0.7472
1.2	-1.8210	1.7255	-3.2681	0.3685	-0.6469
1.4	-1.8061	1.6701	-3.2350	0.3167	-0.5670
1.6	-1.7890	1.6466	-3.2085	0.2762	-0.5032
1.8	-1.7722	1.6243	-3.1891	0.2441	-0.4515
2.0	-1.7568	1.6094	-3.1755	0.2183	-0.4089
3.0	-1.7013	1.5796	-3.1469	0.1425	-0.2765
4.0	-1.6697	1.5723	-3.1396	0.1060	-0.2084
5.0	-1.6499	1.5698	-3.1372	0.0845	-0.1671
6.0	-1.6365	1.5688	-3.1361	0.0702	-0.1394

TABLE 2.3

Ground state properties of a shallow donor near the (111) surface of germanium. ($\gamma = 0.05134$, entries and units are as in Table (2.1).)

R	E	\bar{T}	\bar{V}_1	\bar{V}_2	\bar{V}_3
0.2	-2.3013	2.2378	-3.7971	1.2923	-2.0343
0.4	-2.5389	2.4841	-4.4397	1.0238	-1.6071
0.6	-2.5485	2.4160	-4.4679	0.7463	-1.2428
0.8	-2.5035	2.2929	-4.3725	0.5673	-0.9912
1.0	-2.4538	2.2164	-4.3039	0.4523	-0.8185
1.2	-2.4104	2.1721	-4.2622	0.3747	-0.6951
1.4	-2.3743	2.1460	-4.2369	0.3195	-0.6030
1.6	-2.3447	2.1298	-4.2211	0.2785	-0.5320
1.8	-2.3203	2.1194	-4.2108	0.2469	-0.4757
2.0	-2.2998	2.1124	-4.2038	0.2216	-0.4300
3.0	-2.2343	2.0981	-4.1896	0.1470	-0.2898
4.0	-2.1980	2.0943	-4.1848	0.1100	-0.2183
5.0	-2.1785	2.0132	-4.1847	0.0879	-0.1749

The ground state energies of the 'isotropic effective mass' silicon and the real silicon systems are presented graphically in Fig. 2.1, while the germanium system is given in Fig. 2.2. There are basically three regions of different behavior depicted in these graphs. At large R the impurity levels are approaching their indicated bulk levels. Also there now exist minima which occur at approximately $2.6 a_0^*$, $1.0 a_0^*$ and $0.5 a_0^*$ for the 'isotropic' silicon, real silicon and germanium systems respectively. Finally when the impurity is close to the surface there is a steep rise in the electronic energy. The main difference in the behavior of the energy as a function of the impurity distance from the surface between these three systems lies in the location and the depth of the energy minimum. This difference is due to the changing value of γ , the effective mass ratio and can be explained in the following manner. In the bulk situation, the change in the wavefunction due to $\gamma < 1.0$ in Eq. (2.34) is to *compress* (the wavefunction) slightly in the z -direction²³. Since the surface is perpendicular to the z -axis, this means that an impurity wavefunction for a specific value of the effective mass ratio will experience a lesser perturbation than the wavefunction corresponding to a large value of the effective mass ratio. Consequently, the minimum in energy will occur at smaller *scaled* distances from the surface as the value of the effective mass ratio is decreased. Note that this argument is true only for the *scaled* Hamiltonian, and that the minimum energy of a donor in germanium occurs at a *larger* distance than it does for a donor in silicon.

Fig. 2.1 Ground state energy of a shallow donor impurity near the (001) surface of silicon. Also included are the results for an isotropic effective mass. The bulk values are given by the lines under the B. Units are those of effective Rydbergs and effective Bohr radii as defined in text.

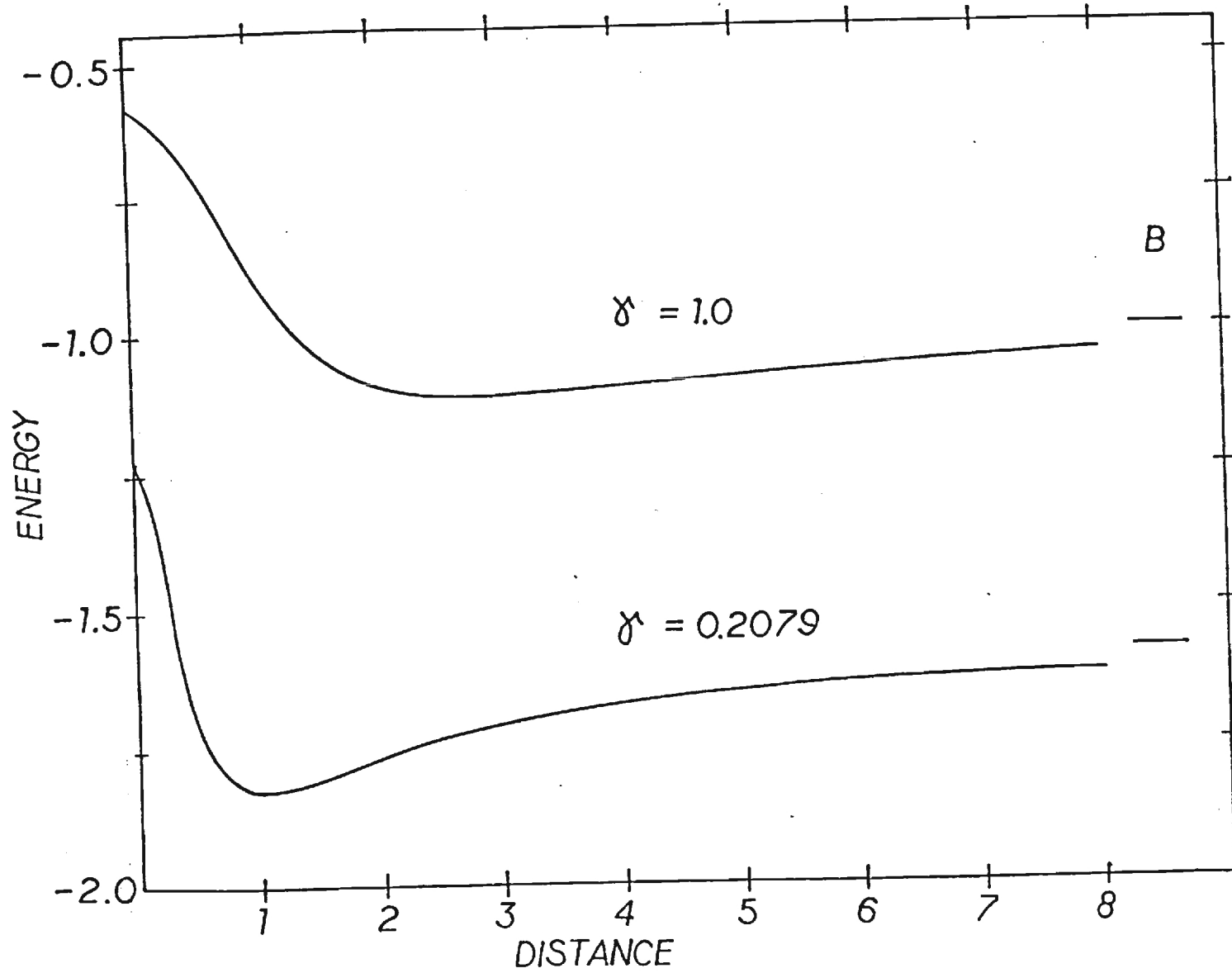
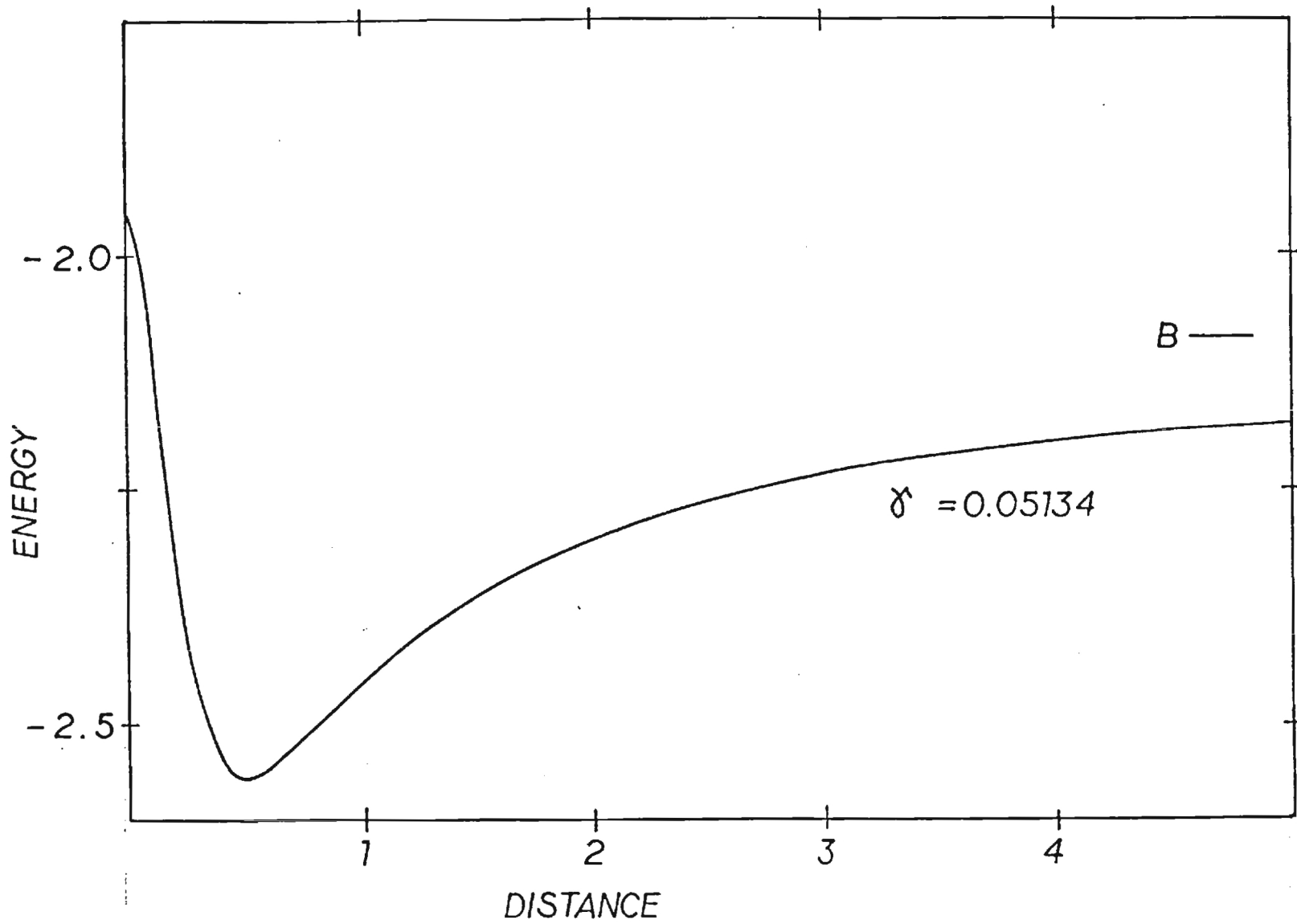


Fig. 2.2 Ground state energy of a shallow donor impurity near the (111) surface of germanium.



The excited state energies for a donor impurity near the (001) surface of silicon and the (111) surface of germanium are presented in Figures 2.3 and 2.4. The approach to the bulk values of the energy levels of the excited states takes place at a slower rate due to the larger 'spatial' extent of these states. Note that because the states labelled (0,3) and (1,1) (recall that the first label refers to the value of the m quantum number while the second give its position in the spectrum of levels with the same m quantum number) possess different azimuthal quantum numbers, there is not, as it might appear, an avoided crossing between them.

In a manner analogous to that of Sec. 1.4 the total interaction energy of a shallow donor with the surface can be constructed. This interaction energy consists of the change of the ground state energy from its bulk value, the interaction of the positive impurity with its positive image and the interaction of the positive impurity with the negatively charged image electron. As before this last quantity is given by an expectation value and cannot be calculated until the electronic problem has been solved. At small distance the 'proton'-image proton term will dominate to give a repulsive potential, however both of the remaining quantities give negative contributions so that a minimum appears in the interaction energy. The interaction energy of a donor impurity with a surface in a 'isotropic' silicon, the actual ($\gamma = .2079$) silicon, and the germanium media have been constructed from Tables 1.1, 1.2 and 1.3. These energies are presented in Fig. 2.5. The minima in these curves appear at slightly

Fig. 2.3 Excited states of a shallow donor impurity near the (001) surface of silicon.

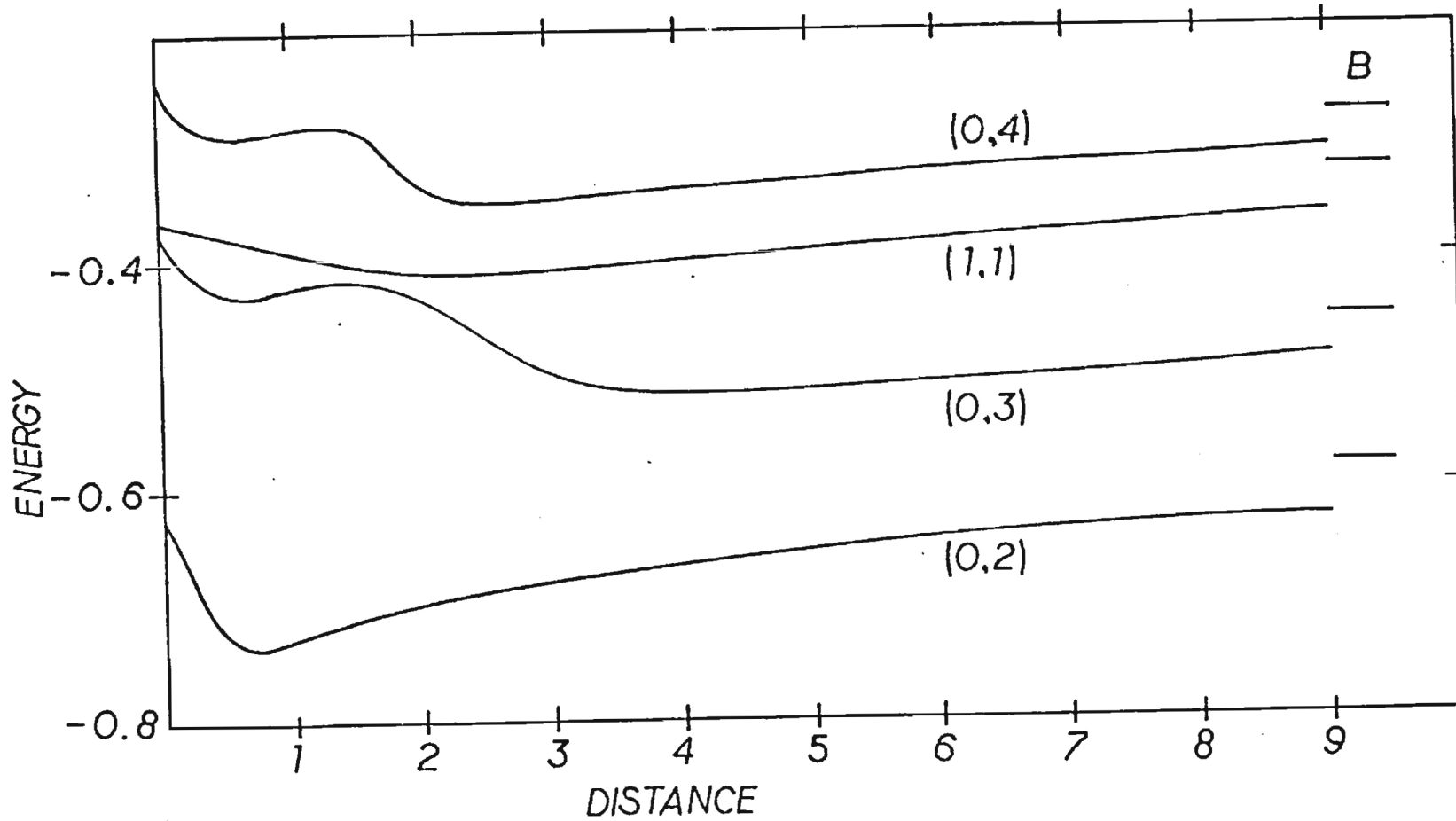


Fig. 2.4 Excited states of a shallow donor impurity near the (111) surface of germanium.

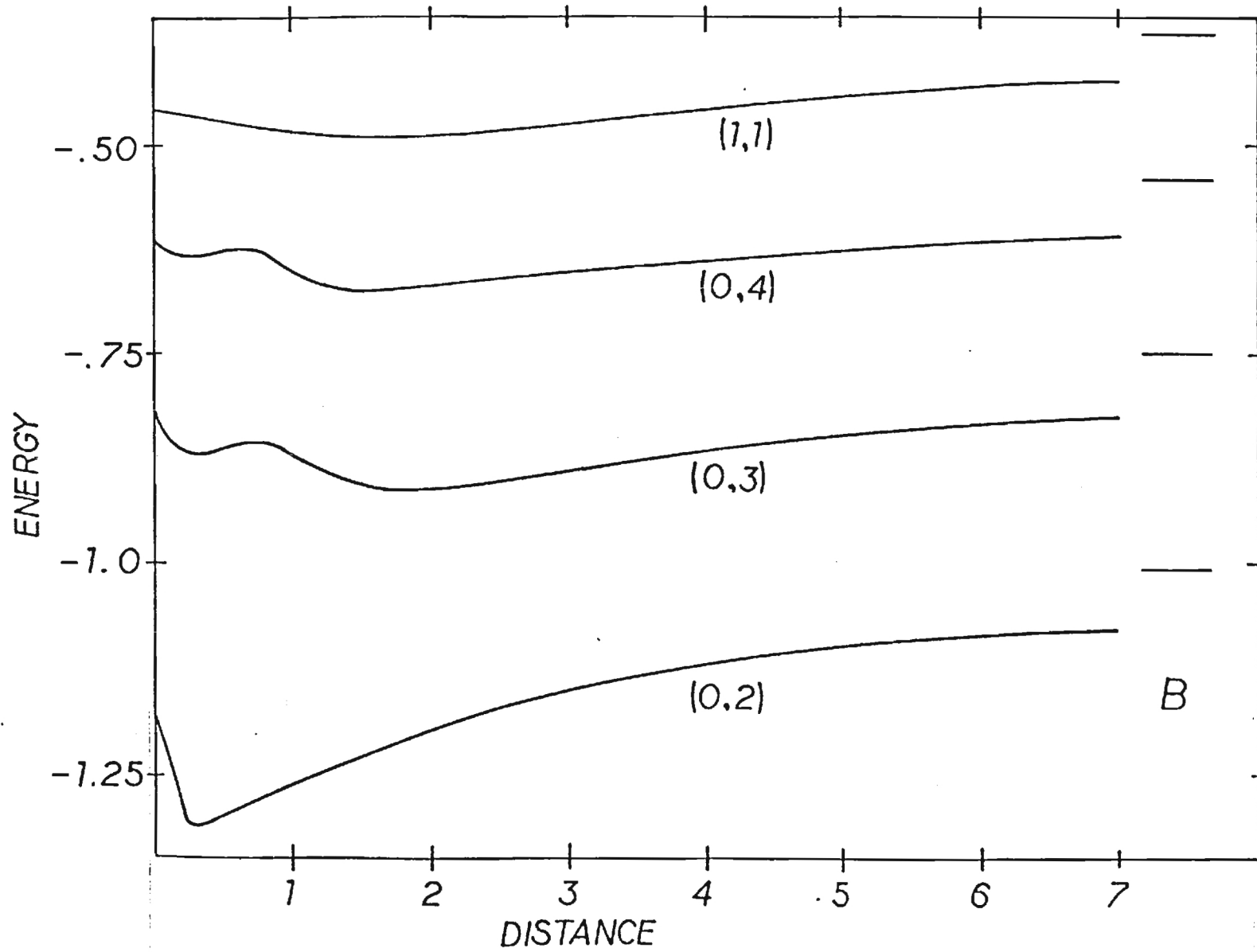
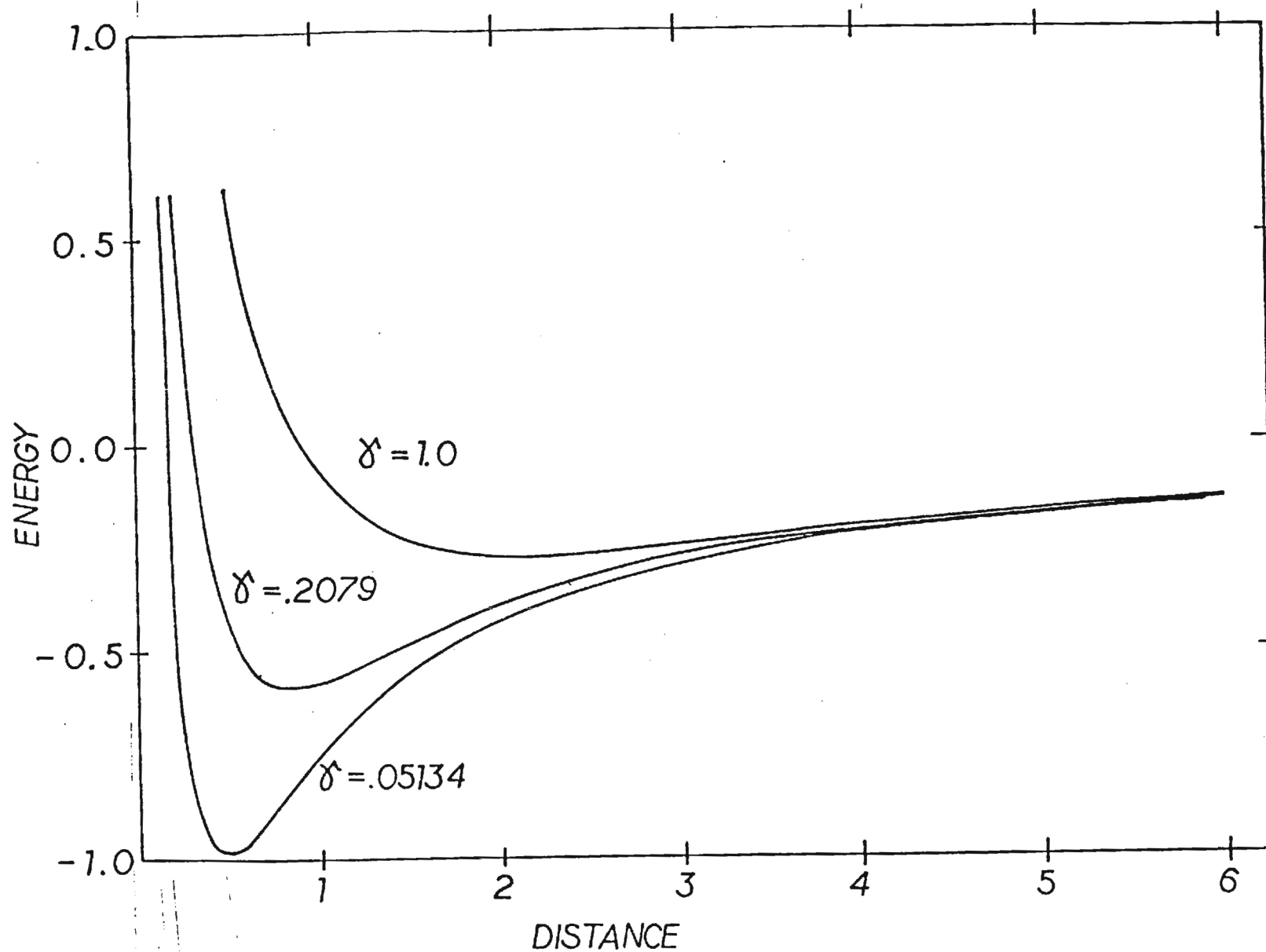


Fig. 2.5 Interaction energy of a shallow donor impurity with the surface of a semiconductor for three different systems.



smaller distances than the corresponding minima in the ground state electronic energies. The minimum interaction energy for a donor impurity near the (111) surface of germanium occurs at a distance of approximately $0.5 a_0^{*Ge}$, while for the silicon system this scaled distance increases to about $0.8 a_0^{*Si}$, and finally for the $\gamma = 1$ case to $\sim 2.0 a_0^{*Si}$. In angstroms these distances are given by 50 Å, 25 Å and 63 Å respectively. While it would be perhaps erroneous to suggest that donor impurities would actually tend to cluster at these distances because of the many simplifying assumptions, we might now suspect that the concentration of donor impurities would show a maximum at a certain distance from the surface; and this distance would be larger in germanium than in silicon.

2.4 A Donor Impurity Near the Si/SiO₂ Interface of a M.O.S.

Field Effect Transistor

The acronym MOSFET is derived from the combination Metal-Oxide-Semiconductor-Field Effect Transistor, and such a device is pictured schematically in Fig. 2.6. The metal gate is used to apply an electric field perpendicular to the surface of the semiconductor, from which it is insulated by an oxide layer. An n-type inversion layer can be produced in a p-type semiconductor at the surface if the energy bands near the surface are bent down enough so that the bottom of the conduction band lies near or below the Fermi level. Such a situation is referred to as an inversion layer since the majority carrier type in that region is the opposite of the bulk

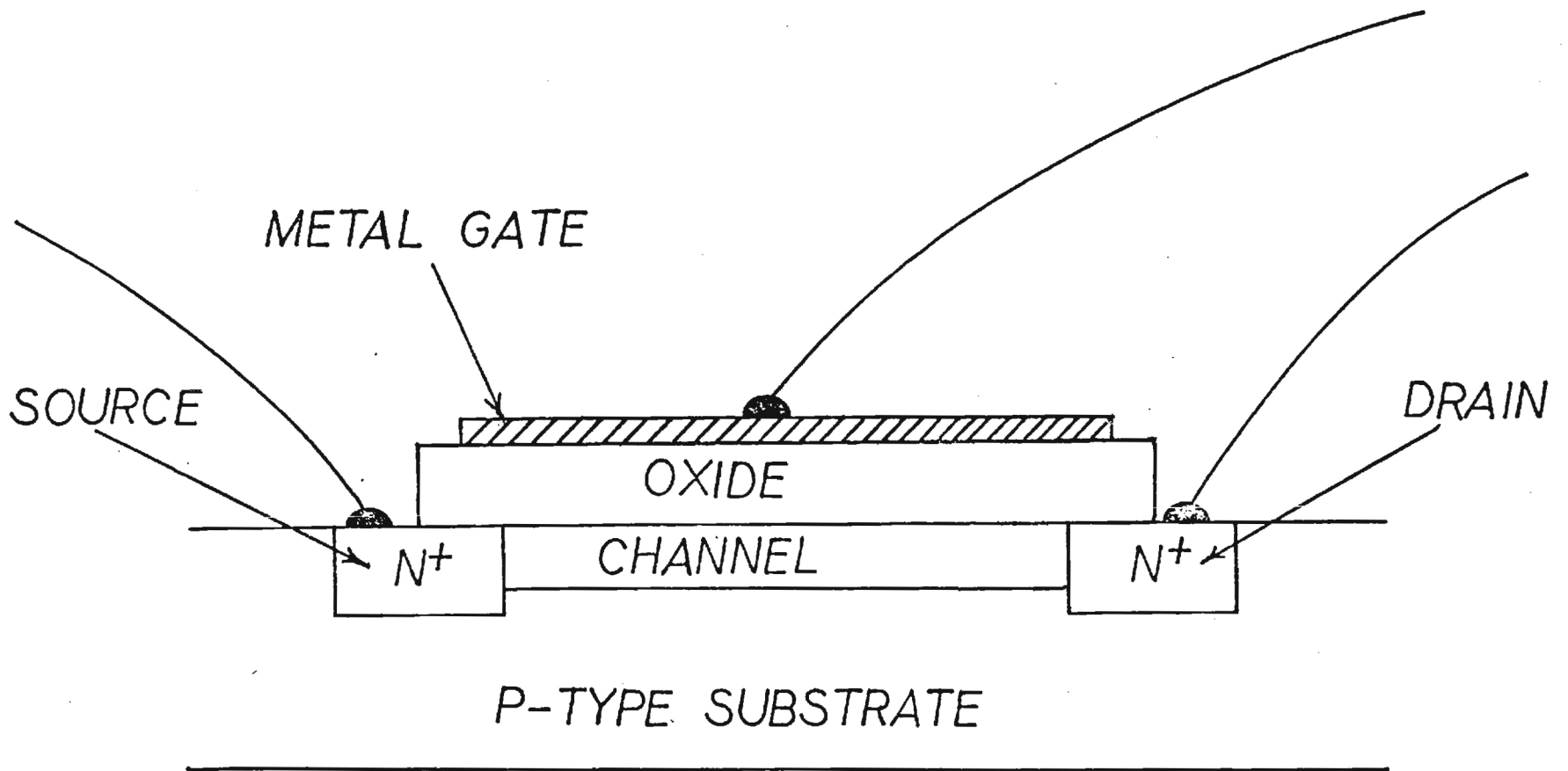


Fig. 2.6 Schematic of a metal-oxide-semiconductor field effect.

majority carrier. The band bending required to produce an inversion layer can be produced from the field applied by the metal gate.

If the electric field is strong enough, electrons in the conduction band can become quantized in the direction perpendicular to the surface, while remaining in a continuum for motion parallel to the surface. One of these quantized states is known as an electric sub-band and to a good first approximation these sub-band energies can be modelled as the eigenvalues of a one dimensional potential well.³² Referring to Fig. 2.6, when the gate voltage is large enough, an essentially two dimension conductance can be observed between the electrodes marked source and drain.

Recently, Hartstein and Fowler^{34,35} have observed an effect in the conductance, as a function of gate voltage, in a MOSFET that can be attributed to the formation of an impurity band. Briefly, the experiment consisted of drifting Na^+ ions close to Si-SiO_2 interface and then measuring the conductance of the channel as a function of gate voltage. What is observed is the appearance of a peak in the conductance below the threshold for 2-dimensional metallic conduction. This is illustrated in Fig. 2.7. By measuring the conductivity of the peak as a function of temperature, the binding energy of an electron to one of the impurities can be determined from the slope of a plot of the log of the conductivity versus the inverse of the temperature. We note here that the impurity is generally thought to be located several angstroms away from the interface; but it is located in the oxide layer while the electron is located in the

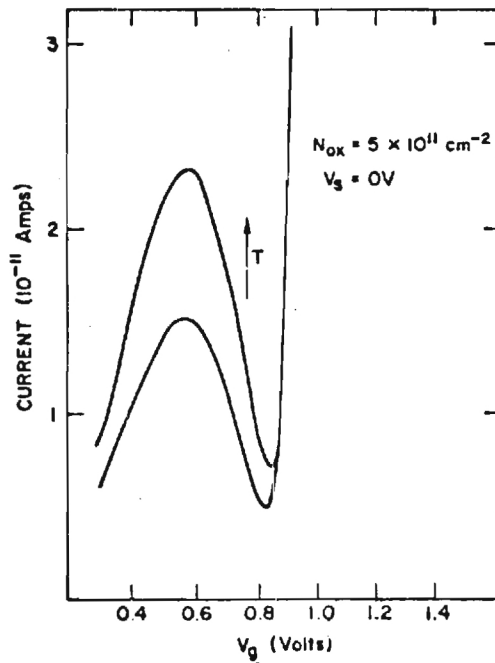


Fig. 2.7 The experimental results of Hartstein and Fowler for the channel conductivity of a MOS field effect transistor. Note the peak in the conductivity below the onset of metallic conduction indicating the formation of an impurity band.

semiconductor inversion layer.

As in the previous section, only the (001) surface of silicon shall be considered. Now, however, the dielectric constant of region B (see Fig. 1.1) will be taken to be that of SiO_2 , that is $\epsilon_2 = 3.8$. For the sake of comparison with other theoretical results, in the following the dielectric constant of silicon shall be taken as $\epsilon_1 = 11.8$. Since the discontinuity in energy as an electron passes from the silicon to the silicon dioxide is about 3 eV, the boundary condition $\psi = 0$ at the interface shall again be applied³².

There are two modifications of the Hamiltonian of the last section to make it applicable to the present problem. First, the positively charged impurity is located in the oxide layer which changes the constant factor in its interaction with the electron; and connected with this, the image of the impurity is absent. Second, the change in the potential energy of the electron due to the presence of the electric field must be taken into account. The electric field can be a complicated function of the perpendicular distance to the interface, however a reasonable first approximation is to employ a constant field³².

These considerations lead us to a Hamiltonian given by

$$\mathcal{H} = \frac{-\hbar^2}{2m_i^*} \left(\frac{\partial^2}{\partial x^2} + \frac{\partial^2}{\partial y^2} \right) - \frac{\hbar^2}{2m_e^*} \frac{\partial^2}{\partial z^2} - \frac{2e^2}{(\epsilon_1 + \epsilon_2)r} - \frac{(\epsilon_2 - \epsilon_1)e^2}{4\epsilon_1(\epsilon_1 + \epsilon_2)(R - r \cos \theta)} + eE(R - r \cos \theta) \quad (2.45)$$

where ϵ_1 and ϵ_2 are the dielectric constants of silicon and silicon dioxide respectively and E is the local electric field. As before this equation is scaled to bulk units

$$\mathcal{H} = -\left(\frac{\partial^2}{\partial x^2} + \frac{\partial^2}{\partial y^2}\right) - \gamma \frac{\partial^2}{\partial z^2} - \frac{4\epsilon_1}{(\epsilon_1 + \epsilon_2)F} \frac{-(\epsilon_2 - \epsilon_1)}{2(\epsilon_1 + \epsilon_2)(R - r \cos \theta)} + 2\epsilon_1^3 \left(\frac{m}{m_t^*}\right)^2 \hat{E}(R - r \cos \theta) \quad (2.46)$$

This must be solved subject to the condition that $\psi = 0$ when $R = r \cos \theta$. All distances are in effective Bohr radii and all energies are in effective Rydbergs (Eq. 2.43). Once the matrix elements involving the field term have been included in the Hamiltonian matrix, the energy levels are obtained in the manner previously discussed.

The binding energy of the electron in the present case is not simply given as the absolute value of the ground state of Eq. (2.46). This is due to the fact that the electron is making a transition to the first electric sub-band and not to a bulk-like conduction band. In the absence of the impurity potential the Hamiltonian (2.46) becomes

$$\mathcal{H}_0 = -\gamma \frac{d^2}{dz^2} - \frac{(\epsilon_2 - \epsilon_1)}{2(\epsilon_1 + \epsilon_2)Z} + K E Z \quad (2.47)$$

In Eq. (2.47) E is to be in electrostatic units and therefore K has the value

$$K = 1.166 \times 10^{-7} * \epsilon_1^3 \left(\frac{m}{m_t^*}\right)^2 \quad (2.48)$$

Of course, the electron in this system also experiences the potential jump upon entering the silicon dioxide and the boundary condition $\psi(0) = 0$ must be applied.

If the repulsive image term of Eq.(2.47) were absent the system would be the exactly solvable one of a triangular potential well where the eigenfunctions are given by the Airy functions. When the image term is present a simple variational calculation yields very accurate values for the electric sub-band energy levels. A trial function of the form

$$\psi(z) = e^{-\alpha z/2} \sum_{n=0}^N A_n z^{n+1} \quad (2.49)$$

is chosen. Notice that this trial function satisfies the correct boundary conditions. As in the previous situations, the linear variational parameters A_n lead to a matrix equation whose eigenvalues are optimized by varying the parameter α . The binding energy of the electron is therefore given by

$$E_b = E(\mathcal{H}_0) - E(\mathcal{H}) \quad (2.50)$$

and is dependent upon the electric field through Eqs.(2.46) and (2.47).

This system has been considered by several different authors recently. Martin and Wallis³⁶ have used a simple variational form to calculate binding energies only when the impurity is located on the interface. Lipari³⁷ has utilized a basis set which is certainly

correct when the impurity is on the interface but may not be so when the impurity is at a finite distance from the semiconductor/oxide interface. Hipolito and Campos³⁸ have used the variational forms of Martin and Wallis to calculate the effect of electrons in the electric sub-bands screening the impurity potential and thus changing the binding energy. This screening shall not be considered further in this report.

The binding energy of an electron to a donor impurity located on the interface between the silicon and silicon dioxide as a function of electric field is presented in Fig. 2.8. The results of Martin and Wallis and those of Lipari, which are the same as in the present calculation are presented. Because of the simple variational form the results of Martin and Wallis lie below those of Lipari and of the present calculation. The binding energy given by Fig. 2.8 is larger than that found experimentally by Harstein and Fowler, but as shall be seen when the impurity is moved off the interface and into the oxide layer the binding energy decreases.

The binding energy of the electron at zero field is exhibited in Figs. 2.9 and 2.10 as a function of impurity distance from the interface. In the first of these figures the donor impurity is located in the silicon layer while the second locates the impurity in the silicon dioxide layer. As can be readily seen there is a large discrepancy between the present calculation and the results of Lipari. This is most likely caused by Lipari's use of an incorrect basis set. While noting the importance of the boundary

Fig. 2.8 Binding energy of an electron to a donor impurity located on the interface between the silicon and silicon dioxide as a function of electric field. Energy is in units of effective Rydbergs while the electric field is given in electrostatic units (esu).

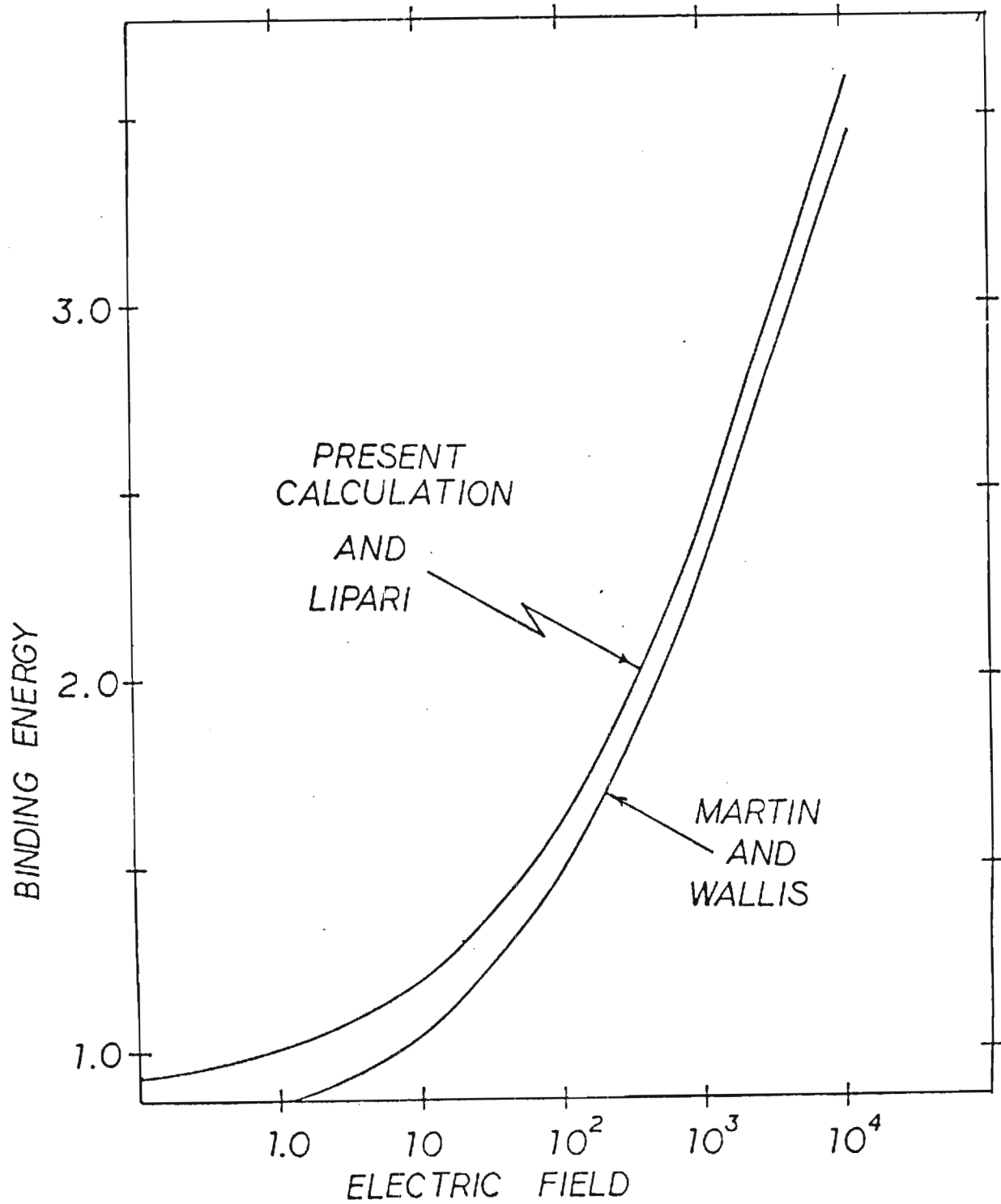


Fig. 2.9 Binding energy at zero field as a function of impurity distance into the silicon (semiconductor) layer.

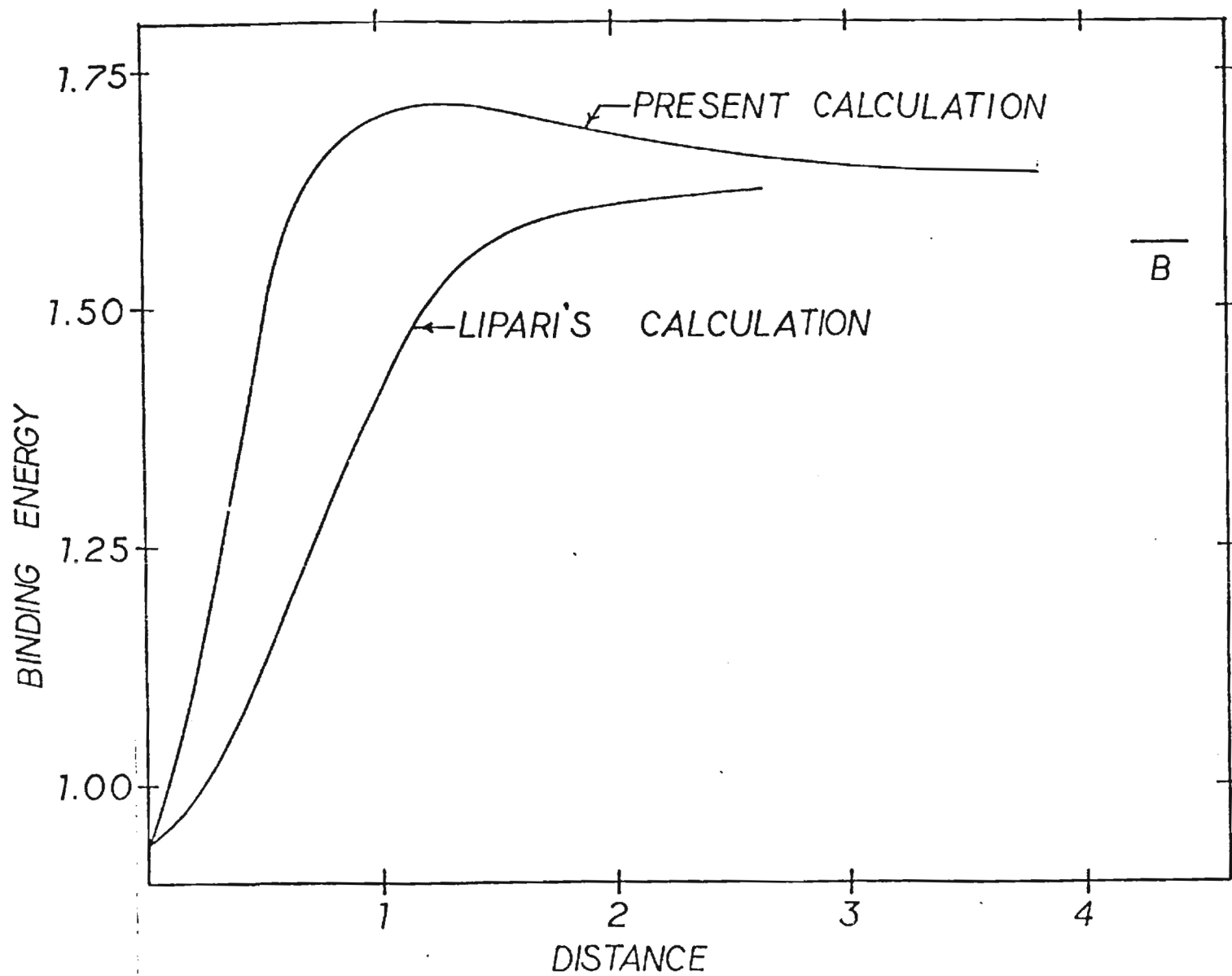
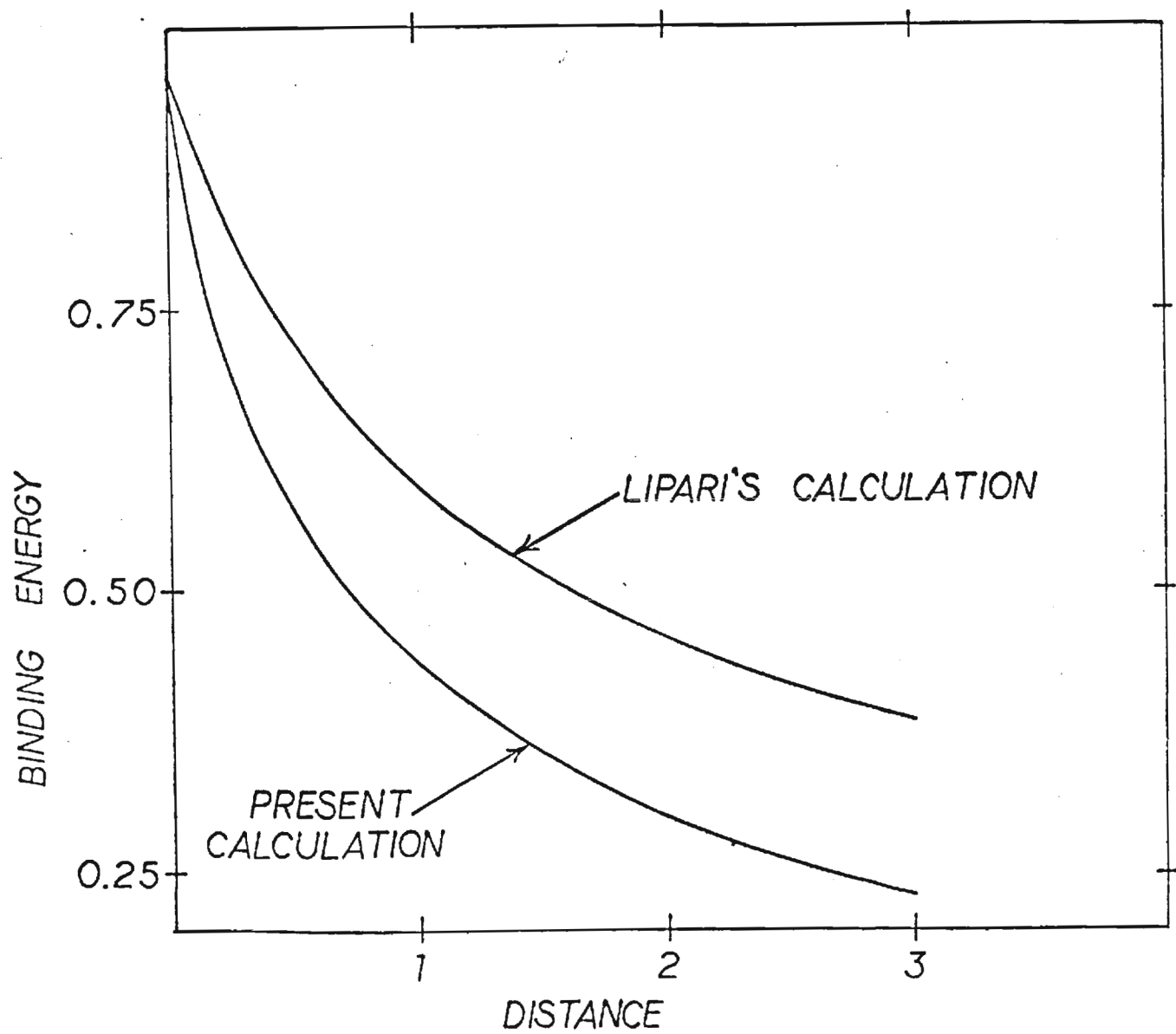


Fig. 2.10 Binding energy at zero field as a function of impurity distance into the silicon dioxide layer.



condition $\psi = 0$ on the interface, Lipari chooses as a basis set

$$\psi_m(\vec{r}) = \sum_i f_i(r) Y_{\ell_i}^m(\theta, \varphi) \quad (2.51)$$

where

$$f_i(r) = \sum_j c_{ij} e^{-\alpha_j r} \quad (2.52)$$

and the C_{ij} and α_j are the linear and non-linear variational parameters respectively. Later it is noted that only the $\ell = \text{odd}$ terms contribute to the ground state in Eq. (2.51) ($m=0$). But this is only correct when the impurity is located on the interface and this is illustrated by the coincidence of the results at $R=0.0$. The point to note in this connection is that the binding energy of the electron decreases more rapidly as a function of impurity distance from the interface (when in the oxide layer) than has been calculated by Lipari.

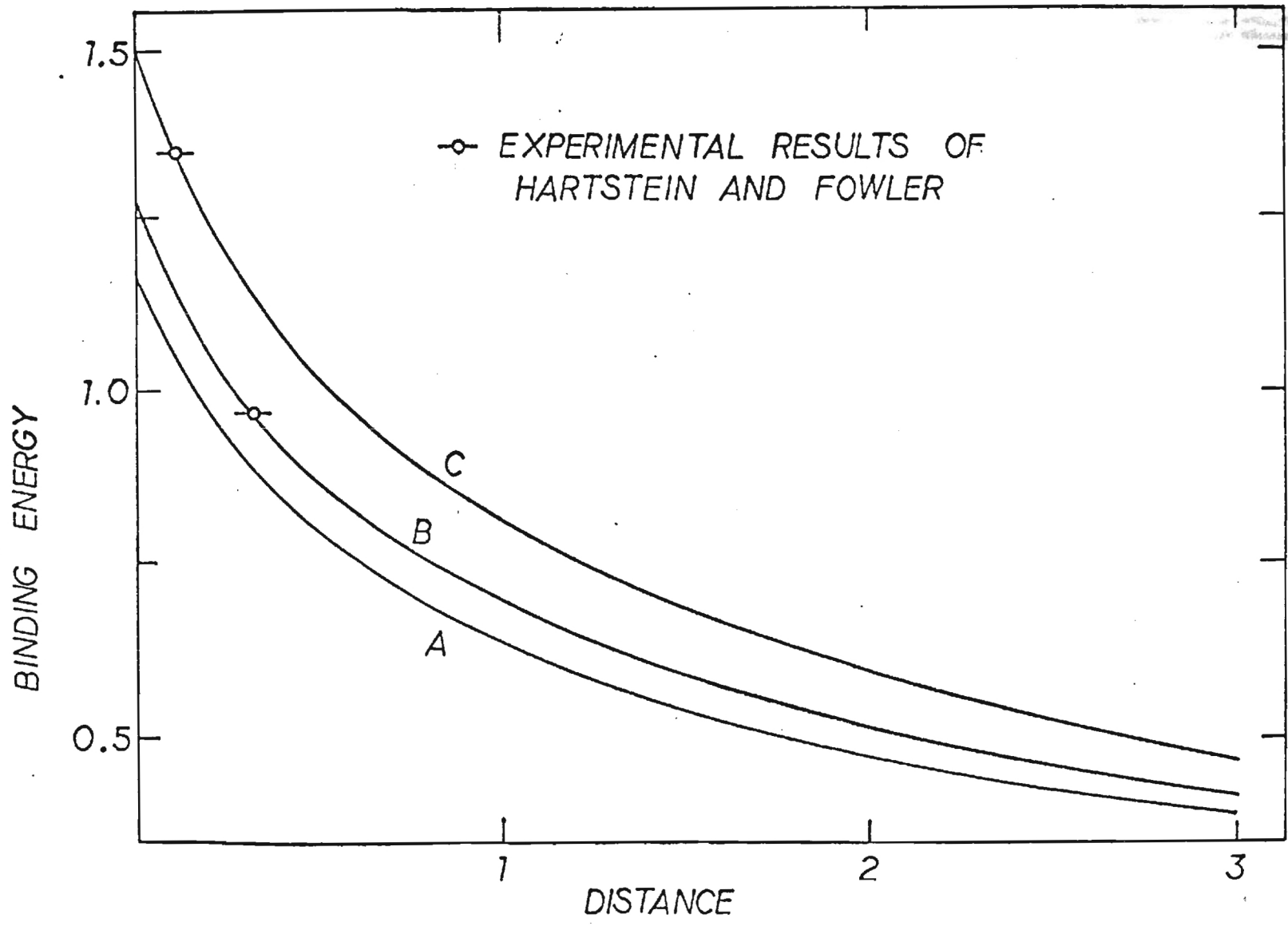
The electron binding energy to an impurity center located in the oxide layer for several electric field strengths has been calculated and these results are presented in Table 2.4 and Fig. 2.11. Also shown are the experimental results of Hartstein and Fowler who have found that for electric fields of 19.9 and 60.4 esu the binding energies are 18 and 25 meV, respectively. These results differ from those of Lipari inasmuch as distance from the interface does not turn out to be the same for both field strengths. The binding energy of 18 meV for the field strength of 19.9 esu occurs at approximately 10 \AA , while that for the 25 meV binding energy at the 60.4 esu field

TABLE 2.4

Binding energy as a function of impurity distance into the oxide layer for several values of the electric field strength.

R	$\epsilon = 0.0$ esu	$\epsilon = 10.0$ esu	$\epsilon = 19.9$ esu	$\epsilon = 60.4$ esu
0.0	0.9423	1.1949	1.2903	1.5062
0.2	0.7327	0.9723	1.0566	1.2373
0.4	0.6143	0.8437	0.9198	1.0762
0.6	0.5347	0.7553	0.8298	0.9627
0.8	0.4763	0.6891	0.7530	0.8762
1.0	0.4311	0.6369	0.6960	0.807
1.2	0.3949	0.5942	0.6492	0.7499
1.4	0.3650	0.5584	0.6097	0.7017
1.6	0.3398	0.5277	0.5757	0.6602
1.8	0.3183	0.5010	0.5461	0.6239
2.0	0.2996	0.4775	0.5199	0.5920
3.0	0.2336	0.3912	0.4234	0.4747

Fig. 2.11 Binding energy at several field strengths as a function of impurity distance into the silicon dioxide layer. The experimental results of Hartstein and Fowler are also included. The curve A is at 10 esu, B at 19.9 esu and C at 60.4 esu electric field strength.



strength occurs at $\sim 4 \text{ \AA}$ into the oxide layer.

APPENDIX A

ENERGIES FOR SOME EXCITED STATES OF THE
HYDROGEN/IMPENETRABLE WALL SYSTEM

Table A.1 Properties of the fourth excited state of the hydrogen/ impenetrable wall system. $E(m,p)$ denotes the energy of the p -th eigenvalue with an azimuthal quantum number of m . Note the discontinuity in the properties between $R=3.4a_0$ and $R=3.6a_0$ indicating a level crossing.

R	$E(0,4)$	$\bar{\mu}_z$	\bar{T}	\bar{V}
0.0	-0.0625	-	0.0625	-0.1250
0.2	-0.0637	-22.77	0.0649	-0.1286
0.4	-0.0650	-21.91	0.0676	-0.1326
0.6	-0.0663	-21.04	0.0705	-0.1368
0.8	-0.0677	-20.16	0.0736	-0.1413
1.0	-0.0692	-19.27	0.0770	-0.1463
1.2	-0.0709	018.38	0.0808	-0.1517
1.4	-0.0726	-17.47	0.0851	-0.1576
1.6	-0.0744	-16.55	0.0898	-0.1642
1.8	-0.0764	-15.62	0.0952	-0.1716
2.0	-0.0785	-14.66	0.1013	-0.1799
3.0	-0.9359	- 9.45	0.1540	-0.2476
3.2	-0.9793	- 8.29	0.1724	-0.2703
3.4	-0.1029	- 7.10	0.1947	-0.2976
3.6	-0.1085	-18.45	0.1145	-0.2229
3.8	-0.1088	-18.36	0.1143	-0.2231
4.0	-0.1091	-18.29	0.1141	-0.2232
5.0	-0.1100	-18.01	0.1133	-0.2233

Table A.2 Properties of the fifth excited state of the hydrogen/ impenetrable wall system.

R	E(1,2)	μ_z	\bar{T}	\bar{V}
0.0	-0.0625	-	0.0625	-0.1250
0.2	-0.0641	-25.33	0.0658	-0.1299
0.4	-0.0659	-24.39	0.0695	-0.1354
0.6	-0.0678	-23.44	0.0737	-0.1415
0.8	-0.0698	-22.46	0.0784	-0.1482
1.0	-0.0720	-21.48	0.0835	-0.1555
1.2	-0.0744	-20.51	0.0888	-0.1632
1.4	-0.0768	-19.58	0.0942	-0.1710
1.6	-0.0793	-18.67	0.0993	-0.1786
1.8	-0.0818	-17.83	0.1040	-0.1858
2.0	-0.0842	-17.06	0.1080	-0.1923
3.0	-0.0944	-14.17	0.1189	-0.2132
4.0	-0.1009	-12.42	0.1209	-0.2218
5.0	-0.1048	-11.29	0.1202	-0.2250

REFERENCES

1. A. Michels, J. DeBoer and A. Bijl, *Physica* 4, 981 (1937).
2. A. Sommerfeld and H. Welker, *Ann. Phys.* 32, 56 (1938).
3. S. R. De Groot and C. A. TenSeldom, *Physica* 12, 669 (1946).
4. L. W. Bruch and Th. W. Ruijgrok, *Surf. Sci.* 79, 508 (1979).
5. J. D. Levine, *Phys. Rev.* 140, 586 (1965).
6. L. Brillouin, *Comptes Rendus Acad. Sci.* 204, 1863 (1937).
7. G. D. Wasserman, *Proc. Cambridge Phil. Soc.* 44, 251 (1947).
8. N. Cabrera, *Cahirs Phys.* 31, 24 (1948).
9. H. Feshbach, *Phys. Rev.* 65, 307 (1944).
10. P. M. Morse and H. Feshbach, Methods of Theoretical Physics (McGraw Hill Book Co., New York, 1953).
11. L. Schiff, Quantum Mechanics (McGraw Hill Book Co., New York, 1968).
12. Ref. 10, Chapter 9.
13. S. H. Gould, Variational Methods for Eigenvalue Problems (University of Toronto Press, Toronto, 1966).
14. S. T. Epstein, The Variational Method in Quantum Chemistry (Academic Press, New York, 1974).
15. H. L. Davis, *J. Chem. Phys.* 37, 1508 (1962).
16. P. O. Löwdin and H. Shull, *Phys. Rev.* 101, 1730 (1956).
17. J. O. Hirschfelder and J. F. Kincaid, *Phys. Rev.* 52, 658 (1937).
18. J. C. Slater, *J. Chem. Phys.* 1, 687 (1933).
19. G. G. Kleiman and U. Landman, *Phys. Rev.* B8, 5484 (1973);
U. Landman and G. G. Kleiman, Surface and Defect Properties of Solids, M. W. Roberts and J. M. Thomas, Eds., The Chemical Society (London, 1977). Vol. 6, pp. 1-105;
E. Zaremba and W. Kohn. *Phys. Rev.* B15, 1769 (1977).

20. L. K. Haines and D. H. Roberts, Am. J. of Phys. 37, 1145 (1969).
21. M. W. Cole, Phys. Rev. 82, 4239 (1970).
22. A. Animalu, Intermediate Quantum Theory of Crystalline Solids (Prentice-Hall, Inc., Englewood Cliffs, 1977).
- 23a. W. Kohn and J. M. Luttinger, Phys. Rev. 98, 915 (1955).
- 23b. W. Kohn, Solid State Phys. 5, 257 (1957).
24. S. T. Pantelides, Rev. Mod. Phys. 50, 797 (1978).
25. B. W. Levinger and D. R. Frankl, J. Phys. Chem. Solids 20, 281 (1961).
26. J. C. Hensel, H. Hasegawa, and M. Nakayama, Phys. Rev. 138, A225 (1965).
27. R. A. Faulkner, Phys. Rev. 184, 713 (1969).
28. R. J. Bell, W. T. Bousman, Jr., G. M. Goldman and D. G. Rathbun, Surf. Sci. 7, 293 (1967).
29. B. V. Petukhov, V. L. Pokrouskii, and V. Chaplik, Soviet Physics - Solid State 9, 51 (1967).
30. A. A. Karpushin, Soviet Physics - Solid State 10, 2793 (1969).
31. A. A. Karpushin, Soviet Physics - Solid State 11, 1748 (1970).
32. F. Stern and W. E. Howard, Phys. Rev. 163, 816 (1967).
33. L. J. Sham and M. Nakayama, Surf. Sci. 73, 272 (1978).
34. A. Hartstein and A. B. Fowler, Phys. Rev. Lett. 34, 1435 (1975).
35. A. Hartstein and A. B. Fowler, Surf. Sci. 73, 19 (1978).
36. B. G. Martin and R. F. Wallis, Phys. Rev. B18,
37. N. O. Lipari, J. Vac. Sci. Technol. 15, 1412 (1978).
38. O. Hipolite and V. B. Campos, Phys. Rev. B19, 3083 (1979).

II. PUBLICATIONS

(Report period starting September 1979)

1. "Microscopic Theory of Thermal Desorption and Dissociation Processes Catalyzed by a Solid Surface", Phys. Rev. B 21, 3256 (1980).
Gopa De and Uzi Landman (GIT); Mark Rasolt (ORNL).
2. "Lattice Relaxation at Metal Surfaces: An Electrostatic Model", Phys. Rev. B 21, 448 (1980).
Uzi Landman and N. R. Hill (GIT); Mark Mostoller (ORNL).
3. "Substrate Effects on Long-Range Order and Scattering from Low-Dimensional Systems", Phys. Rev. B (August 15, 1980).
C. L. Cleveland, C. S. Brown and Uzi Landman.
4. "Substrate Effects on Long-Range Order and Scattering from Low-Dimensional Systems" in "Ordering in Two-Dimensions", S. K. Sinha, Ed. (North-Holland, 1980).
C. L. Cleveland, C. S. Brown and Uzi Landman.
5. "Epitaxial Crystallization from a Melt", in "Ordering in Two-Dimensions", S. K. Sinha, Ed. (North Holland, 1980).
Uzi Landman, C. L. Cleveland and C. S. Brown.
6. "Epitaxial Crystallization from a Melt: A Surface Molecular Dynamics Study", Phys. Rev. Letts. (1980).
Uzi Landman, C. L. Cleveland and C. S. Brown.
7. "Correlation Effects on Frequency Dependent Conductivity: Application to Superionic Conductors", Solid State Comm. 32, 1207 (1979).
M. F. Shlesinger.
8. "Recombination Reactions in Aqueous Glasses", J. Non-Cryst. Solids.
M. F. Shlesinger.
9. "Desorption and Dissociation on Surfaces: Modern Views", in "Surface Reactions", Uzi Landman, Ed. (AIP, N.Y., 1980).
Uzi Landman.

10. "Transport and Diffusion Controlled Reactions on Heterogeneous Catalytic Surfaces", in "Surface Reactions", Uzi Landman, Ed. (AIP, N.Y., 1980).
M. F. Shlesinger and Uzi Landman.
11. "Prospects for Studying Chemisorption Kinetics Using Current Fluctuations",
Surface Science, 95, 67 (1980).
G. S. De and H. Suhl.
12. "Surface Reactions", a book edited by Uzi Landman (AIP, N.Y., 1980).

Publications Documented in the 1979 Annual Report
which appeared in print since.

1. "Stochastic Theory of Multistate Diffusion in Perfect and Defective Systems. I. Formalism", Phys. Rev. B 19, 6207 (1979).
Uzi Landman and M. F. Shlesinger.
2. "Stochastic Theory of Multistate Diffusion in Perfect and Defective Systems. II. Case Studies", Phys. Rev. B 19, 6220 (1979).
Uzi Landman and M. F. Shlesinger.
3. "Electron Scavenging in Glasses", J. Chem. Phys. 70, 4813 (1979).
M. F. Shlesinger.
4. "Conditions for a Rate-Maximizing Temperature in Heterogeneous Catalysis", J. Catalysis 61, 270 (1980).
M. F. Shlesinger and Uzi Landman.
5. "Quadrupole Interaction in the Scattering of H₂ from the Surface of LiF: Rotational Transitions", Phys. Rev.
N. R. Hill.
6. "High Frequency Vibrational Modes at Stepped Pt(111) Surfaces", Phys. Rev. B 20, 1775 (1979).
Mark Mostoller (ORNL), Uzi Landman.

III. CONFERENCE TALKS

APS Meeting, March 1980, (NYC).

APS Bulletin 25(3), 292 (1980).

Substrate Effects on Long-Range Order and Scattering from Low-Dimensional Systems. * Charles L. Cleveland, Charles S. Brown, and Uzi Landman, Georgia Institute of Technology. -- Using solvable models it is shown that coupling 1D and 2D lattices to substrates produces significant alterations in their long-range order and scattering characteristics. These effects persist even if the coupling is rather weak. Analytical expressions for Peierls's long-range-order parameter, $\langle \delta^2 \rangle$, are obtained and their asymptotic behaviour evaluated. The asymptotic forms reduce to the known results for strict 1D and 2D systems when the coupling to the substrate vanishes. Using the expressions for $\langle \delta^2 \rangle$ the frequency integrated dynamical structure factors, $n_S(Q)$, for scattering from these "Quasi-1D and 2D" systems are evaluated. The results demonstrate the alterations introduced by the coupling and provide functional forms which could be used to fit neutron scattering data from adsorbed layers.

*Supported by U.S. DOE Contract No. EG-S-05-5489

APS Bulletin 25(3), 234 (1980).

DH I Lattice Relaxation at Metal Surfaces: An Electrostatic Model. Uzi Landman, Kees N. Hill,** Georgia Institute of Technology, and Mark Mosteller, OPML, Tenn. -- Surface relaxation in metals is investigated via a method that combines the contribution to the force on ions in surface layers due to the delocalized valence electron distribution with that due to the interaction with the positive ionic charges in the planar nets. Three models for the electrostatic density in the surface region are studied and compared: (a) an abrupt termination (b) an exponential variational form (c) self-consistent distribution derived from the jellium model. Pseudopotential corrections are also investigated. Ions in an arbitrary number of layers are allowed to relax and the equations for static equilibrium are solved by a fast converging iterative scheme. The surface structures of the low-index faces of Ag, Li, Na and Cu are investigated yielding results consistent with available LEIS analyses. The importance of multi-layer relaxation mechanisms, the dependence on the model for the surface electron charge density and effects due to pseudopotential corrections are demonstrated.

*Supported by US DOE Contract No. EG-S-05-5489 and No. W-7405-eng-26

**Present address, Univ. of Virginia, Charlottesville.

APS Bulletin 25(3), 434 (1980).

NH 6 Correlation Effects on Frequency Dependent Conductivity: Application to Superionic Conductors. MICHAEL SHERINGBER, Georgia Tech. -- The Scher-Lax model for the calculation of A.C. conductivity is modified to allow for temporal and spatial correlations. If, due to, say, lattice relaxation effects, an ion is most likely to continue to move in the same direction (caterpillar mechanism), then the real part of the conductivity will saturate, at large frequencies, below the D.C. level. The reverse will be true if a bounce-back mechanism dominates. These two types of correlations may be related to the behavior of the superionic conductors AgI and Na- β -alumina, respectively. The degree of disorder in the hopping sites determines the distribution of the ionic transition rates which in turn governs the details of the conductivity curve. The frequency dependent conductivity due to the motion of an ionic dimer is also analyzed.

EPITAXIAL CRYSTALLIZATION FROM A MELT AND SURFACE MELTING:

A SURFACE MOLECULAR DYNAMICS STUDY*

Uzi Landman, C. L. Cleveland and C. S. Brown

School of Physics

Georgia Institute of Technology

Atlanta, Ga. 30332

The processes of epitaxial crystal growth and surface melting are studied using a newly developed Surface Molecular Dynamics technique. In order to investigate surface processes and in particular non-equilibrium surface phenomena such as crystallization, we allow for a dissipative dynamic coupling between a surface region -- in which periodic boundary conditions parallel to the surface plane only are imposed -- and a bulk reservoir which possesses the full 3D periodic boundary conditions. The full dynamics of both parts is computed by integrating the coupled classical equations of motion. The bulk unit block as well as the surface region contain 500 particles each. In the study of epitaxial crystallization an equilibrated surface system (exposing the (100) face for Argon) equilibrated at $T = 47.9^{\circ}\text{K}$ was prepared and put in contact with an equilibrated liquid sample (500 particles) at: (a) $T = 88.3^{\circ}\text{K}$ and (b) a supercooled liquid at $T = 47.9^{\circ}\text{K}$. The evolution of these combined non-equilibrium systems was followed monitoring the structure characteristics of the system (particle density profiles, pair distribution functions, Voronoi polyhedra signatures, translational and orientational order parameters) and its dynamical correlations. It is observed that in case (a), upon solid/liquid contact the outermost solid surface region disorders in layers followed by the development of a layered structure in the liquid region. In case (b) an "explosive" crystallization occurs. Upon achieving equilibrium a crystalline form is obtained. The ability of epitaxial crystallization to anneal certain surface structural defects is demonstrated.

* Supported by U.S. DOE Contract No. EG-77-S-05-5489.

Presented at:

"Ordering in 2D", Lake Geneva, Wisconsin, May, 1980.

SUBSTRATE EFFECTS ON LONG-RANGE ORDER AND SCATTERING
FROM LOW-DIMENSIONAL SYSTEMS*

Charles L. Cleveland, Charles S. Brown and Uzi Landman

School of Physics

Georgia Institute of Technology

Atlanta, Ga. 30332

Using solvable models it is shown that coupling 1D and 2D lattices to substrates produces significant alterations in their long-range order and scattering characteristics. These effects persist even if the coupling is rather weak. Analytical expressions for Peierls's long-range-order parameter, $\langle \delta_n^2 \rangle$, are obtained and their asymptotic behaviour evaluated. The asymptotic forms reduce to the known results for strict 1D and 2D systems when the coupling to the substrate vanishes. Using the expressions for $\langle \delta_n^2 \rangle$ the frequency integrated dynamical structure factors, $S(\vec{Q})$, for scattering from these "Quasi-1D and 2D" systems are evaluated. The results demonstrate the alterations introduced by the coupling and provide functional forms which could be used to fit neutron scattering data from adsorbed layers.

*Supported by U.S. DOE Contract No. EG-S-05-5489.

Presented at:

"Ordering in 2D", Lake Geneva, Wisconsin, May, 1980.

EPITAXIAL CRYSTALLIZATION FROM A MELT

AND SURFACE MELTING: A SURFACE

MOLECULAR DYNAMICS STUDY^{*}

C. L. Cleveland, C. S. Brown and Uzi Landman

School of Physics

Georgia Institute of Technology

Atlanta, Ga. 30332

The processes of epitaxial crystal growth and surface melting are studied using a newly developed Surface Molecular Dynamics technique. In order to investigate surface processes and in particular non-equilibrium surface phenomena such as crystallization, we allow for a dissipative dynamic coupling between a surface region-in which periodic boundary conditions parallel to the surface plane only are imposed-and a bulk reservoir which possesses the full 3D periodic boundary conditions. The full dynamics of both parts is computed by integrating the coupled classical equations of motion, using appropriate interaction pair-potentials (Lennard-Jones for rare gas systems and pseudo-potentials for Rubidium). The bulk unit block as well as the surface region contain 500 particles each. In the study of epitaxial crystallization an equilibrated surface system (exposing the (100) face for Argon) equilibrated at $T = 47.9^{\circ}\text{K}$ was prepared and put in contact with an equilibrated liquid sample (500 particles) at: (a) $T = 88.3^{\circ}\text{K}$ and (b) a supercooled liquid at $T=47.9^{\circ}\text{K}$. The evolution of these combined non-equilibrium systems was followed for thousands of time steps (where the basic unit $t = 1.633 \times 10^{-14}$ sec), monitoring the structure characteristics of the system (particle density profiles, pair distribution functions, coordination, Voronoi polyhedra signatures, translational and orientational order parameters) and its dynamical correlations (kinetic coefficients). It is observed that in case (a), upon solid/liquid contact the outermost solid surface region disorders in layers followed by the development of a layered structure in the liquid region. The process of ordering is accompanied by the expulsion of latent heat which propagates (influencing the media in a nonlinear manner) via collective modes and eventually dissipates in the bulk. In case (b) an "explosive" crystallization of the supercooled liquid occurs. Upon achieving equilibrium a crystalline form is obtained. The ability of epitaxial crystallization to anneal certain structural defects in the surface region of the substrate is demonstrated. Details of the microscopic mechanisms of crystallization and surface melting are discussed.

^{*} Supported by U.S. DOE Contract No. EG-77-S-05-5489.

American Physical Society

March 24, 1980

Physics and Astronomy
Classification Scheme
Number 71.70

Suggested title of session in
which paper should be placed
Hydrogen-Bonded Silicon

Ab-initio Calculations on Hydrogen-bonded Silicon Clusters. A. C. Kenton, M. W. Ribarsky, Georgia Institute of Technology.*-- Unrestricted Hartree-Fock (UHF) molecular cluster calculations for the groundstate and various excited electronic states have been carried out for a Si_5H_{12} cluster for several different Si-H bond lengths. Each cluster is geometrically arranged in a diamond crystalline lattice. The adequacy of using a frozen core potential for the five silicon atoms has been established by comparison to a calculation allowing relaxation of the core on the one central silicon atom. The determination of the "band gap" of the cluster by using Koopmans' theorem versus ΔSCF calculations has shown electronic relaxation to be a significant factor. The cluster band gap is shown to appreciably change for the various Si-H bond lengths, yet the charge densities in the Si-Si bond regions remain similar illustrating the adequacy of the central bonding region. The charge densities that have been obtained are comparable to experimental x-ray and theoretical local and non-local pseudopotential slab calculations describing bulk silicon. Methods other than hydrogen saturators for describing the bulk boundary conditions will be discussed. *Supported in part by NSF Contract DMR77-22851 and US DOE Contract EG-S-05-5489

IV. PERSONNEL

1. Uzi Landman - Professor of Physics, Georgia Tech; Principal Investigator.
2. E. W. Montroll - Einstein Professor of Physics (University of Rochester) and Adjunct Professor to the School of Physics, Georgia Tech; in an adjunct capacity.
3. Dr. C. L. Cleveland - Post-doctoral Fellow.
4. Dr. R. Penã[~] - Post-doctoral Fellow (since Feb. 1, 1980).
5. Dr. R. Barnett - Post-doctoral Fellow (since Feb. 1, 1980).
6. Dr. M. F. Shlesinger - Research Scientist (until Jan. 31, 1980).
7. Dr. G. S. De - Post-doctoral Fellow (until Dec. 31, 1979).
8. D. F. MacMillen - Graduate Student (graduated).
9. C. S. Brown - Graduate Student.
10. L. Efsthathiou - Graduate Assistant (until June 30, 1980).
11. C. Kenton - Graduate Student.